

6/12

A NEUTRON DIFFRACTION STUDY OF  
THE STRUCTURE AND STRUCTURAL MODIFICATION OF  
MOLTEN ZINC HALIDES AND NICKEL HALIDES

by

Dennis A. Allen

A thesis submitted to the University of Leicester  
for the degree of Doctor of Philosophy

November 1989

UMI Number: U497255

All rights reserved

INFORMATION TO ALL USERS

The quality of this reproduction is dependent upon the quality of the copy submitted.

In the unlikely event that the author did not send a complete manuscript and there are missing pages, these will be noted. Also, if material had to be removed, a note will indicate the deletion.



UMI U497255

Published by ProQuest LLC 2015. Copyright in the Dissertation held by the Author.  
Microform Edition © ProQuest LLC.

All rights reserved. This work is protected against  
unauthorized copying under Title 17, United States Code.



ProQuest LLC  
789 East Eisenhower Parkway  
P.O. Box 1346  
Ann Arbor, MI 48106-1346



7500478647

x791593833

## CONTENTS

	Page
Abstract	v
Acknowledgments	vi
List of tables	vii
List of figures	viii
CHAPTER 1. NEUTRON SCATTERING AND MOLTEN SALTS	
1.1 Why Study Molten Salts?	1
1.2 Technological Interest in Molten Salts	2
1.3 Why Use Neutrons?	4
1.4 Previous Studies of Molten Salts	6
1.4.1 Molten Alkali Halides (1:1 Salts)	6
1.4.2 Molten Alkali-Earth Halides (2:1 Salts)	7
1.5 Structural Modification of Molten Salts	8
CHAPTER 2. THE THEORETICAL BACKGROUND TO LIQUID STRUCTURE DETERMINATION BY NEUTRON DIFFRACTION	
2.1 Description of a Liquid Structure	12
2.2 The Differential Scattering Cross-Section	13
2.3 Coherent and Incoherent Scattering	14
2.4 The Relationship Between $d\sigma/d\Omega$ and $g(r)$	15
2.5 A Scattering Experiment and the Static Approximation	17
2.6 Multi-Component Liquids	18
2.7 Theoretical Modelling of Liquid State Structures	21
2.7.1 Computer Simulations of Liquids	23
CHAPTER 3. EXPERIMENTAL DETAILS	
3.1 Neutron Scattering Requirements	26
3.2 Steady-State Neutron Diffraction	27
3.2.1 The D4B Diffractometer	27
3.3 Pulsed Neutron Diffraction	28
3.3.1 The Liquids and Amorphous Materials Diffractometer (LAD)	29
3.3.2 The General Purpose Powder Diffractometer (GPPD)	30

3.4	Sample Preparation	31
3.4.1	Preparation of the Mixtures	32
3.5	Neutron Diffraction Experimental Procedure	33
CHAPTER 4. THE ANALYSIS OF NEUTRON DIFFRACTION DATA		
4.1	Introduction	38
4.2	The Analysis of Steady-State Neutron Diffraction Data	38
4.2.1	Initial Data Treatment	38
4.2.2	Outline of the Data Reduction Procedure - Without Corrections	39
4.2.3	Multiple Scattering	40
4.2.4	Absorption Correction	42
4.2.5	Correction for Inelastic Scattering	43
4.2.6	The Calculation of $F(Q)$ for Steady-State Diffraction Data	45
4.3	The Analysis of Time-of-Flight Neutron Diffraction Data	47
4.3.1	Initial Data Treatment	47
4.3.2	The Multiple Scattering and Absorption Corrections	47
4.3.3	The Placzek Correction for Time-of-Flight Diffraction Data	48
4.3.4	The Calculation of $F(Q)$ for Time-of-Flight Diffraction Data	50
4.4	The Separation of Partial Structure Factors	51
4.4.1	Isotopic Substitution	51
4.4.2	The Long Wavelength Limit and the Sum Rule	53
4.5	Fourier Transformation to Real Space	55
4.6	Structural Features in the Distribution Functions	59
4.6.1	Peak Positions, Heights and Widths	59
4.6.2	Coordination Numbers	59
CHAPTER 5. THE APPLICATION OF THE MAXIMUM ENTROPY METHOD TO LIQUID STRUCTURE FACTOR DATA		
5.1	Introduction	63
5.2	Maximum Entropy - An Overview	64
5.3	Description of the Maximum Entropy Algorithm	66
5.4	The Image-Data Transformation	67

5.5	The Default Level for $g(r)$	69
5.5.1	Results of Some Tests	69
5.6	Total Distribution Functions	71
5.7	Summary	72
CHAPTER 6. THE STRUCTURE OF MOLTEN ZINC HALIDES		
6.1	Introduction	77
6.2	Experimental	80
6.3	Results	81
6.4	Summary of Observations	82
6.4.1	Zinc Chloride at 330°C	83
6.4.2	Zinc Chloride at 600°C	84
6.4.3	Zinc Bromide	84
6.4.4	Zinc Iodide	85
6.5	Discussion of Results	86
6.5.1	Tetrahedral Coordination	86
6.5.2	The Cation-Anion Principal Peak in $G(r)$	87
6.5.3	The Anion Structure	88
6.5.4	The Density of Zinc Chloride	89
6.5.5	Intermediate Range Order	89
6.6	Summary	92
CHAPTER 7. THE STRUCTURE OF MOLTEN ZINC CHLORIDE AND POTASSIUM CHLORIDE MIXTURES		
7.1	Introduction	108
7.2	Sample Description and Preparation	109
7.3	First Experimental Run	110
7.4	Second Experimental Run	111
7.5	Results and Structural Parameters	111
7.6	Discussion of Results	113
7.6.1	The Chlorine-Chlorine Structure	113
7.6.2	The Zinc-Chlorine Structure	115
7.6.3	The Potassium-Chlorine Structure	116
7.7	The Pre-Peak	117
7.8	Some Suggestions for Further Work	120
7.9	Summary	121

CHAPTER 8. MOLTEN MIXTURES OF NICKEL IN NICKEL HALIDES	
8.1 Metal-Molten Salt Solutions	136
8.2 Nickel in Nickel Halides	137
8.3 Nickel in Nickel Iodide	138
8.3.1 Experimental	138
8.3.2 Results	140
8.3.3 Summary of Observations	140
8.4 Nickel in Nickel Bromide	141
8.4.1 Experimental	141
8.4.2 Results	143
8.4.3 Summary of Observations	147
8.5 Discussion	149
8.5.1 Sub-Halide Complex Ion Formation	149
8.5.2 Non Complex-Forming Sub-Halide Ions	149
8.5.3 Double Ionisation	150
8.5.4 Intermediate Range Order	152
8.6 Summary	152
8.6.1 Structural Models	153
CHAPTER 9. CONCLUSIONS	
9.1 Introduction	168
9.2 Summary of Results and Suggestions for Further Work	
9.2.1 The Structure of Molten Zinc Halides	168
9.2.2 The Effect of a 'Structure Breaking' Alkali Halide on the Structure of a Network Liquid	171
9.2.3 The Addition of Excess Metal to a Molten 2:1 Salt	173
9.3 The State of Neutron Diffraction Instrumentation for Molten Salts	175
9.4 Concluding Remarks	176
REFERENCES	177

A NEUTRON DIFFRACTION STUDY OF  
THE STRUCTURE AND STRUCTURAL MODIFICATION OF  
MOLTEN ZINC HALIDES AND NICKEL HALIDES

by D.A.Allen

The structures of molten  $\text{ZnCl}_2$ ,  $\text{ZnBr}_2$  and  $\text{ZnI}_2$  have been determined by pulsed neutron diffraction. A tetrahedral configuration of anions around each cation was found for all three salts, which was extremely well defined for  $\text{ZnCl}_2$  and  $\text{ZnBr}_2$ . Intermediate range ordering was also observed for all three salts and was seen to increase through the series from  $\text{ZnCl}_2$  to  $\text{ZnI}_2$ . These observations are discussed with reference to previous studies of molten 2:1 salts, ion polarization effects and directional dependence of interionic forces. The effect of temperature upon the structure of molten  $\text{ZnCl}_2$  has also been investigated.

In addition to this study of pure molten salts, the effect of structural modification of the 'network liquid'  $\text{ZnCl}_2$  by the addition of 'structure breaking' KCl has been studied. Pulsed neutron diffraction patterns were obtained from molten mixtures across the composition range. Upon addition of KCl, the local tetrahedral structure around each zinc ion was found to be very stable, even up to high KCl concentrations, and the intermediate range ordering in  $\text{ZnCl}_2$  not only persists, but was seen to increase, and to still be present even at 81% KCl concentration. Possible explanations of this behaviour are discussed and suggestions for further work are made.

The structural modification of molten nickel halides by the addition of nickel metal has also been studied. A solution of  $\text{NiI}_2$  + 9 molar% Ni has been investigated by pulsed neutron diffraction from two isotopically enriched samples, and a solution of  $\text{NiBr}_2$  + 9 molar% Ni has been investigated by steady-state neutron diffraction from three isotopic samples. There was no evidence for subhalide complex ion formation involving more than one metal atom. The results suggest that nickel is ionising according to the equation  $\text{Ni} \rightarrow \text{Ni}^{2+} + 2\text{e}^-$ , with nickel ions occupying existing sites within the liquid structure and electrons acting so as to screen the interionic potentials.

The maximum entropy method has been discussed and applied to the problem of structure factor data analysis. This method proved to be useful in the interpretation of some of the data presented in this thesis.

## ACKNOWLEDGMENTS

I would like to thank Dr R.A. Howe for his guidance and supervision throughout the course of this work and Dr N.D. Wood for much helpful discussion and instruction, especially during the early stages of my Ph.D.

Thanks are also due to the technical staff of the Physics department, particularly Mr J.S.G. Taylor and Mr S.C. Thornton, for their expert technical support. I am particularly grateful to Mr A. Wardle for his many glass working skills and his instruction, and for his patience and helpfulness in doing jobs - often at short notice.

For the preparation of the isotopic samples and for some chemical analysis I am indebted to Mr P. Gullidge at the University of Bristol.

The scientific and technical staff at RAL, ILL and IPNS are also thanked for their support in carrying out the experiments, particularly Dr W.S. Howells and Dr P. Chieux. I also wish to thank the SERC for the award of a studentship.

Finally, I would like to express my gratitude to my parents for their support and encouragement throughout my education, and to Miss C. Rimmer for her help and grammatical advice during the writing of this thesis.

## LIST OF TABLES

	Page
1.1 Diffraction studies of molten 2:1 salts	11
3.1 LAD instrument parameters	34
3.2 GPPD instrument parameters	35
6.1 Physical and structural parameters for molten 2:1 halides	94
6.2 Data analysis parameters for the molten zinc halides	95
6.3 Structural features of the molten zinc halides	96
7.1 Data analysis parameters and the contributions of the partials to the coherent scattering for the ZnCl <sub>2</sub> -KCl mixtures	122
7.2 Structural parameters of the Zn-Cl peak for the ZnCl <sub>2</sub> -KCl mixtures	123
7.3 Contributions made by the two S <sub>ClCl</sub> (Q)'s to the total F(Q) model fits	124
7.4 The pre-peak parameters for the ZnCl <sub>2</sub> -KCl mixtures	124
8.1 Isotopic compositions, scattering lengths and data analysis parameters for the NiI <sub>2</sub> +9%Ni samples	154
8.2 Isotopic compositions, scattering lengths and data analysis parameters for the NiBr <sub>2</sub> +9%Ni samples	155
8.3 Structural parameters for molten NiBr <sub>2</sub> +9%Ni and pure NiBr <sub>2</sub>	156

## LIST OF FIGURES

	Page
2.1 The scattering of a plane wave by an assembly of point particles	13
3.1 The D4B diffractometer	36
3.2 The LAD diffractometer	37
5.1 Maximum entropy test results with flat and smoothly varying default levels	74
5.2 ME test results with a sharply varying default level and with good and poor quality data sets	75
5.3 Comparison of ME solutions obtained from full and truncated data sets	76
6.1 The partial distribution functions for molten $\text{ZnCl}_2$	97
6.2 Electrical conductivities of molten zinc halides	98
6.3 Raw data from LAD measured by the $20^\circ$ detectors	99
6.4 Raw data from LAD measured by the $90^\circ$ detectors	100
6.5 $F(Q)$ for $\text{ZnCl}_2$ at $330^\circ\text{C}$ for each detector angle	101
6.6 $F(Q)$ for $\text{ZnBr}_2$ for each detector angle	102
6.7 $F(Q)$ for $\text{ZnI}_2$ for each detector angle	103
6.8 Combined $F(Q)$ 's for the molten zinc halides	104
6.9 Total distribution functions for the zinc halides	105
6.10 $F(Q)$ for $\text{NiI}_2$ at $830^\circ\text{C}$ and $900^\circ\text{C}$	106
6.11 Model fits to the total $G(r)$ 's for the zinc halides using the recombined and rescaled partials	107
6.12 $I(Q)$ and $T(r)$ for vitreous $\text{ZnCl}_2$	107
7.1 The phase diagram of the $\text{ZnCl}_2$ -KCl system	125
7.2 $F(Q)$ for the 50% KCl solution at $450^\circ\text{C}$ for each of the detector angles	126
7.3 Comparison of the $F(Q)$ 's for the 33% and 50% KCl solutions at $340^\circ\text{C}$ and $450^\circ\text{C}$ , and for the 67% KCl solution from the two separate experiments	127
7.4 $F(Q)$ 's for all of the $\text{ZnCl}_2$ -KCl solutions studied	128
7.5 Total $G(r)$ 's for all of the $\text{ZnCl}_2$ -KCl solutions	129
7.6 Maximum entropy solutions to fit the high KCl concentration $F(Q)$ data using flat default levels	130

7.7	ME solutions to fit the high KCl concentration $F(Q)$ data using default levels which are zero in the low $r$ region	131
7.8	Model fit to $F(Q)$ for the 33% KCl solution using recombined $S(Q)$ 's for the two pure salts	132
7.9	Model fit to $F(Q)$ for the 50% KCl solution using recombined $S(Q)$ 's for the two pure salts	133
7.10	Model fit to $F(Q)$ for the 67% KCl solution using recombined $S(Q)$ 's for the two pure salts	134
7.11	Behaviour of the pre-peak with KCl concentration	135
8.1	$F(Q)$ for natural $NiI_2+9\%Ni$ for each detector angle	157
8.2	$F(Q)$ for 'zero' $NiI_2+9\%Ni$ for each detector angle	158
8.3	$S_{II}(Q)$ and $g_{II}(r)$ for $NiI_2+9\%Ni$ and pure $NiI_2$	159
8.4	$F'(Q)$ and $G'(r)$ for $NiI_2+9\%Ni$ and pure $NiI_2$	160
8.5	Raw data from D4B for natural and 'zero' $NiBr_2+9\%Ni$ and for the empty container and furnace	161
8.6	$F(Q)$ 's for natural, 'zero' and '62' $NiBr_2+9\%Ni$	162
8.7	Partial structure factors for $NiBr_2+9\%Ni$	163
8.8	$g_{BrBr}(r)$ . Fourier transforms and maximum entropy solutions for $NiBr_2+9\%Ni$ and pure $NiBr_2$	164
8.9	$g_{NiBr}(r)$ . Fourier transforms and maximum entropy solutions for $NiBr_2+9\%Ni$ and pure $NiBr_2$	165
8.10	$g_{NiNi}(r)$ . Fourier transforms and maximum entropy solutions for $NiBr_2+9\%Ni$ and pure $NiBr_2$	166
8.11	The partial distribution functions for $NiBr_2+9\%Ni$	167
8.12	A hexagonal close packed structural model	167

## CHAPTER 1

### NEUTRON SCATTERING AND MOLTEN SALT STRUCTURE

#### 1.1 Why Study Molten Salts?

The liquid state is the least understood of the three main phases of matter. In lacking the long range order and periodicity of the crystalline phase, it has defied the successful theoretical treatment that Bloch's theorem affords. For the gaseous state, the relatively low density means that the short range interactions between particles can either be ignored, as for an ideal gas, or approximately corrected for, as with a van der Waals gas. At higher densities, these approximations break down and for the liquid state, the structure and properties are dominated by the particle interactions.

In order to more fully understand the liquid state, it is profitable to study simple systems such as condensed inert gases, molten salts or liquid metals. These consist of single atoms or ions, and the interparticular forces and the dynamics should be simpler than for the more complex molecular systems.

In condensed inert gases, the interatomic forces are relatively short range and can be adequately described using Lennard-Jones potentials. For example, see Yarnell et. al. (1973). For ionic liquids, longer range Coulombic forces are also present, and these play a major role in determining the structure and dynamics of the liquid. For liquid metals, there exists the additional contribution from ion-ion Coulomb interactions screened by a conduction electron gas, as well as ion-electron and electron-electron interactions. Ionic solutions consisting of molecular solvents and ionic solutes, are another class of ionic liquid which have attracted much attention. The situation here is complicated by the fact that potentials involving molecules depend upon molecular orientation, and often include contributions from other types of forces such as hydrogen bonding and dipole-dipole interactions.

Monatomic molten salts represent the simplest class of ionic liquids: their structure and dynamics are dominated by

simple long range Coulomb forces and short range repulsions, and they lack the complications of potentials that depend upon molecular orientation. It is for this reason that much effort has been directed in recent years to the understanding of the structure and dynamics of molten salts, through both experimental observation and theoretical modelling.

## 1.2 Technological Interest in Molten Salts

As well as the theoretical interest in the understanding of molten salts, there is also widespread industrial use of molten salts, as well as many potential uses. The following are a few examples.

i) The extraction of metals, especially aluminium, from their ores is one of the chief industrial uses of molten salts. Alkali metals, first row transition metals and the refractory group, as well as the lanthanides and actinides, are all currently extracted from their salts using either electrolytic or redox processes. In addition, liquid metal purification involving the oxidation of impurities is achieved using molten salts.

ii) The thermal properties of molten salts (their high heat capacity per unit volume and their good thermal conductivity) together with their generally good wetting properties, ensures the rapid heat transfer that is necessary for some bulk modifications of metals. For example annealing, quenching and tempering. In addition, surface modifications of metals, such as carburising, nitriding, boriding, siliciding and metalliding, are possible using molten salts containing the appropriate elements, as well as the anodizing and cleaning of metallic surfaces.

iii) The electroplating of high purity, corrosion resistant metals can be achieved using molten salt electrolytes. The relatively low resistance of such melts when compared with other ionic media, means that Ohmic losses are reduced. These losses, however, are often still sufficient to maintain the salt in its molten state.

All of the above processes involve metal-molten salt interactions, and there exists the possibility of the formation of metal-salt solutions in the region of the surface of the metal. The nature of such solutions can have a direct effect upon the efficiency of any electrochemical process, as well as on the quality of any deposited surface. Other uses of molten salts include the following.

iv) Batteries and fuel cells exist which have molten salt electrolytes. Although the high temperatures necessary for operation are generally a disadvantage, batteries of this type often have a low internal resistance and high efficiency, as well as a high energy storage capacity and power delivery per unit mass, compared with conventional aqueous electrolyte cells. Applications in electrically powered transport and power station load levelling are a possibility.

v) Glass manufacture involves the cooling of ionic liquids, or their mixtures, in such a way that they do not crystallize. This often involves rapid quenching. Clearly, liquid state structure and dynamics is important when considering the possibility of glass formation and the structure of glasses formed from the melt. Glasses have traditionally been made from silicates, borosilicates, borates, phosphates and germanates. Recently, however, there has been much interest in chalcogenide and halide glasses, because of their superior transmission in the infrared region. Some halide based glasses also have good transmission in the visible and near ultraviolet regions, and may prove particularly useful. Possible applications include infrared windows and the transmission of high power laser beams by fibres. In particular, zinc halide based glasses have received some attention (see for example Ma et. al. 1986). Most halide glasses are formed from a molten mixture of two or more halide salts. The zinc chloride-potassium chloride system, studied for this thesis, is a glass former in the zinc chloride rich region (Jiang et. al. 1986).

Reactions between glass surfaces and molten salts which involve cation exchange can result in high surface stresses,

which can produce glasses of improved strength.

This is by no means an exhaustive list of the possible technological uses of molten salts. For a fairly comprehensive treatment of molten salt technology, the reader is referred to Lovering (1982).

### 1.3 Why Use Neutrons?

Liquid structure is usually described by radial distribution functions,  $g_{\alpha\beta}(r)$ . These are a measure of the probability of finding a  $\beta$  type particle at a distance  $r$  away from an  $\alpha$  type particle. In a two component liquid there are three partial distribution functions and, as is shown in chapter 2, these are related to their corresponding partial structure factors,  $S_{\alpha\beta}(Q)$ , by Fourier transformation. A diffraction experiment on a multi-component liquid determines a linear combination of these structure factors, weighted by the atomic concentrations and scattering powers of the elements. This is the total structure factor. If the partial structure factors (and hence the partial distribution functions) are to be determined for a two component liquid, it is necessary to carry out three experiments on samples with differing atomic scattering powers.

To investigate atomic scale structure by diffraction, radiation of a wavelength of comparable scale is required. Thermal neutrons, X-rays and electrons can all have the required wavelength. The neutron has been used extensively in the last thirty years to study liquid structures despite the high cost of neutron sources. The following considerations explain why the neutron has been such a valuable probe of liquid structure.

X-rays are a relatively cheap form of radiation and, with the advent of synchrotron sources, very high intensity beams are available. Although traditional X-ray diffraction is limited to the determination of total diffraction patterns, anomalous X-ray diffraction has potential as a technique for partial structural investigations of multi-component systems. However, the range of momentum transfer

available is determined by the X-ray wavelengths at the absorption edges of the elements present. For the zinc and nickel salts studied here, this would limit the momentum transfer to less than about  $9\text{\AA}^{-1}$ . This is substantially less than the range that is required in order to avoid significant loss of structural information.

Energy dispersive X-ray diffraction uses a polychromatic beam incident on the sample, and fixed angle solid-state detectors to determine photon energies after scattering. The high intensity available over a large range of momentum transfer makes this a promising technique for obtaining total diffraction patterns, but it is still in its infancy.

Extended X-ray absorption fine structure (EXAFS) is a technique which has proved useful as a chemically specific probe of the local structure around atoms. It is particularly useful for investigating the local structure around atoms which are in low concentration - information which is not normally accessible by diffraction methods. However, only nearest neighbours are determined to any reasonable degree of accuracy, and this is not usually as good as that obtainable by diffraction methods. Also, the slab geometry required for an absorption experiment, creates serious problems for the investigation of high vapour pressure corrosive liquids such as molten salts.

Due to the strong scattering of electrons by atoms, electron diffraction is usually limited to the investigation of surfaces and thin films. Also, the strong scattering makes the theoretical treatment of electron scattering difficult, especially the consideration of multiple scattering.

The use of neutrons for the study of molten salts has been largely due to the possibility of partial structural investigations of multi-component liquids using isotopic substitution. Because neutrons are scattered by nuclei and the scattering power of a nucleus depends upon its structure, the mean scattering power of an element within a liquid is dependent upon the isotopic composition of that element. Varying the distribution of isotopes will change the mean scattering power of the element. High flux nuclear reactor sources are now available which enable accurate determination

of partial structure factors with favourable systems. Nickel salts are particularly favourable (see section 4.4). In addition, high momentum transfers (in excess of  $40\text{\AA}^{-1}$ ) are possible using pulsed neutron sources. Both reactor and pulsed sources have been used for the work presented in this thesis.

#### 1.4 Previous Studies of Molten Salts

The first use of isotopic substitution to investigate the structure of a liquid was by Enderby et. al. (1966) to study a copper-tin alloy using the substitution of copper isotopes. The first application to the study of a molten salt was by Page and Mika (1971), who studied copper(I) chloride using chlorine isotopic substitution. Because of the limited availability of suitable isotopes, most studies to date have been of chlorides, but recently, three molten nickel halides have been studied using nickel isotopic substitution (Wood and Howe, 1988).

##### 1.4.1 Molten Alkali Halides (1:1 Salts)

Neutron scattering investigations of the partial structures of the complete set of molten alkali chlorides have been carried out by Howe and McGreevy (1988, LiCl), Edwards et. al. (1975, NaCl), Derrien and Dupuy (1975, KCl), Mitchell et. al. (1976, RbCl) and Locke et. al. (1985, CsCl). These salts, and also the alkali bromides and iodides, have been modelled by Monte-Carlo (MC) and molecular dynamics (MD) computer simulations using rigid ion potentials which were generally of the Born-Mayer-Huggins form (Huggins and Mayer, 1933). Good agreement has been found between simulation and experiment for the smaller cation chlorides, and the structural trends with cation size are well understood in terms of ion packing, Coulomb interaction, overlap repulsions and van der Waals forces. However, for the larger cation salts, polarizable ion models (and hence many-body effects) have been necessary to obtain agreement with experiment (see, for example Gartrell-Mills and McGreevy, 1988). For a complete set of MC simulations of molten alkali halides, and

a comprehensive list of previous computer simulations of molten alkali halides, see Baranyai et. al. (1986).

#### 1.4.2 Molten Alkali Earth Halides and Other 2:1 Salts

For salts with doubly charged cations and singly charged anions (referred to as 2:1 salts), the situation is less well understood. The molten 2:1 systems studied so far are listed in table 1.1, together with the ion sizes and some comments on their structures. These include partial structural studies of all of the alkali earth chlorides (except beryllium, which has a large neutron absorption cross-section and radium), zinc chloride and the nickel halides.

There have only been a few computer simulation studies of 2:1 salts. de Leeuw (1978a,b and 1979) used MC and MD simulations to study molten strontium chloride with rigid ion potentials. Some degree of agreement with the experimental results of McGreevy and Mitchell (1982) is seen for the  $g_{+-}(r)$  and  $g_{--}(r)$ , but the simulations overestimate the degree of structural ordering of the cation species. MD simulations of molten zinc chloride by Woodcock et. al. (1976) and Gardner and Heyes (1985) using Born-Mayer-Huggins type potentials, have predicted  $g_{+-}(r)$ ,  $g_{--}(r)$  and coordination numbers which are in general agreement with the experimental results of Biggin and Enderby (1981a). However, they totally fail to correctly predict the observed  $g_{++}(r)$ . The main failing is the position of the first peak, which is observed to be at a much lower  $r$  than that predicted by the simulations.

So far, no completely successful simulation of a molten 2:1 salt has been achieved. However, Ballone et. al. (1986) studied molten zinc chloride analytically using the hypernetted chain (HNC) approximation. They obtained qualitative agreement with the experimental results by using screened Coulomb forces and a simulated angular dependence of interionic forces (achieved by distance dependent dielectric screening). Distortion of the electronic shells of ions by neighbouring ions and the resulting angular dependence of interionic forces, is believed to play a significant role in

determining the liquid state structure of many 2:1 salts (see for example Pastore et. al., 1986).

The anion to cation size ratio clearly plays a role in determining the liquid state structure of 2:1 salts. This can be seen from the cation-anion coordination numbers listed in table 6.1. So also does the electronegativity of the ions. Wood and Howe (1988) employed a reduced charge transfer model based on electronegativity difference considerations to account for the observed trends in the liquid state structure for the nickel halide series. However, much work still needs to be done to understand the different roles of ion size and ionicity, as well as the role of electronic structure in molten 2:1 salts. In particular, the intermediate range ordering between cations, which has been observed for several molten 2:1 salts including the nickel halides, appears to be dependent upon anion size, and may arise from bond directionality. This appears in the cation-cation structure factor as a diffraction peak at around  $1\text{\AA}^{-1}$ . This feature is very prominent in molten zinc chloride. For this thesis, the zinc halide series has been studied to supplement the existing work on molten nickel halides. The zinc ion, although similar in size to the nickel ion, is electronically distinct in possessing a full 3d shell.

### 1.5 Structural Modification of Molten Salts

In addition to continuing the programme of research into the structure of pure molten salts, work has also been undertaken on the subject of the structural modification of molten salts, both by the dissolution of excess metal and by the mixing of two salts. In particular, the effect upon the 'network' structure of molten zinc chloride of the addition of 'structure breaking' alkali halide has been investigated by time-of-flight neutron diffraction. Previous structural studies of molten zinc chloride have shown it to consist of  $\text{ZnCl}_4^{2-}$  tetrahedral units which are corner linked via bridging  $\text{Cl}^-$  ions. From Raman scattering studies (Ellis, 1966), the addition of alkali halide to such a liquid is believed to reduce stretching modes associated with bridging halide ions and to produce isolated structural units. The evolution of

short range and intermediate range structure within the  $\text{ZnCl}_2$ -KCl system has been investigated across the composition range.

Although much experimental data now exists for the structure of pure molten salts, comparatively little work has been done to determine structure in metal-molten salt solutions. It was established by many workers during the decade of 1955 to 1965 that dissolved metals do indeed form true solutions with their salts, rather than colloidal dispersions as had once been believed. The review by Bredig (1964) gives a summary of this early work. Electrical measurements on such systems have established that two classes of solution exist: those which are 'metallic' solutions, in which the added metal takes up the same valence state as the cation and imparts nearly free electrons to the melt; and those, such as some transition metal halides, in which the metal takes up a lower oxidation state in the melt, forming a 'subhalide'.

Controversy has arisen over the possible existence of subhalide complexes in such solutions. These consist of clusters of ions containing cations of a lower oxidation state than is normally present in the melt. However, very little direct structural information exists. For this reason, the effect upon the structures of molten nickel iodide and nickel bromide of the addition of excess nickel has been investigated by both time-of-flight and steady-state neutron diffraction. In particular, the question of whether there is any structural evidence for the formation of subhalide complexes in these systems has been addressed. It is the metal-metal partial structure which is of most interest in such an investigation, and the particularly favourable conditioning afforded by the use of nickel isotopes has enabled this partial to be determined to a greater accuracy than would have been possible for any other 2:1 salt. The results are compared with the previous partial structural investigations of the pure nickel halides.

The format of this thesis is as follows. The theoretical basis of liquid structure determination using neutron scattering is dealt with in chapter 2, where a

discussion of the theoretical modelling of liquid state structures is also given. A description of both steady-state and time-of-flight diffraction experiments is given in chapter 3, together with descriptions of the instruments used and some details of the sample preparation methods. Chapter 4 deals with the data analysis procedures for both types of diffraction experiment, including the application of corrections, whilst the application of the maximum entropy method to the derivation of radial distribution functions from structure factor data is discussed in chapter 5. Chapters 6, 7 and 8 present the results of neutron diffraction investigations of the zinc halides,  $\text{ZnCl}_2\text{-KCl}$  mixtures and  $\text{NiI}_2\text{+Ni}$  and  $\text{NiBr}_2\text{+Ni}$  solutions. Also included in chapter 6 are the results of a study of the effect of temperature upon the structure factor of molten  $\text{NiI}_2$ . Chapter 9 summarises the work and draws some conclusions, as well as giving some suggestions for further work.

Table 1.1. Neutron diffraction studies of molten 2:1 salts.

Salt	Cation radius (Å)	Anion radius (Å)	Comments	Author
BaCl <sub>2</sub>	1.35	1.81	Trends with cation size from BaCl <sub>2</sub> to MgCl <sub>2</sub> : decrease in cation-anion coord. no. from 7.7 to 4.3, decrease in first shell penetration by anions. Intermediate range order between cations observed for CaCl <sub>2</sub> and MgCl <sub>2</sub> .	Edwards et al, 1978
SrCl <sub>2</sub>	1.12	1.81		McGreevy & Mitchell, 1982.
CaCl <sub>2</sub>	0.99	1.81		Biggin & Enderby, 1981b.
MgCl <sub>2</sub>	0.65	1.81	Planar cation-anion structure proposed.	Biggin et al, 1984
MnCl <sub>2</sub>	0.80	1.81	Total F(Q) only. Appears similar to MgCl <sub>2</sub> .	Biggin et al, 1984
NiCl <sub>2</sub>	0.69	1.81	Anions are tetrahedrally coordinated around the nickel ion. Increasing intermediate range order from NiCl <sub>2</sub> to NiI <sub>2</sub> .	Newport et al, 1985
NiBr <sub>2</sub>	0.69	1.95		Wood & Howe, 1988
NiI <sub>2</sub>	0.69	2.16	First shell penetration of cations.	Wood et al, 1988
ZnCl <sub>2</sub>	0.74	1.81	Tetrahedrally coordinated anions around each cation. Intermediate range order is strong.	Biggin & Enderby, 1981a.

## CHAPTER 2

### THE THEORETICAL BACKGROUND TO LIQUID STRUCTURE DETERMINATION BY NEUTRON DIFFRACTION

#### 2.1 Description of a Liquid Structure

The most useful way of describing the microscopic structure of a liquid is by distribution functions, the most common of which is the pair distribution function  $g(\underline{r})$ . This is defined so that if an atom or ion has its nucleus at point  $\underline{r}=0$ , then the probability of finding another at the same instant with its centre inside a small volume element  $dV$  at position  $\underline{r}$  is

$$(N/V)g(\underline{r})dV \qquad (2.1)$$

where  $N$  is the number of particles in the system and  $V$  is its volume. This definition implies that  $g(\underline{r})$  describes an average in time and over the volume of the liquid and, because a liquid is in general isotropic,  $g(\underline{r})$  reduces to  $g(r)$  and is called a radial distribution function.

Higher order distribution functions can also be defined. For example,  $g_3(\underline{r}_1, \underline{r}_2)$  is defined as the probability of finding two atoms at  $\underline{r}_1$  and  $\underline{r}_2$  with a third at the origin and is called a three body distribution function. These higher order functions are necessary to fully describe a liquid structure, but they cannot be directly determined by experiment.

One of the aims of a neutron diffraction experiment on a disordered system is to determine the radial distribution function and this chapter describes how this is achieved by measuring the differential neutron scattering cross-section. The final section of this chapter extends this determination of  $g(r)$  to the case of multi-component liquids such as molten salts.

## 2.2 The Differential Scattering Cross-Section

In order to determine the pair distribution function from a scattering experiment, it is necessary to measure the differential scattering cross-section which is defined by

$$\frac{d\sigma}{d\Omega} = \frac{\text{scattered flux into solid angle } d\Omega}{\text{incident flux}}$$

If the incident neutrons are considered to be plane waves of the form  $\psi^i = \exp(i\mathbf{k}_0 \cdot \mathbf{r})$ , where  $\mathbf{k}_0$  is the wave vector ( $|\mathbf{k}_0| = 2\pi/\lambda_0$ ), then the wave scattered from particle  $j$  at position  $\mathbf{r}_j$  close to an arbitrary origin is spherically symmetric and has the form

$$\frac{-b_j}{|\mathbf{r} - \mathbf{r}_j|} \exp\{i\mathbf{k} \cdot (\mathbf{r} - \mathbf{r}_j)\} \quad (\text{see Bacon, 1962}).$$

This is illustrated in figure 2.1, and is true if the scattering is elastic, so that the magnitude of the scattered wave vector,  $|\mathbf{k}'|$ , is equal to  $|\mathbf{k}_0|$ .  $b_j$  is the scattering length of the nucleus and is in general complex, but the imaginary part is only significant for nuclei with high absorption cross-sections.

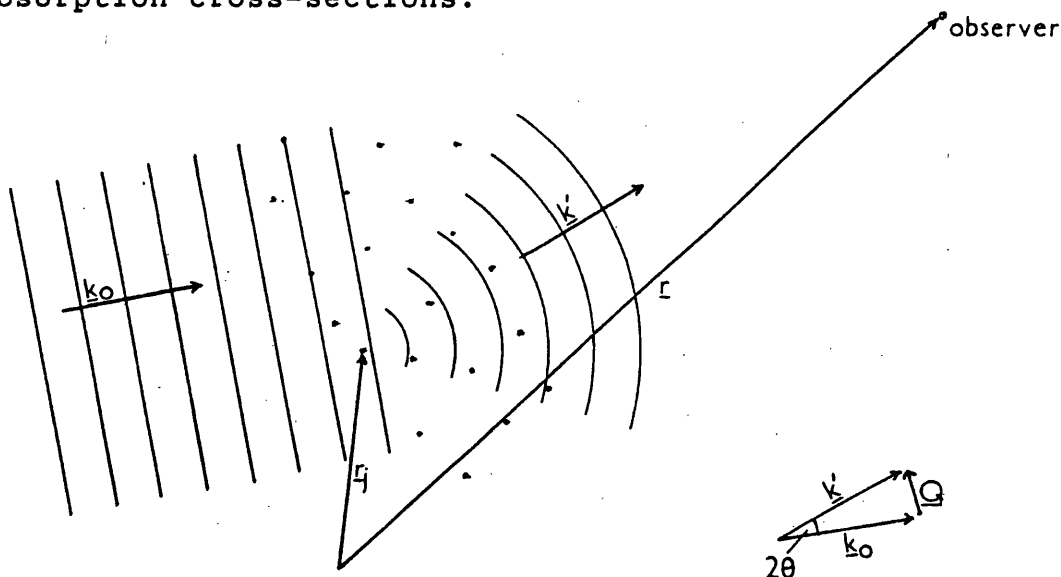


Figure 2.1. The scattering of a plane wave from an assembly of point particles.

The total scattered wave observed at position  $\underline{r}$  due to scattering from an assembly of  $N$  particles is

$$\psi^{sc} = \sum_j^N b_j \exp(ik_o |\underline{r}-\underline{r}_j|) \exp(ik_o \cdot \underline{r}_j) / |\underline{r}-\underline{r}_j|$$

where the last exponential term is the phase of the incident wave at each nucleus  $j$ . In the far-field approximation, where  $|\underline{r}|$  is very much greater than  $|\underline{r}_j|$ , this becomes

$$\psi^{sc} = \frac{-\exp(ik_o r)}{r} \sum_j^N b_j \exp(i\underline{Q} \cdot \underline{r}_j) \quad (2.2)$$

(see for example Gunn, 1988)

where  $\underline{Q} = \underline{k}' - \underline{k}_o =$  the momentum transferred from the nucleus to the scattered neutron divided by  $\hbar$ .

In order to calculate the scattered flux into solid angle  $d\Omega$ , the square of the modulus of the wave function at distance  $r$  should be multiplied by  $r^2$  so that

$$\frac{d\sigma}{d\Omega} = r^2 \frac{|\psi^{sc}|^2}{|\psi^i|^2} = \langle \sum_j^N \sum_k^N b_j b_k \exp[i\underline{Q} \cdot (\underline{r}_j - \underline{r}_k)] \rangle. \quad (2.3)$$

Here, the brackets  $\langle \dots \rangle$  denote an average over the volume of the sample and over the time of an experiment.

### 2.3 Coherent and Incoherent Scattering

The scattering length of a nucleus is determined by the interaction potential between the target nucleus and a neutron. It will therefore be different for each isotope within a species and, since the neutron has a nonzero spin, it will also depend upon the nuclear spin. Within a sample these isotopes will be randomly distributed and, except at very low temperatures, the spins randomly orientated.

It is convenient to divide the average in equation 2.3 into two parts; a part given by the scattering from a system of nuclei which all have the mean scattering length  $\bar{b}$  (this is called coherent scattering) and a part given by the scattering from individual nuclei (incoherent scattering).

So that 
$$\frac{d\sigma^{\text{coh}}}{d\Omega} = \frac{NN}{\sum_{jk} \bar{b}} \langle \exp[i\mathbf{Q} \cdot (\underline{r}_j - \underline{r}_k)] \rangle \quad (2.4)$$

where  $\bar{b} = \frac{1}{N} \sum_i b_i$  is known as the coherent scattering length

and 
$$\frac{d\sigma}{d\Omega} = \frac{d\sigma^{\text{coh}}}{d\Omega} + \frac{d\sigma^{\text{inc}}}{d\Omega}. \quad (2.5)$$

The coherent scattering cross-section is defined as

$$\sigma^{\text{coh}} = 4\pi\bar{b}^2,$$

and the total scattering cross-section is

$$\sigma^{\text{tot}} = 4\pi\bar{b}^2.$$

If the deviation of the scattering length of the  $j^{\text{th}}$  nucleus from  $\bar{b}$  is  $\beta_j$ , then

$$\frac{d\sigma}{d\Omega} = \frac{NN}{\sum_{jk}} \langle \Sigma(\bar{b} + \bar{b}(\beta_j + \beta_k) + \beta_j\beta_k) \exp[i\mathbf{Q} \cdot (\underline{r}_j - \underline{r}_k)] \rangle.$$

The mean of the second term is zero, since  $\Sigma\beta_j=0$ , and the third term averages out to be zero when  $j \neq k$ , so this term is  $N\Sigma\beta_j^2$  which is  $N$  times the variance. So, for 2.5 to be satisfied,

$$\frac{d\sigma^{\text{inc}}}{d\Omega} = N(\bar{b}^2 - \bar{b}^2). \quad (2.6)$$

The incoherent cross-section is defined as

$$\sigma^{\text{inc}} = \sigma^{\text{tot}} - \sigma^{\text{coh}} = 4\pi(\bar{b}^2 - \bar{b}^2).$$

#### 2.4 The Relationship Between $d\sigma/d\Omega$ and $g(r)$

Since neutrons have a wavelength which is several orders of magnitude greater than the size of a nucleus, the nuclei can be considered as point particles represented by  $\delta$ -functions and, at a given instant in time, the density at a point  $\underline{r}$  within the system is given by

$$\rho(\underline{r}) = \sum_j^N \delta(\underline{r} - \underline{r}_j). \quad (2.7)$$

The probability of finding two nuclei separated by  $\underline{r}$  is

$$\rho_0 g(\underline{r}) = \frac{1}{N} \langle \sum_{jk} \delta(\underline{r} - (\underline{r}_j - \underline{r}_k)) \rangle - \delta(\underline{r}) \quad (2.8)$$

where  $\rho_0$  is the mean number density ( $N/V$ ), and the last term is included so that the self-correlation (when  $\underline{r}=0$  and  $\underline{r}_j = \underline{r}_k$ ) is not counted. This can be re-written as

$$\frac{1}{N} \langle \sum_{jk} \delta(\underline{r} - (\underline{r}_j - \underline{r}_k)) \rangle - \rho_0 = \rho_0 (g(\underline{r}) - 1) + \delta(\underline{r}). \quad (2.9)$$

The Fourier transform of the right hand side of equation 2.9 is

$$1 + \rho_0 \int (g(\underline{r}) - 1) \exp(-i\underline{Q} \cdot \underline{r}) d\underline{r}$$

and the Fourier transform of the left hand side is

$$\begin{aligned} & \frac{1}{N} \langle \sum_{jk} \int \exp(-i\underline{Q} \cdot \underline{r}') \delta(\underline{r} - \underline{r}') d\underline{r}' \rangle \\ &= \frac{1}{N} \langle \sum_{jk} \exp(-i\underline{Q} \cdot \underline{r}') \rangle - \rho_0 \int \exp(-i\underline{Q} \cdot \underline{r}) d\underline{r}, \text{ where } \underline{r}' = \underline{r}_j - \underline{r}_k. \end{aligned}$$

The last term corresponds to the forward scattering from each particle and is not normally measured in a diffraction experiment so it can be neglected. Relating this to 2.4, we have

$$\frac{1}{N^2} \frac{d\sigma^{\text{coh}}}{d\Omega} = 1 + \rho_0 \int (g(\underline{r}) - 1) \exp(-i\underline{Q} \cdot \underline{r}) d\underline{r} = S(\underline{Q}). \quad (2.10)$$

This is the definition of the static structure factor,  $S(\underline{Q})$ . For an isotropic system, this can be integrated over the spherical coordinate polar angles to obtain the Fourier sine transform

$$S(Q) = 1 + \rho_0 \int_0^\infty 4\pi r^2 (g(r) - 1) \frac{\sin(Qr)}{(Qr)} dr, \quad (2.11)$$

and the inverse transform is

$$g(r) = 1 + \frac{1}{\rho_0 (2\pi)^3} \int_0^\infty 4\pi Q^2 (S(Q)-1) \frac{\sin(Qr)}{(Qr)} dQ. \quad (2.12)$$

So if  $d\sigma^{\text{coh}}/d\Omega$  could be measured over the complete range of momentum transfer from 0 to  $\infty$ , then we would have a complete knowledge of  $g(r)$ . In practice, it is desirable to measure  $d\sigma/d\Omega$  over as large a  $Q$  range as possible.

## 2.5 A Scattering Experiment and The Static Approximation

Because neutrons of the wavelength required for diffraction experiments have thermal energies, energy transfer between the neutron and a target atom may be significant. This is useful as a probe of dynamical behaviour in condensed-matter physics, but in the case of diffraction it requires that an approximation be made in order to measure  $d\sigma/d\Omega$ . The double differential cross-section is defined as the fraction of neutrons scattered into the solid angle  $d\Omega$ , having transferred (lost or received) energy within the range  $\hbar d\omega$ ,

$$\text{so that } \frac{d\sigma}{d\Omega} = \int_{-\infty}^{\infty} \frac{d^2\sigma}{d\Omega d\omega} d\omega. \quad (2.13)$$

In practice, a detector at a scattering angle  $2\theta$  counts neutrons scattered at that angle regardless of whether or not any energy transfer has occurred within the sample. Also, the detector will have an efficiency that will be energy dependent ( $D(k)$ ) and the count rate of the detector will also depend upon the speed of the neutrons arriving at it. So the measured differential cross-section will be

$$\frac{d\sigma}{d\Omega} = \int_{-\frac{E_0}{\hbar}}^{\infty} D(k) \frac{k}{k_0} \frac{d^2\sigma}{d\Omega d\omega} d\omega \quad (2.14)$$

const.  $\theta$

where  $k_0$  and  $k$  are the magnitudes of the incident and final wave vectors (which are proportional to the speed of the

neutron), and  $E_0$  is the incident neutron energy.

If a neutron has a mass  $m$  and is scattered through an angle  $2\theta$  then the energy and momentum transfer are related by

$$\frac{\hbar Q^2}{2m} = 2E_0 + \hbar\omega - 2(E_0^2 + \hbar\omega E_0)^{\frac{1}{2}} \cos 2\theta \quad (\text{Windsor, 1981}).$$

If  $E_0$  is very much greater than  $\hbar\omega$  then this can be approximated to

$$Q = \frac{4\pi}{\lambda_0} \sin\theta. \quad (2.15)$$

This is known as the Static Approximation and makes the integration at constant  $\theta$  in equation 2.14 equivalent to an integration at constant  $Q$ , which is what is required because we need  $d\sigma/d\Omega$  as a function of  $Q$ . This approximation holds well for X-rays, which have high energies at the wavelength required for diffraction experiments. Neutrons, however, have energies comparable with the thermal energies of the atoms in a liquid, so that corrections have to be made for inelastic scattering. This is dealt with in section 4.2.5.

## 2.6 Multi-Component Liquids

So far, only the case of scattering from a single component system has been considered. This will now be extended to the general case of a multi-component liquid. One can describe the structure of such a liquid by a set of partial distribution functions  $g_{\alpha\beta}(r)$ , which give the probability of finding an atom of species  $\beta$  at a distance  $r$  away from an atom of species  $\alpha$ . The equivalent partial static structure factors  $S_{\alpha\beta}(Q)$ , are, using the Faber-Ziman definition (Faber and Ziman, 1965),

$$S_{\alpha\beta}(Q) = 1 + \rho_0 \int (g_{\alpha\beta}(\underline{r}) - 1) \exp(-i\underline{Q} \cdot \underline{r}) d\underline{r}. \quad (2.16)$$

An alternative definition of partial structure factors is due to Powles (1973) and Page and Mika (1971) who used the concentration-dependent definition

$$S_{\alpha\beta}(\underline{Q}) = \delta_{\alpha\beta} + \frac{2C_{\alpha}C_{\beta}\rho_{\Omega}}{(C_{\alpha}+C_{\beta})} \int (g_{\alpha\beta}(\underline{r})-1) \exp(-i\underline{Q}\cdot\underline{r}) d\underline{r}.$$

Bhatia and Thornton (1970) defined partial structure factors which were derived from Fourier transforms of the number density and concentration fluctuations. These are related to the Faber-Ziman structure factors by

$$S_{NN}(\underline{Q}) = C_{\alpha}^2 S_{\alpha\alpha}(\underline{Q}) + C_{\beta}^2 S_{\beta\beta}(\underline{Q}) + 2C_{\alpha}C_{\beta} S_{\alpha\beta}(\underline{Q})$$

which is the number-number structure factor,

$$S_{CC}(\underline{Q}) = C_{\alpha}C_{\beta} \{ C_{\alpha} [S_{\alpha\alpha}(\underline{Q}) - S_{\alpha\beta}(\underline{Q})] - C_{\beta} [S_{\beta\beta}(\underline{Q}) - S_{\alpha\beta}(\underline{Q})] \}$$

which is the concentration-concentration structure factor, and

$$S_{NC}(\underline{Q}) = C_{\alpha}C_{\beta} \{ 1 + C_{\alpha}C_{\beta} [S_{\alpha\alpha}(\underline{Q}) + S_{\beta\beta}(\underline{Q}) - 2S_{\alpha\beta}(\underline{Q})] \}$$

which is the number-concentration structure factor. These Bhatia-Thornton structure factors are useful when relating structure to thermodynamic quantities, but it is the Faber-Ziman definitions which have been adopted for this work.

From equations 2.5 and 2.10 we can write

$$\frac{d\sigma}{d\Omega} = N(\bar{b}^2 - \bar{b}^2) + N\bar{b}^2 S(\underline{Q}). \quad (2.17)$$

The scattering cross-section from a multi-component liquid will contain a linear combination of contributions from the partial structure factors, weighted by the concentrations and scattering lengths of each species,

$$\text{so that } \frac{d\sigma}{d\Omega} = N \sum_{\alpha} C_{\alpha} \bar{b}_{\alpha}^2 + N \sum_{\alpha\beta} C_{\alpha} C_{\beta} \bar{b}_{\alpha} \bar{b}_{\beta} [S_{\alpha\beta}(\underline{Q}) - 1]. \quad (2.18)$$

One can define a total structure factor by analogy with 2.10 to be

$$\frac{1}{N} \frac{d\sigma}{d\Omega} = F(\underline{Q}) + \Delta \quad (2.19)$$

$$\text{where } \Delta = \sum_{\alpha} C_{\alpha} \bar{b}_{\alpha}^{-2} \quad (2.20)$$

$$\text{and } F(Q) = \sum_{\alpha\beta} C_{\alpha} C_{\beta} \bar{b}_{\alpha} \bar{b}_{\beta} [S_{\alpha\beta}(Q) - 1]. \quad (2.21)$$

Unlike  $S(Q)$ , which is dimensionless,  $F(Q)$  has the dimensions of  $L^2$  and is usually measured in barns ( $10^{-24} \text{cm}^2$ ). It is asymptotic to zero at high  $Q$ . It is  $F(Q)$  that has been determined from diffraction experiments on multi-component liquids in this thesis. A direct Fourier transform of  $F(Q)$  using equation 2.12 will give the total distribution function

$$G(r) = 1 + \frac{1}{\rho_0 (2\pi)^3} \int_0^{\infty} 4\pi Q^2 F(Q) \frac{\sin(Qr)}{(Qr)} dQ \quad (2.22)$$

$$\text{where } G(r) = \sum_{\alpha\beta} C_{\alpha} C_{\beta} \bar{b}_{\alpha} \bar{b}_{\beta} [g_{\alpha\beta}(r) - 1], \quad (2.23)$$

which is a linear combination of the individual partial distribution functions and is asymptotic to zero at high  $r$ .

If one wishes to extract the partial structure factors, and hence the partial distribution functions, from the total structure factor, then the technique of isotopic substitution which is described in section 4.4.1, can be employed. The different values of  $\bar{b}_{\alpha}$  and  $\bar{b}_{\beta}$  obtained by doing an experiment with different isotopic enrichments within a chemical species, yields simultaneous equations with a set of unknowns ( $S_{\alpha\beta}(Q)$ ) to be determined. Anomalous X-ray scattering is another means of varying the coefficients in equation 2.18, in which the scattering power of an atom is changed by using a wavelength near the absorption edge of a species.

For a two component liquid

$$F(Q) = 2C_1 C_2 b_1 b_2 (S_{12}(Q) - 1) + C_1^2 b_1^2 (S_{11}(Q) - 1) + C_2^2 b_2^2 (S_{22}(Q) - 1) \quad (2.24)$$

where  $C_1$  and  $C_2$  are the concentrations of species 1 and 2, and  $b_1$  and  $b_2$  are the mean coherent scattering lengths of species 1 and 2. For a system with  $n$  components, there will

be  $n(n+1)/2$  partial structure factors contributing to the total structure factor.

Details of the method of extracting the total and partial structure factors and distribution functions from measured scattering intensities are described in chapter 4.

## 2.7 Theoretical Modelling of Liquid State Structures

In order to test the validity of theoretical interparticle potentials, or to derive interparticle potentials from experimentally determined structure factors, it is desirable to have a relationship between the pair distribution function,  $g_{\alpha\beta}(r)$ , and the potentials,  $\phi_{\alpha\beta}(r)$ . To derive such a relationship, it is necessary to make the assumption that the total potential energy of the system is the sum of the potential energies between its  $N$  constituent particles, so that the interactions are considered to be pairwise additive. The total potential energy is

$$\Phi(\underline{r}_1, \underline{r}_2, \dots, \underline{r}_N) = \sum_{1 \leq i < j < N} \phi(r_{ij}).$$

This assumption holds if the potential between any two particles is unaffected by the presence of others. It breaks down, for example, when ions are polarized by the close presence of another ion.

If a potential of mean force,  $U(r_{12})$ , is defined by writing the pair distribution function in its Boltzmann form,

$$g(r_{12}) = \exp[-U(r_{12})/kT],$$

then the total force acting on atom 1 can be considered as the pair force between atoms 1 and 2, plus the forces between atom 1 and all of the other atoms. So that

$$-\frac{\partial U(r_{12})}{\partial \underline{r}_1} = -\frac{\partial \phi(r_{12})}{\partial \underline{r}_1} - \int \frac{n_3(\underline{r}_1, \underline{r}_2, \underline{r}_3)}{\rho_0^2 g(r_{12})} \frac{\partial \phi(r_{13})}{\partial \underline{r}_1} d\underline{r}, \quad (2.25)$$

where  $n_3(\underline{r}_1, \underline{r}_2, \underline{r}_3)$  is a three body correlation function, which is defined so that the probability that the volume

elements  $d\underline{r}_1$ ,  $d\underline{r}_2$  and  $d\underline{r}_3$ , at position vectors  $\underline{r}_1$ ,  $\underline{r}_2$  and  $\underline{r}_3$  are occupied by atoms, is  $n_3(\underline{r}_1, \underline{r}_2, \underline{r}_3) d\underline{r}_1 d\underline{r}_2 d\underline{r}_3$ . This three body function is not determinable by experiment. In order to proceed further, therefore, it is necessary to use some approximate form of  $n_3$ .

One can, for example, make the approximation used by Yvon (1935) and Born and Green (1947), who used the superposition approximation due to Kirkwood (1935).

$$n_3(\underline{r}_1, \underline{r}_2, \underline{r}_3) = \rho_0^3 g(r_{12}) g(r_{31}) g(r_{23}).$$

Using this method, equation 2.25 becomes an equation involving only pair distribution functions and it reduces to the soluble YBG equation. This approximation holds if one particle in the three body function is so far away from the other two that its potential does not affect the total interaction of all three. This is valid for low densities, but rarely works well for liquids.

Two other important approximations are the Percus-Yevick (PY) and Hypernetted Chain (HNC) equations.  $n_3$  is written as a cluster expansion (see for example Hansen and McDonald, 1986) and the higher order terms are neglected. The results are expressed in terms of a direct correlation function,  $c(r)$ . This is related to the total correlation function,  $h(r)$ , which is defined simply as  $h(r) = g(r) - 1$ , by the Ornstein-Zernike relation

$$h(r) = c(r) + \rho_0 \int c(|\underline{r}-\underline{r}'|) h(r') d\underline{r}'. \quad (2.26)$$

Using the PY approximation,  $c(r)$  is related to  $\phi(r)$  and  $g(r)$  by

$$c(r) = g(r) \{1 - \exp[\phi(r)/kT]\}.$$

With the HNC approximation, the relationship becomes

$$c(r) = h(r) - \ln[g(r)] - \phi(r)/kT.$$

Again, these approximations work best at low densities, but they are more accurate than the YBG method. Because the HNC retains one extra term in the cluster expansion, it is expected to yield more accurate results than the PY method. It has, therefore, been a favoured method of obtaining analytical solutions for  $g(r)$ .

Another approximation often used for ionic liquids is the Mean Spherical Approximation (MSA), which makes the assumption that the ions behave like charged spheres of diameter  $\sigma$ . The potential is infinite within this sphere, so that

$$\begin{aligned} g(r) &= 0 && \text{for } r < \sigma \\ \text{and } c(r) &= -\phi(r)/kT && \text{for } r \geq \sigma. \end{aligned}$$

This does not prove to be a good approximation and it greatly overestimates the effects of ion size on the structure when applied to real ionic liquids.

### 2.7.1 Computer Simulations of Liquids

With the advent of powerful computers, two important methods of testing theoretical models of liquids, solids and dense gases have become widely used. These are the Monte Carlo (MC) and Molecular Dynamics (MD) computer simulation methods. They involve the derivation of macroscopic structural and thermodynamic quantities from the consideration of a microscopic ensemble of interacting particles. These particles are in a cell which has dimensions of only a few particle diameters. In principle, computer simulation methods can yield exact predictions of the structure and behaviour of systems for a given set of interparticle potentials, since no assumptions need to be made about higher order correlation functions and the potentials may be of any form. In practice, however, the number of particles considered is limited to about  $10^3$ , and the dimensions of the cell, together with the practicalities of implementing a simulation, limit the accuracy attainable.

In a MC simulation, the particles are given an initial distribution within the cell and the total potential energy,  $\Phi$ , is calculated from given interparticle potentials,  $\phi_{\alpha\beta}$ . Because the position of each particle is known, the potentials need not be pairwise additive. By successive random displacements of the particles new configurations are generated and each one is either 'accepted' or 'rejected' according to a criterion which ensures that in the limit of an infinite number of steps, each configuration occurs with a probability which is proportional to the Boltzmann factor,  $\exp(-\Phi/kT)$ .  $T$  is the chosen absolute temperature of the system. Ensemble averages of functions which depend upon the particle positions, such as distribution functions or potential energy, can be obtained from several thousand acceptable configurations.

In order to minimise the surface effects associated with such a small cell, which is typically a cube with a side length of about ten particle diameters, periodic boundary conditions are usually imposed, whereby the cell is surrounded by repeated images of itself. Spatial fluctuations of a range that is longer than the cell dimensions are not accessible and the distribution functions obtained are unreliable for distances of greater than half the cell length. The MC method has been applied to all of the molten alkali halides (Baranyai et. al. 1986), and the generally good agreement between the simulations and the experimentally derived distribution functions is a reflection of both the good choice of interionic potentials for these systems, and the success of the MC method.

In a MD simulation the particles are initially assigned positions within the cell and velocities according to a Maxwell-Boltzmann distribution for the temperature of interest. From the chosen interparticle potentials, the particle trajectories are then computed using the classical equations of motion, in short time steps of typically  $10^{-14}$  to  $10^{-15}$  seconds. After an initial relaxation time, during which the system comes to equilibrium (typically  $10^{-13}$  to  $10^{-12}$  seconds), the subsequent trajectories of the particles are used to evaluate structural and thermodynamic properties

of the system. Dynamical information is also obtainable from MD simulations, so the method can also be used to study diffusion, particle vibrations and collective modes within liquids and solids, as well as phenomena such as the formation of ionic clusters. Again, pairwise additivity is not an essential requirement of the interparticle potentials.

The same limitations and inaccuracies inherent in the MC method, due to the small size of the cell and the periodic boundary conditions, also apply for the MD method. In addition, spurious time recurrences can arise as local disturbances propagating off one face of the cell will reappear at the opposite face. Nevertheless, MD simulations have proved to be a very useful technique for testing theoretical interparticle potentials and for obtaining experimentally inaccessible information for many liquids. When compared with experimental results, the accuracy obtained for distribution functions is often comparable with experimental uncertainties, but for ionic liquids, which have long range interactions, the results are often less accurate.

## CHAPTER 3

### EXPERIMENTAL DETAILS

#### 3.1 Neutron Scattering Requirements

The structure of a liquid can be defined in terms of a radial distribution function. It is the aim of a neutron diffraction investigation to measure the differential coherent scattering cross section and thereby extract the structure factor in order to derive the radial distribution function.

To do this satisfactorily, a large range of momentum transfer ( $Q$  range) is required with  $Q$  values ranging from less than  $\sim 0.7\text{\AA}^{-1}$ , in order to extrapolate to the long wavelength limit, and up to greater than  $15\text{\AA}^{-1}$ , in order to be able to approximate the upper limit in equation 2.12. In addition, since the substitution of isotopes produces only small changes in the total scattering spectra, the separation of the partial structure factors of a multi-component liquid using isotopic substitution requires a high statistical accuracy. The basic requirements therefore, for a neutron diffraction investigation of a liquid structure, are a high flux neutron source and an instrument capable of measuring the scattering intensity as a function of  $Q$  over the range required.

There are two fundamentally different methods of doing this. The first is the steady-state or reactor method, in which a steady flux of monochromatic neutrons from a nuclear reactor is scattered by the sample and the scattered intensity is measured by detectors as a function of scattering angle  $2\theta$  - i.e.  $\lambda$  is fixed,  $\theta$  is varied. The second is the pulsed or time-of-flight (TOF) method, in which a pulsed beam of polychromatic neutrons is incident upon the sample and the scattered spectra is measured by detectors at fixed angles as a function of wavelength. The wavelength is determined by recording the time-of-flight and thereby the velocity of a detected neutron. So  $\theta$  is fixed and  $\lambda$  is the variable.

Both of these methods have been used during the course of this thesis and the first part of this chapter describes

them both in detail. The second part deals with sample preparation.

### 3.2 Steady-State Neutron Diffraction

For steady-state diffraction experiments, high energy neutrons from a reactor core are slowed down to thermal energies suitable for a diffraction experiment, by collisions with light atoms in a moderator. Typical moderators used are liquid methane, water and graphite and the distribution of neutron energies from a moderator is a Maxwellian determined by the moderator temperature. Neutrons are extracted by collimators which define the angular spread of the incident beam for an experiment. From this thermal distribution of neutron energies a single wavelength is selected by Bragg scattering from a crystal.

#### 3.2.1 The D4B Diffractometer

The neutron scattering experiments for  $\text{NiBr}_2$  and  $\text{NiBr}_2+\text{Ni}$  were carried out on the D4B diffractometer at the Institute Laue-Langevin in Grenoble, France. This is a two axis instrument with one axis ( $\omega$ ) being the crystal monochromator to select either  $0.7\text{\AA}$  or  $0.5\text{\AA}$  neutrons, and the sample sits on the other axis ( $\theta$ ) about which two detector banks move. This instrument is shown in figure 3.1.

Neutrons leave the graphite hot source (at 2000K) and pass along a collimator to be monochromated by an 002 reflection from a zinc crystal (for a wavelength of  $0.7\text{\AA}$  used in these experiments). Second order reflection is eliminated by an iridium filter. The neutrons travel in a vacuum, in order to eliminate air scattering, and enter an evacuated sample chamber, which contains the furnace, after passing through a beam monitor which measures the incident flux on the sample. The beam height is determined by neutron-absorbing boron nitride flags positioned in front of the furnace.

The furnace consists of a 0.125mm vanadium foil cylindrical heating element of diameter 23mm which passes a high current ( $\sim 200\text{A}$ ), on the axis of which sits the sample in

a boron nitride cup. The vanadium foil gives a furnace background with only small Bragg peaks, and the boron nitride cup prevents scattering from the sample support tube.

The scattered neutrons pass through a thin aluminium wall and are detected by two evacuated 64-element  $^3\text{He}$  multidetectors. The element separation is  $0.1^\circ$  for detector 1 and  $0.2^\circ$  for detector 2, these being at 1.5m and 0.75m from the  $\theta$  axis respectively. During an experiment, detector 1 covers the lower angles and detector 2 the higher angles, with a region of overlap to check for agreement between the two. The total angular range covered is  $1.6^\circ \leq 2\theta \leq 131^\circ$  giving a range of momentum transfer of  $0.25\text{\AA}^{-1} \leq Q \leq 16.3\text{\AA}^{-1}$  for  $0.7\text{\AA}$  neutrons.

During data acquisition, these detectors move round in small ( $\sim 1.5^\circ$ ) steps after the monitor count (a measure of the total incident flux) has reached a preset value. This eliminates the effect of intensity changes in the reactor core over the period of the experiment which can be longer than twelve hours. The total number of neutrons detected by each element at each step, together with the monitor count and scattering angle, is recorded on magnetic disk for subsequent analysis.

### 3.3 Pulsed Neutron Diffraction

The pulsed neutron sources used during the course of this work were proton synchrotrons, in which high energy protons ( $\sim 500\text{MeV}$ ) are accelerated by a radio-frequency field and are incident upon a heavy metal target (typically uranium or  $^{238}\text{U}$ ). The proton beam hits the target in short pulses ( $\sim 0.5\mu\text{s}$ ) and high energy neutrons are produced by spallation within the target (a process of chipping or splintering off particles from nuclei). These neutrons have to be moderated, but for a pulsed source moderation is not completed so as not to over-broaden the neutron pulse and thus compromise resolution. In addition, limited moderation enables higher energy neutrons which have not yet been thermalised (epithermal neutrons) to be used for higher energy and higher  $Q$  experiments. The greater  $Q$  range available from a pulsed source enables a better real space resolution for a

diffraction experiment.

Neutrons leaving a moderator are guided by a collimator, through a monitor and directly onto a sample to be scattered and detected by fixed angle detectors. By measuring the time of arrival ( $t$ ) of a detected neutron, its velocity ( $v$ ) and therefore its wavelength can be deduced using the de Broglie relation

$$\lambda = h/mv = ht/mL \quad (3.1)$$

where  $L$  = the total length of the flight path of the neutron (source to sample to detector). Each time of arrival can then be converted to  $Q$  using equations 2.15 and 3.1 (assuming elastic scattering), thus giving a complete range of  $Q$  for each pulse of neutrons.

### 3.3.1 The Liquids and Amorphous Materials Diffractometer(LAD)

The LAD diffractometer at the SERC's Rutherford-Appleton Laboratory (Oxfordshire) was used for the measurements on zinc halides, zinc chloride and potassium chloride mixtures and the effect of temperature on  $\text{NiI}_2$  presented in this thesis. It is shown in figure 3.2. The pulse rate for the Spallation Neutron Source (SNS) at RAL is 50Hz and a liquid methane moderator thermalises the neutrons for LAD. The primary flight path from source to sample is 10m, and the secondary flight path from sample to detectors is nominally 1m.  $^3\text{He}$  detectors are fixed at angles of  $\pm 5^\circ$ ,  $\pm 10^\circ$ ,  $\pm 20^\circ$ ,  $\pm 35^\circ$ ,  $\pm 58^\circ$  and  $\pm 90^\circ$ , and two time-focussed banks (for which all neutrons arriving simultaneously have the same  $Q$  values) are at  $145.6^\circ$  to  $150^\circ$  on either side. For the  $\text{ZnCl}_2$  - KCl mixtures experiment the  $^3\text{He}$  detectors at  $20^\circ$ ,  $35^\circ$ ,  $58^\circ$  and  $90^\circ$  had been replaced by 8 9-element arrays of scintillators.

Incoming neutrons first pass through a fission chamber monitor (used for normalising the data to the total incident flux) before reaching the furnace and sample to be scattered. Neutrons arriving at the detectors are binned into time bins of width  $\Delta t$ , where  $\Delta t/t = \text{a constant} = 10^{-3}$ . A correction has to be made for the time interval between the pulse trigger

(from the incoming protons), from which the time is measured, and the time at which neutrons leave the moderator. This correction itself has an uncertainty due to the finite pulse width on emergence from the moderator ( $\sim 10\mu\text{s}$ ). Data is recorded as the number of counts for each time channel for each detector. The resolution for this instrument ranges from  $\Delta Q/Q = 0.004$  for the  $150^\circ$  detector banks, to  $\Delta Q/Q = 0.12$  for the  $5^\circ$  detectors.

The parameters for this instrument are shown in table 3.1. The  $Q$  ranges given are for the wavelength range  $0.2\text{\AA} < \lambda < 2\text{\AA}$  - typical for the SNS. However, the actual  $Q$  ranges used for each experiment were determined by the ranges over which agreement between counters could be achieved (see section 4.3.4). This usually gave a total  $Q$  range over which good statistical accuracy was achievable ranging from less than  $0.5\text{\AA}^{-1}$  to greater than  $30\text{\AA}^{-1}$ .

The samples were heated in a vanadium foil furnace which has been designed and built at Leicester specifically for use with a time-of-flight diffractometer. Within this furnace, sample tubes of length 0.5m and internal diameter  $\approx 8\text{mm}$  stand on a ceramic cup which, together with a guide tube at the top of the furnace, locates the sample centrally in the beam. The beam is 2cm wide and 4cm high.

### 3.3.2 The General Purpose Powder Diffractometer (GPPD)

The isotopic substitution measurements for  $\text{NiI}_2 + \text{Ni}$  were made on the GPPD at Argonne National Laboratory, Illinois, USA, using an Intense Pulsed Neutron Source (IPNS). With this pulsed neutron source, 500MeV protons are incident upon a uranium target at a pulse repetition rate of 30Hz. On GPPD the primary and secondary flight paths are 19.96m and 1.5m respectively. The principle is the same as that for LAD, but this instrument has moveable banks of  $^3\text{He}$  detectors which are electronically, rather than geometrically, time-focussed and measure the number of neutrons arriving in a fixed time interval  $\Delta t$ . The instrument configuration for the experiment is described in table 3.2.

The GPPD accepts the same Leicester-built vanadium foil furnace as LAD, and this was used for this experiment.

### 3.4 Sample Preparation

Before use in a neutron diffraction experiment all of the salts had to be thoroughly and carefully dried. The method used for this was heating under vacuum. The chemicals were supplied in powdered form with water of crystallization or as anhydrous, but even the anhydrous salts had to be dried due to their hygroscopic nature. The details for each sample are given in the relevant results chapter.

The salts were carefully loaded into necked fused silica drying tubes in a dry argon-filled evacuable glove box. These drying tubes were typically of 6-7mm internal diameter and 1mm wall thickness. They were then transferred in a vacuum vessel to a drying furnace. The salts were then evacuated to about  $5 \times 10^{-2}$  mbar and slowly warmed over a 24 hour period to 100°C. It was found that most of the water was driven off during this stage, but further drying was necessary. A pressure of about  $10^{-5}$  Torr was usually achieved with a diffusion pump before the temperature was raised slowly to 250-300°C. The rate of rise was determined for each of the salts by the rate at which water was driven off and an upper pressure limit of  $5 \times 10^{-5}$  Torr was set. The final drying temperature was the temperature that was necessary for no further water to be driven off, except in the case of  $\text{ZnCl}_2$ , which has an appreciable vapour pressure ( $9 \times 10^{-3}$  Torr at 200°C), for which the upper limit was set at 110°C and the pressure was  $5 \times 10^{-2}$  mbar. It was kept at this temperature for four to five days. The usual total drying time was three to four days.

After drying, the vacuum vessel was closed and removed to the glove box, which was then evacuated to a pressure of less than  $10^{-4}$  Torr before being filled with dry argon. So that any leakage of gas during handling would tend to be outwards, rather than inwards, the glove box was pressurised to slightly more than atmospheric pressure. The samples could then be handled and the tubes sealed with rubber tubing and clips prior to their being sealed at their necks. Before sealing however, the pressure of argon in each of the tubes was reduced to 1/2 - 2/3 atm. All subsequent handling operations with the dried salts were in the glove box.

Once sealed, the samples could then be melted. This

pre-melting served three purposes. First, by converting from powdered to pellet form, it reduced the amount of dead space in the final tubes which was important considering the high vapour pressure of the nickel halides at their melting points (two to four atm.); secondly, it made it easier and more accurate to weigh the samples and load them into their final tubes; and thirdly, it served as a test as to whether the samples were properly dried, since any water present would react at the melting temperatures to produce gaseous products and high pressures in the small volume.

The sealing of these pellets into their final experimental tubes (of slightly larger internal diameter) was carried out on a lathe, by sealing down onto a fused silica plug inside the sample tube, which again contained argon at a pressure of  $2/3$  atm. Dead space was kept to a minimum by sealing as close to the pellet as possible. The final tubes also had 1mm walls which, although undesirable, because it meant that a significant fraction of the scattering was from the container, was considered safer than thinner tubes from a containment point of view.

#### 3.4.1 Preparation of the Mixtures

The isotopic mixtures of  $\text{NiI}_2+\text{Ni}$  and  $\text{NiBr}_2+\text{Ni}$  were supplied with nickel metal powder already mixed with the powdered salt by Mr P.Gullidge at the isotopic preparation unit in Bristol. After drying, these mixtures were melted for 10 hours to ensure mixing and then frozen. For the natural  $\text{NiI}_2+\text{Ni}$  and  $\text{NiBr}_2+\text{Ni}$ , the pure salts were prepared in pellet form and then weighed before being sealed, with a weighed amount of Ni wire, in an intermediary tube to be melted for 15 hours prior to sealing in their final tubes.

The  $\text{ZnCl}_2\text{-KCl}$  mixtures were prepared by mixing weighed quantities of the two dried salts in the glove box, and then melting in a sealed quartz tube for 24 hours. Some chemical attack of the quartz by the high KCl concentration mixes did occur. After breaking open, slight roughness of the inner tube surface and some sticking of the salt to the tube was observed. No such attack occurred for the nickel halides or the pure zinc halides.

The combination of high melting point, high vapour pressure and corrosiveness makes the study of molten nickel halides extremely difficult. More suitable containers for neutron scattering (such as vanadium or Ti-Zr null-matrix alloy) are ruled out because they are chemically attacked.

### 3.5 Neutron Diffraction Experimental Procedure

For all of the neutron diffraction experiments, spectra were measured as a function of time-of-flight or angle for the samples in their containers, the empty container in the furnace, the empty furnace, a vanadium rod without the furnace (of a similar size to the sample) and the empty diffractometer (without the furnace) which was the background for the vanadium measurements.

The time for each run was allocated (as far as was possible) according to the scattering power of each sample/container/furnace. Several sample scans were taken for the steady-state experiment on  $\text{NiBr}_2 + \text{Ni}$  to check for any changes in the sample due to vapour transport of sample out of the beam, rising of bubbles to the surface or incomplete mixing of the two components. Similarly, for the TOF measurements on mixtures, the sample data was stored several times during the run so that comparisons could be made and any changes in scattering with time observed. It should also be noted that it has been known for molten salts in fused quartz tubes to explode. It was therefore wise to store the data frequently even when no sample changes were likely, such as for the pure zinc halides.

Specific details for each experiment are given in the relevant results chapters.

Table 3.1. Instrument parameters for the Liquids and Amorphous Materials Diffractometer.

Detector angle(2 $\theta$ )/ $^{\circ}$	Momentum transfer range <sup>+</sup> / $\text{\AA}^{-1}$	Comments
4.8	0.26 - 2.6	
9.6	0.53 - 5.3	
20.3 <sup>*</sup>	1.1 - 10.9	Scint. range = 18.9-21.5
35.0 <sup>*</sup>	1.9 - 18.9	Scint. range = 33.8-36.7
58.1 <sup>*</sup>	3.1 - 30.5	Scint. range = 56.7-59.6
89.8 <sup>*</sup>	4.4 - 44.4	Scint. range = 88.1-91.2
145.6	6.1 - 60.7	Two banks of eight time-focussed gas detectors

\* These gas detectors had been replaced by scintillator detectors for the second  $\text{ZnCl}_2$ -KCl experiment. The ranges covered by these scintillators are shown in the last column.

<sup>+</sup> These ranges are for a wavelength range of 0.2 $\text{\AA}$  to 2.0 $\text{\AA}$ .

Table 3.2. Instrument parameters for the General Purpose Powder Diffractometer.

Detector angle/°	$\Delta t/\mu\text{S}$	Number of time bins	Momentum transfer range <sup>+</sup> / $\text{\AA}^{-1}$
19.99	80	191	0.6 - 4.4
30.01	60	255	0.9 - 6.5
60.00	30	511	1.8 - 12.6
90.00	20	767	2.5 - 17.8
149.93	15	1023	3.5 - 24.3

<sup>+</sup> These ranges correspond to a wavelength range of 0.5 $\text{\AA}$  to 3.5 $\text{\AA}$ .

Neutrons were counted from a time of 1000 $\mu\text{S}$  to 16300 $\mu\text{S}$  in time bins of duration  $\Delta t$ .

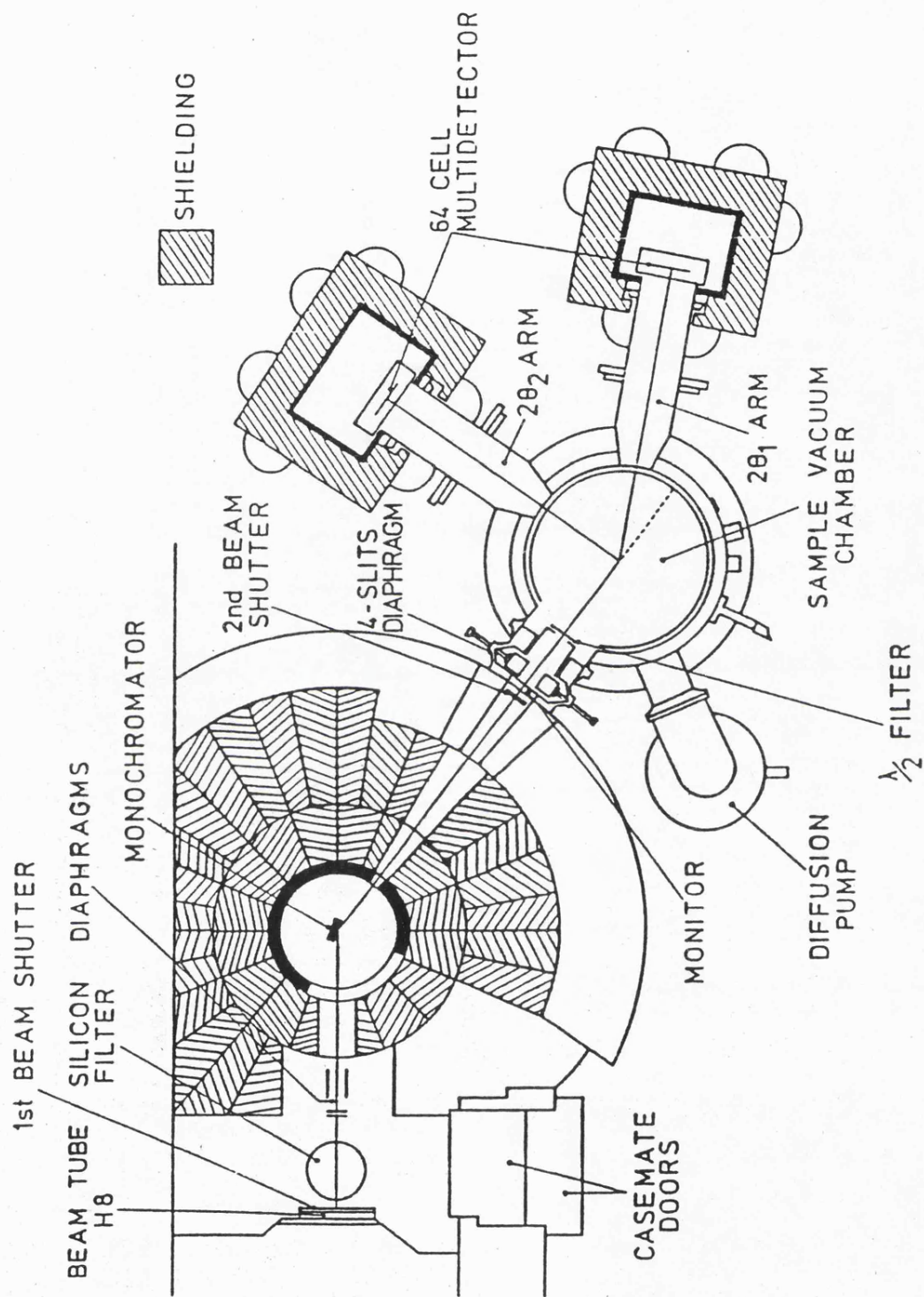


Figure 3.1. The D4B diffractometer at the Institut Laue-Langevin.

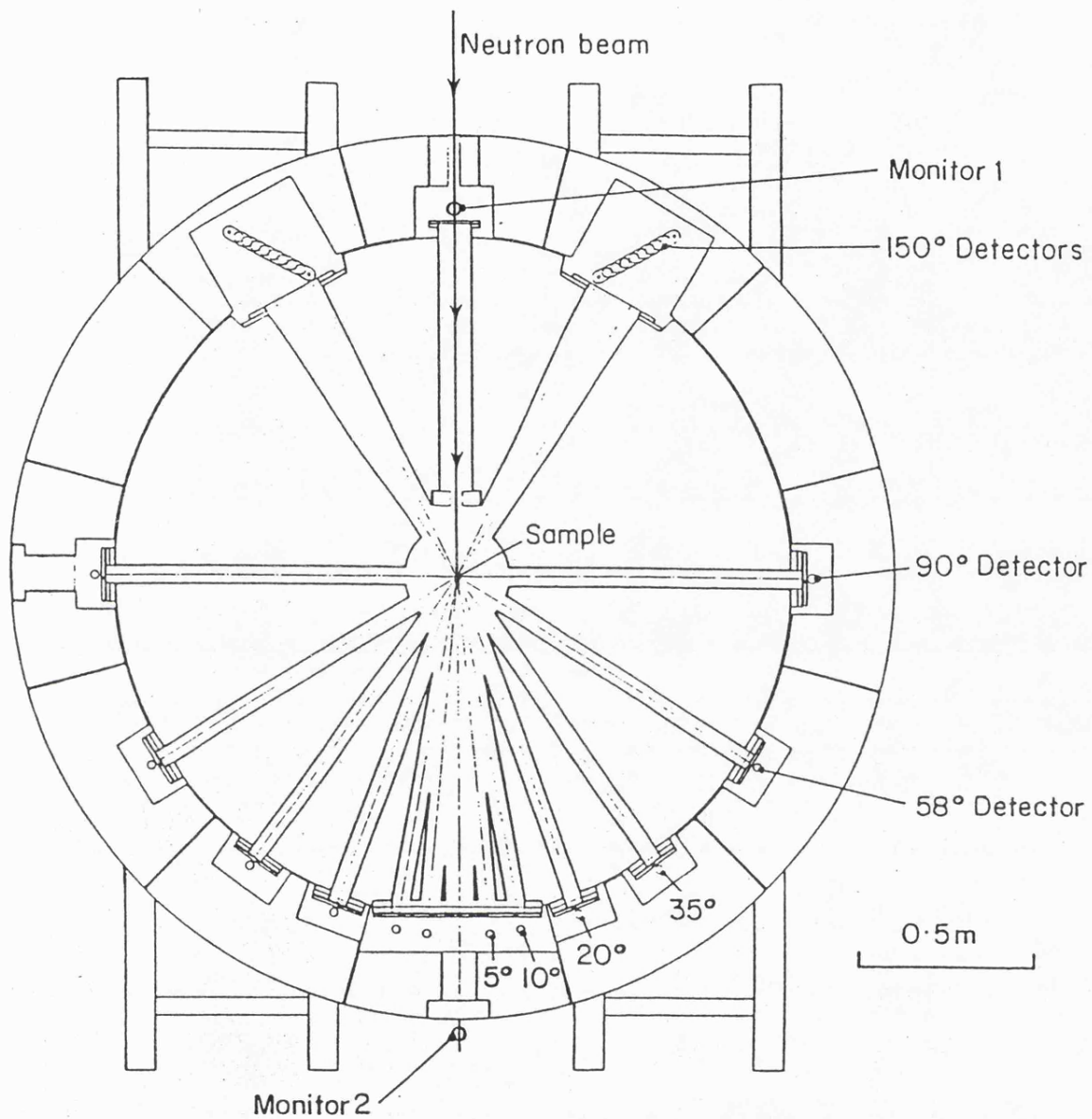


Figure 3.2. The Liquids and Amorphous Materials Diffractometer at ISIS.

## CHAPTER 4

### THE ANALYSIS OF NEUTRON DIFFRACTION DATA

#### 4.1 Introduction

If a differential cross-section is to be obtained from neutron scattering data, a number of corrections need to be applied to the measured intensity. As well as incoherent scattering, there is the possibility of multiple scattering within the liquid and inelastic scattering events which have been ignored so far. Also, the liquid must be held in a container in a furnace, both of which give rise to scattering which must be subtracted from the total intensity in order to obtain the scattering intensity for the sample. However, the scattering from an empty container and furnace is not the same as that from the container and furnace when a sample is present, due to absorption and scattering within the sample and container.

If partial structure factors are to be extracted from the data and Fourier transformation applied to the data to obtain radial distribution functions, then both good statistical accuracy and careful attention to systematic errors is needed. This chapter deals with the process of obtaining structure factors from the measured intensities, including the application of corrections, first of all for a steady-state experiment, then for time-of-flight measurements. The separation of partial structure factors is dealt with in section 4.4 and Fourier transformation to real space distribution functions is discussed in section 4.5.

#### 4.2 The Analysis of Steady-State Neutron Diffraction Data

##### 4.2.1 Initial Data Treatment

During a steady-state diffraction experiment on D4B, the intensity is measured as a function of scattering angle ( $2\theta$ ) by two arrays of multidetectors which move round in small steps which are typically  $1.5^\circ$  and  $2^\circ$  for detector banks 1 and 2 respectively. At any instant they cover angular ranges of  $6^\circ$  and  $8^\circ$  respectively. Thus at each angle, neutrons are counted by four different multidetector elements

during the course of a run, except at the extremes of each angular range for each detector. So the first stage of data analysis is to group together the data collected at each angle by the individual multidetector elements, weighted by the predetermined detector element efficiencies.

#### 4.2.2 Outline of the Data Reduction Procedure - Without Corrections

The scattering intensity from the sample,  $I_s(\theta)$ , is the measured intensity from the sample in its container,  $I_{sc}^e(\theta)$ , with the empty container intensity subtracted from it.

$$I_s = I_{sc}^e - I_c^e$$

The total differential cross-section can then be obtained by calibrating the instrument using a reference scatterer of similar physical size, such as vanadium, which has almost totally incoherent (and therefore structureless) scattering.

$$\frac{d\sigma}{d\Omega} = \frac{I_s}{I_v} \left\{ N_v \sigma_{s,v} \right\}$$

where  $I_v$  is the scattering intensity from a vanadium bar in the same position as the sample,  $\sigma_{s,v}$  and  $\sigma_{s,s}$  are the total scattering cross-sections of vanadium and the sample, and  $N_v$  and  $N_s$  are the total number of scattering sites in the incident beam for the vanadium bar and the sample respectively. This calibration takes into account instrument dependent parameters such as detector solid angle and the flux on the sample for a given monitor count. From this total differential cross-section, the calculated incoherent scattering can be subtracted (see section 2.3) to obtain the coherent differential cross-section and the total static structure factor.

The application of corrections to the measured scattering intensity follows the method of North et. al. (1968) and will be dealt with in the following sections.

### 4.2.3 Multiple Scattering

The cross-section derived in section 2.2 assumes that only single scattering events occur. In practice, there is a non-negligible probability that a neutron will undergo two or more scattering events within a sample and its container. Therefore a calculated multiple scattering intensity has to be subtracted from the measured scattering intensity. The applied correction will, of course, depend upon the sample geometry and has been calculated for the case of a cylindrical sample bathed in a homogeneous neutron beam by Blech and Averbach (1965). This is the method used here. They used the same approach as Vineyard (1954) who calculated the multiple scattering from a thin slab and showed it to be isotropic.

If the incident neutron flux is  $I_0$ , then the number of neutrons per unit solid angle undergoing primary scattering from a volume element  $dV$  is

$$dI_1 = \frac{1}{4\pi} (N\sigma_s I_0) \exp(-\alpha L_1) dV$$

where  $N$  is the atomic number density in atoms per  $\text{cm}^3$ ,  $\alpha$  is the total linear absorption coefficient (from both the total scattering and absorption cross-sections),  $\sigma_s$  is the total scattering cross-section and  $L_1$  is the path length of the incoming beam within the sample. The total primary scattering is obtained by integrating over the whole volume of the sample.

$$I_1 = \int_V \exp(-\alpha L_2) dI_1$$

where  $L_2$  is the path length of the scattered beam within the sample. Similarly, the total  $n^{\text{th}}$  order scattering is

$$I_n = \int_V \exp(-\alpha L_2) dI_n$$

and  $dI_n$  can be written as

$$dI_n = \left\{ N\sigma_s \int_V \frac{dI_{n-1}}{4\pi L^2} \exp(-\alpha L) dV \right\} dV'$$

where  $L$  = the path length between the  $n^{\text{th}}$  and the  $n+1^{\text{th}}$  scattering events.

$$\text{If } \frac{I_n}{I_{n-1}} = \frac{I_2}{I_1} = \delta',$$

then the total multiple scattering can be written as the sum of a geometric progression

$$I_m = I_2 + I_3 + \dots = I_1 \{ \delta' / (1 - \delta') \}.$$

This assumption is true if  $\delta'$  is appreciably smaller than unity, and for this reason sample sizes are usually chosen so that the total scattering is not more than 10%.

To calculate  $\delta'$ , Blech and Averbach wrote

$$\delta' = \frac{\sigma_s}{\sigma_t} \delta$$

where  $\sigma_t$  is the total cross-section (absorption and scattering) and

$$\delta = \frac{\int_V \int_{V'} \exp(-\alpha L / 4\pi L^2) \cdot \exp(-\alpha(L_1 + L_2)) \, dV dV'}{\int_V \exp(-\alpha(L_1 + L_2)) \, dV}.$$

So far, this is a general treatment for any sample geometry.  $\delta$  can be solved numerically for a cylinder of given radius and height by evaluating the integrals using cylindrical coordinates.

A convenient way of including the effect of multiple scattering is to define a multiple scattering cross-section

$$\sigma_m = \sigma_2 + \sigma_3 + \dots,$$

$$\text{but } \sigma_n = \sigma_{n-1} (\sigma_s / \sigma_t) \delta \quad \text{and} \quad \sigma_1 = \sigma_s,$$

$$\text{so } \sigma_m = \sigma_s \{ \delta' / (1 - \delta') \}. \quad (4.2)$$

To correct for multiple scattering, it is then necessary to multiply the scattering cross-section by a factor  $(1+\Delta^m)$ , where  $\Delta^m = \sigma_m/\sigma_s$ . Typical values of the fraction of multiple scattering for the samples used in this work were 14% of the total scattering for natural  $\text{NiBr}_2+\text{Ni}$ , 9.5% for  $^{62}\text{NiBr}_2+\text{Ni}$  and 7% for 'zero'  $\text{NiBr}_2+\text{Ni}$ .

#### 4.2.4 Absorption Correction

Because the incident flux at a point within the sample or container will be less than the initial incident flux, due to scattering and absorption within the sample and container, a correction has to be made. The method used for this was that due to Paalman and Pings (1962) who considered the case of X-ray scattering from a cylindrical sample and container. If  $I_c^e$  is the experimentally determined scattering intensity from the empty container, and  $I_{s+c}^e$  the measured intensity from the sample and its container, Paalman and Pings calculated that the true sample scattering (i.e. without a container and corrected for absorption) is given by

$$I_s = \frac{I_{s+c}^e}{A_{s,sc}} - \frac{I_c^e A_{c,sc}}{A_{s,sc} A_{c,c}} \quad (4.3)$$

where the factors  $A_{i,j}$  are the absorption factors determined by scattering within medium  $i$  ( $s$ =sample,  $c$ =container) following absorption in  $j$  ( $sc$ =absorption in sample and container). For the calculation of the absorption factors, the sample and container are divided into sectors and annular rings forming area elements of approximately constant size, and the attenuations  $\exp(-\alpha_s l_s)$  and  $\exp(-\alpha_c l_c)$  are calculated at the centre of each element. Here,  $l_s$  and  $l_c$  are the path lengths in the sample and container respectively.

The absorption correction for the vanadium normalisation is handled in a similar way, but is simpler since there is no container present. The correction reduces to

$$I_v = \frac{I_v}{A_{v,v}} \quad (4.4)$$

Ideally the scattering from the furnace should also be treated in the same way, but this is unnecessarily complicated since the scattering from the heating element is usually only a small fraction of the total, and treating it simply as a background is a good approximation (see McGreevy, 1981).

#### 4.2.5 Correction for Inelastic Scattering

As mentioned in section 2.5 the differential cross-section is obtained by integration of the double differential cross-section at constant  $Q$  so that

$$\frac{d\sigma}{d\Omega} = \int_{-\infty}^{\infty} \frac{d^2\sigma}{d\Omega d\omega} d\omega.$$

const.  $Q$

The double differential cross-section can also be split up into coherent and incoherent parts and the scattering function  $S(\underline{Q}, \omega)$  defined so that

$$\left(\frac{d^2\sigma}{d\Omega d\omega}\right)^{\text{coh}} = N\bar{b}^2 \left(\frac{k}{k_0}\right) S^{\text{coh}}(\underline{Q}, \omega)$$

and  $\left(\frac{d^2\sigma}{d\Omega d\omega}\right)^{\text{inc}} = N(\bar{b}^2 - \bar{b}^2) \left(\frac{k}{k_0}\right) S^{\text{inc}}(\underline{Q}, \omega)$  (van Hove, 1954).

We then have

$$\frac{d\sigma^{\text{coh}}}{d\Omega} = N\bar{b}^2 \int_{-\infty}^{\infty} \left(\frac{k}{k_0}\right) S^{\text{coh}}(\underline{Q}, \omega) d\omega.$$

const.  $Q$

However, in both fixed wavelength and time-of-flight experiments, the detector carries out the integration of neutron energies at constant  $\theta$ , so that the measured coherent cross-section is

$$\left(\frac{d\sigma}{d\Omega}\right)_{\text{exp}}^{\text{coh}} = N\bar{b}^2 \int_{-\frac{E_0}{\hbar}}^{\infty} D(k) \left(\frac{k}{k_0}\right) S^{\text{coh}}(\underline{Q}, \omega) d\omega.$$

const.  $\theta$

The method used to correct for this inaccuracy is that due to Placzek (1952), who treated the case for a detector with efficiency  $D(k) \propto 1/v$  and expanded  $S(Q, \omega)$  in a Taylor series in powers of  $(Q^2 - Q_0^2)$  before expanding  $(Q^2 - Q_0^2)$  in powers of  $\hbar\omega/E_0$ . Yarnell et. al. (1973) extended this to the general case of an arbitrary  $D(k)$ . The result of this treatment is a correction factor which has to be included with the structure factor to obtain the measured differential cross-section at a given scattering angle  $2\theta$ .

$$\left(\frac{d\sigma}{d\Omega}\right)_{\text{exp}}^{\text{coh}} = N\bar{b}^2 D(k_0) \left\{ S(Q) - \frac{4C_1 \sin^2\theta}{\mu_m} + \frac{16C_2 \sin^4\theta}{\mu_m^2} \right. \quad (4.5)$$

$$\left. - 4C_3 \frac{\sin^2\theta}{\mu_m E_0} k_B T + \frac{1}{2\mu_m} \left( \frac{4\sin^2\theta}{\mu_m} + \frac{k_B T}{E_0} \right) + \dots \right\}$$

where  $\mu_m$  is the ratio of the atomic and neutron masses and  $D(k_0)$  is the detector efficiency at the incident neutron energy.  $D(k_0)$  will cancel when the measured cross-section is normalised to the vanadium scattering. The constants  $C_1$ ,  $C_2$  and  $C_3$  are dependent upon the detector efficiency and its first and second derivatives with respect to  $k$  at the value for elastic scattering  $k_0$ .

This correction can be conveniently incorporated as an addition to the coherent and incoherent scattering, so that

$$\left(\frac{d\sigma}{d\Omega}\right)^{\text{coh}} = N\bar{b}^2 [S(Q) + P(Q)] \quad (4.6)$$

$$\text{and } \left(\frac{d\sigma}{d\Omega}\right)^{\text{inc}} = N(b^2 - \bar{b}^2) [1 + P(Q)] \quad (4.7)$$

$$\text{where } P(Q) = \frac{1}{\mu_m} \left\{ \frac{k_B T}{2E_0} - C_1 \frac{Q^2}{k_0^2} - C_3 \frac{k_B T Q^2}{E_0 k_0^2} \right\}. \quad (4.8)$$

Clearly the effect of inelastic scattering becomes less significant for heavier atoms and the  $Q$  dependent part increases with increasing  $Q$ . The Placzek correction was applied to the vanadium scattering data for the reactor experiment assuming a  $1/k$  detector, but was neglected for the sample scattering because of the problem of choosing an effective atomic mass for  $\mu_m$  for a multi-component liquid. Wood (1987) calculated the magnitude of the Placzek

correction for  $\text{NiCl}_2$  on D4 using the mass of the chlorine atom for  $\mu_m$  (the worst possible case) and the values of the detector coefficients for D4 used by Bertagnolli et. al. (1976). He obtained a result of  $P(Q) = 0.009 - 0.00018Q^2$ , which is very small (1% at  $10\text{\AA}^{-1}$ ). For  $\text{NiBr}_2+\text{Ni}$ , the effect of inelastic scattering is expected to be less because of the heavier anion.

The above expression derived by Yarnell et. al. assumes that the target atoms behave like free atoms when they recoil. The effect of energy transfer to collective modes within the liquid has been neglected but, from inelastic scattering data for ionic liquids, this effect is expected to be small compared with that due to the quasielastic scattering.

#### 4.2.6 The Calculation of $F(Q)$ for Steady-State Diffraction Data

The intensity of sample scattering, after having subtracted the container scattering and having corrected for absorption using equation 4.3, is now

$$I_S = \alpha(\theta) \left\{ \left( \frac{d\sigma}{d\Omega} \right)_{\text{sample}} + N_S \sigma_S \Delta_S^m \right\}, \quad (4.9)$$

where  $N_S$  is the number of scattering sites in the beam,  $\sigma_S$  is the total sample scattering cross-section,  $\alpha(\theta)$  is a machine constant dependent upon detector solid angle and efficiency and the incident neutron flux, and  $\Delta_S^m$  is the multiple scattering cross-section from section 4.2.3.

Similarly the vanadium scattering intensity, after correction for absorption by equation 4.4 and including the Placzek correction of equation 4.7, is

$$I_V = \alpha(\theta) \left\{ \left( \frac{d\sigma}{d\Omega} \right)_{\text{van}} + N_V \sigma_V^{\text{inc}} \Delta_V^m \right\} \left\{ 1 + P_V(Q) \right\}$$

since there is virtually no coherent scattering from vanadium.

Because  $\sigma^{\text{inc}} = 4\pi(b^2 - \bar{b}^2)$ ,

$$I_v = \alpha(\theta) N_v \sigma_v^{\text{inc}} \left\{ \frac{1}{4\pi} + \Delta_v^m \right\} \left\{ 1 + P_v(Q) \right\}. \quad (4.10)$$

All of the quantities in equation 4.9 are either known, calculated or measured except  $\alpha(\theta)$ , which can be calculated from the measured vanadium scattering using equation 4.10 to obtain  $(d\sigma/d\Omega)_{\text{sample}}$  on an absolute scale from the measured  $I_s$ .

The evaluation of the absorption and multiple scattering corrections of equations 4.2, 4.3 and 4.4 involve numerical integrations which are very time consuming. Because the corrections are slowly varying functions of  $\theta$ , they need only be evaluated at a few points and a polynomial can be fitted to these values. For the case of the steady-state diffraction data, the corrections were evaluated at eight different  $2\theta$  values from  $0^\circ$  to  $140^\circ$  in  $20^\circ$  steps. A sixth order polynomial was fitted to the absorption, multiple scattering and, for the vanadium, Placzek correction, which was subsequently interpolated at the values of  $2\theta$  for which data points were measured. Similarly, the vanadium scattering intensity was smoothed with a cubic polynomial, after background subtraction and the application of corrections, prior to dividing it into equation 4.9 to yield the total static structure factor for the sample.

Uncertainty in the scattering and absorption cross-sections and the number of scattering sites in the beam (due to an imperfect knowledge of the density or bubbles in the sample) can lead to a systematic error in  $F(Q)+1$  causing it to be asymptotic to a value other than 1.0 at high  $Q$ . A renormalisation factor is therefore normally required.

For the steady-state diffraction data from D4B,  $F(Q)$  was calculated for each detector bank separately and excellent agreement between the two detectors was observed. All of the subsequent analysis: the combination of data for the different counters, the separation into partial structure factors, the binning and interpolation of data and Fourier transformation to yield radial distribution functions, is the same for both steady-state and time-of-flight data, and is dealt with in sections 4.4 to 4.6.

## 4.3 The Analysis of Time-of-Flight Neutron Diffraction Data

### 4.3.1 Initial Data Treatment

Time-of-flight (TOF) diffraction data was obtained using the pulsed neutron sources at Argonne and RAL. The diffraction spectrum at each detector angle consists of the measured scattering intensity (in number of neutrons per time channel) as a function of time of flight. Neglecting the effect of inelastic scattering, the time of flight of a neutron is simply related to its wavelength by equation 3.1 and, for a given scattering angle, to the momentum transfer given by equation 2.15. In order to obtain the differential cross-section a similar procedure to that used for the steady-state experiment is followed for container, background and furnace subtraction, and vanadium normalisation, together with associated corrections. Allowance must be made for the incoming neutron pulse shape as a function of wavelength, as the fixed monitor count method used for the steady-state experiment no longer applies. To achieve this, the spectra measured at each detector angle and the measured incoming monitor spectrum are converted to wavelength, and the scattering spectra divided by the monitor spectrum which is interpolated by a cubic spline method at the wavelength values for which scattering data is available. Note that since the secondary flight length (from sample to detector) is different for each detector, although the time bins for each measured spectrum are the same, the wavelength values are not. For the results presented here, this interpolation method did not introduce significant inaccuracies since the signal to noise ratio for the monitor spectrum was very much better than that for the scattering spectra, which therefore dominated the errors.

### 4.3.2 The Multiple Scattering and Absorption Corrections

The method used to apply the corrections to the measured data and extract the structure factors is that outlined by Howells (1986). The multiple scattering correction is essentially the same as that for the steady-state experiment, and inelastic scattering is ignored in its

evaluation as this would be a correction to a correction and very small. The same integration used in section 4.2.3 to calculate  $\Delta^m$  is used here also.

The multiple scattering is still angle independent and need only be evaluated once for all of the detector angles but, because of the wavelength dependence of the absorption cross-section of a nucleus,  $\Delta^m$  needs to be calculated as a function of wavelength. Again, because of the time involved for the evaluation of the integrals,  $\Delta^m$  is calculated at only a few representative wavelengths and a polynomial fitted which enables interpolation at the required wavelengths. The absorption cross-section at 1.798Å is required as input to the corrections programme and a  $\sigma_a \propto 1/v$  absorption law is assumed. Typical values for the fraction of multiple scattering for  $ZnCl_2$  (the strongest scatterer used) were 19% of the total scattering at 0.1Å and 13% at 3Å. For the vanadium bar, typical values of 17% and 14% were calculated at these wavelengths.

Similarly, the absorption correction factors  $A_{i,j}$  of section 4.2.4 are evaluated by the same method as a function of wavelength at the same representative points, and a polynomial fitted for interpolation. The absorption correction is angle dependent, so each detector angle is treated separately.

#### 4.3.3 The Placzek Correction for Time-of-flight Diffraction Data

The problem with inelastic scattering for the case of a steady-state experiment is that the detector performs an integration at constant  $\theta$  rather than at constant  $Q$ . This is also the case for a time-of-flight experiment but, in addition to this inaccuracy, there is the added complication that inelastically scattered neutrons, whose speed has been changed, diverge in time during the secondary flight path from those which have been elastically scattered, and thereby are counted in the 'wrong' time bins. Thus the measured intensity is not only a sum at constant angle of elastically and inelastically scattered neutrons, it is also a sum of neutrons with the same total flight time ( $t$ ) regardless of

their initial energies.

The application of the Placzek correction to TOF diffraction data has been discussed by Sinclair and Wright (1974) and Howells (1986). Because of this second summation at constant time of flight which the detector performs, the effect of the incident pulse shape must be included for extracting  $d\sigma/d\Omega$  from the measured intensity. This is given by

$$\left(\frac{d\sigma}{d\Omega}\right)_{\text{exp}}^{\text{total}} = \int_{\substack{-E_0 \\ \hbar^0 \\ \text{const.}\theta \\ \text{const.}t}}^{\infty} \frac{\phi(t_0)}{\phi(t_e)} \frac{dt_0}{dt_e} \frac{D(k)}{D(k_e)} \frac{d^2\sigma}{d\Omega d\omega} d\omega$$

where  $\phi(t)dt$  is the flux of incident neutrons with a time of flight between  $t$  and  $t+dt$ ,  $k_e$  and  $t_e$  are the wavenumber and time of flight of elastically scattered neutrons and  $t_0 = L(m/2E_0)^{1/2}$  with  $E_0$  being the incident neutron energy. Sinclair and Wright applied the same method as Placzek – an expansion of  $S(Q, \omega)$  in terms of  $(Q^2 - Q_e^2)$  – and also expanded  $dt_0/dt_e$  as a power series in  $\hbar\omega/E_0$  to yield a result similar to equation 4.5 for  $P(Q)$ . However, the constants  $C_1$ ,  $C_2$  and  $C_3$  for the TOF case not only depend upon the detector efficiency and its first and second  $k$  derivatives, but also the corresponding derivatives of the apparent neutron flux defined by  $\phi'(t) = D(k)\phi(t)$ . Thus any calculation of the Placzek correction for a TOF diffractometer requires a good knowledge of the incident pulse shape.

Like the steady-state case, the Placzek correction for a TOF experiment is more significant at higher angles. In contrast to the steady-state case, the  $Q$ -dependent part of  $P(Q)$  becomes less significant at high  $Q$  for a given detector angle, as this corresponds to higher neutron energies for which  $E_0 \gg \hbar\omega$  and the approximation of equation 2.15 is more accurate.

For the analysis used in this thesis for TOF data, the Placzek correction was not applied because of the difficulty and uncertainty of its evaluation. As for the reactor case, it is likely to be small. However, as the  $Q$  ranges covered by the detectors at different angles overlapped it was possible,

by comparison of the spectra, to identify the ranges over which the neglect of inelastic scattering and the calculation of the absorption corrections were valid, since both of these are angle and wavelength dependent.

#### 4.3.4 The Calculation of $F(Q)$ for Time-of-Flight Diffraction Data

In the data analysis procedure the measured scattering spectra are treated separately, so that total structure factors are obtained for each detector angle. The same treatment outlined in section 4.2.6 still applies but the machine constant,  $\alpha(\theta, \lambda)$ , is now a function of wavelength. The same vanadium normalisation technique is used, but the measured vanadium spectrum cannot be fitted with a low order polynomial since its shape is structured even after division by the monitor spectrum. Instead, the vanadium spectra are smoothed with a cubic spline function, with the knots having zero weighting over the regions of the spectra which contain vanadium Bragg peaks.

The structure factors are evaluated point by point and the corrections applied as for the steady-state case. Again, a renormalisation was required which was the same for all of the counter banks on GPPD, but was angle-dependent for LAD. However, after renormalisation all of the spectra did match, except for the lowest angle detectors ( $2\theta = 5^\circ$ ). The combination of structure factor data measured at different scattering angles is not in general a trivial problem, since the instrument resolution function is different at each scattering angle. For a resolution which is determined by the uncertainty in the scattering angle  $\Delta\theta$ ,  $\Delta Q/Q = \cot\theta \cdot \Delta\theta$ , so that it is poorest at the lowest scattering angles. However, for the liquids studied here on GPPD and LAD, the diffraction peaks had sufficient natural width so as not to be resolution broadened, except for the lowest angle detectors on LAD, which were therefore not included in the composite structure factors.

The  $Q$  ranges over which each counter is included in the final composite  $F(Q)$  are decided by comparison of the spectra for each detector angle, bearing in mind that the neglected

Placzek correction is least significant at low angles and high neutron energies. The acceptable data from each counter (or bank of counters) is then included in a composite spectrum which is subsequently binned into constant  $\Delta Q$  intervals by averaging the data points using a flux-weighting technique: each data point is weighted by  $1/\sigma^2$  where  $\sigma$  is its error. This counter combination method is also used for the combination of the data from the two detector banks on D4B.

The rest of this chapter deals with the data processing which is common to both steady-state and time-of-flight data: the separation into partial structure factors, Fourier transformation to yield distribution functions, and the calculation of various structural parameters.

#### 4.4 The Separation of Partial Structure Factors

##### 4.4.1 Isotopic Substitution

The total structure factor measured for a multi-component liquid consists of a linear combination of the partial structure factors,  $S_{\alpha\beta}(Q)$ , weighted by coefficients determined by the atomic concentrations and the coherent scattering lengths of the components of the liquid (equation 2.21). By changing the distribution of isotopes of an atomic species from their natural distribution, it is possible to alter the coefficients of equation 2.21 by changing  $\bar{b}$ . The effect of such an isotopic substitution upon the physical and chemical properties of a system should be minimal, especially for the comparatively heavy nickel ions substituted here, and one would not expect to observe any change in the static structure factors.

The three simultaneous equations for  $F(Q)$  resulting from measurements on three samples of different isotopic composition, can be written in matrix form as

$$[A].[X(Q)] = [F(Q)] \quad (4.11)$$

$$\text{where } [A] = \begin{bmatrix} C_a^2 b_a^2 & C_b^2 b_b^2 & 2C_a C_b b_a b_b \\ C_a^2 b_a'^2 & C_b^2 b_b'^2 & 2C_a C_b b_a' b_b' \\ C_a^2 b_a''^2 & C_b^2 b_b''^2 & 2C_a C_b b_a'' b_b'' \end{bmatrix}.$$

$C_\alpha$  and  $b_\alpha$  are the atomic fraction and coherent scattering length of species  $\alpha$ , and the primes denote the different coherent scattering lengths of the isotopically substituted species a – in this case the nickel species.

$$[X(Q)] = \begin{bmatrix} (S_{aa}(Q) - 1) \\ (S_{bb}(Q) - 1) \\ (S_{ab}(Q) - 1) \end{bmatrix}, \quad \begin{array}{l} \text{the desired partial} \\ \text{structure factors,} \end{array}$$

$$\text{and } [F(Q)] = \begin{bmatrix} F_1(Q) \\ F_2(Q) \\ F_3(Q) \end{bmatrix}, \quad \begin{array}{l} \text{the three measured total} \\ \text{structure factors.} \end{array}$$

This has a unique formal solution obtained by direct inversion,  $[X] = [A]^{-1}[F]$ . The certainty with which  $[X]$  can be determined from a measured  $[F]$  will depend upon the conditioning of 4.11, which is a measure of how sensitive  $[X]$  is to small changes in  $[F]$  (experimental error) and  $[A]$  (uncertainty in scattering lengths).

Edwards et. al. (1975) defined the conditioning of 4.11 by a normalised determinant of  $[A]$ ,

$$|A|_n = \left| \frac{a_{ij}}{\left( \sum_{j=1}^3 a_{ij} \right)^{\frac{1}{2}}} \right|$$

where  $a_{ij}$  are the matrix elements of  $[A]$ . Well conditioned equations have  $|A|_n$  of the order  $\pm 1$ . In determining  $S_{\alpha\beta}(Q)$  by the isotopic substitution method, one should chose isotopes so as to achieve the best conditioning. In practice, however, the best conditioning possible is limited by the availability of suitable isotopes. Most partial structural investigations of molten salts to date have used isotopic substitution of  $^{35}\text{Cl}$  (with  $b=1.17 \times 10^{-12}$  cm) and  $^{37}\text{Cl}$  (with  $b=0.308 \times 10^{-12}$  cm) to yield typical values of  $|A|_n = 0.03$  (Edwards et. al. 1975). Nickel salts, however, are particularly favourable to good conditioning because of the existence of the isotopes  $^{58}\text{Ni}$  (with  $b=1.44 \times 10^{-12}$  cm) and  $^{62}\text{Ni}$  (with  $b=-0.87 \times 10^{-12}$  cm – the negative scattering length representing a phase change upon scattering). This latter isotope, with its negative

scattering length, enables a mixture to be made with  $\bar{b}=0$  which is referred to as 'zero' nickel. The values of  $|A|_n$  for a series of experiments by Wood (1987) to determine the structure of molten nickel halides, were 0.22, 0.40 and 0.57 for  $\text{NiCl}_2$ ,  $\text{NiBr}_2$  and  $\text{NiI}_2$  respectively. This compares very favourably with the previously used chlorine isotopic substitution.

This good conditioning enables a direct solution for [X] for the nickel halides, rather than a solution employing one of the algorithms described by McGreevy and Mitchell (1982) which used the physical limitations of one of the  $S_{\alpha\beta}(Q)$  to reduce the uncertainty in the other two. Such an algorithm is often necessary in solving [X] and usually involves a smoothing of the data prior to transformation, due to the large statistical errors in  $S_{\alpha\beta}(Q)$  which give rise to truncation errors in the  $g_{\alpha\beta}(r)$  (see section 4.5).

For the analysis of the  $\text{NiBr}_2+\text{Ni}$  and  $\text{NiI}_2+\text{Ni}$  data presented in this thesis, the  $S_{\alpha\beta}(Q)$  were determined point by point from the measured  $F(Q)$ 's and, since the statistical quality of the data was good enough for direct transformation, no smoothing procedure was used. More details, including the coefficients used for the separation of the partials, are given in the relevant results chapter.

#### 4.4.2 The Long-Wavelength Limit and the Sum Rule

There are a number of useful constraints which the final derived partial structure factors must satisfy in order to be physically acceptable solutions. These constraints are useful since systematic errors may be introduced into the data processing procedure through uncertainty in the number of scattering sites in the beam, the scattering cross-sections and the application of the corrections.

i) The Faber-Ziman partial structure factors must be asymptotic to 1.0 at high  $Q$ . Correspondingly, from equation 2.21,  $F(Q)$  is asymptotic to zero at high  $Q$ . This test is easily carried out by eye for TOF results, for which data exists at  $Q$  values greater than any oscillations in  $F(Q)$  about the asymptotic limit. For the steady-state case

however, the structure factors for liquids have not usually reached their asymptotic limits at the maximum  $Q$  value of the instrument ( $\approx 16.2 \text{ \AA}^{-1}$  for D4B).

ii) The long wavelength limit of the partial structure factors can be uniquely determined from the isothermal bulk compressibility,  $K_T$ , of the liquid. This was demonstrated by Kirkwood and Buff (1951) who calculated the relationship for a two component liquid to be

$$S_{\alpha\beta}(0) = \rho_0 k_B T K_T - \frac{\delta}{C_\alpha} \alpha\beta + 1 \quad (4.12)$$

where  $k_B$  is the Boltzmann constant and  $T$  is the absolute temperature. If the compressibility is known, then this relationship can be used both to check the normalisation of the data by seeing if the measured structure factor is heading to the right value of  $S(0)$  at its low  $Q$  end, and to extrapolate the data to  $S(0)$  for the purposes of evaluating the integral for the Fourier transformation. The  $S(0)$  limits of the partial structure factors are related by

$$S_{aa}(0) = K' - \frac{C_b}{C_a}, \quad S_{bb}(0) = K' - \frac{C_a}{C_b}$$

$$\text{and } S_{ab}(0) = 1 + K',$$

where  $K' = \rho_0 k_B T K_T$ . Therefore, even if  $K_T$  is not known, the three values to which the partial structure factors are extrapolated must be chosen consistently in accordance with these relationships. Fortunately, because of its  $Q$  dependence, the transform is insensitive to this region of the structure factor. For the total structure factors,

$$F(0) = \rho_0 k_B T K_T (C_a b_a + C_b b_b)^2 - (C_a b_a^2 + C_b b_b^2).$$

iii) In real space, the partial radial distribution functions must become zero at low  $r$  since two nuclei cannot occupy the same position at the same time, thus equation 2.12 becomes

$$g_{\alpha\beta}(0) = 0 = 1 + \frac{1}{2\pi^2 \rho_0} \int_0^\infty Q^2 (S_{\alpha\beta}(Q) - 1) dQ$$

$$\text{so that } \int_0^{\infty} Q^2 (S_{\alpha\beta}(Q) - 1) dQ = -2\pi^2 \rho_0. \quad (4.13)$$

This is the sum rule (Enderby et al. 1966) and for the total structure factors it can be written as

$$\int_0^{\infty} Q^2 F(Q) dQ = -2\pi^2 \rho_0 (C_a b_a + C_b b_b)^2. \quad (4.14)$$

Any systematic errors present, for example incorrect normalisation or incorrectly calculated corrections, will yield a wrong value for this integral. But, because of its  $Q^2$  dependence and the statistical errors in the data, the value of this integral fluctuates with the choice of  $Q_{\max}$  for the upper integration limit, so that the usefulness of the sum rule is limited.

#### 4.5 Fourier Transformation to Real Space

The reciprocal space total and partial structure factors and the real space total and partial distribution functions, are related by Fourier sine transformation – see equations 2.12 and 2.22. As was mentioned in section 2.4, if we have a complete knowledge of a structure factor over the entire range of momentum transfer from 0 to  $\infty$ , then we have a complete knowledge of the corresponding distribution function. In practice, however,  $F(Q)$  and  $S(Q)$  will contain errors and their ranges will be limited by the instrument. At the low  $Q$  end, extrapolation to the long wavelength limit is required and a low order polynomial is used for this. At the high  $Q$  end, the truncation of the structure factor at  $Q_{\max}$  and its errors must be taken into account when transforming the data for a number of reasons.

i) If the structure factor still has significant oscillations at the point of truncation, then a direct transformation will yield a result which is a convolution of the structure factor with a step function. This step function has a value of 1.0 over the range of available data and drops to 0 at the point of truncation. This will show itself as

spurious oscillations in  $g(r)$  of period  $\pi/Q_{\max}$  over the entire range of  $r$ , which can have an amplitude comparable to that of the structure in  $g(r)$ , especially at low  $r$  due to the  $1/r$  dependence of the Fourier transform. For the TOF data presented in this thesis this was not a problem, since data was collected for  $Q$  values of greater than  $50\text{\AA}^{-1}$  – well beyond the region of reciprocal space over which liquid structure factors extend. For the steady-state results, the structure factors still had some structure at the point of truncation.

ii) If the statistical accuracy of the data is poor within the high  $Q$  region, due to a low count rate or ill-conditioning of equation 4.11, then spurious ripples in  $g(r)$  can arise from Fourier transformation of unsmoothed structure factor data because of the  $Q$  dependence of the transform. A smoothing algorithm has often been adopted for extracting the  $S_{\alpha\beta}(Q)$ , which results in the transformation of smooth functions and thus avoids the introduction of ripples into  $g(r)$ . This does not mean, however, that  $g(r)$  is more accurately known.

iii) The resolution in real space is determined by the value of  $Q_{\max}$  used for the transform. This is usually the maximum  $Q$  value for which useful data is available – i.e. the highest  $Q$  value that the instrument can measure in the steady-state case or, for the TOF case, the highest  $Q$  for which the statistical accuracy is good enough to resolve any oscillation in the structure factors and for which the neglect of inelastic scattering is still valid. This second limit can be determined from observation of the  $F(Q)$ , since the neglect of inelastic scattering has the effect of producing a droop in the calculated  $F(Q)$  at high  $Q$ .

If the data is truncated at a value of  $Q_{\max}$ , then in real space the distribution function is convoluted with a peak shape function whose central peak has a FWHM of  $3.791/Q_{\max}$  (Wright and Leadbetter, 1976). This resolution is usually not sufficient to avoid broadening the first peak in  $g_{+-}(r)$  (the cation-anion distribution function) and reducing its height.

The low frequency ripples in  $g(r)$ , due to either statistical noise at high  $Q$ , truncation or some other discontinuity in  $S(Q)$  (for example a remaining Bragg peak from the furnace scattering), cannot usually be smoothed out without smoothing the underlying distribution function as well. However, this was possible (except over the principal peak in  $g(r)$ ) for TOF data with values of  $Q_{\max}$  greater than  $\sim 20\text{\AA}^{-1}$ , which gave short period truncation ripples.

A common method used to reduce the effects of truncation is to use a modification function,  $M(Q)$ , by which the data is multiplied prior to transformation and which has the effect of bringing  $S(Q)$  smoothly to its asymptotic limit before it reaches  $Q_{\max}$ . Two such functions are those due to Lorch (1969)

$$M(Q) = \frac{\sin(Q\Delta/2)}{(\Delta/2)} \quad \text{where } \Delta = \frac{2\pi}{Q_{\max}}$$

and the cosine window function

$$M(Q) = \frac{1}{2} \left[ 1 + \cos\left(\frac{\pi(Q-fQ_{\max})}{Q_{\max}(1-f)}\right) \right]^{1/x} \quad \text{for } Q_{\max}(1-f) < Q < Q_{\max}$$

$$\text{and } M(Q) = 1 \quad \text{for } Q < Q_{\max}(1-f)$$

where typically  $x = 2$  or  $3$  and  $f$  (the fraction of the data over which  $M(Q)$  is applied) is between  $0.2$  and  $0.3$ . For both of these functions  $M(Q)$  is set to zero for  $Q > Q_{\max}$ . For most of the Fourier transforms used for this thesis no modification function was required, since data was either available to a  $Q$  value greater than that of any observed structure in  $S(Q)$ , or the structure in  $S(Q)$  was sufficiently small in amplitude at  $Q_{\max}$  for the effect of truncation to be negligible. When a modification function was used, the cosine window function was adopted. Although useful, the use of a modification function does mean that  $g(r)$  is convoluted with a peak shape function which has satellite ripples and, for the Lorch function, a FWHM of  $5.437/Q_{\max}$  (Windsor, 1981). This reduces the real space resolution.

In order to distinguish real features in  $g(r)$  from those which are due to truncation, a procedure can be adopted which involves transforming the data with several values of  $Q_{\max}$  and different modification functions, as well as non-modified transformation. This procedure was used for the analysis of the  $\text{ZnCl}_2$ -KCl mixtures data, for which the effects of noise on  $g(r)$  were significant. A helpful property of  $g(r)$  for removing Fourier transform artefacts and identifying some systematic errors in the data, is its value of zero at low  $r$ . Edwards (1977) investigated the effects on  $g(r)$  of incorrect normalisation of the data and of a small slope on the data, and these effects were largely confined to a region  $r < 2\text{\AA}$ . These errors are therefore easy to identify and eliminate.

To summarise, for a solution of  $g(r)$  to be acceptable, it must satisfy the following constraints:

i) It must be a smoothly varying function of  $r$ .

ii) It must be zero in the low  $r$  region. An indication of the extent of this region is given by the sum of the two ionic radii for the particular distribution function concerned.

iii) Upon back-transformation it must give a function,  $S(Q)$ , which fits the data within the experimental errors. Furthermore, a given set of  $g_{\alpha\beta}(r)$ 's must, upon transformation, be able to generate the measured  $F(Q)$ 's after recombination in order to be an acceptable set of functions.

This may seem a very stringent condition upon the final acceptable  $g(r)$ 's but, because of the ill-conditioning of the transform ( $S(Q)$  to  $g(r)$  - equation 2.12), the infinite number of acceptable  $g(r)$ 's that will fit the data may not be well determined, especially at low  $r$ . The next chapter deals with a method of uniquely selecting one from this infinite set of acceptable solutions.

#### 4.6 Structural Features in the Distribution Functions

Once having transformed the structure factors to yield real space radial distribution functions, it is useful, for the purposes of comparison with other results, to have a quantitative measure of the main real space structural features.

##### 4.6.1 Peak Positions, Heights and Widths

The standard method of peak fitting, using a least-squares fit for a model function (Gaussian or Lorentzian for example), is not appropriate for the case of liquid distribution functions because the peak shapes in  $g(r)$  are not generally of standard form, and the presence of ripples and absence of any error bars makes the reliability of such a fit difficult to determine. The method used here to determine peak positions, heights and widths in  $g(r)$  and  $r^2g(r)$ , was to transform the data with several values of  $Q_{\max}$  without a modification function and to average the values (estimated by eye) observed for the several truncations. Reducing  $Q_{\max}$  to a value below that required to completely resolve the main peak in  $g(r)$  clearly results in peak broadening and height reduction, so care is needed in estimating peak parameters by this method. Often only a lower limit for peak height and an upper limit for peak width can be determined. The peak positions in  $r^2g_{\alpha\beta}(r)$  will be referred to as  $\bar{r}_{\alpha\beta}$ .

##### 4.6.2 Coordination Numbers

The number of nearest neighbours around a given type of atom is of interest in the study of liquids and amorphous materials, since it gives a good indication of the local structural arrangement and can be a useful guide to structural changes upon melting. However, for a non-crystalline material, the coordination number is not unambiguously determinable as it is for the crystalline state. It nevertheless remains a useful concept and a number of definitions exist.

The number of  $\beta$  type atoms within a shell defined by radii  $r_1$  and  $r_2$  ( $r_2 > r_1$ ) around an  $\alpha$  type atom is, by the

definition of  $g(r)$  given in section 2.1,

$$n_{\alpha\beta} = \int_{r_1}^{r_2} 4\pi r^2 \rho_{\beta} g_{\alpha\beta}(r) dr \quad (4.16)$$

where  $\rho_{\beta}$  is the number density of  $\beta$  type atoms and is equal to  $\rho_0 C_{\beta}$ . For the coordination number, we wish to know the total number of  $\beta$  type atoms within the first shell around an  $\alpha$  type atom. This can be defined by

$$n_{\alpha\beta} = \int_0^{r_{\max}} 4\pi r^2 \rho_{\beta} g_{\alpha\beta}(r) dr$$

where  $r_{\max}$  is the value of  $r$  which marks the end of the first coordination shell. The extent of this coordination shell is not uniquely defined for an ionic liquid, since  $g(r)$  rarely drops to a value of zero after the first peak, and this gives rise to ambiguity in the value of  $n_{\alpha\beta}$ .

One definition which does not rely on knowing the extent of the first coordination shell, is the  $rg(r)$  symmetric method due to Coulson and Rushbrooke (1939), based on a quasi-crystalline model. For this method  $n_{\alpha\beta}$  is defined by

$$n_{\alpha\beta} = 2 \int_0^{r'_{\max}} 4\pi r \rho_{\beta} [rg_{\alpha\beta}(r)]_{\text{SYM}} dr.$$

This involves integrating the principal peak in the function  $rg(r)$  up to its maximum at  $r'_{\max}$  and then doubling the result. This method assumes that the function  $rg(r)$  is symmetric about its maximum (hence the name) but there is no physical reason why this should be so.

A common method of evaluation is the  $r^2g(r)$  symmetric method, for which the coordination number is defined by

$$n_{\alpha\beta} = 2 \int_0^{r'_{\max}} 4\pi \rho_{\beta} [r^2 g_{\alpha\beta}(r)]_{\text{SYM}} dr.$$

The function  $r^2g(r)$  is integrated up to the principal peak maximum at  $r'_{\max}$  and the area doubled. This method assumes

that the function  $r^2g(r)$  is symmetric, but this is clearly not so for many experimentally determined  $r^2g(r)$ . Nevertheless, it was used in this thesis for the purposes of comparison with previous results which have been obtained using this method.

A third and favoured method of evaluation is that of integration of  $r^2g(r)$  up to the first minimum following the principal peak,  $r_{\min}$ , so that the coordination number is defined by

$$n_{\alpha\beta} = \int_0^{r_{\min}} 4\pi\rho_{\beta}r^2g_{\alpha\beta}(r)dr.$$

This makes no assumption about the shape of the principal peak in  $r^2g(r)$ , but will give an overestimate of  $n_{\alpha\beta}$  when applied to total distribution functions if there is any significant first shell penetration. This method will also give an ill-defined value for  $n_{\alpha\beta}$  when applied to  $g(r)$ 's which have minima which are broad and flat, because of the  $r^2$  dependence of the integral and the uncertainty, for such a  $g(r)$ , in the choice of  $r_{\min}$ . McGreevy et. al. (1986) showed that this last method gives the best estimate of coordination number for computer simulation results of molten alkali halides.

It is this last method which has been adopted here, since the systems studied have been particularly favourable to its use, having deep minima after the first peak. Sometimes  $r_{\min}$  has been defined as the first minimum in  $g(r)$  rather than  $r^2g(r)$  (see for example Newport et. al. 1985) and, for the purposes of comparison, this was also used in some cases.

A final method involves the extrapolation of  $r^2g(r)$  to zero on the high  $r$  side of the first peak. This can reduce any uncertainty due to first shell penetration, but the form of the extrapolation is arbitrary. As first shell penetration was not a problem in coordination number evaluation for the total distribution functions presented here, this method was not used.

All of these methods give different results for  $n_{\alpha\beta}$  and many authors have failed to state which method they have used

when quoting values for coordination numbers. March and Tosi (1984) regard the coordination numbers evaluated by the symmetric methods and those evaluated by integration to the first minimum, as two distinct types of coordination number; namely 'close-contact' and 'nearest-neighbour' coordination numbers. It is important to be clear which method has been used.

## CHAPTER 5

### THE APPLICATION OF THE MAXIMUM ENTROPY METHOD TO LIQUID STRUCTURE FACTOR DATA

#### 5.1 Introduction

Chapter 4 dealt with the extraction of structural information in the form of distribution functions from neutron diffraction data for liquids. The problems introduced by an incomplete knowledge of the structure factor, due to errors and a limited range of observation in  $Q$  space, were discussed in section 4.5 where traditional methods of dealing with them: a low order polynomial fit at low  $Q$ , a window function in the region of truncation and smoothing of the data, were also dealt with. In recent years the technique of maximum entropy image reconstruction, widely used in astronomy but also in many other fields for the extraction of information from incomplete and noisy data, has been applied to data from neutron scattering experiments, including the determination of distribution functions from structure factor data.

Because any measured data set for  $F(Q)$  or  $S(Q)$  is limited in range, assumptions have to be made about these functions outside of this range if a distribution function is to be obtained by the inverse Fourier transform of equations 2.12 or 2.22. An arbitrary polynomial fit to the long wavelength limit (if known) is used, and  $S(Q)$  is set to 1.0 for  $Q$  values beyond the highest one for which data has been obtained. In addition, a direct inverse transform of the measured data requires that it be interpolated onto a constant  $\Delta Q$  grid for the purposes of integration. This may be difficult and unreliable if there are gaps in the data and, since it does not take into account the errors in the data, equal significance is assigned to all of the data points.

A way of reducing these effects, while making no assumptions about the regions of  $Q$  space for which there are no data, is to fit the data with a transform from  $g(r)$  to  $S(Q)$ . This can be done by a parameter fitting method - for example, using the HNC or MSA with a given pair potential - obtaining solutions with a minimum  $\chi^2$  which fit the data.

However, this necessarily makes assumptions about the form of the interionic potentials, and does not in general obtain acceptable fits to the data. Another approach is to consider each point in  $r$  space as a 'parameter' to be varied in order to fit the data but, since there are an infinite number of points, it is possible to obtain an over-fit with  $\chi^2 = 0$  which follows the noise in the data. There are in fact an infinite number of acceptable solutions with  $\chi^2 \leq M$  (the number of data points), some of which will be physically unreal with negative values of  $g(r)$ . It is desirable to have a way of uniquely selecting a solution which is consistent with the available data and which makes as few assumptions as possible about the unavailable data. The maximum entropy method provides such a solution.

The justification for choosing the solution with the largest entropy as the one that makes the fewest assumptions about the unavailable data is given by Gull and Skilling (1984). The application of the maximum entropy method to the derivation of distribution functions is only justifiable because they can be regarded as probability distributions from their definition (see section 2.1).

## 5.2 Maximum Entropy - An Overview

The definition of the entropy,  $S$ , of a discrete set of probabilities,  $P_i$ , is due to Shannon (1948),

$$S = -\sum P_i \log P_i. \quad (5.1)$$

In the case of image reconstruction  $P_i = f_i / \sum f_i$ , where  $f_i$  are a set of positive numbers which constitute the image. An acceptable image is one which fits the data set,  $D_k$ , when the response function of the observing instrument,  $R(f)$ , is applied to it. For the case of liquid structure factors  $R(f)$  is the Fourier transform of equation 2.11. Gull and Skilling argue that maximisation of the functional  $-\sum P_i \log P_i$  is the only consistent way of selecting a single image from the many possible ones which does not introduce correlations into the image other than those required by the data. A more formal proof of this maximum entropy principle is provided by Shore

and Johnson (1980).

For a distribution function, we have a continuous probability distribution  $P(r)$  and the entropy must be written as

$$S = - \int P(r) \log[P(r)/m(r)] dr \quad (5.2)$$

since  $P(r)$  is now a probability density and is not dimensionless. The probability density in this case is the probability of finding two atoms separated by a distance between  $r$  and  $r+dr$ , divided by  $dr$ , which is of course  $\rho_0 r^2 g(r)$ . The number density is just a scaling factor and will be dropped from the discussion. In the absence of any data one would wish the final image,  $g(r)$ , to default to 1.0 for all  $r$ . This is a totally uniform distribution. The entropy is a maximum when  $P(r) = m(r)$ , so that  $m(r)$  should be considered as the level to which the image  $P(r)$  defaults in the absence of any data - in this case  $r^2$ .

This definition of entropy requires that the  $P_i$  be non-negative (as is always the case for a probability distribution) and therefore only those solutions with  $g(r) \geq 0$  are allowable in a maximum entropy determination of a distribution function. The usefulness of the maximum entropy technique for image reconstruction lies in the fact that, as the image is varied in order to fit the data subject to the constraint that its entropy should be a maximum, any departure from the default level of  $m(r)$  will only be introduced if it is required by the data. Therefore, any feature observed in a maximum entropy solution is only there because the data requires it to be so, and it is not an artefact of the transformation procedure.

The question remains, however, of what is an acceptable fit to the data? With enough points in  $r$  space it should be possible, in the absence of systematic errors, to fit every measured data point, so that  $\chi^2$  is zero. But this is still not allowing for the fact that the data possesses random errors. A  $\chi^2$  test is often used to determine whether a function has fit the data.

$$\chi^2 = \sum_{k=1}^M (F_k - D_k)^2 / \sigma_k^2 \quad (5.3)$$

and a solution ( $F_k$ ) is deemed to have fit the measured data, which has errors  $\sigma_k$ , when  $\chi^2 \leq M$ .

The general purpose algorithm developed by Skilling and Bryan (1984) obtains solutions which have a maximum entropy subject to the constraint that  $\chi^2$  is equal to  $M$ . It is a programme based on this algorithm which has been used for the maximum entropy solutions presented in this thesis.

### 5.3 Description of the Maximum Entropy Algorithm

A subroutine based on the Skilling and Bryan algorithm was supplied by Dr G.J.Daniell of Southampton University. This was adapted for the particular problem of distribution function determination to be used within a programme for liquid structure factor analysis. A brief description of this general purpose algorithm now follows.

We wish to maximise  $S$  subject to the equality constraint that  $\chi^2 = M$ . This is done in the usual way by setting up a Lagrange function,  $L = S - \lambda C$ , where  $C$  is a general constraint statistic (in this case  $\chi^2$ ). The solution will lie at a maximum of  $L$  for some value of the multiplier  $\lambda$ . Because of the non-linearity of the entropy, an iterative procedure is required involving repeated transformations from image space to data space via the response function  $R$ .

The image and data can be regarded as vectors in  $N$  and  $M$  dimensional spaces, where  $N$  is the number of points in the image. The transformation can be written

$$\begin{matrix} [ F_k ] \\ k=1, M \end{matrix} = \begin{matrix} \left[ R_{kj} \right] \\ j=1, N \end{matrix} \begin{matrix} \left[ f_j \right] \end{matrix}. \quad (5.4)$$

The first and second derivatives of  $S$  and  $C$  with respect to the individual  $f_j$  can easily be evaluated and  $\nabla S$  and  $\nabla C$  obtained at any stage from the definition of  $S$  and by transformation to data space respectively. For example:

$$\frac{\partial C}{\partial f_j} = \sum_k 2R_{kj}(F_k - D_k)/\sigma_k^2.$$

As the summation is now on the first index of  $R_{kj}$  and not on the second, as it was for equation 5.4, then the evaluation of  $\nabla C$  involves a multiplication of the residuals,  $(F_k - D_k)$ , by the transpose of the response function matrix.

Starting from the default image of  $P(r) = m(r)$ ,  $C$  is reduced at each iteration whilst the entropy of the image remains close to its maximum for the current value of  $C$ , until the required  $C$  ( $\chi^2 = M$  in this case) is obtained. The algorithm then increases  $S$  while constraining  $C$  to equal its final value until a maximum is found. For a true maximum of  $S$ ,  $\nabla S$  and  $\nabla C$  should be parallel, and the algorithm employs this test to determine whether a maximum entropy solution has been found.

The way in which  $[f_j]$  is varied at each iteration is determined by setting up a subspace defined by several base vectors and maximising  $L$  within this subspace using the calculated  $\nabla L$  and the curvature. However, the 'distance' by which  $[f_j]$  is moved (defined by  $\sum(\delta f_j)^2/f_j$  where  $\delta f_j$  are the changes in the individual  $f_j$ ) is limited to a value between  $0.1\sum f$  and  $0.5\sum f$  so as not to go too far in a particular direction at any iterate. This is necessary because of the non-linearity of the problem.

#### 5.4 The Image-Data Transformation

In order to apply this algorithm to the problem of finding a maximum entropy  $g(r)$  to fit an experimental data set  $S(Q)$ , the Fourier transformation must be represented by the matrix  $[R_{kj}]$  so that the transformation operation on the image (in this case  $r^2g(r)$ ) is the matrix multiplication of equation 5.4. The Fourier transform can be written as

$$Q[S(Q) - 1] = (4\pi\rho_0) \int_0^{\infty} \frac{1}{r} [r^2g(r) - r^2] \sin(Qr) dr$$

which, when approximated to the discrete form and with the upper limit set at a chosen  $r_{\max}$ , is

$$Q_k[S(Q_k) - 1] = (4\pi\rho_0) \sum_{j=1}^N \frac{1}{r_j} [r_j^2 g(r_j) - r_j^2] \sin(Q_k r_j) \Delta r,$$

where  $\Delta r$  is the  $r$  space data interval, so that  $N\Delta r = r_{\max}$ . If we write  $F_k$  equal to  $Q_k[S(Q_k) - 1]$  and  $f_j$  equal to the positive quantity  $r_j^2 g(r_j)$  then, following the subtraction of the 'constant'  $r_j^2$  (it is  $g(r_j)$  which is the variable for a given  $r_j$ ), we have

$$[ F_k ] = \left[ R_{kj} \right] \left[ f'_j \right], \quad (5.5)$$

where  $f'_j = f_j - r_j^2$  and the matrix elements are

$$R_{kj} = \frac{4\pi\Delta r\rho_0}{r_j} \sin(Q_k r_j).$$

The subtraction of the constant  $r_j^2$  before transformation at each iteration is trivial, since it is the derivatives of  $S$  and  $C$  with respect to the  $f_j$  which determines the operation of the programme.

This transition from an integral to a summation is more accurate if the trapezoid rule is used, which involves halving the first and last points in image space for the summation (i.e.  $R_{kj}$  is halved for  $j = 1$  or  $N$ ).  $\Delta r$  should be chosen so that no significant error is introduced into the integration by using this approximate method. In order to check the choice of  $\Delta r$ , a more accurate integration method employing Weddle's rule was used. A distribution function with a fairly sharp peak (the  $g_{\text{NiBr}}(r)$  for the  $\text{NiBr}_2 + \text{Ni}$  data) was transformed using a value of  $\Delta r = 0.025\text{\AA}$ . The result was compared with those obtained by using the trapezoid rule with matrix multiplication, and no significant difference was observed between the two solutions for values of  $\Delta r$  of less than  $0.075\text{\AA}$ . Small differences were seen with a  $\Delta r$  of  $0.1\text{\AA}$ , which gave rise to a slight peak shift in  $g(r)$  upon re-transformation. Typical values for  $\Delta r$  used for the maximum entropy solutions presented in this thesis are  $0.03\text{\AA}$  to  $0.05\text{\AA}$ . Upper limits of  $r_{\max} = 16\text{\AA}$  were usually sufficient to avoid truncation errors in  $S(Q)$ .

During operation, the transform is evaluated at each point in data space for which data is available. This is totally flexible and the data need not be interpolated, nor  $S(Q)$  considered outside of the range of observation.

### 5.5 The Default Level for $g(r)$

If the default level of  $g(r)$  is the structureless  $g(r) = 1$  for all  $r$ , then  $m(r)$  of equation 5.2 is  $r^2$ . This, however, is unrealistic, since it is known that  $g(r)$  must fall to zero at low  $r$  and is typically zero for all  $r$  less than about 0.8 times the sum of the ionic radii. This prior knowledge about  $g(r)$  can be built into the maximum entropy solution by choosing a default level which approaches 1.0 at high  $r$  and which drops to zero at low  $r$ . A problem arises, however, in that the choice of this function is arbitrary and whatever is chosen will affect the final maximum entropy solution. The degree to which the solution depends upon the choice of  $m(r)$  is determined by the quality of the data: the more we know about  $S(Q)$ , in terms of both statistical accuracy and range of observation, the more constrained an acceptable solution for  $g(r)$  will be.

#### 5.5.1 Results of Some Tests

In order to investigate this default level dependence, an artificial data set was produced by truncating the Fourier transform of a known, smooth distribution function at high and low  $Q$ , and then adding gaussian noise of a chosen variance. A smoothed version of the  $g_{\text{NiBr}}(r)$  partial from the molten pure  $\text{NiBr}_2$  data was used and the points at which the transform was evaluated were those corresponding to the real data set for the pure  $\text{NiBr}_2$  data.

Maximum entropy solutions were obtained from data having a  $Q$  range of  $0.3\text{\AA}^{-1} \leq Q \leq 16\text{\AA}^{-1}$  and a large noise variance of 0.1, which had been binned (not interpolated) into constant  $\Delta Q$  bins of  $0.025\text{\AA}^{-1}$ . This had been the case with the actual data (see chapter 8). Solutions were obtained using a flat default level of 1.0, a default level which drops smoothly to zero and one which drops rapidly to zero at

the point at which the leading edge of the first peak is known to be. These solutions are plotted in figure 5.1 and at the top of figure 5.2, and are compared with the original function which is shown as a dashed line in each plot.

The differences between these solutions are small and confined to the region of  $r$  less than  $\approx 3\text{\AA}$ , where the default levels differ and where the solution is ill-constrained due to the  $r$  dependence of the transform. The differences reflect the fact that the solution will hug the default level unless it is required to depart from it because of the data, and the solutions obtained represent the minimum peak heights and peak areas that are required in order to fit the data. Better statistical accuracy for the data will mean a better constrained solution. This is seen in the bottom plot of figure 5.2, where a solution obtained with a noise variance of 0.0275 is compared with that obtained with a variance of 0.1. Both solutions were from flat default levels. The better quality data produces a solution with a higher main peak and deeper first trough, as well as being lower in the low  $r$  region. This more closely fits the original function.

The effect of further truncation of the data is shown in figure 5.3 in both real and reciprocal space. A data file with noise variance of 0.0275 was truncated at  $Q = 8\text{\AA}^{-1}$  and a solution found from the smoothly varying default level used previously. This result is compared with that obtained with a  $Q_{\text{max}}$  of  $16\text{\AA}^{-1}$  (shown dashed) and the first peak is seen to be reduced in height from 5.74 to 5.53 and broadened slightly from a FWHM of  $0.385\text{\AA}$  to one of  $0.423\text{\AA}$ . The corresponding resolutions are  $\Delta r = 0.39\text{\AA}$  and  $0.79\text{\AA}$ .

Ripples in  $g(r)$  are still present for maximum entropy solutions, although to a lesser degree than those found in  $g(r)$ 's obtained by direct inverse transformation (compare, for example, the maximum entropy solutions for the  $\text{NiBr}_2+\text{Ni}$  data with the raw transforms in figures 8.8 to 8.10). Their frequency is reduced for the solution obtained from data with  $Q_{\text{max}} = 8\text{\AA}^{-1}$ , indicating that their origin is in the truncation of the data, just as for the direct inverse transform method. However, the back-transform of the solution obtained for  $g(r)$ , which is shown in the bottom part of figure 5.3, shows an oscillatory behaviour beyond the  $8\text{\AA}^{-1}$  at

which the data was truncated, which appears to fit the missing data even though it was not required to do so. This arises from the fact that most of the information in a structure factor is contained in the mid Q region ( $1\text{\AA}^{-1} < Q < 8\text{\AA}^{-1}$ ), so that a solution which is required to fit only this region of data shows very little difference from one which fits the whole region of Q space. A direct inverse transform of this data set, truncated at  $8\text{\AA}^{-1}$ , would result in very severe ripples in  $g(r)$  due to convolution with a window step function, thus the maximum entropy method is seen to be extremely powerful for data which is terminated at a point at which there are still significant oscillations.

All of these results were obtained after seventy to one hundred iterations and used typically seven to ten minutes of CPU time on a VAX 8650 computer.

## 5.6 Total Distribution Functions

So far, only partial  $g(r)$ 's have been considered, but one may wish to apply the technique to total  $G(r)$ 's as well. These are defined by

$$G(r) = \sum_{\alpha\beta} C_{\alpha} C_{\beta} \bar{b}_{\alpha} \bar{b}_{\beta} [g_{\alpha\beta}(r) - 1]$$

and they approach zero at high  $r$ . When all of the  $g_{\alpha\beta}(r)$  are zero at low  $r$ , then

$$G(0) = -\sum_{\alpha\beta} C_{\alpha} C_{\beta} \bar{b}_{\alpha} \bar{b}_{\beta} = -K.$$

Thus  $G(r)$  is a function which has both positive and negative values and drops to  $-K$  in the low  $r$  region.

For obtaining a maximum entropy solution, the probability distribution considered,  $G'(r)$ , is a linear combination of the individual distribution functions weighted by their coefficients:

$$\text{i.e. } G'(r) = \sum_{\alpha\beta} C_{\alpha} C_{\beta} \bar{b}_{\alpha} \bar{b}_{\beta} g_{\alpha\beta}(r)$$

where  $G'(r) = G(r) + K$ .

The uniform default level,  $m(r)$ , from which the entropy is measured, is then  $m(r) = Kr^2$ , which may be taken to zero at low  $r$  if prior knowledge is to be incorporated. As before,  $G'(r)$  must be converted to  $G(r)$  prior to transformation to  $F(Q)$  - this is trivial.

## 5.7 Summary

The maximum entropy method of structure factor analysis has a number of advantages over traditional methods:

i) The data is fitted with a transform from image to data space, so that only the measured data need be considered and extrapolation beyond the region of observation is not required.

ii) A unique solution is obtained which contains features which arise solely from the available data and not from transformation artefacts.

iii) Random errors in the data are taken into account.

iv) There is the possibility of convoluting the image with the instrument resolution function prior to comparison with the data. This is usually far better conditioned than the deconvolution problem.

v) Truncation errors are considerably reduced, since no discontinuity is introduced into the data. Small features in  $g(r)$  can be positively identified, which before may have been obscured by transform artefacts, particularly at low  $r$ .

For data sets with small error bars that extend over a large  $Q$  range, the maximum entropy method has little advantage. When the zinc halide data was investigated using the maximum entropy method, the solutions obtained were not noticeably better than those obtained by direct Fourier transformation. The maximum entropy method is most useful for extracting information from data which is noisy and limited in range.

This method of distribution function determination takes into account random errors in the data by assigning a significance to each data point in accordance with its error bar. Systematic errors present in the data are not considered and may give rise to ripples in  $g(r)$  or features which are unreal. It may also be the case that negative values of  $g(r)$  are required to fit the data (for example if too much container scattering has been subtracted), in which case it will not be possible to obtain a maximum entropy solution without first eliminating, if possible, the offending systematic error.

For the case of distribution function determination, the uniqueness of the maximum entropy solution is compromised by an arbitrary choice for  $m(r)$  if prior knowledge about  $g(r)$  is to be incorporated into the solution. However, the method is still useful so long as one makes an intelligent choice for  $m(r)$  and bears it in mind when interpreting the result. In chapter 7, an intelligent choice of  $m(r)$  was used to confirm the presence of small peaks in the low  $r$  region of  $G(r)$ 's, which were obscured by noise when straightforward inverse transformation was used. Using a default level of 1.0 for all  $r$  will still give a unique maximum entropy solution even though it does not contain all that we know about  $g(r)$ .

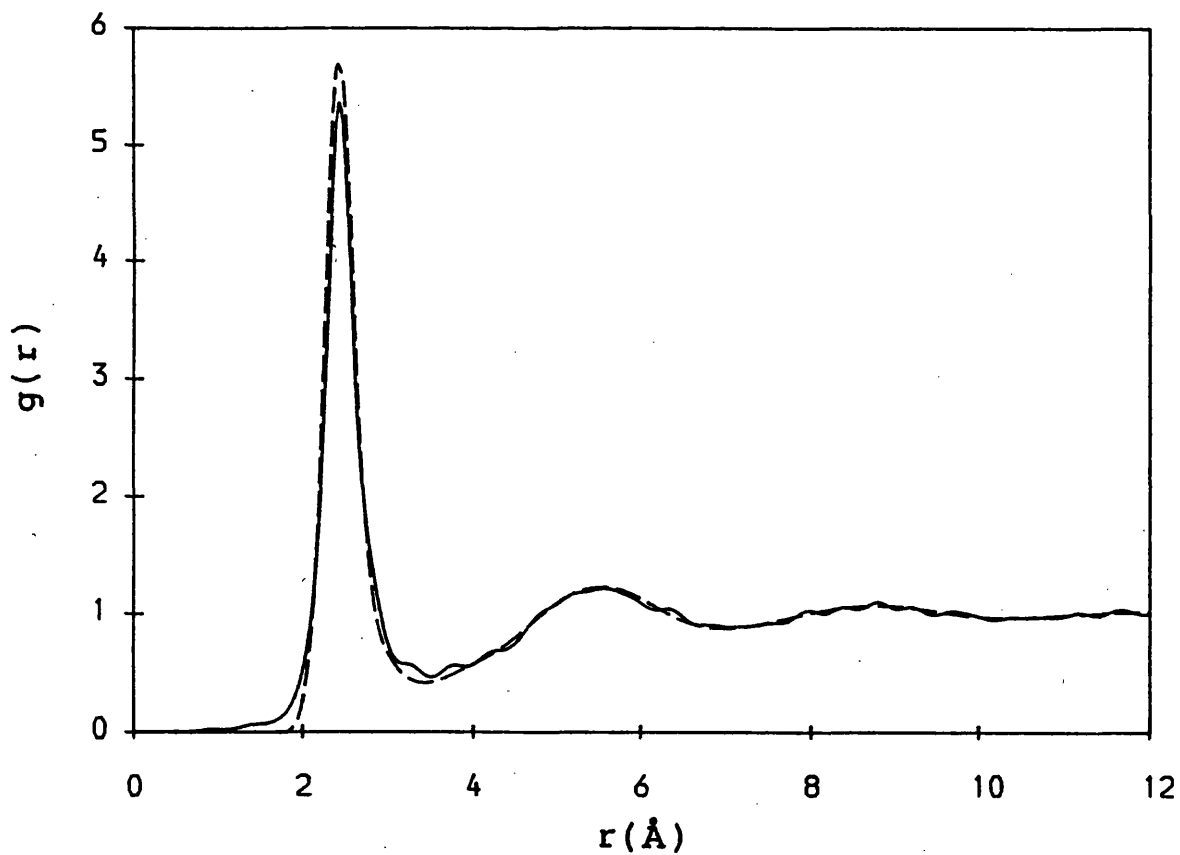
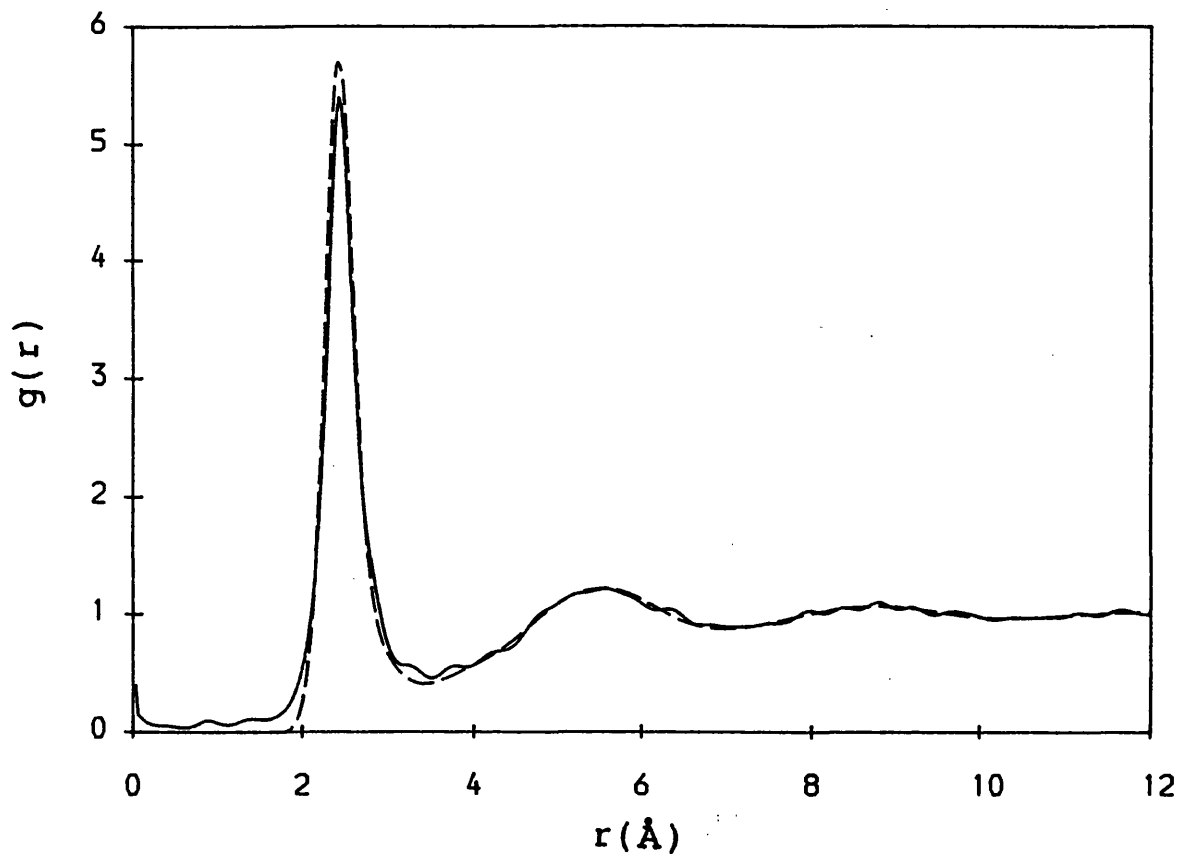


Figure 5.1. Maximum entropy solutions to fit an artificial data set with a noise variance of 0.1, using a flat default level of 1.0 (top) and a default level which drops smoothly to zero over the range  $0 < r < 5 \text{\AA}$  (bottom). The original function, from which the data was created, is shown as a dashed line in both plots.

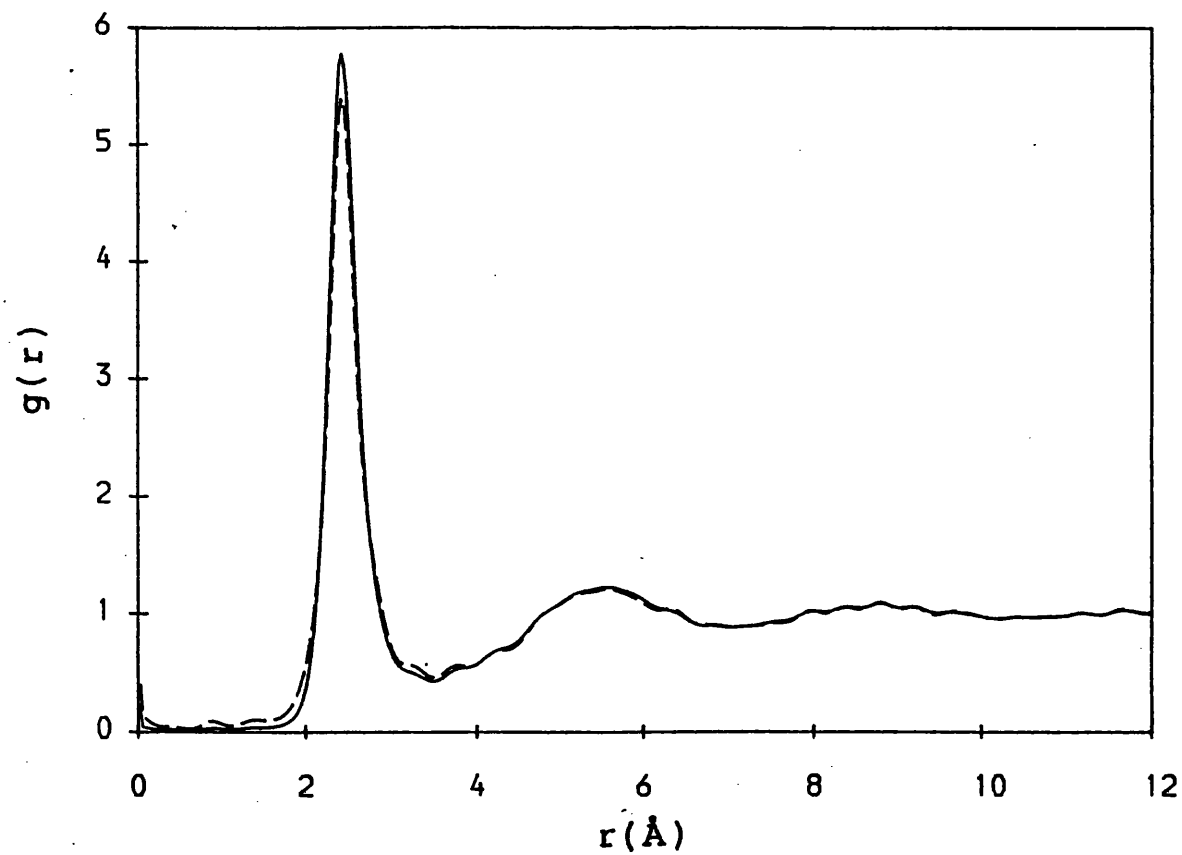
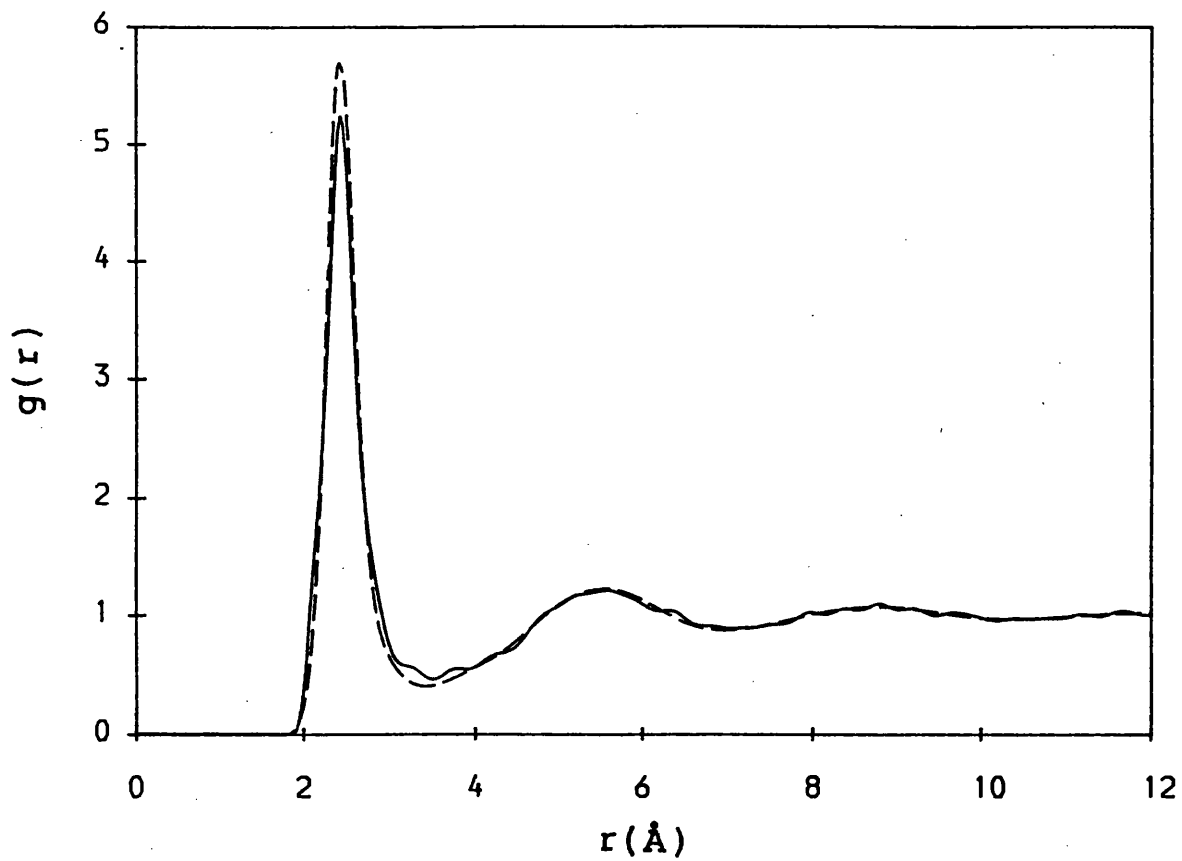


Figure 5.2. Top- Maximum entropy solution to fit the data with a noise variance of 0.1, using a default level which drops rapidly to zero at the leading edge of the first peak. Bottom- Comparison of two solutions using flat default levels, to fit data with noise variances of 0.1 (dashed) and 0.0275 (full).

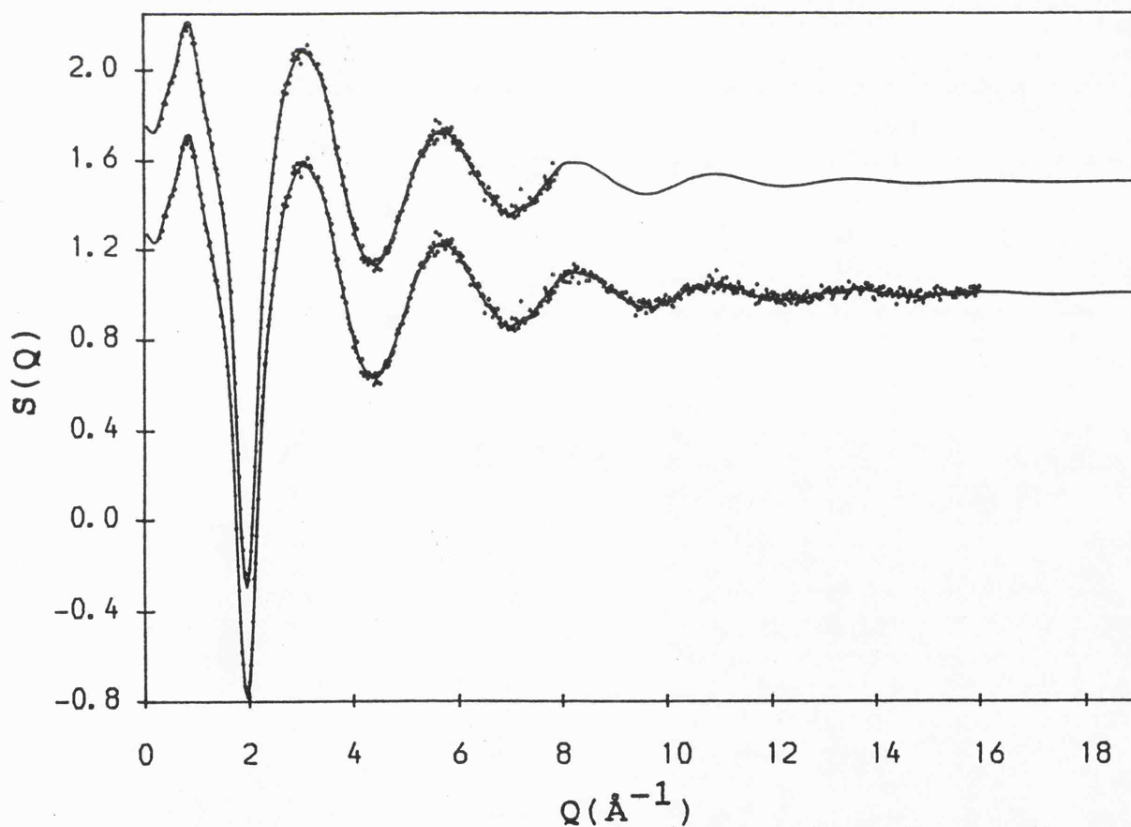
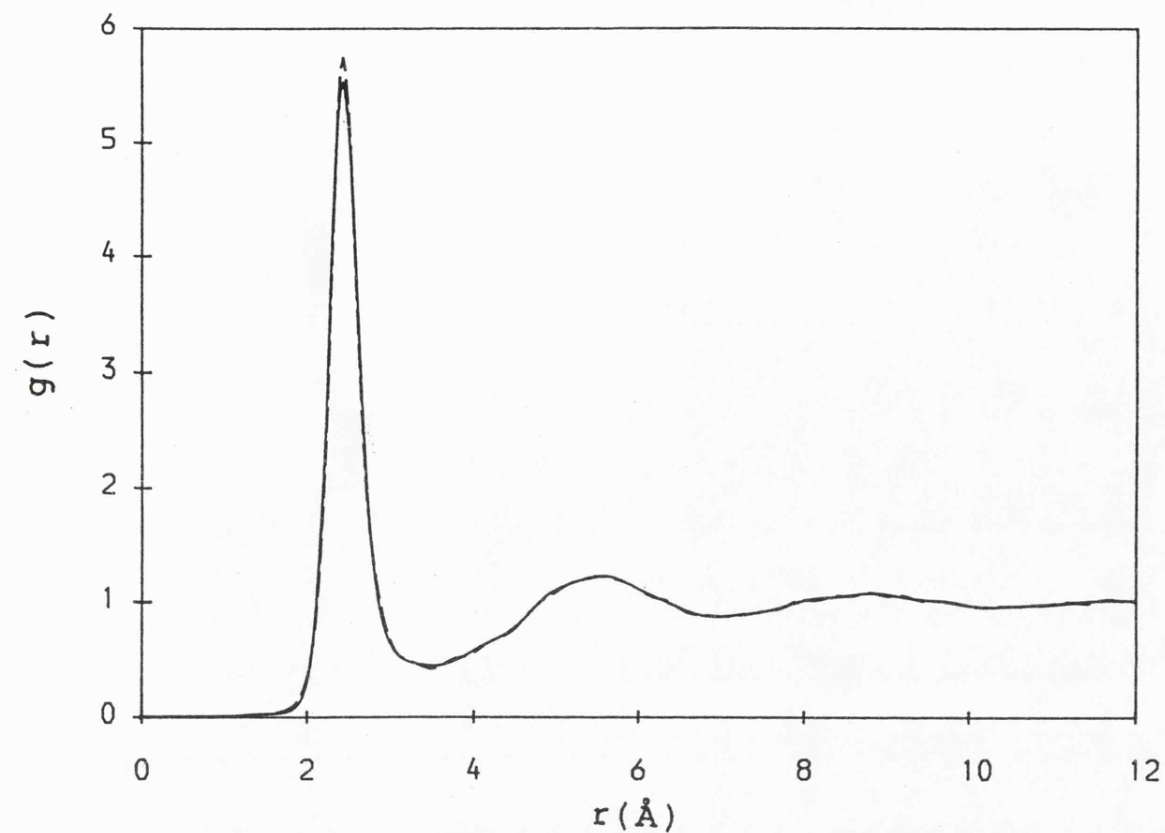


Figure 5.3. Comparisons in real space (top) and reciprocal space (bottom) of maximum entropy solutions obtained from the two data sets shown as dots in the bottom plot. The  $g(r)$  shown dashed was a solution for the data set which extends to  $Q=16\text{\AA}^{-1}$ . The full line was obtained from the truncated data set, which has been displaced by +0.5 in the bottom figure.

## CHAPTER 6

### THE STRUCTURE OF MOLTEN ZINC HALIDES

#### 6.1 Introduction

The structure of molten zinc chloride has been obtained from neutron diffraction measurements using chlorine isotopic substitution by Biggin and Enderby (1981a), and found to be a close-packed structure of chloride ions with zinc ions occupying tetrahedrally coordinated sites. The distribution functions they obtained are shown in figure 6.1. The anomalously low electrical conductivity found for zinc chloride (plotted in figure 6.2), its high viscosity (Mackenzie and Murphy, 1960 and Susic and Mentus, 1975) and its glass-forming ability when supercooled in the strict absence of water (which is rare for pure halides), has led to the description of zinc chloride as a 'network melt' in which  $\text{ZnCl}_4^{2-}$  tetrahedral units are linked via corner sharing of  $\text{Cl}^-$  ions to form a network. This model is supported by Raman studies (Aliotta et. al., 1981) and an inelastic neutron diffraction study (Fairbanks, 1987), in which collective modes associated with intra-tetrahedral motion are observed.

Biggin and Enderby found that the partial radial distribution functions were phased to give complete charge cancellation for distances beyond about  $6\text{\AA}$ , which is a characteristic of the ionisation  $\text{ZnCl}_2 \longrightarrow \text{Zn}^{2+} + 2\text{Cl}^-$ , and they observed a dip in  $S_{\text{ZnCl}}(Q)$  which was coincident with the first main peaks in  $S_{\text{ZnZn}}(Q)$  and  $S_{\text{ClCl}}(Q)$  - a feature which is characteristic of charge alternation (see for example Copestake and Evans, 1982). They concluded that a description in terms of  $\text{ZnCl}_3^-$  or  $\text{ZnCl}^+$  units, which had previously been proposed, was not appropriate. They explained the low electrical conductivity of  $\text{ZnCl}_2$  by suggesting that the mobility of the  $\text{Zn}^{2+}$  ions is restricted due to shielding by the close-packed  $\text{Cl}^-$  ions, and contrasted this with other 2:1 salts, like  $\text{BaCl}_2$  and  $\text{SrCl}_2$ , where first shell penetration of like ions occurs, indicating greater ionic mobility. However, in contrast to molecular dynamics simulations by Gardner and Heyes (1985) and Woodcock et. al. (1976) using ionic potentials, Biggin and Enderby observed near coincidence of

the first peaks in  $g_{\text{ZnZn}}(r)$  and  $g_{\text{ClCl}}(r)$ . If the zinc ions are doubly charged, we would expect, from Coulombic repulsion, the principal peak distance for the cations,  $\bar{r}_{++}$ , to be much greater than that between the anions,  $\bar{r}_{--}$ . Therefore, purely ionic potentials are not adequate in accounting for the structure of liquid  $\text{ZnCl}_2$ . Ballone et. al. (1986) used the HNC approximation to obtain the three partial structures for  $\text{ZnCl}_2$  using a dielectric screening model with angular dependence of interionic forces. They found qualitative agreement with experiment, and a value of  $\bar{r}_{++} = 3.98\text{\AA}$ , compared with  $3.8 \pm 0.1\text{\AA}$  from experiment.

Neutron diffraction studies of  $\text{NiCl}_2$  (Newport et. al., 1985),  $\text{NiBr}_2$  (Wood and Howe, 1988) and  $\text{NiI}_2$  (Wood et. al., 1988) have revealed similar close-packed anion structures, with nickel ions occupying tetrahedrally coordinated sites. The anion structure is observed to remain almost unchanged throughout the series, whereas the Ni-Ni structure shows reduced correlation (interpreted as enhanced ionic mobility) for the  $\text{NiI}_2$ . Wood et. al. (1988) explained this using a reduced charge transfer model, in which the anion valence band hybridises with the unfilled cation d band, resulting in ionic charges of less than those normally expected for 2:1 salts. A structural study of the zinc halide series, for which such a model of reduced charge transfer does not apply, since the  $\text{Zn}^{2+}$  ion has a full d shell, should help to clarify the roles of anion size and electronic structure in determining the liquid state structure.

A feature of the structure factors of many 2:1 salts is the presence of a diffraction peak at  $Q \sim 1\text{\AA}^{-1}$  (before the first main peak) in the cation-cation partial structure factor. The corresponding real space periods for these 'pre-peaks' are between  $6\text{\AA}$  and  $7.5\text{\AA}$ , which is beyond the range of nearest neighbour structure. Therefore this peak has been interpreted as indicating intermediate range ordering between structural units (for example, tetrahedra) within the liquid (Wood et. al., 1988). The range over which this ordering persists can be estimated from the pre-peak widths, and is typically  $15\text{\AA}$  to  $25\text{\AA}$ . This peak has been observed for non-tetrahedral salts, such as  $\text{CaCl}_2$  and  $\text{MgCl}_2$ , as well as for the nickel halides, although it is only a small shoulder on

the leading edge of the first main peak in  $S_{\text{NiNi}}(Q)$  for  $\text{NiCl}_2$ . It increases in height from  $\text{NiCl}_2$  to  $\text{NiI}_2$  and is 0.9 times the height of the first main peak of the  $S_{\text{NiNi}}(Q)$  for  $\text{NiI}_2$ . In contrast to this, the pre-peak observed by Biggin and Enderby in  $S_{\text{ZnZn}}(Q)$  for  $\text{ZnCl}_2$  is already large at 0.7 times the height of the first main peak. If the strength of the pre-peak in the cation-cation structure factor is dependent upon anion size, then this dependence should be observable from total diffraction measurements on natural zinc halides, since the pre-peak is already clearly seen in the total structure factor of natural  $\text{ZnCl}_2$ . A summary of pre-peak sizes for the 2:1 salts studied to date and for this present study, together with other relevant parameters, is listed in table 6.1.

The low melting point of  $\text{ZnCl}_2$  ( $318^\circ\text{C}$ ) enables diffraction data to be obtained at a temperature substantially higher than the melting point in order to ascertain the effect of temperature upon the liquid state structure. It is known from the electrical conductivity and viscosity measurements of Grantham and Yosim (1966) and Mackenzie and Murphy (1960), that the ionic mobilities of  $\text{ZnCl}_2$  and  $\text{ZnBr}_2$  just above their melting points are low, but increase substantially upon heating. Therefore, a diffraction experiment on  $\text{ZnCl}_2$  at  $600^\circ\text{C}$ , where the conductivity is about 200 times higher than at the melting point, was also undertaken, in order to observe any structural changes associated with this increased mobility.

Also reported in this chapter are the results of a previous experiment on LAD to investigate the effect of temperature upon the pre-peak in  $F(Q)$  for natural nickel iodide. All investigations of 2:1 salts so far have been at temperatures near to the melting point, and the question arises of whether the pre-peak is a true feature of the liquid state structure, or whether it derives from incomplete melting?

## 6.2 Experimental

Pulsed neutron diffraction measurements were made using natural samples of  $\text{ZnCl}_2$  at  $330^\circ\text{C}$  and  $600^\circ\text{C}$ , and of  $\text{ZnBr}_2$  and  $\text{ZnI}_2$  at temperatures just above their melting points. The Liquids and Amorphous Materials Diffractometer at RAL was used. The samples were prepared using the vacuum drying method described in section 3.4, and were pre-melted before being loaded into their final tubes which were of 8.2mm internal diameter and 1mm wall thickness. Within the instrument the molten samples extended beyond the irradiated height of 4cm. An investigation by Biggin and Enderby (1981a), using  $\text{ZnCl}_2$  which had been dried with dry HCl and which contained less than 0.1% by weight of water, and two vacuum dried samples of  $\text{ZnCl}_2$ , containing small quantities of water (up to 4% by weight), showed that the neutron diffraction pattern is not significantly changed by the presence of a small percentage of water. The vacuum dried samples used here were expected to contain less water than the 'wet' samples used by Biggin and Enderby.

The coefficients for the structure factors and the densities used for the data analysis are:

for  $\text{ZnCl}_2$

$$F(Q) = 0.036S'_{\text{ZnZn}} + 0.408S'_{\text{ClCl}} + 0.242S'_{\text{ZnCl}}$$
$$\rho = 2.520\text{gcm}^{-3} \text{ at } 330^\circ\text{C} \text{ and } 2.400\text{gcm}^{-3} \text{ at } 600^\circ\text{C}$$

(e.g. Angell and Wong, 1970),

for  $\text{ZnBr}_2$

$$F(Q) = 0.036S'_{\text{ZnZn}} + 0.205S'_{\text{BrBr}} + 0.171S'_{\text{ZnBr}} \quad (6.1)$$
$$\rho = 3.99\text{gcm}^{-3} \text{ at } 420^\circ\text{C} \text{ (Janz, 1967),}$$

and for  $\text{ZnI}_2$

$$F(Q) = 0.036S'_{\text{ZnZn}} + 0.124S'_{\text{II}} + 0.133S'_{\text{ZnI}}$$
$$\rho = 3.846\text{gcm}^{-3} \text{ at } 470^\circ\text{C} \text{ (Janz, 1967),}$$

where  $S'_{\alpha\beta} = S_{\alpha\beta} - 1$ .

Neutron scattering spectra were measured by the fixed angle  $^3\text{He}$  gas detectors for periods of between 34 and 45 hours for each sample, except for the  $\text{ZnCl}_2$  at  $600^\circ\text{C}$  which

was counted for about 12 hours. In addition, the scattering from an empty silica container, the empty furnace and a 3/8" vanadium bar was also measured. After subtraction of the furnace background and the removal of Bragg peaks, the vanadium spectra were fitted with cubic splines. The raw data, normalised to the monitor and binned with six data points in each bin, for the molten  $\text{ZnBr}_2$ , the empty container, the vanadium bar and the empty furnace, is plotted as a function of wavelength for the two combined detectors at  $\pm 20^\circ$  and  $\pm 90^\circ$  in figures 6.3 and 6.4.

Total structure factors were obtained for each individual spectrum after the application of corrections for multiple and incoherent scattering and absorption. Table 6.2 lists the parameters used for the data analysis. These structure factors are shown over the ranges for which they contribute to the final composite  $F(Q)$ 's in figures 6.5 to 6.7, for the  $\text{ZnCl}_2$  at  $330^\circ\text{C}$ ,  $\text{ZnBr}_2$  and  $\text{ZnI}_2$ . They are compared with the back-transforms of the final smoothed  $G(r)$ 's. The ranges over which the individual spectra were combined were those for which good agreement was observed between them in the overlapping regions of  $Q$  space. Although a renormalisation of the spectra was required, and this was different for each angle, the spectra did match well once they had been rescaled. After combining the spectra for all except the  $5^\circ$  counters, the data was binned into constant  $\Delta Q$  bins of  $0.025\text{\AA}^{-1}$  to produce the composite total structure factors shown in figure 6.8. These  $F(Q)$ 's were Fourier transformed, without any window function or smoothing, to give the total distribution functions shown in figure 6.9. Also plotted are the smoothed  $G(r)$ 's from which the back-transforms were obtained.

### 6.3 Results

From these Fourier transforms, structural parameters were obtained by the methods described in section 4.6. These are listed in table 6.3. The coordination numbers were evaluated by the integration of  $r^2G(r)$  up to its first minimum following the principal peak. The errors quoted are estimates which take into account the uncertainties in the

densities and the leading edges of the peaks, as well as the effect of different choices of  $Q_{\max}$  for the transforms and the uncertainties in the locations of the minima in  $r^2G(r)$ . Due to the  $r^2$  dependence of  $n_{\alpha\beta}$ , it is this last term which usually contributes most to the error, but for these systems the minima in  $G(r)$  are deep, so that the coordination numbers obtained by this method are well defined. It has been assumed that this first peak is due entirely to the cross-term,  $g_{ZnX}(r)$ , and that any contributions to this peak from like ion penetration are small. This is justified by consideration of the small coefficient of  $S_{ZnZn}(Q)$ , and the fact that any penetration by the anion-anion first peak in  $g(r)$  would be shown up clearly by a shift in the leading edge of the second peak in  $G(r)$ .

From the results of Biggin and Enderby and the coefficients of equation 6.1, the second peak in the total distribution function for  $ZnCl_2$  is known to arise mainly from the first peak in  $g_{ClCl}(r)$ . The halide-halide structure predominates for all three salts, and the heights and positions of these peaks have naïvely been taken to be those of the first peaks in  $g_{XX}(r)$ . These are listed in table 6.3 together with the ratios of the principal peak positions in  $r^2g_{--}(r)$  and  $r^2g_{+-}(r)$ , which are referred to as  $\bar{r}_{--}$  and  $\bar{r}_{+-}$ . This ratio, together with the coordination number, tells us about the local anion structure around each cation. For a tetrahedral structure, this ratio should be  $(8/3)^{1/2} = 1.633$ . From the Biggin and Enderby results however, it is seen that the second peak in  $g_{ZnCl}(r)$  rises on the high  $r$  side of the first peak in  $g_{ClCl}(r)$ , thus shifting this peak in the total  $G(r)$  to higher  $r$ . From the coefficients of 6.1, this effect is expected to become more significant for the bromide and iodide, so that the values of  $\bar{r}_{--}$  and the ratios  $\bar{r}_{--}/\bar{r}_{+-}$  should be regarded as slight overestimates.

#### 6.4 Summary of Observations

The following observations can be made from the total structure factors and distribution functions shown in figures 6.8 and 6.9.

#### 6.4.1 Zinc Chloride at 330°C

In  $Q$  space, the total structure factor shows good agreement with the results of Biggin and Enderby, but, due to the extended range of observation afforded by a pulsed source, the structure is seen to extend to about  $28\text{\AA}^{-1}$ . The pre-peak which Biggin and Enderby found in the  $S_{\text{ZnZn}}(Q)$  is clearly resolved here in the total structure factor, at a position of  $1.005 \pm 0.01\text{\AA}^{-1}$ . In real space, the main Zn-Cl peak position of  $2.28 \pm 0.01\text{\AA}$  is 0.90 times the sum of the two ionic radii, and is in agreement with their result of  $2.29 \pm 0.02\text{\AA}$ , but its height of  $8.9 \pm 0.2$  and width of  $0.26\text{\AA}$  are resolved to be considerably higher and narrower than their resolution-limited result. Indeed, the peak width observed here is not much greater than the resolution width of  $0.22\text{\AA}$  that is expected for a truncation at  $Q = 28\text{\AA}^{-1}$  for the Fourier transform. The area under this peak reveals a fourfold coordination of chloride ions around each zinc ion within the error. The minimum following this peak is very deep, due to the lack of any first shell penetration by like ions, and gives rise to a small error for the coordination number defined by integration up to this minimum in  $r^2G(r)$ .

From the second peak in  $r^2G(r)$ , the first peak in  $g_{\text{ClCl}}(r)$  is estimated to be at  $3.79 \pm 0.02\text{\AA}$ , and the ratio  $\bar{r}_{\text{ClCl}}/\bar{r}_{\text{ZnCl}}$  is calculated to be  $1.65 \pm 0.02$ . This is greater than the value expected for a perfect tetrahedral configuration and the value of  $1.62 \pm 0.02$  found by Biggin and Enderby. The ratio of the mean nearest neighbour anion-anion distance to the cation-anion separation cannot be greater than that for a tetrahedral arrangement for fourfold coordinated cations, and the values calculated here are almost certainly slightly too high due to the reason stated before.

From these results, the coordination of  $\text{Cl}^-$  ions around each  $\text{Zn}^{2+}$  ion in  $\text{ZnCl}_2$  is confirmed to be tetrahedral, but is seen to be far better defined than had previously been realised.

#### 6.4.2 Zinc Chloride at 600°C

At this elevated temperature (about 300°C above the melting point) the structural features in Q space are, in the main, dampened but not broadened, with visible structure extending to about  $23\text{\AA}^{-1}$ . The pre-peak is still present at this temperature and is thus seen to be a real and persistent feature of the liquid state structure, which does not just arise from incomplete melting. The previous study of molten  $\text{NiI}_2$  at 830°C and 900°C showed a similar result. The total structure factors obtained for natural  $\text{NiI}_2$  at these temperatures are shown in figure 6.10. The height of the pre-peak at 900°C was  $0.28 \pm 0.02$ , which was slightly reduced from its value at 830°C of  $0.31 \pm 0.01$ , and its position was shifted from  $0.872 \pm 0.007\text{\AA}^{-1}$  at 830°C to  $0.858 \pm 0.005\text{\AA}^{-1}$  at 900°C. This shift to lower Q is consistent with thermal expansion. For  $\text{ZnCl}_2$  at 600°C, its height is reduced and width increased, and its position is shifted to the lower Q value of  $0.944 \pm 0.01$ . A summary of pre-peak parameters is found in table 6.3.

In real space, the nearest neighbour Zn-Cl and Cl-Cl peaks have moved to a slightly higher r, and they are broadened and reduced in height from what they were at 330°C. The ratio  $\bar{r}_{\text{ClCl}}/\bar{r}_{\text{ZnCl}}$  is now  $1.67 \pm 0.03$ , and the mean coordination number of  $\text{Cl}^-$  ions around each  $\text{Zn}^{2+}$  ion has dropped to  $3.67 \pm 0.07$ . Truncation of the data for  $\text{ZnCl}_2$  at 330°C at  $18\text{\AA}^{-1}$  prior to transformation, gave rise to a Zn-Cl peak of height 8.4 and width  $0.284\text{\AA}$ , which is still higher and narrower than that found for the higher temperature data. Therefore, this broadening and reduction in height is not just due to reduced data quality.

#### 6.4.3 Zinc Bromide

The total structure factor of  $\text{ZnBr}_2$  shows oscillatory behaviour up to about  $26\text{\AA}^{-1}$ , which is seen in real space as a very high and narrow principal peak in  $G(r)$ , similar to that found for  $\text{ZnCl}_2$  at 330°C. This peak, which is assumed to be due to the first peak in  $g_{\text{ZnBr}}(r)$ , is at  $2.41 \pm 0.01\text{\AA}$  - a value of 0.90 times the sum of the two ionic radii - and its scaled height and width are  $9.3 \pm 0.3$  and  $0.24\text{\AA}$  respectively. From the

coordination number, it can be seen that on average each cation is fourfold coordinated by anions, and from the ratio of  $\bar{r}_{\text{BrBr}}/\bar{r}_{\text{ZnBr}}$  it can be concluded that the local structure is tetrahedral. The tetrahedral units are again very well defined.

A pre-peak is clearly seen for this salt at  $0.94 \pm 0.01 \text{ \AA}^{-1}$  which, at a height of  $0.157 \pm 0.007$ , is larger than that observed for  $\text{ZnCl}_2$ . If this peak is due to the cation-cation partial structure factor (which has always been observed to have been the case so far), and since the coefficient of  $S_{\text{ZnZn}}(Q)$  is the same for all three salts, then it is fair to make a direct comparison of pre-peak strengths from the total structure factors. Although the cross-term partial structure factor,  $S_{\text{ZnX}}(Q)$ , often has a small feature in this region which could contribute to the pre-peak in  $F(Q)$  (see for example figure 8.7), the coefficient for this term decreases from  $\text{ZnCl}_2$  to  $\text{ZnBr}_2$  to  $\text{ZnI}_2$ . Therefore, if this feature is contributing to the pre-peak, this contribution should decrease correspondingly, so that one can be fairly certain that the pre-peak is larger for  $\text{ZnBr}_2$  than for  $\text{ZnCl}_2$ .

#### 6.4.4 Zinc Iodide

The structure factor for this salt appears from the data to extend only as far as about  $15 \text{ \AA}^{-1}$ . However, due to weaker scattering from the iodine nucleus,  $F(Q)$  is noisier than for the other two salts. A pre-peak is observed, this time at even lower  $Q$ , and its height of  $0.167 \pm 0.008 \text{ \AA}$  is the largest for all of the three salts.

In  $G(r)$ , the ratio  $\bar{r}_{\text{II}}/\bar{r}_{\text{ZnI}}$  is now  $1.69 \pm 0.03$ , but this increased value is almost certainly due to the increased cross-term coefficient. In order to investigate the second peak in  $G(r)$  for the zinc halide series, comparisons were made using the digitised partial  $g(r)$ 's obtained from the Biggin and Enderby data for  $\text{ZnCl}_2$ . The  $r$  scales of these partials were rescaled by the sum of the two ionic radii for the three salts and the partials were combined with the coefficients of equation 6.1. The resulting  $G(r)$ 's are compared with the total distribution functions for the three salts in figure 6.11. Good fits were obtained for all three

salts, except over the resolution-limited first peak. The good fits obtained over the second peak in  $G(r)$  for  $ZnBr_2$  and  $ZnI_2$  strengthens the view that the nearest neighbour anion structure for these two salts is the same as that found for molten  $ZnCl_2$ , and that the true value of the ratio  $\bar{r}_{--}/\bar{r}_{+-}$  is that of a tetrahedron. For molten  $ZnI_2$ , the mean coordination number of  $I^-$  ions around each  $Zn^{2+}$  ion is  $4.20 \pm 0.05$ , so this too is a salt in which cations are tetrahedrally coordinated by anions.

The most notable difference between the structure of  $ZnI_2$  and that of the other two zinc halides studied, is the relaxation of the nearest neighbour structure as revealed by the Zn-anion principal peak. Although the nearest neighbour Zn-anion distance is still 0.91 times the sum of the ionic radii for  $ZnI_2$ , this peak is seen to have substantially reduced height and increased width. To test whether this observation was real and not just arising from reduced data quality, the  $ZnCl_2$  at  $330^\circ C$  data and the  $ZnBr_2$  data were truncated at  $16 \text{ \AA}^{-1}$  (below the highest  $Q$  for which structure is resolved for  $ZnI_2$ ), and transformed. The resulting peak heights were 8.0 and 8.2 and the peak widths were both  $0.31 \text{ \AA}$  - values which are still significantly higher and narrower than those found for  $ZnI_2$ .

## 6.5 Discussion of Results

### 6.5.1 Tetrahedral Coordination

From the values of the first shell coordination number and  $\bar{r}_{--}/\bar{r}_{+-}$ , it can be concluded that all of the molten zinc halides possess a tetrahedral arrangement of anions around each cation. Of the 2:1 salts studied to date, a fourfold coordination of anions around each cation has been found for salts with an anion to cation size ratio of greater than about two. For the zinc halides, the coordination number is lower than for the octahedrally coordinated solid state compounds, and the reduction upon melting is typical behaviour for molten salts.

### 6.5.2 The Cation-Anion Principal Peak in G(r)

The position of the principal peak in  $G(r)$ , which arises from the cross-term partial, scales with the sum of the ionic radii, so that  $\bar{r}_{+-}/\sigma_{+-}$  is approximately 0.9 for all three salts. In addition, this peak is observed to be higher and narrower for  $ZnCl_2$  and  $ZnBr_2$  than for any other molten salt studied to date. It is still high for  $ZnI_2$ . Clearly, thermal effects play a role in determining the heights and widths of these peaks and the measurements, except those for  $ZnCl_2$  at  $600^\circ C$ , were at much lower temperatures than those of other molten 2:1 salt studies. However, although  $ZnBr_2$  was investigated at a temperature which was  $90^\circ C$  above that of the chloride, the first peak in  $g_{ZnBr}(r)$  is in fact higher. For the  $ZnI_2$  study, the reduction in the height of this peak and the increase in its width is remarkable, considering that this salt was only  $50^\circ C$  hotter than the  $ZnBr_2$ . It is clear, therefore, that effects other than thermal ones are playing a role in determining the evolution of the shape of this peak through the zinc halide series.

The origin of this extremely well defined first  $Zn^{2+}$ -anion distance for  $ZnCl_2$  and  $ZnBr_2$  probably lies in a relatively long lifetime for the  $ZnX_4^{2-}$  structural unit, with little movement of  $Zn^{2+}$  ions into and out of the first coordination shell. This is also reflected in the deep minima following this peak. From inelastic neutron scattering measurements (Fairbanks, 1987) it is known that molten  $ZnCl_2$  exhibits very little ionic diffusion at  $368^\circ C$ , but the quasielastic scattering increases markedly when the temperature is raised to  $568^\circ C$ . Low ionic diffusion rates for both ionic species have also been reported from the molecular dynamics simulation study of Woodcock et. al. (1976). The magnitude and temperature dependence of the ionic diffusion is reflected by the conductivity and viscosity data, where it can be seen that  $ZnBr_2$  also possesses a low conductivity and a high viscosity.

The reduction in the height of this first peak for  $ZnI_2$  could be due to the greater ionic mobility suggested by the higher conductivity near the melting point. However, the conductivity for  $ZnCl_2$  at  $600^\circ C$  is greater than that of  $ZnI_2$  at  $470^\circ C$ , whereas the principal peak is still higher and much

narrower. From inelastic neutron scattering measurements on molten  $\text{ZnBr}_2$  and  $\text{ZnI}_2$ , it should be possible to gain information on the diffusion of ions within the melts from the quasielastic scattering, as well as on collective motions within these liquids. Other possible explanations for the reduced short range cation-anion ordering in molten  $\text{ZnI}_2$  lie in the rigidity of the  $\text{ZnX}_4$  tetrahedral unit itself. Either in the anion positions relative to one another and the zinc ions, or in the position of the zinc ions at the centre of the tetrahedra. In the former case, one would expect to observe a corresponding reduction of height and broadening of the anion-anion peak in  $G(r)$  for  $\text{ZnI}_2$  - this is not observed. Indeed, from the model fits presented in figure 6.11, it can be seen that the nearest neighbour anion structure is very similar for all three salts. This leaves the latter case, in which the tetrahedral arrangement of anions is just as well defined in  $\text{ZnI}_2$ , but at a given temperature the zinc ion is more mobile within its tetrahedral 'cage' in  $\text{ZnI}_2$  than it is in the other two salts.

### 6.5.3 The Anion Structure

It appears, from the good model fits to  $G(r)$  for  $\text{ZnBr}_2$  and  $\text{ZnI}_2$  using the rescaled partials due to Biggin and Enderby, that the principal peak position in  $g_{--}(r)$  also scales with the sum of the two ionic radii rather than simply with the anion diameter. Although a separation of  $S_{--}(Q)$  has not been obtained, from the upper limits to  $\bar{r}_{--}$  and from the expected trend in the errors in  $\bar{r}_{--}$ , due to the increasing significance of the second peak in  $g_{+-}(r)$ , one can draw this conclusion. Therefore, the anion structure of these three zinc halides is not merely close-packed, but is determined by the cation-anion interaction. The same trend in anion structure was noted for the molten nickel halide series by Wood and Howe (1988), where the  $\bar{r}_{--}$  distance varies from being 0.2Å greater than the anion diameter for  $\text{NiCl}_2$ , to being 0.2Å less than the anion diameter for  $\text{NiI}_2$ . It is more appropriate to describe the structures of the zinc halides as a set of linked  $\text{ZnX}_4^{2-}$  entities, with the Zn-X distance fixed at 0.9 times the sum of the ionic radii, rather than as a

close-packed anion structure with interstitial  $\text{Zn}^{2+}$  ions.

#### 6.5.4 The Density of Zinc Chloride

The density of molten  $\text{ZnCl}_2$  is known accurately from many previous investigations. The experimentally observed decrease in the density between  $330^\circ\text{C}$  and  $600^\circ\text{C}$  is only partially accounted for by a uniform, isotropic expansion of the structure due to the Zn-Cl distance increasing from  $2.28\text{\AA}$  at  $330^\circ\text{C}$  to  $2.29\text{\AA}$  at  $600^\circ\text{C}$ , with a corresponding expansion of the rest of the structure. However, the mean coordination number of  $\text{Cl}^-$  ions around each  $\text{Zn}^{2+}$  ion also changes, decreasing slightly over this temperature range. This can only be interpreted as an increase in the number of threefold or twofold coordinated zinc ions, or equivalently, as the appearance of voids in the network as the temperature increases. This change in coordination number can account for the rest of the density change.

Information on the temperature dependence of the coordination number distribution is not given in the reports of the molecular dynamics simulations for molten  $\text{ZnCl}_2$ . This information would be useful for confirming whether the formation of  $\text{ZnCl}_3^-$  structural units (not necessarily molecular ions) is the source of the observed density change.

#### 6.5.5 Intermediate Range Order

The pre-peak observed for molten 2:1 salts has been attributed to a periodic structure in real space with a period of  $2\pi$  divided by the peak position and a coherence length of  $2\pi$  divided by the full width at half maximum. Table 6.3 lists the real space periods,  $R$ , calculated for the intermediate range ordering in the molten zinc halides. From the ratio of these distances to the sum of the ionic radii,  $\sigma_{+-}$ , it can be seen that  $R$  scales with  $\sigma_{+-}$  and not with the anion diameter. This is consistent with the previous conclusion that it is the cation-anion interaction which dominates the structure as a whole, rather than a close packing of anions. Similar values of  $R/\sigma_{+-}$  are obtained for the nickel halides (equal to 2.51, 2.47 and 2.48 for  $\text{NiCl}_2$ ,

NiBr<sub>2</sub> and NiI<sub>2</sub> respectively), so that the periodicity of the intermediate range ordering, measured in units of  $\sigma_{+-}$ , is the same for both the nickel and zinc halide series.

The principal peak distance in  $g_{++}(r)$  for the nickel halides and zinc chloride is nearly coincident with that in  $g_{--}(r)$ . In a closely packed, corner linked structure, this implies that the angle formed by the centres of neighbouring occupied tetrahedra and their shared corner is approximately the same as the internal tetrahedral angle. This similarity of M-X-M and X-M-X angles and the scaling of cation-anion distances with  $\sigma_{+-}$  is consistent with the observed dependence of R upon the two ionic radii, since the nearest neighbour cation-cation separation must scale with  $\sigma_{+-}$ , along with the anion-anion separation.

The full width at half maxima of these pre-peaks gives a measure of the ranges over which this ordering between tetrahedral units persists. These ranges are estimated to be about 18Å, 21Å and 22Å respectively for ZnCl<sub>2</sub>, ZnBr<sub>2</sub> and ZnI<sub>2</sub>. These values are between 6.9 and 7.8 times the sum of the ionic radii, corresponding to about three times R for all three salts.

A trend can clearly be seen from the pre-peak heights for the zinc halides; the peak height increases through the series from ZnCl<sub>2</sub> to ZnI<sub>2</sub>. The same trend was observed for the nickel halide series, with the pre-peak rising from 0.2±0.1 for NiCl<sub>2</sub> to 1.32±0.1 for NiI<sub>2</sub>. With the exception of the nickel halides, the magnitude of the pre-peak for the molten 2:1 halides studied to date increases with decreasing electronegativity difference between the two ionic species. Similarly, from the results presented in table 6.1, a trend of increasing pre-peak size with ion size ratio can be seen, with the exception of the nickel halides (when compared with the zinc halides) and MgCl<sub>2</sub>, which has a larger ion size ratio than ZnCl<sub>2</sub>, but exhibits a smaller pre-peak. Neither of these two factors alone (electronegativity difference and ion size ratio) are sufficient to fully account for the observed pre-peak magnitudes.

The investigation of molten ZnCl<sub>2</sub> by Ballone et. al. (1986), using screened Coulomb potentials with simulated angle dependence to model the structure using the HNC

approximation, did qualitatively reproduce the pre-peak in  $S_{\text{ZnZn}}(Q)$ . Their results suggested that an even stronger angular dependence of interionic forces than was able to be simulated is necessary to more accurately reproduce the experimental results of Biggin and Enderby. Thus the origin of the intermediate range ordering between cations in molten 2:1 salts is believed to be in the angular dependence of interionic forces.

Wood and Howe (1988) attribute this directionality to reduced ionicity within the molten nickel halides - a phenomenon which is also discussed for s-p bonded liquids by Rovere and Tosi (1986). The observed trend in the pre-peak heights for the non-transition metal halides reflects the onset of covalency which is associated with a reduction in the electronegativity difference between the ionic species and the increasing polarizability of the anions due to increasing ion size ratios. The pre-peaks observed here for  $\text{ZnBr}_2$  and  $\text{ZnI}_2$  lend further support to the argument that bond directionality associated with covalency is the origin of intermediate range order in molten 2:1 salts. The reduction in the cation-anion separations to values of 0.9 times the sum of the rigid ion radii also suggests a degree of covalent character to the zinc-anion bond. To investigate further the role of covalency and anion polarizability in determining the structure of liquid salts, there is a need for further theoretical studies using appropriate potentials which simulate directional dependence of interionic forces.

Contrary to what one might expect from ion size and electronegativity considerations, the pre-peaks observed for the nickel halide series are smaller than those found for the molten zinc halides. The explanation for this apparently anomalous behaviour for the nickel halides may be found in the electronic structure of the cations. The nickel salts are the only 2:1 salts studied to date by a partial structural investigation, for which the cation possesses a partially filled d shell and they are, therefore, the only salts studied for which the reduced charge transfer model, proposed by Wood et. al. (1988), is appropriate. In this model, the anion valence band hybridises with the cation d band, which results in some of the electronic charge from the nickel 4s

states being found in the hybridised d band. Support for this model is found in the electronic structure calculations for liquid NiTe and NiSe by Strange and Barnes (1985), who calculated electronic charge transfer from anion p states to nickel d states. If reduced charge transfer is occurring via this mechanism for the nickel halides, rather than simply by incipient covalency due to anion polarization, then this could be a possible explanation for the reduction in intermediate range ordering for the nickel halide series when compared with  $\text{MgCl}_2$  and the zinc halide series - the reduced charge of the nickel cation being responsible for a reduction in anion polarization.

## 6.6 Summary

The structure of three zinc halides has been investigated and the local coordination of anions around each cation has been found to be tetrahedral and very well defined for  $\text{ZnCl}_2$  and  $\text{ZnBr}_2$ . The iodide however, shows a more relaxed first shell structure, due possibly to a greater mobility of  $\text{Zn}^{2+}$  ions in molten  $\text{ZnI}_2$ . For all three halides studied, the nearest neighbour cation to anion separation was 0.9 times the rigid ion separation, and from model fits to the data, using rescaled partial distribution functions for  $\text{ZnCl}_2$ , it appears that the anion structure also scales with the sum of the rigid ion radii for the three salts.

A pre-peak at  $Q \approx 1.0\text{\AA}^{-1}$  has been observed in the total structure factors of all three halides. This peak, which is indicative of some intermediate range ordering between the cations in molten 2:1 salts, is stable with an increase in temperature and grows in height through the series from  $\text{ZnCl}_2$  to  $\text{ZnI}_2$ . This trend is consistent with that observed for other molten 2:1 halides where the pre-peak increases with decreasing electronegativity difference between the two species and increasing ion size ratio. The observations support the argument that intermediate range ordering has its origin in a directional dependence of interionic potentials, arising from a degree of covalency associated with ion polarization and reduced electronegativity difference between the species. The corresponding real space period of the

medium range structure also scales with the sum of the ionic radii through the series, which indicates that the medium as well as the short range structure is determined by the cation-anion interaction for all three halides. A comparison with the structure of the molten nickel halide series reveals that the nickel salts possess a lower degree of medium range cationic ordering than one would expect from the observed trend with electronegativity difference and ion size. The explanation for this may be found in the electronic structure of the cation, and its role in producing reduced charge transfer between the ionic species.

A study of molten  $\text{ZnCl}_2$  at  $282^\circ\text{C}$  above its melting point was also undertaken. The pre-peak position was shifted to a lower  $Q$  value, which is consistent with thermal expansion. On the whole, the structure changes little with this increase in temperature, with peaks being reduced in height and broadened as expected. However, there is evidence from the Zn-Cl coordination number and nearest neighbour peak position, and from the known density, that there is an increase in the number of voids in the network structure as the temperature is increased.

For comparison, the neutron diffraction results from vitreous  $\text{ZnCl}_2$  by Desa et. al. (1982) are shown in figure 6.12. The functions shown are the normalised diffraction pattern,  $I(Q)$ , and the real space correlation function,  $T(r)$ . The diffraction pattern  $I(Q)$  is remarkably similar in form to that of the liquid and also displays a pre-peak at approximately the same position, although it is in fact smaller in magnitude for the glass. In real space, the Zn-Cl principal peak distance at  $2.288 \pm 0.01 \text{ \AA}$  is in agreement with that found here for the liquid, as is the mean coordination number of 3.8. From their results, Desa et. al. concluded that vitreous  $\text{ZnCl}_2$  also consists of a closely packed array of  $\text{Cl}^-$  ions with  $\text{Zn}^{2+}$  ions occupying tetrahedrally coordinated sites so as to maximise corner sharing of the resulting  $\text{ZnCl}_4^{2-}$  tetrahedra.

Table 6.1. Summary of physical and structural parameters for molten 2:1 halides.

Salt	Ion size ratio	Electroneg. difference	$\bar{r}_{+}$ rigid ion separation	Ratio $\bar{r}_{-}/\bar{r}_{+}$	Coord. number $n_{+}$	Trough depth in $g_{+-}$	Penetration into first shell	Pre-peak height	Main peak positions in $g_{++}$   $g_{--}$
BaCl <sub>2</sub>	1.35	2.27	0.98	1.26	7.7	0.3	40% Cl	0	4.9   3.86
SrCl <sub>2</sub>	1.62	2.21	0.99	1.31	6.9	0.3	30% Cl	0	4.95   3.8
CaCl <sub>2</sub>	1.83	2.16	0.99	1.34	5.4	0.2	10% both	0.8	3.6   3.73
MgCl <sub>2</sub>	2.74	1.85	1.01	1.41	4.3	0.1	None	2.0	3.6   3.6
MnCl <sub>2</sub>	2.26	1.61	0.96	1.43	4.0	—	—	—	—   3.6
NiCl <sub>2</sub>	2.62	1.25	0.93	1.61	4.7	0.3	5% Ni	0.2	3.7   3.5
NiBr <sub>2</sub>	2.84	1.05	0.92	1.61	4.6	0.4	5% Ni	1.0	3.7   3.69
NiI <sub>2</sub>	3.19	0.75	0.91	1.57	4.2	0.6	30% Ni	1.3	3.9   4.0
ZnCl <sub>2</sub>	2.45	1.51	0.90	1.62	3.9	0.2	None	3.3	3.8   3.71
ZnBr <sub>2</sub>	2.65	1.31	0.90	<1.68	3.9	0.1	—	(4.4)	—   —
ZnI <sub>2</sub>	2.98	1.01	0.91	<1.69	4.2	0.1	—	(4.7)	—   —

Table 6.2. Parameters used for the analysis of the diffraction data for the zinc halides, together with the melting points and experimental temperatures.

Sample	ZnCl <sub>2</sub>	ZnBr <sub>2</sub>	ZnI <sub>2</sub>
Temperature (°C)	330 and 600	420	470
Melting point (°C)*	318	394	446
Density (gcm <sup>-3</sup> )	2.52 <sup>+</sup> and 2.40	3.99 <sup>++</sup>	3.85*
Anion coherent scatt. length (10 <sup>-12</sup> cm)**	0.9579	0.679	0.528
Total scattering cross-section (barns)**	12.51	5.30	3.71
Absorption cross-section (barns)**	22.70	4.97	4.50

Coherent scattering length of zinc =  $0.568 \times 10^{-12}$  cm.\*\*

\* From Janz (1967)

\*\* Sears (1984)

+ Angell and Wong (1970)

++ Salstrom (1933)

Table 6.3. Structural parameters for the molten zinc halides.

	ZnCl <sub>2</sub> at 330°C	ZnCl <sub>2</sub> at 600°C	ZnBr <sub>2</sub>	ZnI <sub>2</sub>
<u>Real space:</u>				
Main peak position/Å in $r^2g(r)$ ( $\bar{r}_{+-}$ )	2.29±0.01	2.31±0.01	2.42±0.01	2.63±0.03
in $g(r)$	2.28±0.01	2.29±0.01	2.41±0.01	2.60±0.01
Sum of ion sizes( $\sigma_{+-}$ )	2.55*	2.55*	2.69*	2.90*
$\bar{r}_{+-}/\sigma_{+-}$	0.90	0.91	0.90	0.91
Scaled peak height	8.9±0.2	7.5±0.3	9.3±0.3	6.3±0.2
Peak width(FWHM) / Å	0.26±0.01	0.33±0.01	0.24±0.01	0.46±0.02
Depth of first trough	0.16±.06	0.22±0.16	0.10±0.03	0.05±0.03
Coord.no. by integr. to 1 <sup>st</sup> min. in $r^2g(r)$	3.93±0.06	3.67±0.07	3.9±0.1	4.20±0.05
Second peak position in $r^2g(r)$ ( $\bar{r}_{--}$ )	3.79±0.02	3.86±0.05	4.08±0.03	4.44±0.03
$\bar{r}_{--}/\bar{r}_{+-}$	1.65±0.02	1.67±0.03	1.68±0.02	1.69±0.03
<u>Reciprocal space:</u>				
Pre-peak position/Å <sup>-1</sup>	1.005±0.01	0.944±0.01	0.943±0.01	0.878±0.01
Pre-peak height	0.140±0.008	0.13±0.01	0.157±0.007	0.167±0.008
Pre-peak width (FWHM)	0.36±0.04	0.38±0.05	0.30±0.04	0.29±0.05
R-space period (R)	6.25±0.06	6.66±0.07	6.66±0.07	7.16±0.08
R/ $\sigma_{+-}$	2.45±0.03	2.61±0.03	2.48±0.03	2.47±0.03

\* From Pauling (1960).

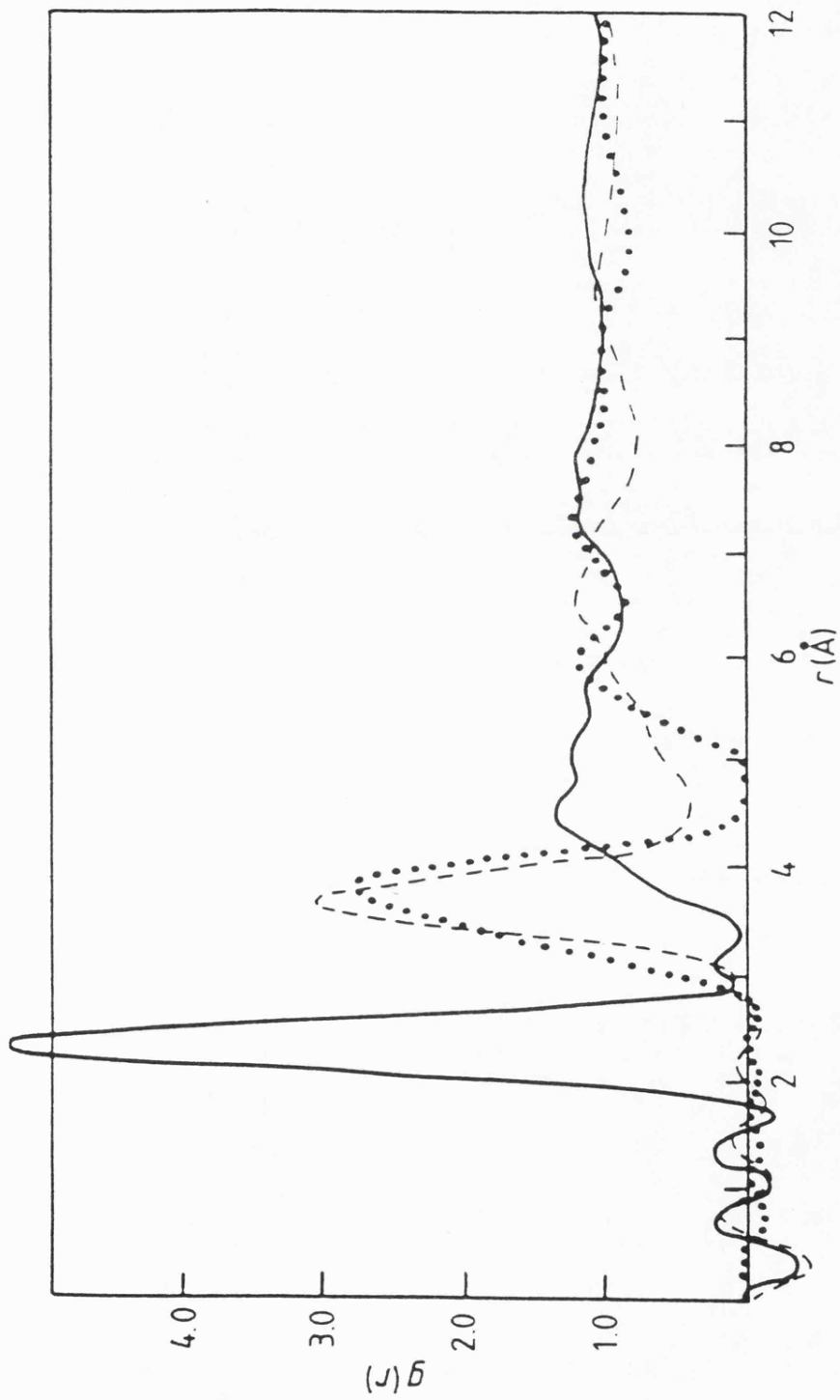


Figure 6.1. The three radial distribution functions for molten zinc chloride obtained by Biggin and Enderby (1981a). Full curve,  $g_{\text{ZnCl}}$ ; broken curve,  $g_{\text{ClCl}}$ ; dotted curve,  $g_{\text{ZnZn}}$ .

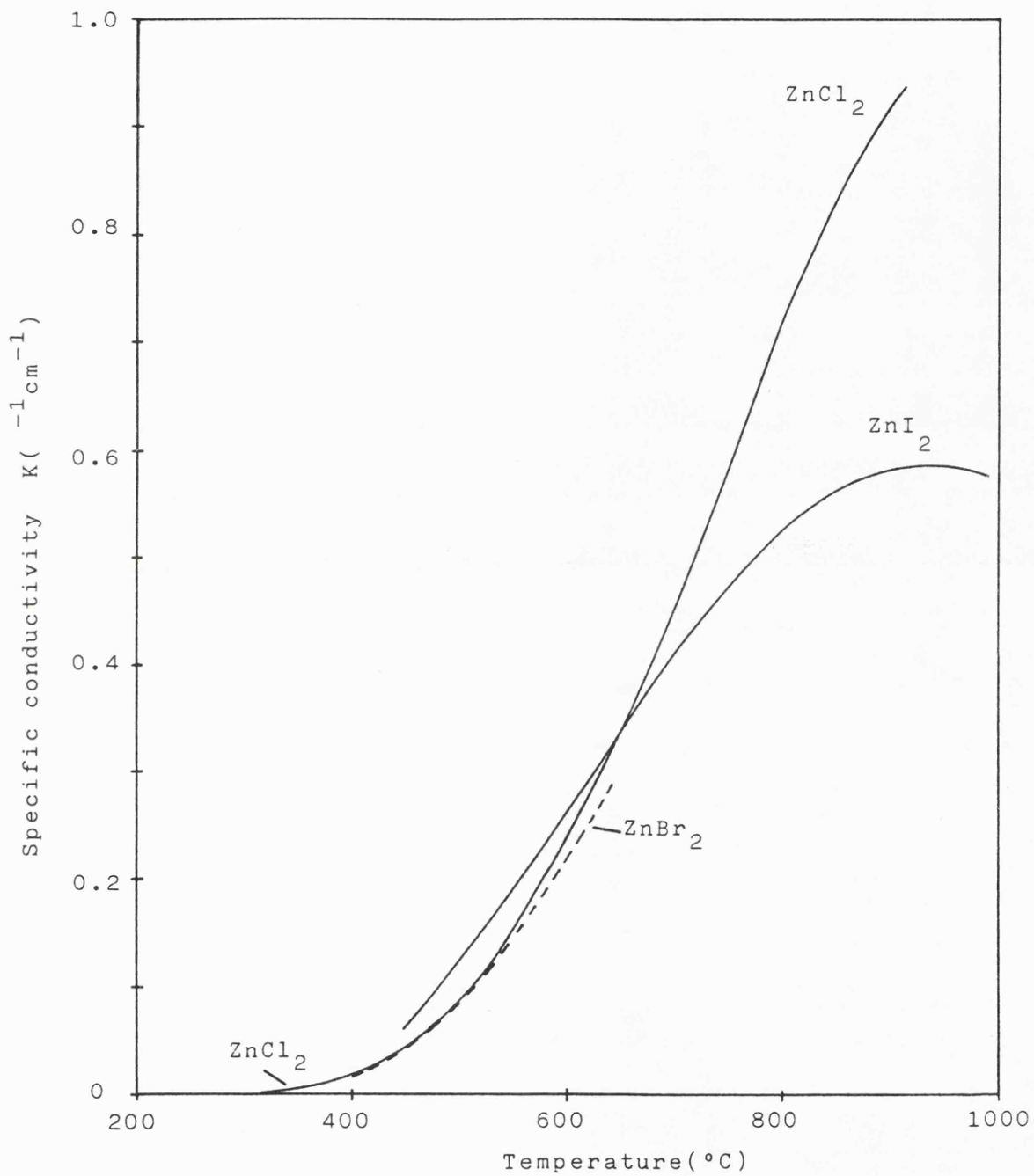


Figure 6.2. The temperature dependence of the electrical conductivities of the molten zinc halides. From Bockris et. al. (1960) and Grantham and Yosim (1966).

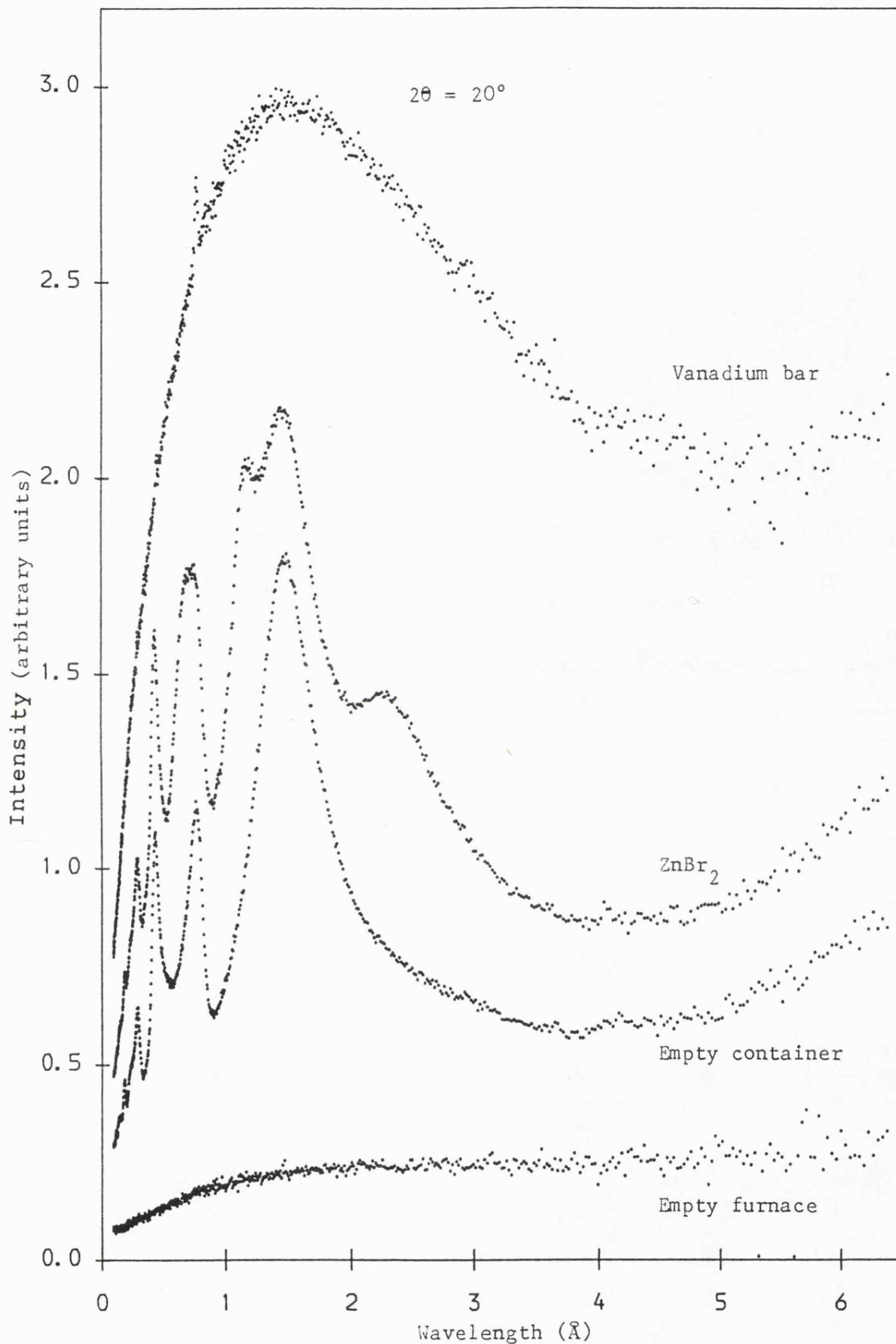


Figure 6.3. The normalised scattering intensity measured on LAD by the two  $20^\circ$  detectors.

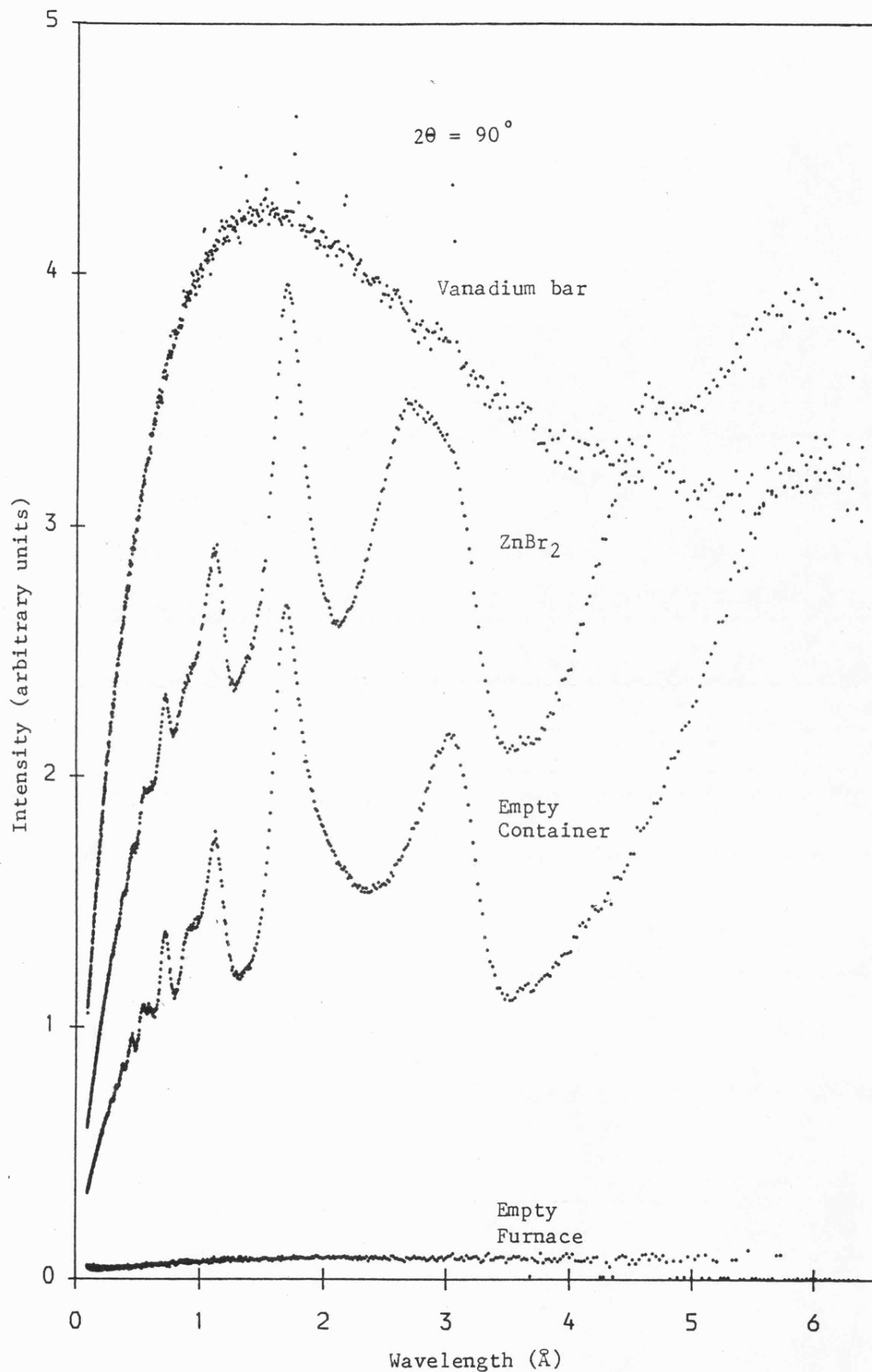


Figure 6.4. The normalised scattering intensity measured on LAD by the two 90° detectors.

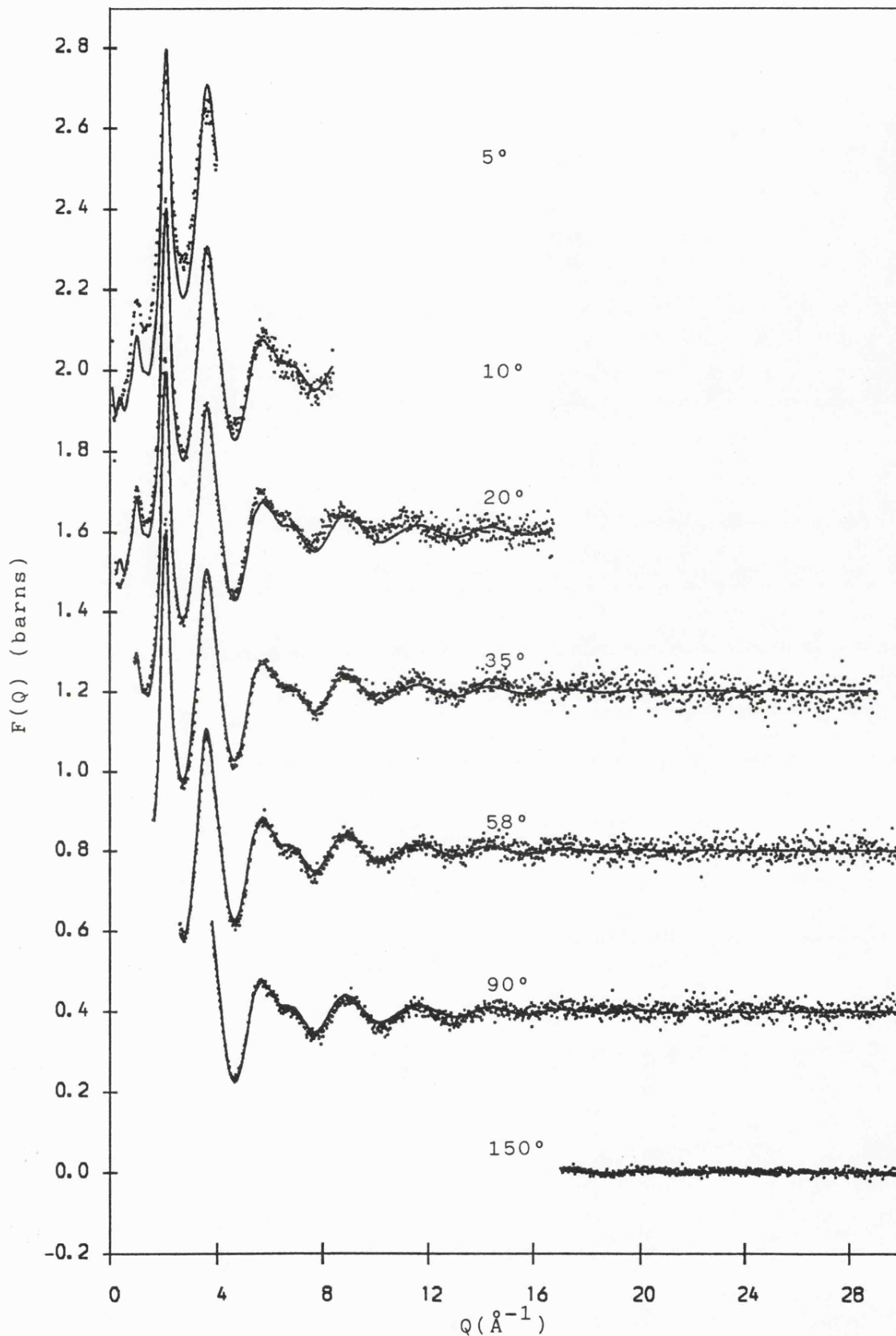


Figure 6.5. The total structure factor of  $\text{ZnCl}_2$  at  $330^\circ\text{C}$ . The data is shown for each of the scattering angles over the ranges which contribute to the final  $F(Q)$  and successive curves are displaced by 0.4. The full line is the back-transform of the smoothed distribution function.

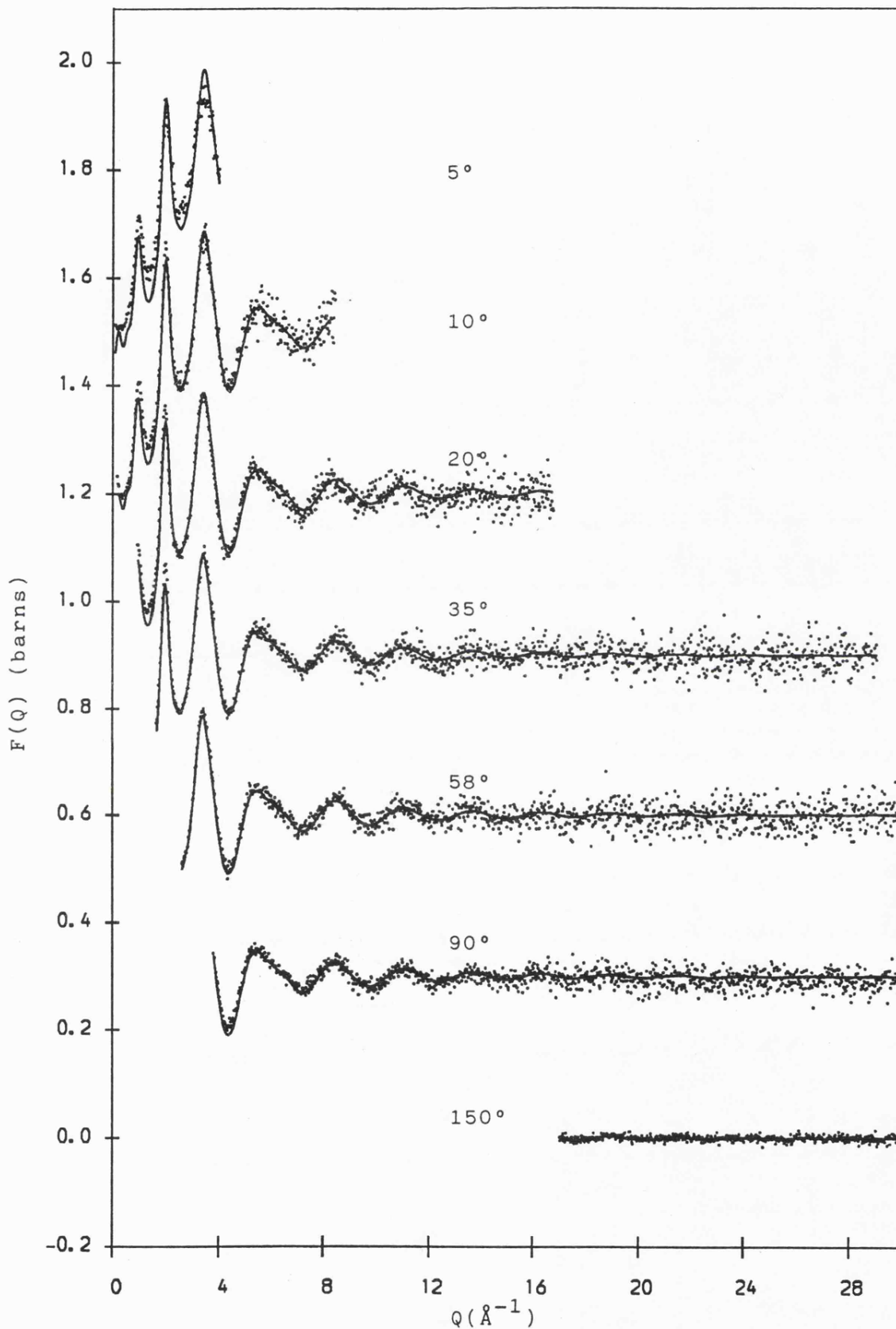


Figure 6.6. The total structure factor of  $\text{ZnBr}_2$  shown separately for each angle. Successive curves are displaced by 0.3.

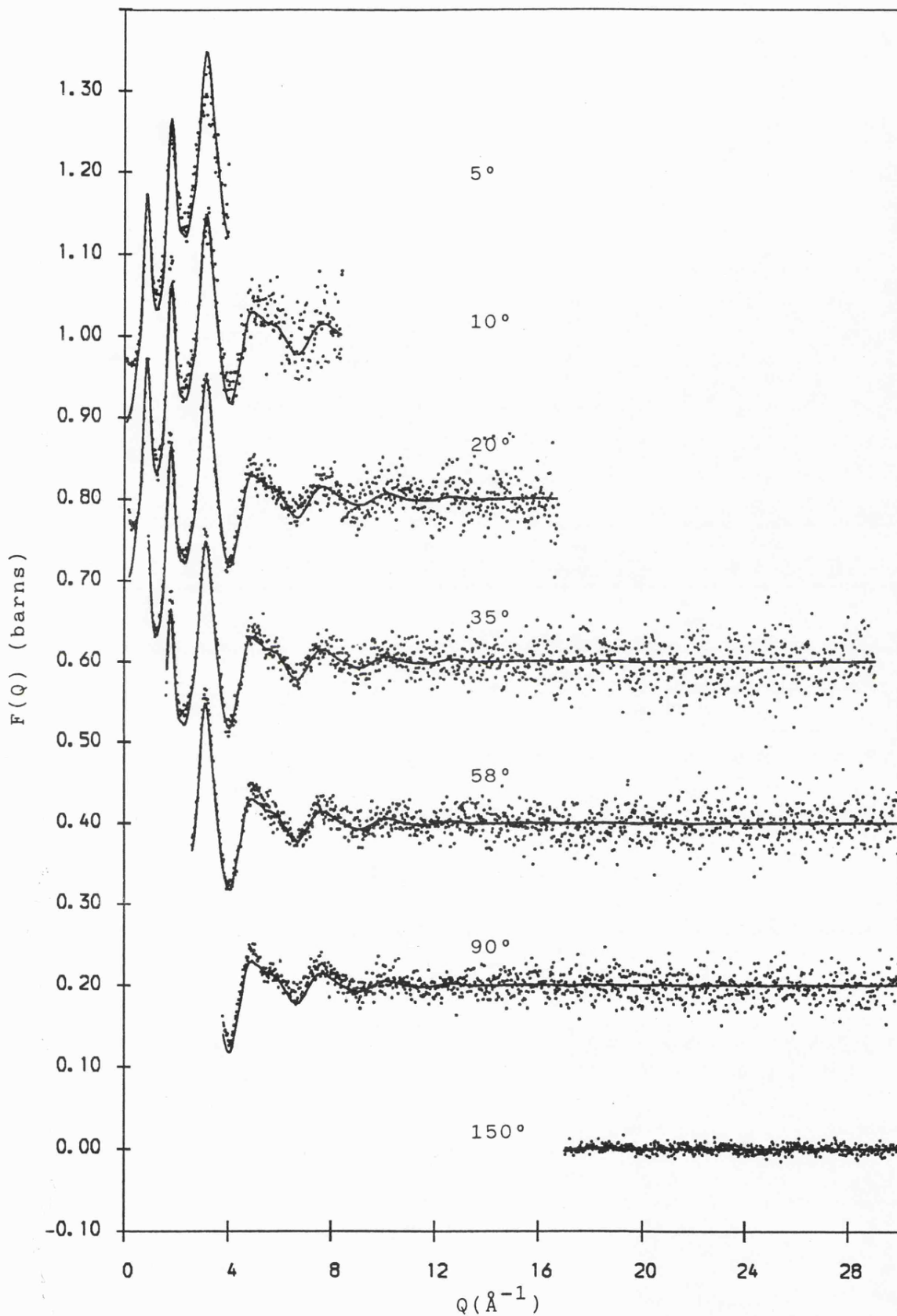


Figure 6.7. The total structure factor of  $\text{ZnI}_2$  shown separately for each detector angle. Successive curves are displaced by 0.2.

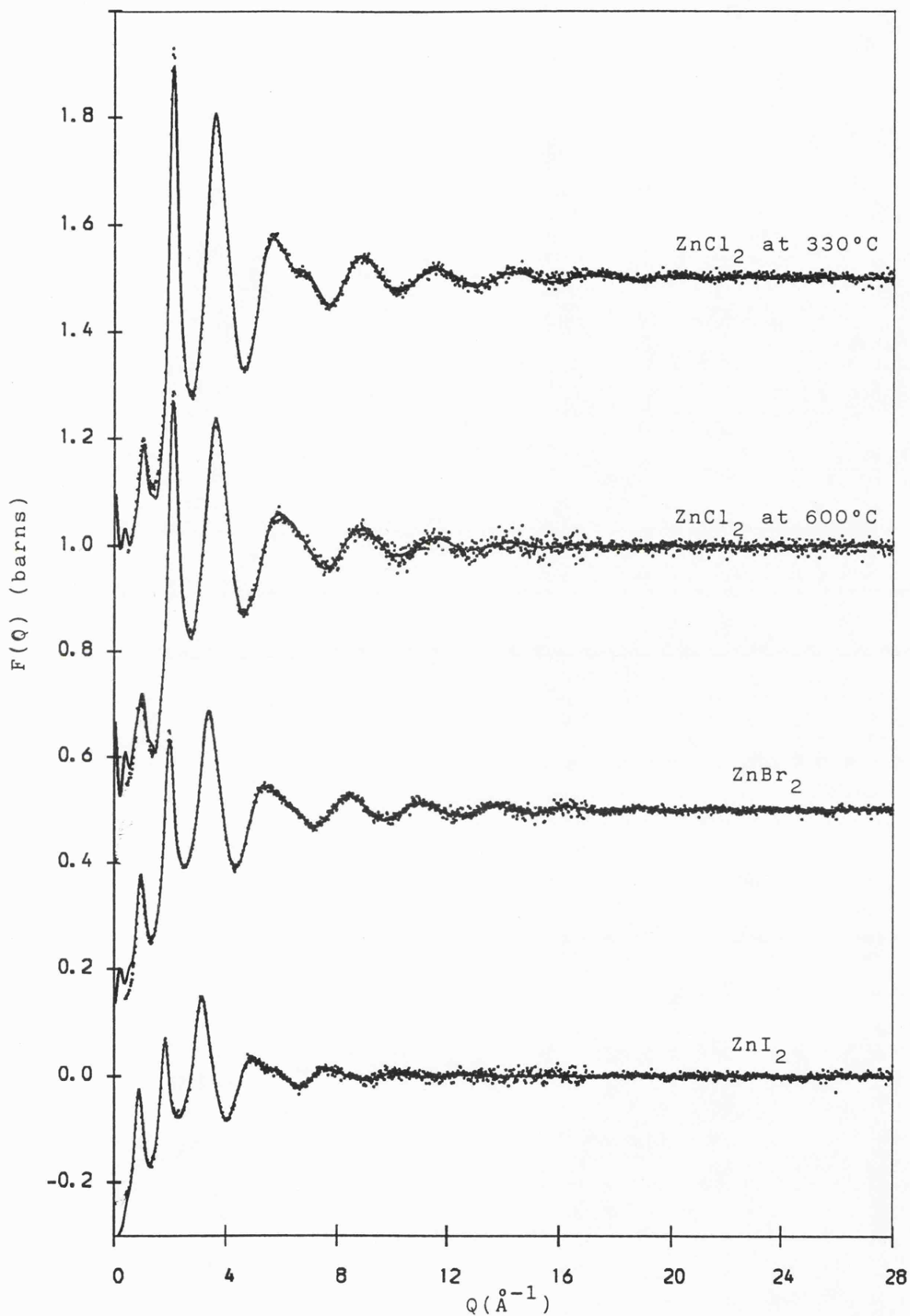


Figure 6.8. Total structure factors for the zinc halides obtained from a flux-weighted combination of the separate angle spectra. The data are fitted with the back-transforms of the smoothed  $G(r)$ 's and each successive data set is displaced by 0.5.

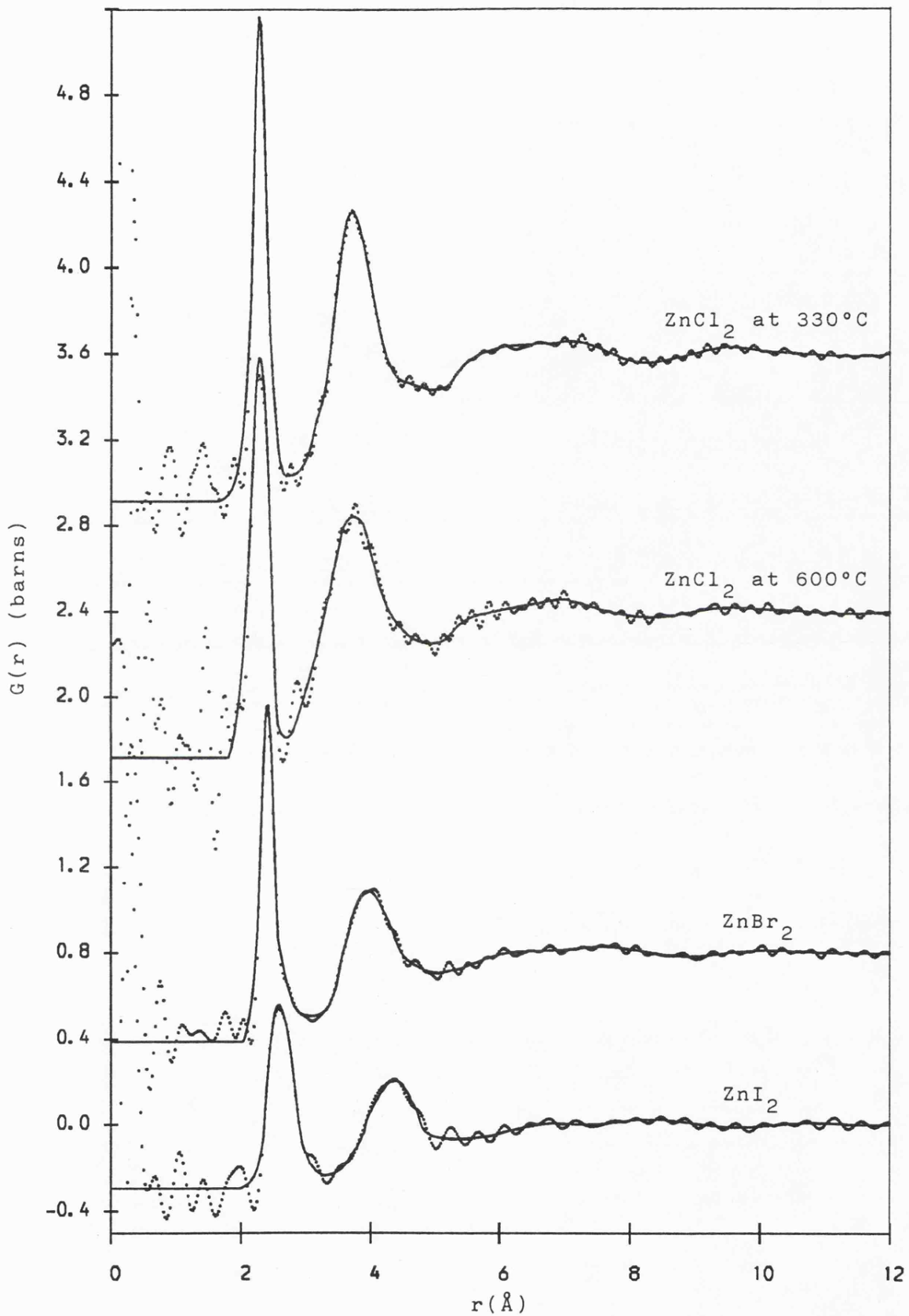


Figure 6.9. Total distribution functions for the zinc halides. The dots are the Fourier transforms of the unsmoothed  $F(Q)$ 's and the full lines are smoothed functions from which the back-transforms were obtained.

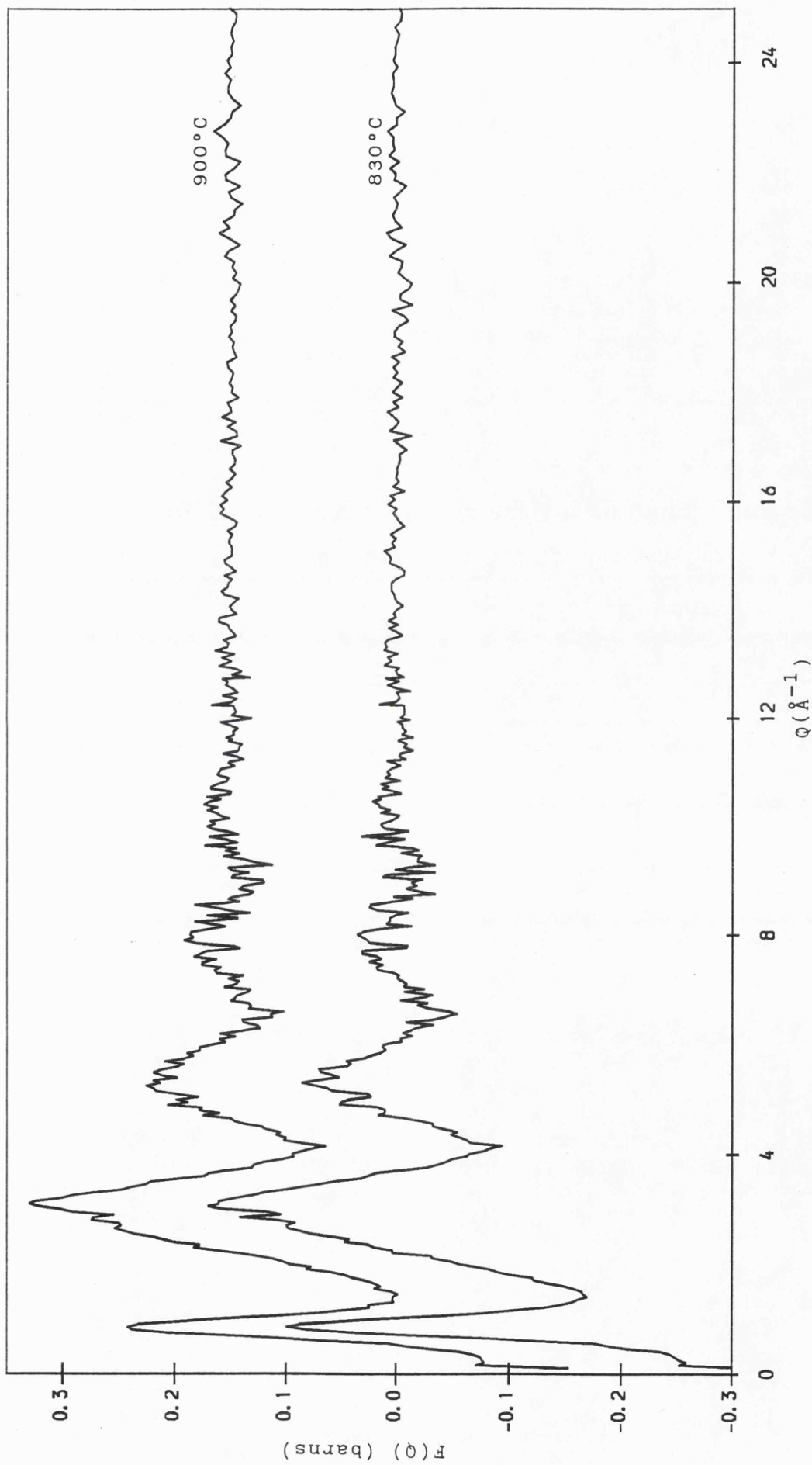


Figure 6.10. The total structure factors of  $\text{NiI}_2$  at  $830^\circ\text{C}$  and  $900^\circ\text{C}$  (displaced by 0.15).

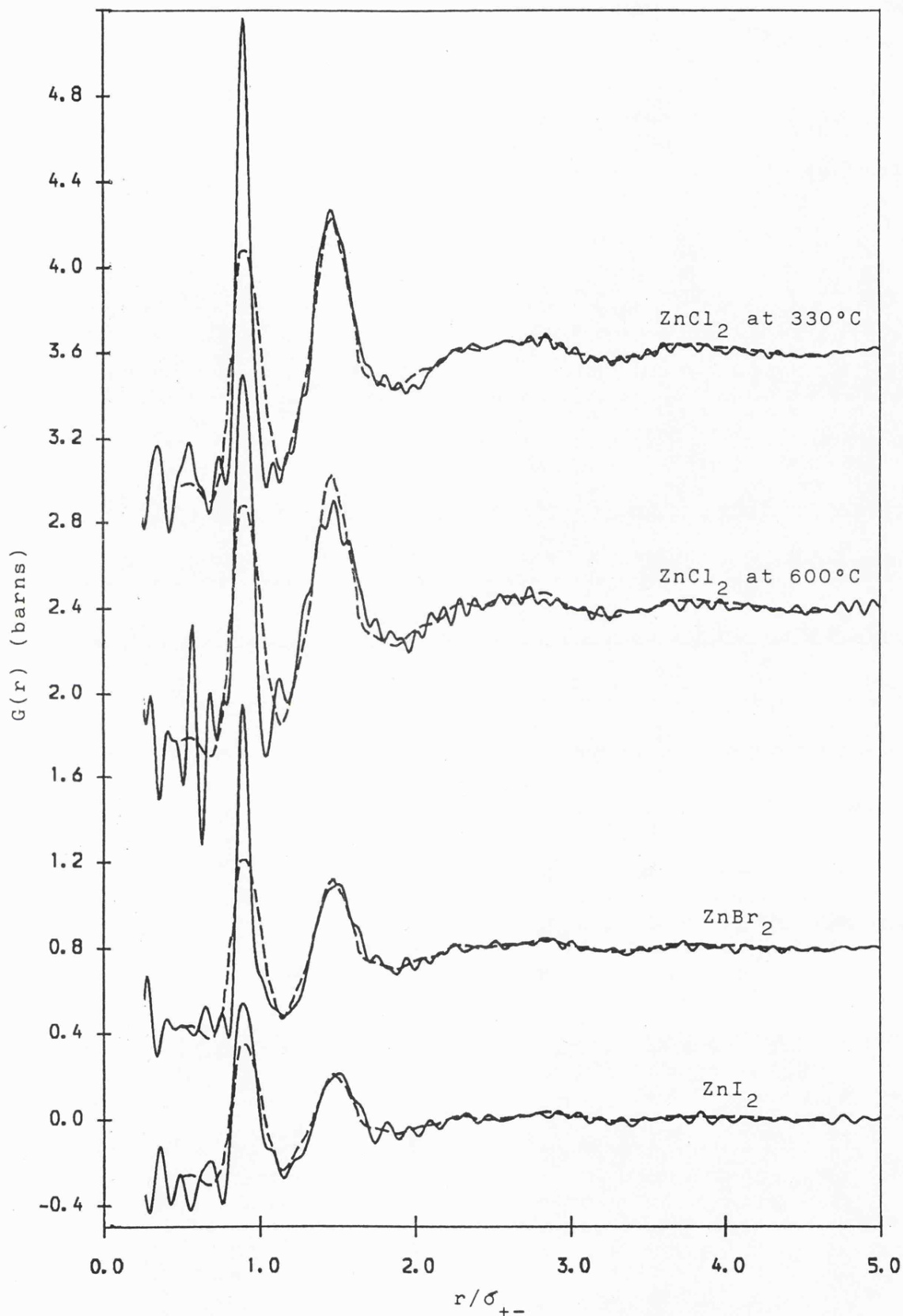


Figure 6.11. Total distribution functions for the molten zinc halides (full lines) compared with the recombined  $\text{ZnCl}_2$  partials due to Biggin and Enderby (dashed lines). The  $r$  axes have been rescaled by the sum of the rigid ion sizes for each salt.

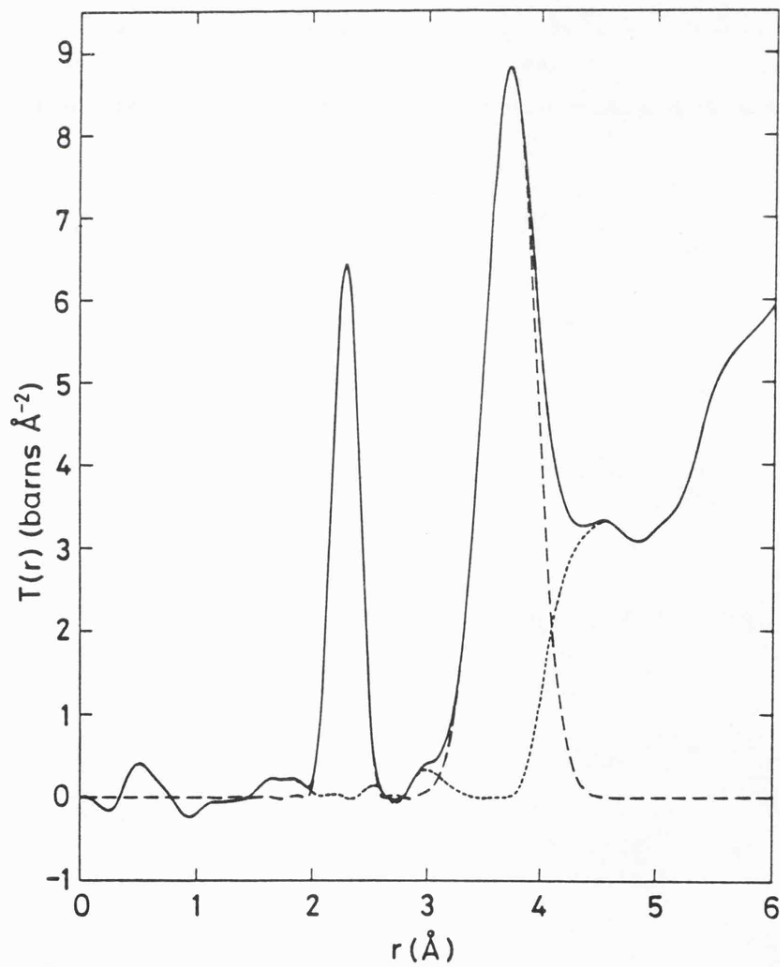
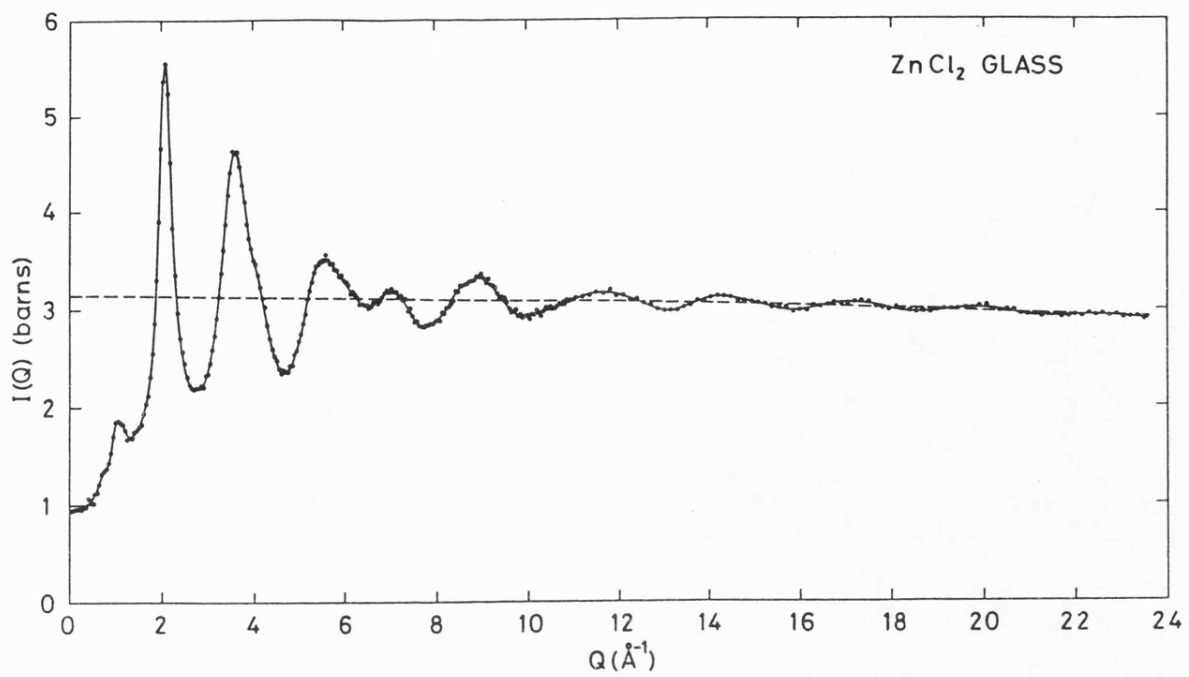


Figure 6.12. The normalised diffraction pattern,  $I(Q)$ , and correlation function,  $T(r)$ , for vitreous  $ZnCl_2$ . From Desa et. al. (1982).

## CHAPTER 7

### THE STRUCTURE OF MOLTEN ZINC CHLORIDE AND POTASSIUM CHLORIDE MIXTURES

#### 7.1 Introduction

The structure of molten  $\text{ZnCl}_2$  has been investigated by neutron and X-ray diffraction and EXAFS studies (Wong and Lytle, 1980) and is discussed in chapter 6. Results are presented there which show that the local structural arrangement of anions around each cation is very well defined and that a similar structural arrangement is found for  $\text{ZnBr}_2$  and  $\text{ZnI}_2$ . In addition, intermediate range ordering between  $\text{Zn}^{2+}$  ions within tetrahedrally coordinated sites is present for all three halide salts studied.

Raman scattering studies on molten mixtures of zinc halides with alkali halides (Ellis, 1966) have shown that when an alkali halide is added to molten  $\text{ZnCl}_2$  and  $\text{ZnBr}_2$ , stretching modes associated with bridging chloride ions between tetrahedral units are reduced, while bands related to isolated  $\text{ZnCl}_n^{2-n}$  units emerge. This has led to the description of the alkali halide as a 'network breaker' or 'structure breaker' which breaks the polymeric network of molten zinc halides by providing extra halide ions. This enables isolated  $\text{ZnX}_n^{2-n}$  complexes to form, with a sea of alkali metal counter ions. Similar complex formation has been observed for molten chlorides of Be, Mg and Ca with alkali chlorides (Sakai. et. al., 1984 and Brooker and Huang, 1980) and molten  $\text{CdCl}_2$ -alkali halide mixtures (Clarke et. al., 1972).

If the intermediate range ordering has its origin in angular dependence of interionic potentials, leading to the equivalence of the bridging Zn-Cl-Zn and the tetrahedral Cl-Zn-Cl angles, then one would expect it to disappear with the formation of isolated (and presumably uncorrelated)  $\text{ZnCl}_n^{2-n}$  units. This chapter describes a time-of-flight neutron diffraction experiment to investigate the short range structure within the system  $\text{ZnCl}_2$ -KCl over the full composition range, as well as to look at the effect upon the intermediate range order between tetrahedral units, of the

addition of a 'network breaking' alkali halide. In order to follow the structural changes which occur upon mixing the two salts, measurements were made over the composition range, with particular attention being paid to the KCl rich end of the phase diagram where, after a preliminary investigation using mixtures of 33.3%, 50% and 66.7% KCl concentration, most of the local structural change is observed to occur.

## 7.2 Sample Description and Preparation

Pulsed neutron diffraction measurements were made using samples of  $\text{ZnCl}_2$ -KCl mixtures having KCl concentrations of 33.3%, 50%, 66.7%, 81%, 90%, 95% and pure KCl. The exact concentrations, coherent scattering coefficients and densities used for the analysis of these three component liquids are shown in table 7.1, where the percentage contribution to the total coherent scattering from each component is also shown.

The samples were prepared using the vacuum drying technique described in section 3.4. Quantities of the two pure salts were dried separately and the dried powders were weighed out and mixed in an argon filled glove box before being sealed into fused quartz tubes and melted for twenty four hours at 800°C, some 30°C above the melting point of KCl. For the preliminary experiment with mixtures of 33.3%, 50% and 66.7% KCl concentration, a pre-melting temperature of 460°C was chosen (above the liquidus) and held for four hours. Figure 7.1 shows the phase diagram for this system obtained by Perry. The two salts mix readily across the composition range, with three eutectics at around 27%, 50% and 71% KCl concentrations, and with solid state compound formation at 1/3, 60% and 2/3 KCl concentrations. The phase diagram of this ternary system was also studied by Duke and Fleming (1957), who also determined the density and electrical conductivity.

For the second experiment, 'gold label'  $\text{ZnCl}_2$  of 99.999% purity and KCl of 99.99+% purity were used - supplied by Aldrich Chemical Company; the preliminary experiment had used American Chemical Society standard reagents. Attempts were made to produce samples of concentration around 75% KCl,

but this was unsuccessful because the quartz tubes cracked upon cooling once the sample had solidified after melting, possibly due to chemical bonding to the glass.

All of the final sample tubes were of a nominal 8mm internal diameter and 1mm wall thickness, but each was carefully measured before use.

### 7.3 First Experimental Run

Pulsed neutron scattering measurements were made using the Liquids and Amorphous Materials Diffractometer at RAL. The procedure described in section 3.5 was followed for the initial preliminary experiment. Normalisation of the measured spectra was achieved using a vanadium rod of 8.36mm diameter, which was suspended in the empty instrument (i.e. without the furnace). The scattering intensity from this rod was smoothed and the Bragg peaks were removed by the method described in section 4.3.4. The samples investigated were 33.3% KCl + 66.7% ZnCl<sub>2</sub> at 340°C and 450°C, 50% KCl + 50% ZnCl<sub>2</sub> at 340°C and 450°C and 66.7% KCl + 33.3% ZnCl<sub>2</sub> at 450°C. The reduced data, after the container scattering has been subtracted and after having been normalised and corrected for incoherent and multiple scattering and absorption, is shown for the 50% KCl + 50% ZnCl<sub>2</sub> mixture at 450°C in figure 7.2. F(Q) is shown separately for each of the detector angles used, over the ranges which were used to make the final composite F(Q) seen in figure 7.3. Also in figure 7.3 are the composite F(Q)'s for the same sample at 340°C and for the 33.3% KCl sample at 340°C and 450°C, together with the results for the 66.7% KCl sample at 450°C for the two separate runs.

The ranges over which the individual spectra matched and were used to produce the final composite F(Q)'s, were chosen for each sample, but typically covered the wavelength range of  $0.3\text{\AA} < \lambda < 1.25\text{\AA}$ . The low resolution 5° detectors were not included.

#### 7.4 Second Experimental Run

During the second experimental run at ISIS, pulsed neutron diffraction data was collected for samples of 81%, 90%, 95% and 100% KCl concentration. Scattering from the empty furnace at room temperature at the beginning and end of the experiment was also measured and no difference was observed between the two runs, which were subsequently combined to provide the background intensity. Scattering from an empty container was also measured, as well as that from an 8mm vanadium bar placed in the furnace. This was done to ensure that the vanadium bar was in the same position as the samples and empty container.

As a check on the microscopic mixing of the two components, data for the mixtures was recorded after every two or three hours. After normalisation of the data for each counting period to the corresponding monitor count, no change in the scattering was observed to occur with time for any of the mixtures over the time of the experiment, which was typically eight hours. It was therefore concluded that the mixing of the two salts was completed during the sample preparation and that no changes were occurring during the diffraction experiment.

In the period between carrying out the preliminary and the second experiments the instrument had been upgraded, with the gas detectors at  $\pm 20^\circ$ ,  $\pm 35^\circ$ ,  $\pm 58^\circ$ , and  $\pm 90^\circ$  having been replaced by scintillator detectors. A consistency check was therefore made by measuring the scattering from the same 66.7% KCl sample used previously, in order to identify any changes introduced by the instrument modification. The total structure factor obtained for the second run with the scintillator detectors is compared with the previous result using all gas detectors in figure 7.3. No significant differences are observed.

#### 7.5 Results and Structural Parameters

The total structure factors, combined over the same ranges that were used before, together with the previous results are plotted in figure 7.4. Figure 7.5 shows the corresponding total distribution functions. The positions,

heights and widths of the first peaks in real space were obtained by the method described in section 4.6 and are listed in table 7.2.

The availability of the partial structure factors for the two pure salts from the investigations of Biggin and Enderby (1981a) and Derrien and Dupuy (1975), helps considerably in the analysis of the total structure factor data for this three component system. In particular, the principle peak in  $g_{\text{ZnCl}}(r)$  is readily distinguishable in the total  $G(r)$  for the mixtures, and no other pair of ions in this system can be expected to approach each other this closely - the  $\text{K}^+$  ion having a much larger radius than the  $\text{Zn}^{2+}$  ion. The first peak in  $g_{\text{ClCl}}(r)$  is also clearly identifiable in the total  $G(r)$  for pure  $\text{ZnCl}_2$ , and its behaviour with increasing KCl concentration can be followed.

The mean coordination number of  $\text{Cl}^-$  ions around each  $\text{Zn}^{2+}$  ion has been evaluated by integration of  $r^2G(r)$  to the first minimum following this peak and the results obtained are listed in table 7.2. These values are fairly well determined, since the minimum following the first Zn-Cl peak remains deep for all the mixtures for which this peak has been observed.

In order to extract information in the low  $r$  region, fits to the structure factor data were obtained using the maximum entropy technique for the mixtures of 66.7%, 81%, 90%, 95% and pure KCl concentrations. Both a flat default level of  $G_{\text{T}}(r)=0$  and a default which drops to the  $G_{\text{T}}(0)$  level at the point at which the leading edge of the first K-Cl peak is known to be, were used to obtain the solutions shown in figures 7.6 and 7.7. The default levels used are also shown. From the maximum entropy solutions the Zn-Cl peak at  $r \approx 2.3\text{\AA}$  is clearly visible even for the 95% KCl concentration solution, whereas for the direct transform distribution functions, this peak is lost in the low  $r$  noise for the higher KCl concentration solutions. Some residual low  $r$  structure is seen in these maximum entropy solutions and is probably due to systematic errors such as slight inaccuracies in the normalisation of the different spectra or inelastic scattering effects. However the peak at  $r \approx 2.3\text{\AA}$  is always in the same place as that found for the pure  $\text{ZnCl}_2$  and is

therefore identified as belonging to the  $g_{\text{ZnCl}}(r)$ . Peak positions, scaled heights and coordination numbers obtained from these maximum entropy solutions are listed in table 7.2 also. It should be noted that the coordination numbers obtained from the maximum entropy solutions with default levels which drop to  $G_{\text{T}}(0)$  at low  $r$ , should be regarded as lower limits, since the peak at this position only rises above the low  $r$  default level as much as is required in order to fit the data. The range of values obtained from the two default levels for the peak heights, gives some indication of the uncertainty in this peak height (both solutions are acceptable fits to the data), but the peak remains strong for all of the concentrations studied, assuming that this peak is due entirely to the Zn-Cl contribution.

The first Cl-Cl peak is also clearly identifiable in the total distribution function of pure  $\text{ZnCl}_2$  from the partial structure factors obtained by Biggin and Enderby (1981a), and its behaviour with increasing KCl concentration can be followed since it is still clearly visible up to 81% KCl concentration.

## 7.6 Discussion of Results

### 7.6.1 The Chlorine-Chlorine Structure

From the coefficients of the structure factors listed in table 7.1, it can be seen that the chlorine-chlorine partial structure factor contributes more than 50% of the total coherent scattering for all of the mixtures across the composition range. The  $F(Q)$ 's are therefore dominated by the  $S_{\text{ClCl}}(Q)$ .

The partial structure factor data of Biggin and Enderby has shown that the structure of pure  $\text{ZnCl}_2$  is dominated by closely packed chloride ions, and from the total structure factor data presented in figure 7.4 for the  $\text{ZnCl}_2$  rich mixtures, it can be seen that this chlorine structure is largely unperturbed by the addition of KCl to the melt. The anion structure of pure KCl is very different from that found in  $\text{ZnCl}_2$ , yet the structure factor at 66.7% KCl concentration looks more like that of pure  $\text{ZnCl}_2$  than that of pure KCl. The same is also seen from the distribution functions, which look

very similar for all concentrations up to 66.7% KCl concentration. The main Cl-Cl peak found for pure  $\text{ZnCl}_2$  is still present at 81% KCl concentration, and there is nothing to suggest that it disappears at higher concentrations of KCl; it is just reduced in magnitude. Thus the short range anion structure found in pure  $\text{ZnCl}_2$  is also found at high KCl concentrations for these mixtures.

From the available partial structure factors from Biggin and Enderby and Derrien and Dupuy, attempts were made to model the total structure factors and distribution functions by recombining the  $S_{\alpha\beta}(Q)$  using the coefficients listed in table 7.1. Only the Zn-K term is unknown, but this is never more than 3.2% of the total coherent scattering. The first peak in  $g_{\text{ZnCl}}(r)$  is known to be resolution limited due to the limited  $Q$  range of the data, therefore, for these model fits, this peak has been substituted by the rescaled first peak from the total  $G(r)$  for  $\text{ZnCl}_2$  at  $330^\circ\text{C}$ . The mean nearest neighbour Cl-Cl distance for pure KCl is  $4.8\text{\AA}$  and  $n_{\text{ClCl}} = 12.3 - 16.2$ . This compares with  $3.71\text{\AA}$  and  $8.6 \pm 0.5$  for pure  $\text{ZnCl}_2$ . Thus two quite different chlorine structures are available for modelling the data. The results of these model fits supported the conclusion that the short range anion structure in the  $\text{ZnCl}_2$ -KCl mixtures is very similar to that found in pure  $\text{ZnCl}_2$  right up to at least 66.7% KCl concentration, and that some of this structure persists to even higher KCl concentrations.

The data was fitted in the following way. At first, an admixture of the two chlorine structures ( $S_{\text{ClCl}}(\text{ZnCl}_2)$  and  $S_{\text{ClCl}}(\text{KCl})$ ) was tried using coefficients appropriate to the zinc and potassium concentrations in the mixtures. These clearly did not fit the data, having too large a contribution from the  $S_{\text{ClCl}}(\text{KCl})$  and too little from the  $S_{\text{ClCl}}(\text{ZnCl}_2)$ . Fits were obtained in reciprocal space (except for the pre-peak) and real space for the mixtures with 33.3%, 50% and 66.7% KCl concentration, when the contributions from  $S_{\text{ClCl}}(\text{KCl})$  were reduced to 1/2, 1/2 and 1/4 what they should be if weighted by the proportion of chlorine from the potassium chloride, and the  $S_{\text{ClCl}}(\text{ZnCl}_2)$  contribution increased accordingly, so that the total  $S_{\text{ClCl}}(Q)$  contribution from both sources was what it should be

according to the coefficients of table 7.1. The coefficients used for the fits are listed in table 7.3. Fits could not be obtained by this method for the higher KCl concentration mixtures. These fitted models together with the coefficients used are shown in figures 7.8 to 7.10.

### 7.6.2 The Zinc-Chlorine Structure

The total distribution functions shown in figures 7.5 to 7.7 and the peak parameters listed in table 7.2, show that the first Zn-Cl peak remains strong and in the same position for the mixtures as it is for the pure  $\text{ZnCl}_2$ , right up into the extreme KCl rich region of the phase diagram. Although uncertain in the KCl rich mixtures, due to the small coefficients for this term and the noise at low  $r$  in the Fourier transforms, the peak position remains constant within the errors and its scaled height remains greater than 8.5 for the concentrations studied. The coordination number obtained by integrating  $r^2g(r)$  under this peak up to the first minimum following it remains at around 4.0 for all concentrations up to 81% KCl. Beyond this it becomes very uncertain and any residual container scattering or noise in  $G(r)$  could greatly contribute to its value. The stability of this peak and its coordination number of 4, together with the persistence of the Cl-Cl main peak at around 3.7Å up to at least 81% KCl, shows that the zinc ion in these mixtures is fourfold coordinated with chloride ions and that the arrangement is still tetrahedral, thus confirming that  $\text{ZnCl}_4^{2-}$  tetrahedral units still exist in these melts, even in the high KCl concentration mixtures, although these results do not prove that decoupled  $\text{ZnCl}_4^{2-}$  complex ions are the main structural entity.

The Raman scattering results of Ellis (1966) and Itoh et. al. (1982) have shown that bonds associated with collective motions in a  $(\text{ZnCl}_2)_n$  polymeric network decrease as KCl is added to pure  $\text{ZnCl}_2$  and as the temperature increases. It has been suggested by those authors that the observed emergent bands at  $290\text{cm}^{-1}$  and  $305\text{cm}^{-1}$  should be assigned to the species  $\text{ZnCl}_3^-$  and  $\text{ZnCl}_2$  respectively, but the  $n_{\text{ZnCl}}$  coordination numbers obtained here remain at

approximately 4 for all of the concentrations up to 90% KCl. Therefore if these species are formed, then they must be present in low concentration. The strength of the Zn-Cl peak in  $G(r)$  indicates that the  $ZnCl_4^{2-}$  unit is very stable in these mixtures, but the apparent decrease in the average number of  $Cl^-$  ions around each  $Zn^{2+}$  ion with increasing temperature for the pure  $ZnCl_2$  and 33% and 50% KCl solutions, suggests that  $ZnCl_3^-$  or  $ZnCl_2$  species may be formed by thermal dissociation.

Duke and Fleming (1957) proposed from their electrical conductivity measurements of  $ZnCl_2$ -KCl mixtures that  $K^+$  ions dominate the conduction from concentrations of about 30% KCl up to pure KCl. The formation of isolated and stable  $ZnCl_4^{2-}$  species, leaving  $K^+$  ions relatively free, is consistent with this proposal, and ought to give rise to a sharpening up of the principle peak in  $g_{ZnCl}(r)$ , since there would be no external constraints upon the structure of the tetrahedra through corner linking to others. The scaled height of this peak is observed to increase, but its height and width become uncertain at high KCl concentrations. Another investigation of the 81% KCl mixture using chlorine isotopic substitution is shortly to be conducted on LAD. This is expected to yield more accurate information about the Zn-Cl structure at high KCl concentrations.

### 7.6.3 The Potassium-Chlorine Structure

From the partial structural investigations by Derrien and Dupuy, the first two peaks in the total  $G(r)$  for pure KCl can be attributed to the first peaks in  $g_{KCl}(r)$  at 3.1Å and  $g_{ClCl}(r)$  at 4.8Å. The height of the peak at 3.1Å drops rapidly as  $ZnCl_2$  is added to KCl. In addition, the model fits of figures 7.8 to 7.10 show a poor fit in real space over the region 2.6Å to 3.4Å for the salt mixtures; with the observed  $G(r)$  being lower over this region than the model fit using the known  $ZnCl_2$  and KCl partials. This is the region of the main K-Cl peak for pure KCl and the poor fit could indicate a loss of K-Cl structural ordering due to high  $K^+$  ion mobility or reduced K-Cl attraction due to chloride ion polarization towards the central zinc ion in the  $ZnCl_4^{2-}$  complexes.

In contrast to the stability of the zinc chloride structure, the structure of potassium chloride is greatly modified by the addition of only 5-10% of zinc chloride, with the main K-Cl peak at 3.1Å being substantially reduced in height, and the formation of  $\text{ZnCl}_4^{2-}$  tetrahedral complexes.  $g_{\text{KK}}(r)$  makes only a minor contribution to the total  $G(r)$ , so that nothing can be said about it from this study.

### 7.7 The Pre-Peak

The diffraction peak observed at  $1.01\text{Å}^{-1}$  in the total structure factor of  $\text{ZnCl}_2$  at 330°C and at  $0.94\text{Å}^{-1}$  at 600°C, has been resolved by isotopic substitution of chlorine to originate from the Zn-Zn partial structure factor (Biggin and Enderby, 1981a). From all of the other partial structural investigations of molten 2:1 salts which exhibit this same feature, it has been seen that it is the cationic species which displays intermediate range order and gives rise to this peak. The pre-peak positions and heights for all of the  $\text{ZnCl}_2$ -KCl mixtures for which it is observed are listed in table 7.4, together with the height, scaled by the coefficient of the  $S_{\text{ZnZn}}(Q)$  for each system. The heights have been estimated by measuring perpendicularly from the top of the peak to an interpolated base line below the peak. From these values it is clear that this peak is not reduced in height as the potassium chloride is added, but its height, when account is taken of the diminishing zinc concentration, is in fact greatly increased, and reaches a maximum observed value of greater than 20 at 66.7% KCl concentration. It is still visible as a small hump for the 81% KCl solution, but its magnitude for this  $F(Q)$  is not well determined given the noise in the data and the small coefficient for the  $S_{\text{ZnZn}}(Q)$ . There is also a systematic shift to higher  $Q$  with increasing potassium chloride concentration, and to lower  $Q$  with increasing temperature as expected from thermal expansion.

In order to compensate for the different temperatures at which these samples were investigated, the peak position for pure  $\text{ZnCl}_2$  has been interpolated from its values at 330°C and 600°C, to the estimated position at 450°C, and the peak position at 820°C for the 81% KCl solution has been

extrapolated to its estimated value at 450°C using the known density behaviour with temperature for these mixtures. These temperature adjusted pre-peak positions and scaled heights are plotted in figure 7.11, where the behaviour with KCl concentration can be clearly seen. If this pre-peak in  $F(Q)$  is still arising from the  $S_{ZnZn}(Q)$  contribution, then its persistence for these mixtures means that the intermediate range ordering between the zinc ions within the tetrahedral units is not reduced as these units themselves become decoupled by the addition of 'excess' chloride ions, but it is indeed enhanced. Two possible explanations for this observed behaviour are now considered.

i) That the intermediate range ordering between zinc ions is not dependent upon the presence of a network and persists even when this network is broken. From other studies it is known that intermediate range order exists in systems with a high degree of ionic mobility which could not be considered as network melts. For example  $NiI_2$ , which from quasielastic neutron scattering and electrical conductivity measurements is believed to exhibit superionic behaviour for the cation below the melting point (Wood, 1989) and a high cationic mobility in the liquid phase, also has a high degree of intermediate range cationic ordering (Wood et. al. 1988).

If the network is being broken in  $ZnCl_2$ , then ordering between  $Zn^{2+}$  ions must arise through the packing of isolated  $ZnCl_4^{2-}$  units; these having preferred orientations to one another and, being isolated, are more free to orientate themselves in preferred directions. The main features in this structural investigation at the  $ZnCl_2$  rich end of the composition range, arise from the short range Zn-Cl and Cl-Cl structures and are characteristic of the structure of the tetrahedral units themselves rather than their orientation to one another. The second and third neighbour correlations have little effect upon the observed structure factors and distribution functions. We can therefore say little about the packing of the ionic complexes from the results.

Molecular dynamics studies by Saboungi et. al. (1984) and Blander et. al. (1986) for the systems  $MX$ ,  $AX_3$  and solutions of these of 25%, 50% and 75%  $MX$  concentration,

containing  $M^+$ ,  $A^{3+}$  and  $X^-$  ions, have shown that not only local ordering within  $AX_n^{3-n}$  complexes, but also ordering beyond local configurations can be reproduced using purely ionic potentials. The structure of the ionic complexes was seen to be octahedral for an anion to polyvalent cation size ratio of  $\leq 1.32$  and tetrahedral for a ratio of  $\geq 1.52$ . Ordering between these complexes shows itself in preferred A-X-A and A-A-A triplet angles. The angular distributions of triplets involving  $M^+$  ions in their 50% mixture did not exhibit well defined peaks, showing that the alkali ion in their simulated salt mixture was not in such well defined sites and therefore not playing a direct role in the inter-complex ordering.

For the ionic radius ratio which is most like that found in pure  $ZnCl_2$  of 2.45 (they used a maximum size ratio of 1.752) they found that the fraction of bridging  $X^-$  ions in A-X-A bridges was reduced from 21% at 25% MX concentration to 3.9% at 50% and 0.3% at 75% MX concentrations; thus confirming the 'network breaking' role of the alkali halide in  $AX_3$ -MX mixtures with this ion size ratio. There was a higher degree of bridging for the lower ion size ratios.

Complex ions such as  $AX_n^{3-n}$  would, from their consideration of the potential well in which  $X^-$  ions reside around  $A^{3+}$  ions, have a relatively long lifetime in dilute solutions of  $AX_3$  in MX, because of the need for the formation of an A-X-A bridge in order to remove an  $X^-$  ion from the first coordination shell of an  $A^{3+}$  ion. Saboungi et. al. and Blander et. al. used only an ionic Tosi-Fumi potential to simulate these stable ionic complexes. Although the zinc ion is only doubly charged, the potential well in which  $Cl^-$  ions reside around  $Zn^{2+}$  ions ought still to be deep in comparison to that around a  $K^+$  ion. The first shell coordination around each  $Zn^{2+}$  ion for the  $ZnCl_2$ -KCl mixtures is observed to be very stable even at the higher temperatures, as shown by the scaled height of the Zn-Cl peak in the total distribution functions. However, in the absence of any computer simulation data for this system, one cannot say with certainty whether ionic potentials are sufficient to reproduce both the stable  $ZnCl_4^{2-}$  complex ions and the intermediate range order observed for these mixtures. A molecular dynamics simulation of  $ZnCl_2$ -KCl mixtures should answer these questions.

ii) That the intermediate range ordering within the mixtures is between potassium ions as well as zinc ions. The assumption so far has been that the observed pre-peak in the total structure factor arises only from the partial structure factor  $S_{\text{ZnZn}}(Q)$ , but there is the possibility for these mixtures that the  $S_{\text{KK}}(Q)$  and  $S_{\text{ZnK}}(Q)$  may exhibit such ordering, even though  $S_{\text{KK}}(Q)$  does not have a pre-peak in the pure KCl data. If this is the case, then ordering could arise from  $\text{K}^+$  ions occupying 'regular' sites between isolated, but to some degree ordered,  $\text{ZnCl}_4^{2-}$  complex ions, and that intermediate range order is found in Zn-Zn, Zn-K and K-K correlations of a similar period and extent to that found in pure  $\text{ZnCl}_2$ . The extent of such ordering in real space can be estimated from the width of this peak in  $F(Q)$ , which although difficult to quantify exactly, because of the uncertainty in the shape of the base of the peak and the trough following it, is seen to be roughly constant for all of the mixtures for which it has been observed.

#### 7.8 Some Suggestions for Further Work

Raman scattering results for the  $\text{ZnCl}_2$ -LiCl system (Ellis, 1966) have shown that the band at  $230\text{cm}^{-1}$  observed for pure  $\text{ZnCl}_2$  and associated with bridging Zn-Cl-Zn stretching modes, is also reduced with the addition of LiCl. From the emergence of a strong polarised band at  $290\text{cm}^{-1}$ , it has been suggested that isolated  $\text{ZnCl}_4^{2-}$  tetrahedra are produced, so that LiCl is playing the same structure-breaking role as KCl. A neutron diffraction experiment using  $^7\text{LiCl}$  instead of KCl could yield more information on cationic ordering within this system.  $^7\text{Li}$  has a coherent scattering length of  $-0.22 \times 10^{-12}\text{cm}$  and will therefore give a negative coefficient for  $S_{\text{ZnLi}}(Q)$  and a very different coefficient for  $S_{\text{LiLi}}(Q)$  compared with  $S_{\text{KK}}(Q)$ . Natural lithium has a smaller, negative scattering length, but  $^6\text{Li}$  has a very high neutron absorption cross-section and would therefore have to be removed. Such a substitution would have little effect on the pre-peak if it is still found only in  $S_{\text{ZnZn}}(Q)$ , but would give rise to a dip or a substantially reduced peak for the higher alkali halide concentrations if the  $S_{\text{ZnLi}}(Q)$  and  $S_{\text{LiLi}}(Q)$  possessed pre-peaks. Such ordering of alkali cations

was not revealed by the molecular dynamics simulation by Saboungi et. al. (1984), but need not be ruled out for this reason.

An experiment using  $^7\text{Li}$  substitution is relevant to the  $\text{ZnCl}_2\text{-KCl}$  system only if the lithium ions behave in the same manner as potassium ions - occupying similar sites within the liquid structure. The local structure around the alkali cation is not easily determinable from diffraction data, since it requires extracting partial structure factors from a three component liquid for which only one component, chlorine, has suitable isotopes for substitution. An EXAFS investigation of a  $\text{ZnCl}_2\text{-KCl}$  mixture or a  $\text{ZnCl}_2\text{-NaCl}$  mixture could be more fruitful in yielding information about the local structure around alkali ions in these type of mixtures.

## 7.9 Summary

This chapter has presented the results of a time-of-flight neutron diffraction investigation of molten mixtures of zinc chloride and potassium chloride which show that the tetrahedral units present in pure zinc chloride persist as potassium chloride is added, and are very stable right across the composition range. The coordination numbers for the average number of chloride ions around each zinc ion have shown that the species  $\text{ZnCl}_3^-$  and  $\text{ZnCl}_2$  do not exist in significant concentrations at lower temperatures, as had previously been thought from Raman studies. As for the pure zinc chloride, the  $\text{ZnCl}_4^{2-}$  units become less stable at higher temperatures.

Intermediate range ordering between tetrahedral units in pure zinc chloride is not reduced as the network is broken by an alkali halide, indeed if the origin of the pre-peak is still to be found only in  $S_{\text{ZnZn}}(Q)$ , then it is greatly enhanced. If however,  $S_{\text{ZnK}}(Q)$  and  $S_{\text{KK}}(Q)$  make a contribution, then the alkali cation is playing a direct role in determining the intermediate range ordering in this system. The substitution of  $^7\text{LiCl}$  for  $\text{KCl}$  could shed light on the role of the alkali cation in producing or enhancing this intermediate range order, as could a molecular dynamics study of the  $\text{ZnCl}_2\text{-KCl}$  system using ionic potentials.

Table 7.1. Data analysis parameters and the coherent scattering contributions of the partials to the total  $F(Q)$  for the zinc chloride and potassium chloride mixtures.

Conc. / %KCl	Pure ZnCl <sub>2</sub>	33.3±0.2	50.1±0.3	66.6±0.3	81.0±0.3	90.0±0.4	94.9±0.4	Pure KCl
Density <sub>3</sub> / gcm	2.52@330°C 2.40@600°C	2.31@340°C 2.25@450°C	2.16@340°C 2.11@450°C	1.98 @ 450°C	1.61 @ 820°C	1.56 @ 820°C	1.53 @ 820°C	1.50 @ 820°C
Coh. Scatt. Coef./barns Zn-Zn	0.0358 (5.2)	0.0202 (3.2)	0.0130 (2.2)	0.0066 (1.2)	0.0024 (0.5)	0.0007 (0.2)	0.0002 (0)	
K-K		0.0022 (0.3)	0.0055 (0.9)	0.0113 (2.1)	0.0188 (3.8)	0.0253 (5.4)	0.0295 (6.4)	0.0344 (7.8)
Zn-K		0.0132 (2.1)	0.0169 (2.9)	0.0172 (3.2)	0.0135 (2.7)	0.0086 (1.8)	0.0049 (1.1)	
Cl-Cl	0.4078 (59.5)	0.3584 (57.9)	0.3303 (56.8)	0.2992 (55.5)	0.2710 (54.2)	0.2518 (53.2)	0.2409 (52.6)	0.2294 (52.0)
Zn-Cl	0.2418 (35.3)	0.1700 (27.5)	0.1306 (22.5)	0.0889 (16.5)	0.0513 (10.3)	0.0271 (5.7)	0.0139 (3.0)	
K-Cl		0.0555 (9.0)	0.0853 (14.7)	0.1161 (21.5)	0.1429 (28.6)	0.1596 (33.7)	0.1685 (36.8)	0.1777 (40.2)

The figures in brackets are the percentage contributions of each partial to  $F(Q)$ . The scattering cross-sections used were from Sears (1984).

$\sigma_c$ /barns     $\sigma_s$ /barns     $\sigma_a$ /barns (at 1.798Å)

Zinc	4.054	4.131	1.11
Potassium	1.73	1.98	2.1
Chlorine	11.531	16.7	33.5

Table 7.2. Structural parameters for the Zn-Cl peak for the zinc chloride and potassium chloride mixtures.

	Position/Å	Scaled height	Width/Å	Coord.no.*
Pure ZnCl <sub>2</sub>				
330°C	2.281±0.003	8.9±0.1	0.26±0.01	3.93±0.06
600°C	2.291±0.005	7.5±0.2	0.33±0.01	3.67±0.06
33.3% KCl				
340°C	2.281±0.004	9.5±0.2	0.26±0.01	4.2±0.1
450°C	2.278±0.007	9.0±0.3	0.27±0.01	3.9±0.1
50% KCl				
340°C	2.26±0.01	8.6±0.8	0.26±0.02	4.1±0.1
450°C	2.279±0.007	8.4±0.4	0.30±0.02	3.84±0.10
66.7% KCl				
Inv. trans.	2.28±0.02	11.7±0.4	0.28±0.02	3.9±0.1
ME Flat	2.26	10.5		
ME Stepped	2.26	11.5		3.9±0.1 <sup>+</sup>
81% KCl				
Inv. trans.	2.28±0.03	12±1	0.43±05	4.1±0.2
ME Flat	2.30	8.3		
ME Stepped	2.27	10.3		3.3±0.2 <sup>+</sup>
90% KCl				
Inv. trans.	2.31±0.04	13±2	0.48±05	4.7±0.3
ME Flat	2.24	11.6		
ME Stepped	2.25	14.4		4.0±0.2 <sup>+</sup>
95% KCl				
ME Flat	2.29	16.8		
ME Stepped	2.28	12.2		

These results were obtained from direct Fourier transformation except for the following:

ME Flat Obtained from the maximum entropy solution with a flat default level of  $G(r)=0$ .

ME Stepped Obtained from the maximum entropy solution with a default level which drops to  $G(0)$  at low  $r$ .

\* Obtained by integration of  $r^2G(r)$  up to the first minimum.

+ Should be regarded as a lower limit.

Table 7.3. Contributions made by the partial structure factors  $S_{\text{ClCl}}(Q)$  from the  $\text{ZnCl}_2$  and  $\text{KCl}$  pure salt structures, to the total  $F(Q)$  model fits of figures 7.7 to 7.9.

	Total Cl-Cl coefficient	In proportion to salt conc.		Values used for fits	
		$\text{ZnCl}_2$	$\text{KCl}$	$\text{ZnCl}_2$	$\text{KCl}$
33.3% $\text{KCl}$	0.3584	0.2867	0.0717	0.3226	0.0358
50% $\text{KCl}$	0.3303	0.2202	0.1101	0.2753	0.0550
66.7% $\text{KCl}$	0.2992	0.1496	0.1496	0.1870	0.1122

Table 7.4. Pre-peak parameters for the zinc chloride and potassium chloride mixtures.

	Position ( $\text{\AA}^{-1}$ )	Height	Scaled height	
Pure $\text{ZnCl}_2$	330°C	1.005±0.01	0.140±0.008	3.9±0.2
	600°C	0.94±0.01	0.13±0.01	3.6±0.3
33.3% $\text{KCl}$	340°C	1.00±0.02	0.098±0.008	4.9±0.4
	450°C	0.98±0.02	0.11±0.01	5.4±0.5
50% $\text{KCl}$	340°C	1.05±0.02	0.109±0.009	8.4±0.7
	450°C	1.03±0.02	0.12±0.01	9.5±0.8
66.7% $\text{KCl}$	First expt.	1.10±0.02	0.166±0.01	25±2
	Second expt.	1.10±0.02	0.17±0.02	26±3
81% $\text{KCl}$	820°C	1.12±0.03	0.026±0.02	11±8

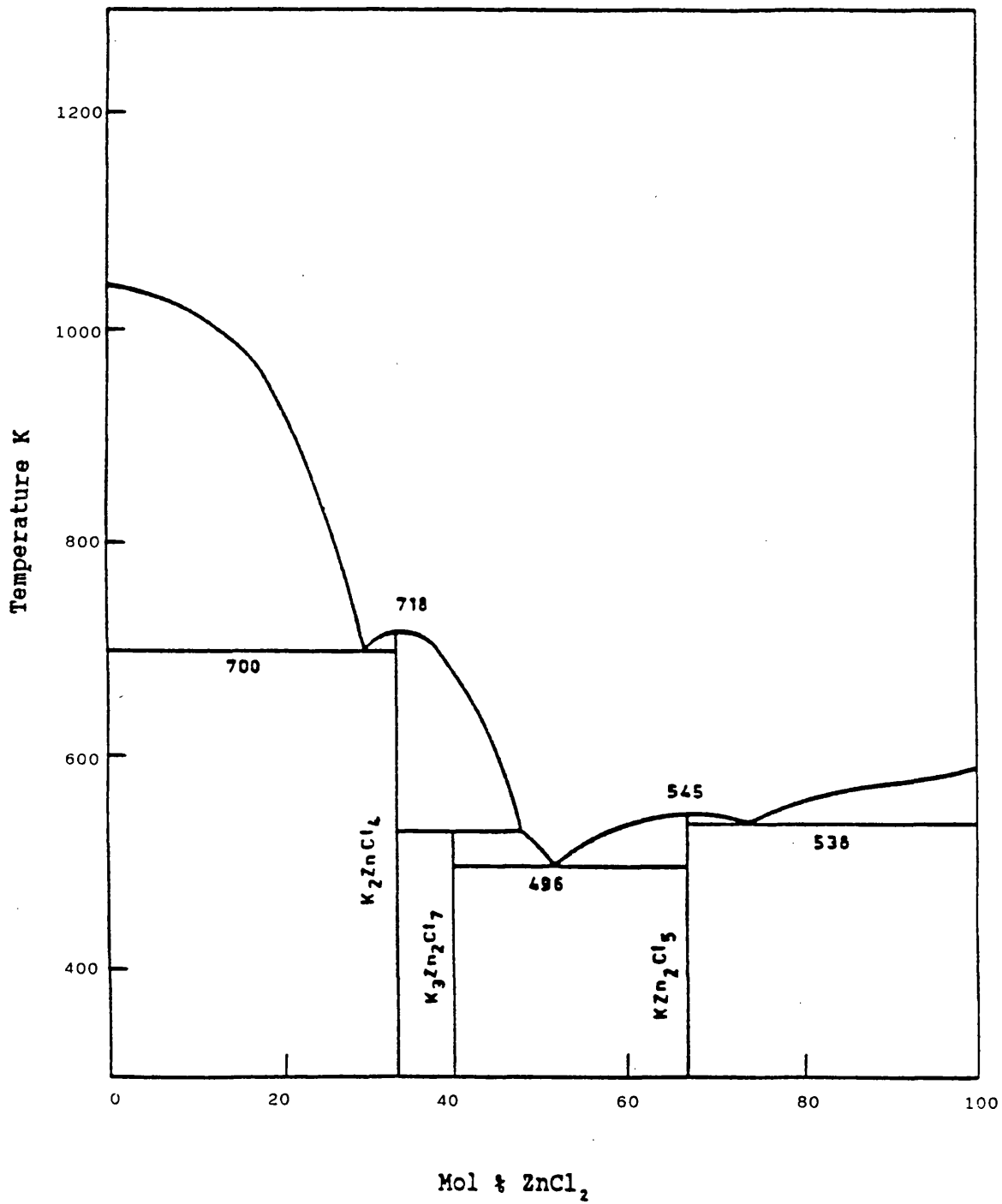


Figure 7.1. The phase diagram of the zinc chloride - potassium chloride system by Perry (1989).

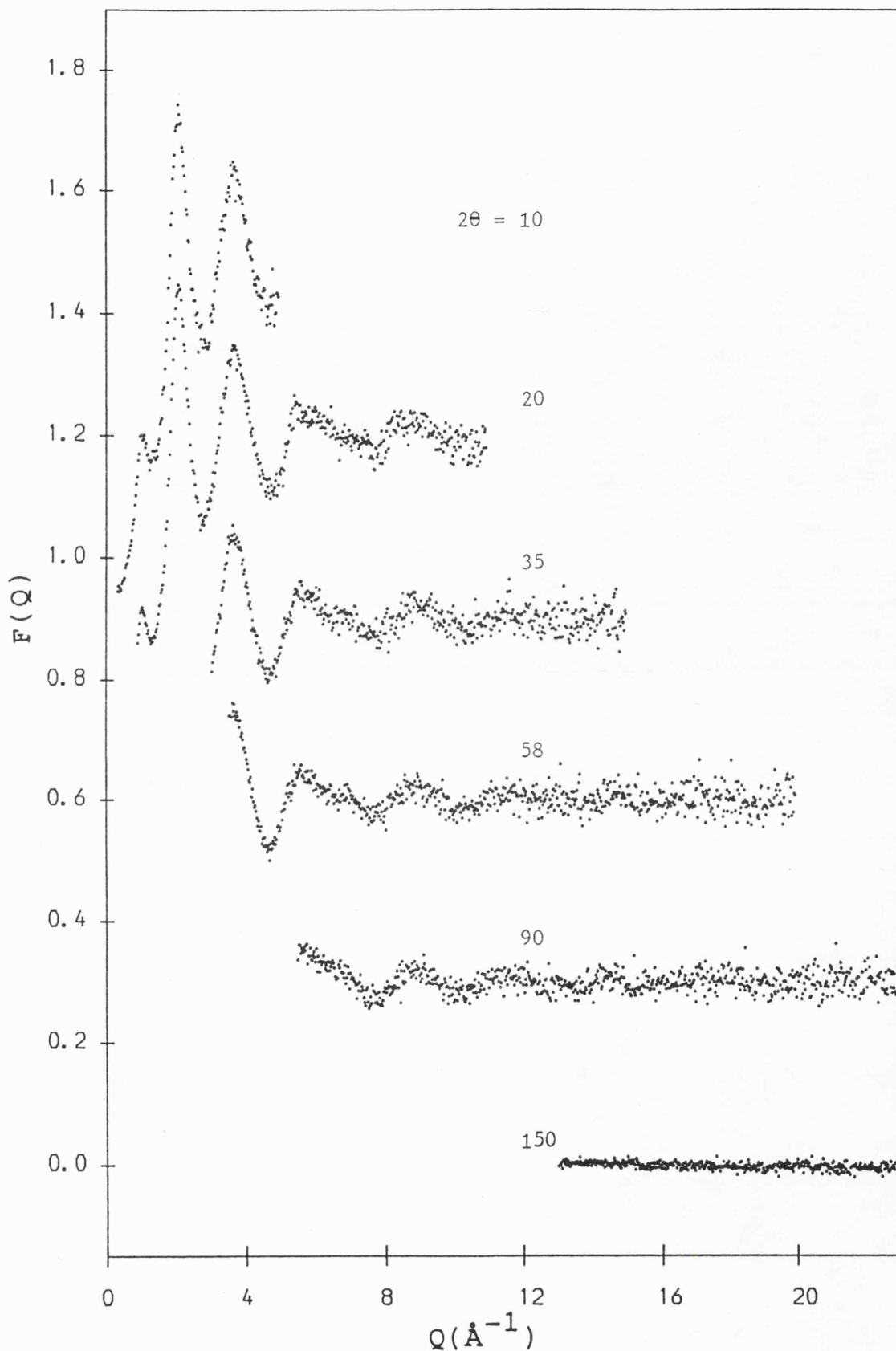


Figure 7.2. The total structure factor of the 50%KCl + 50%ZnCl<sub>2</sub> mixture at 450°C. The data is shown for each detector angle over the ranges which contribute to the final  $F(Q)$ , and data for each successive angle is displaced by 0.3.

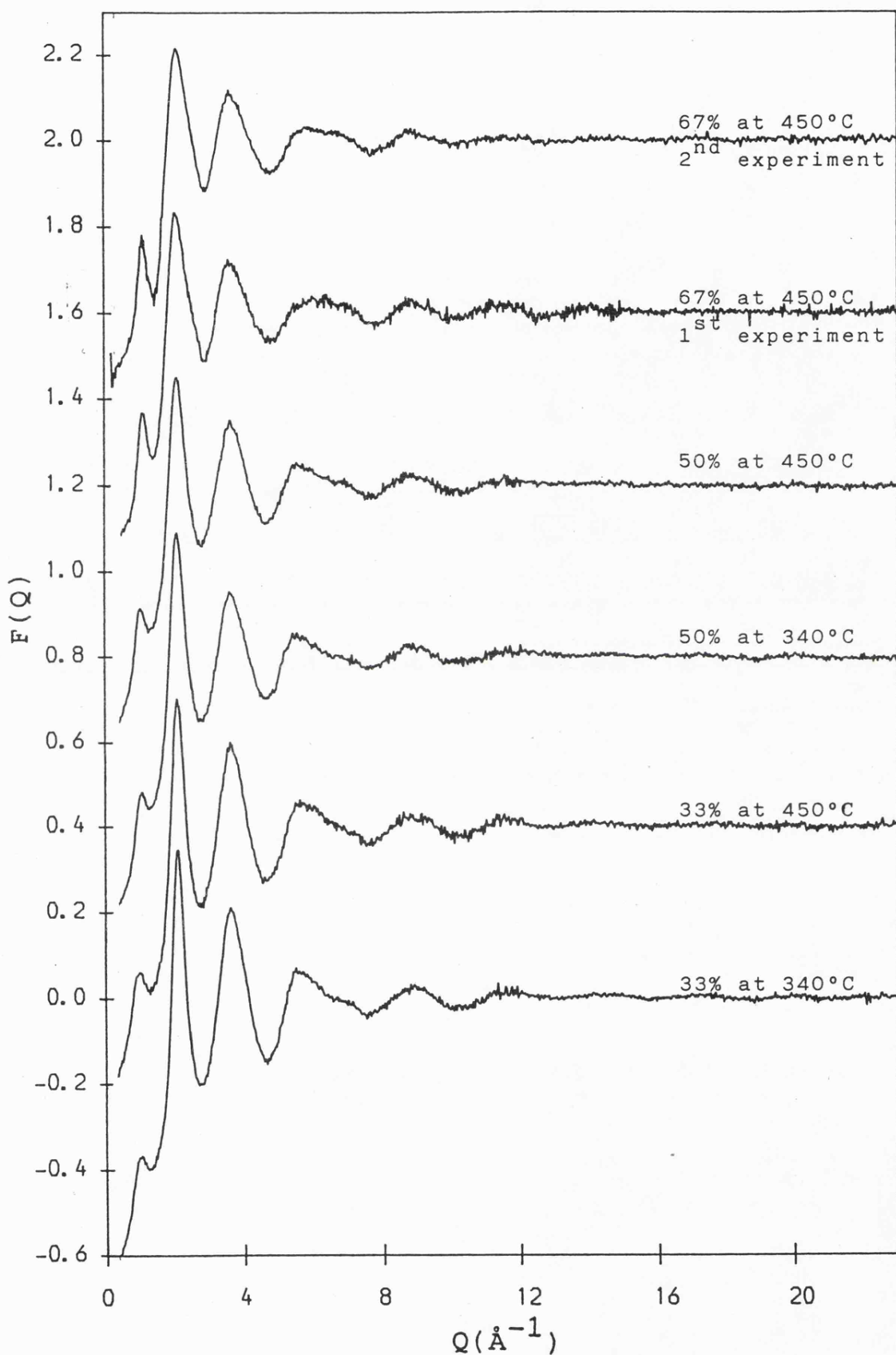


Figure 7.3. Comparison of the total structure factors for the 33.3% and 50% KCl solutions at 340°C and 450°C, and of the data for the 66.7%KCl solution from the two separate experiments.

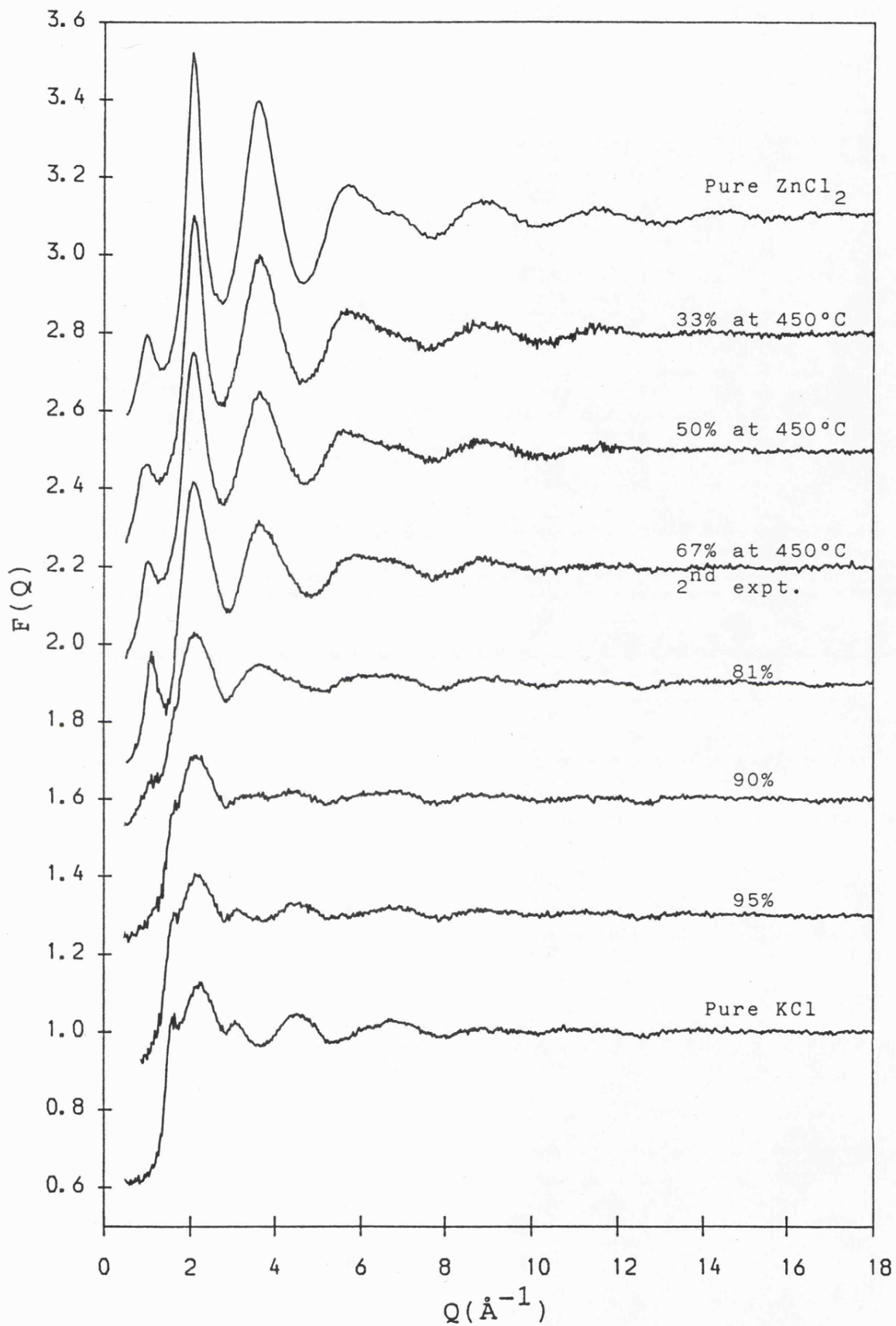


Figure 7.4. Total structure factors for all of the concentrations studied.

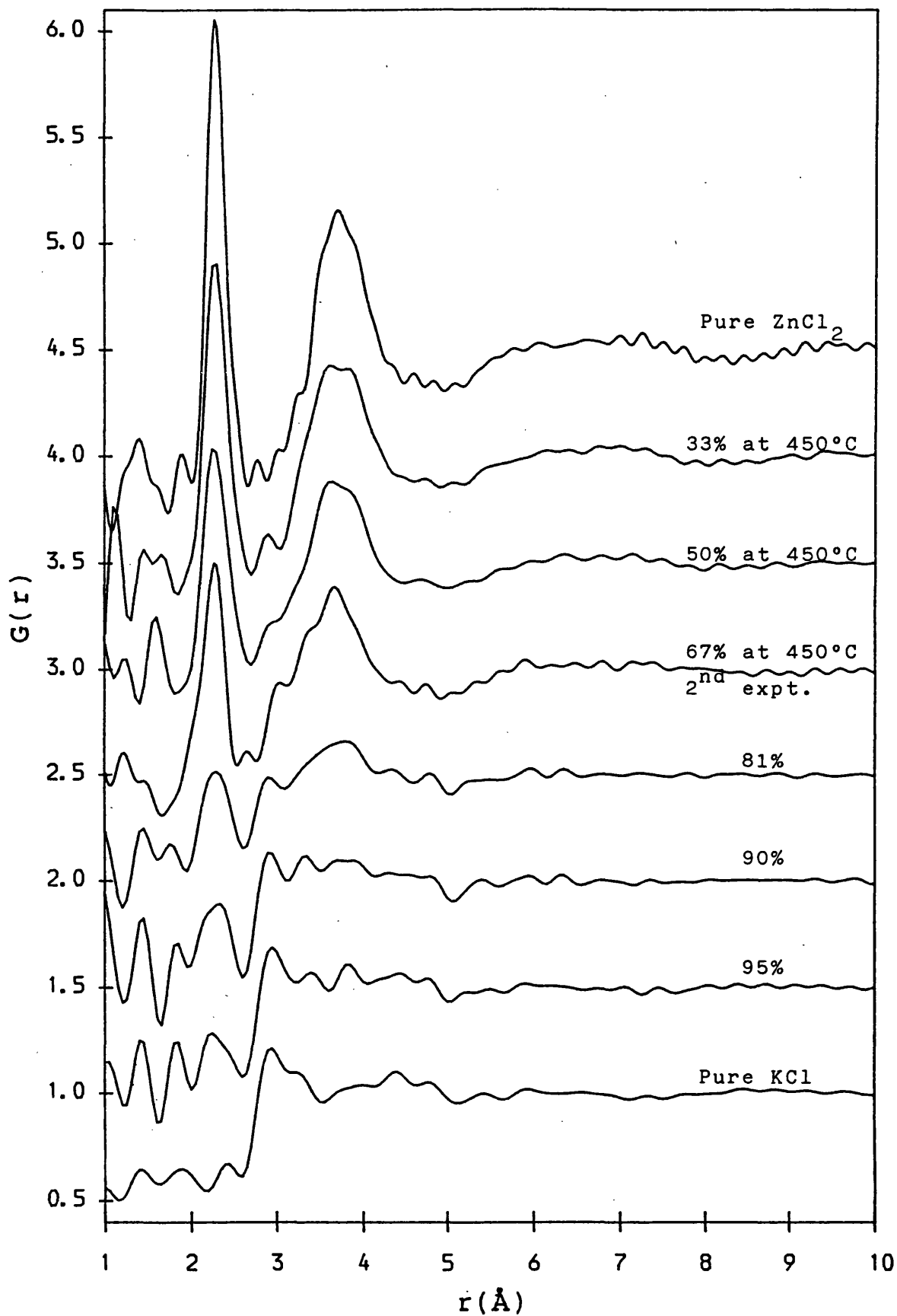


Figure 7.5. Total distribution functions for all of the concentrations studied. These are the Fourier transforms of the unsmoothed data.

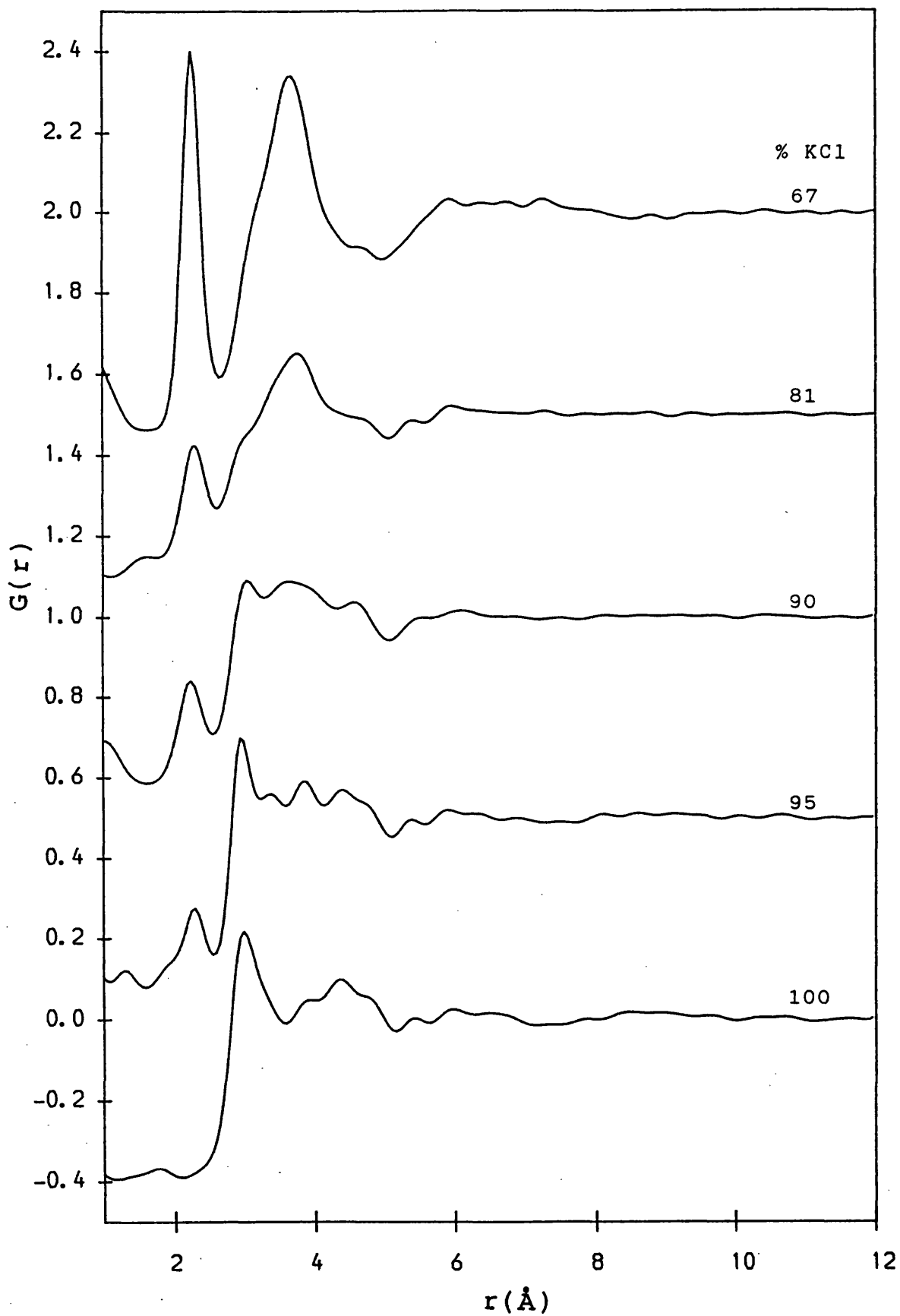


Figure 7.6. Maximum entropy solutions to fit the high KCl concentration structure factor data. The default level used was  $G(r)=1.0$  in all cases, but each successive function has been displaced by 0.5.

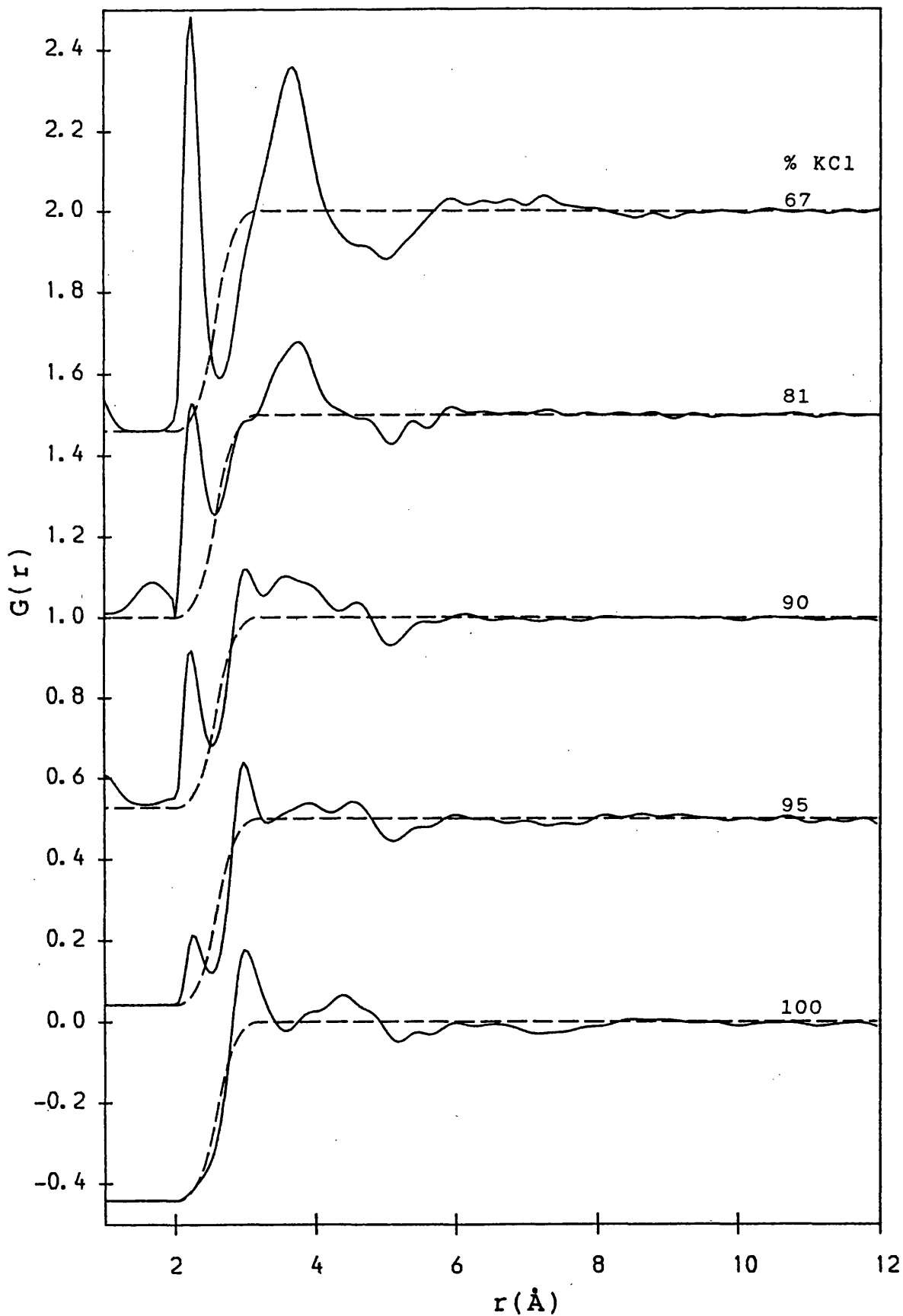


Figure 7.7. Maximum entropy solutions to fit the high KCl concentration structure factor data. The default levels used are shown as broken lines in each plot.

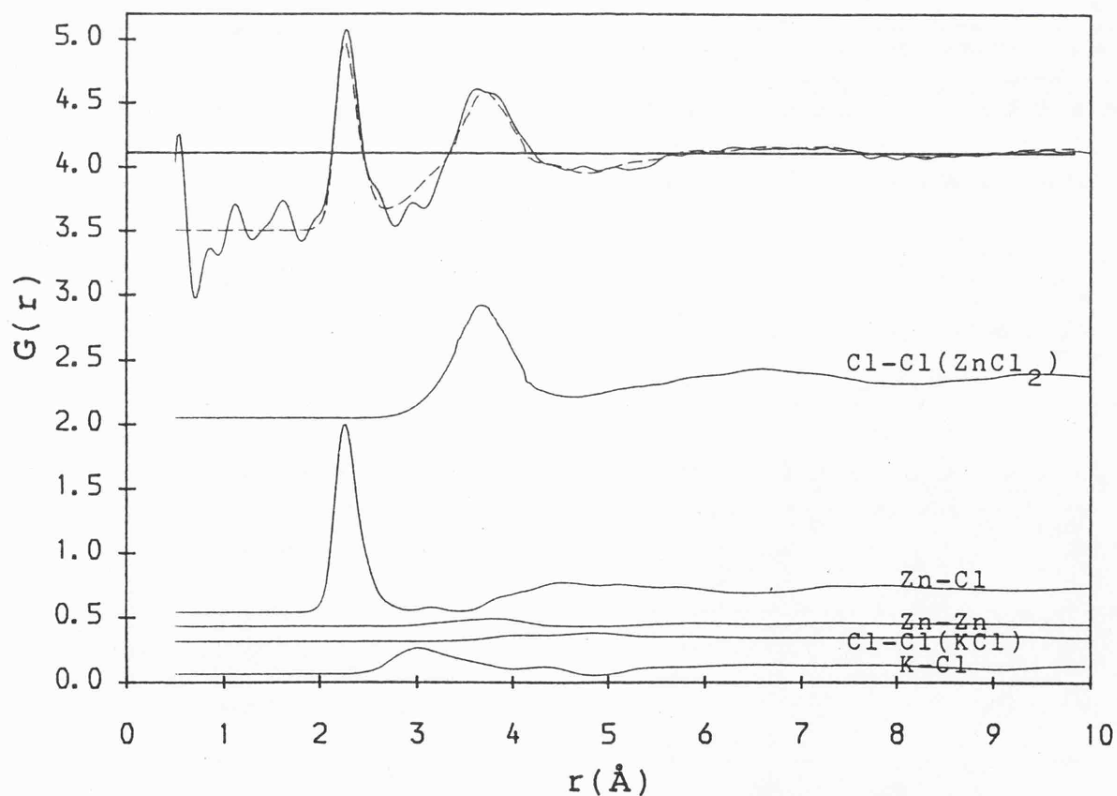
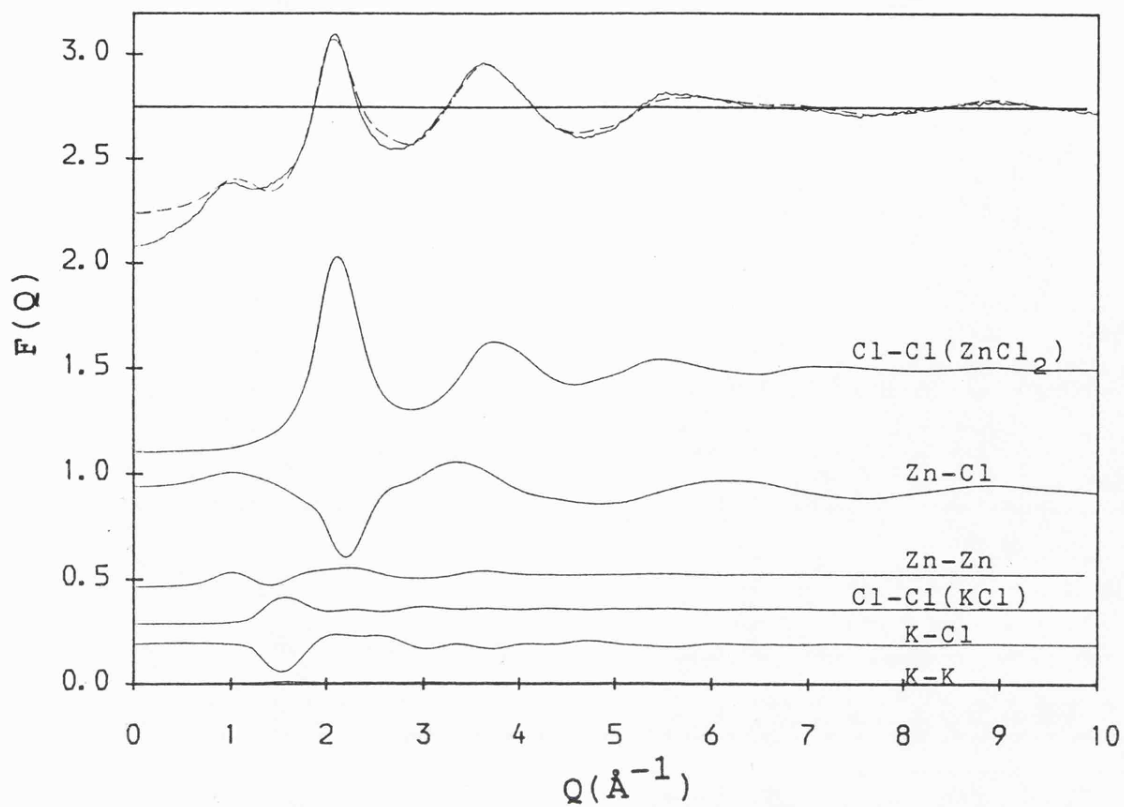


Figure 7.8. The total structure factor and distribution function of the 33%KCl solution at 340°C compared with the recombinated partials. These were recombinated according to the coefficients given in tables 7.1 and 7.3, and the weighted partials are shown at the bottom of each plot. The recombinated  $F(Q)$  and  $G(r)$  are shown as broken lines.

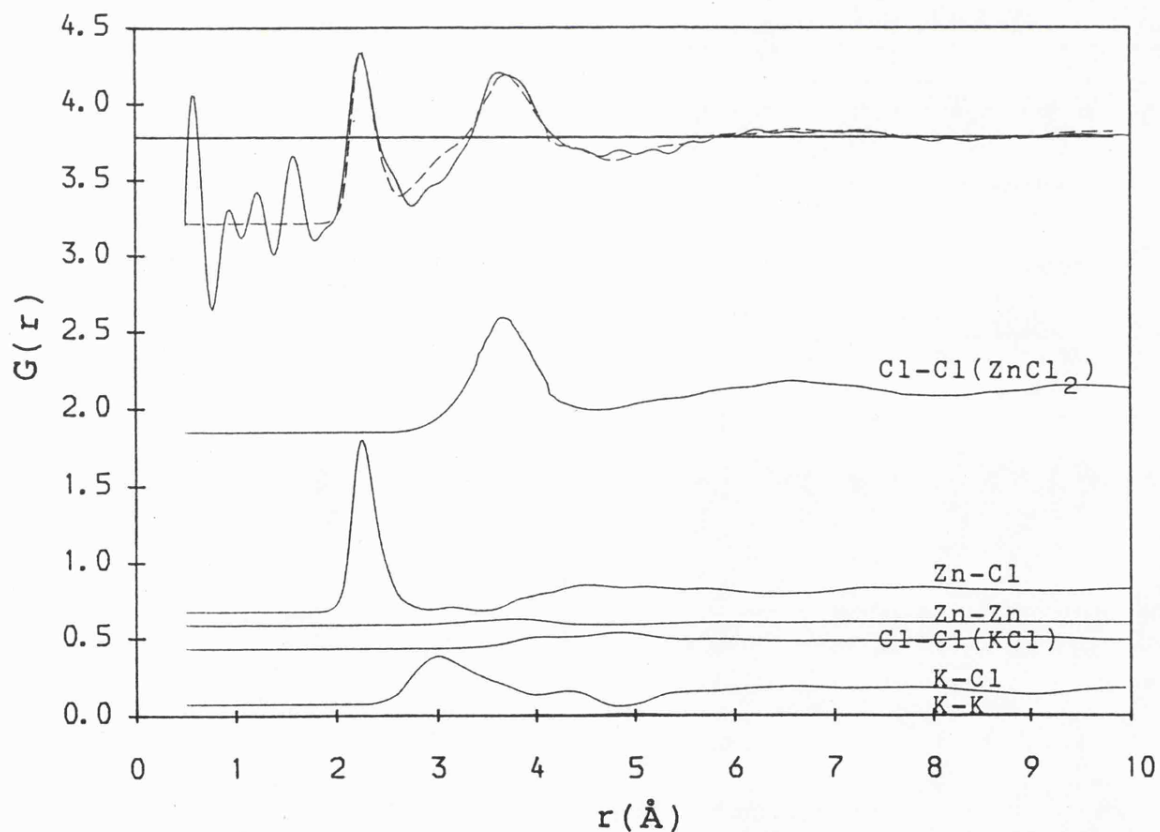
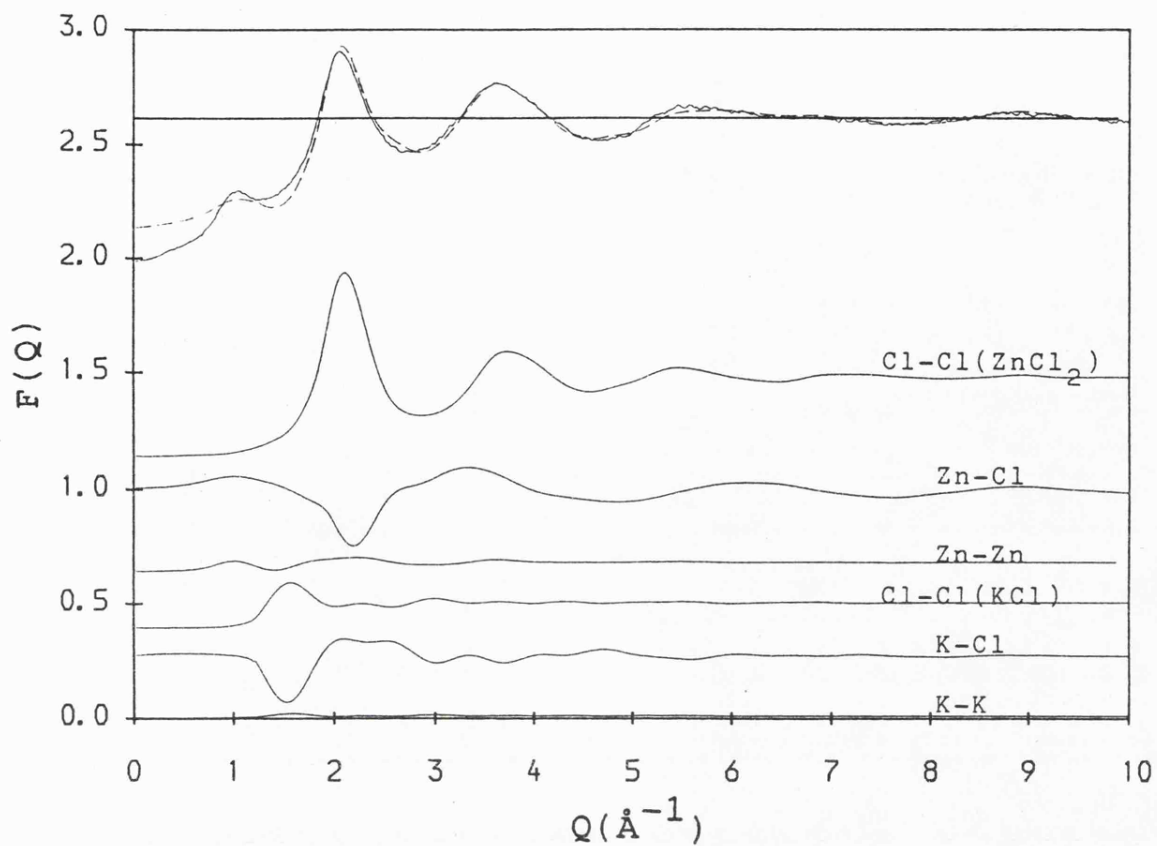


Figure 7.9. The total structure factor and distribution function of the 50%KCl solution at 340°C compared with the recombinated partials (see caption for figure 7.8).

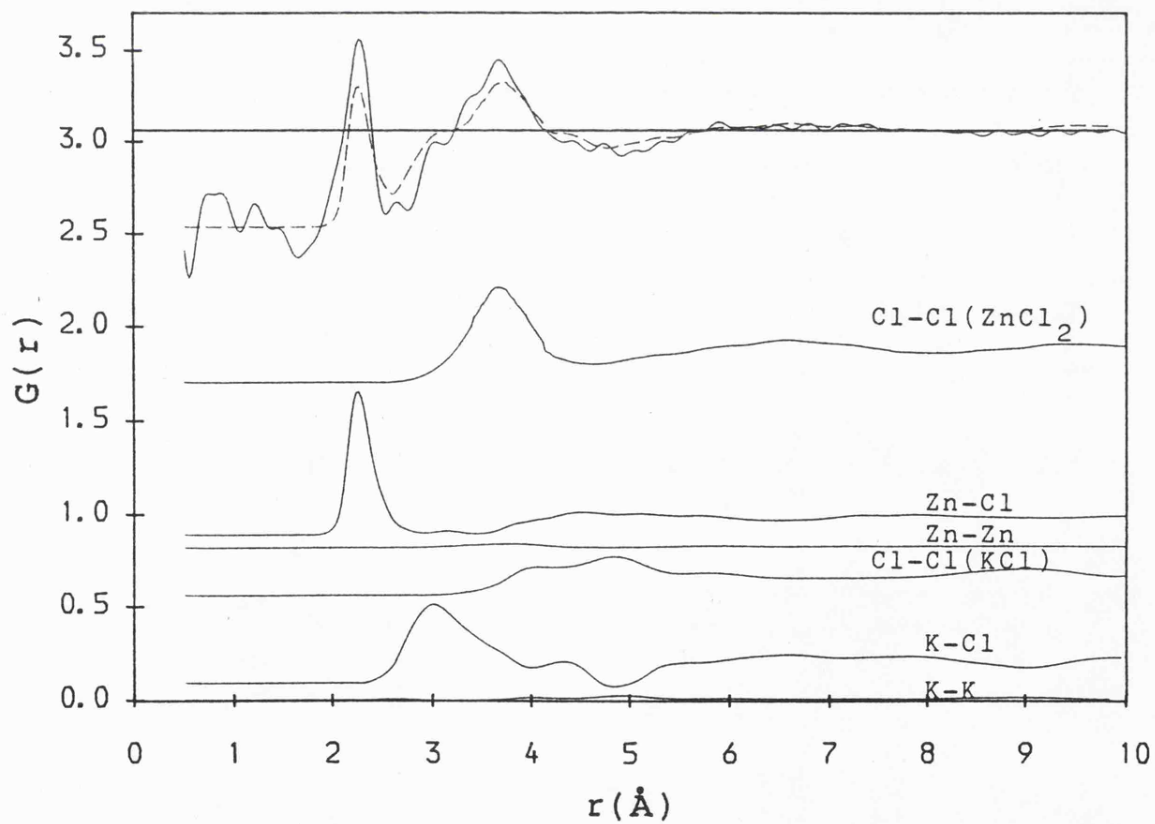
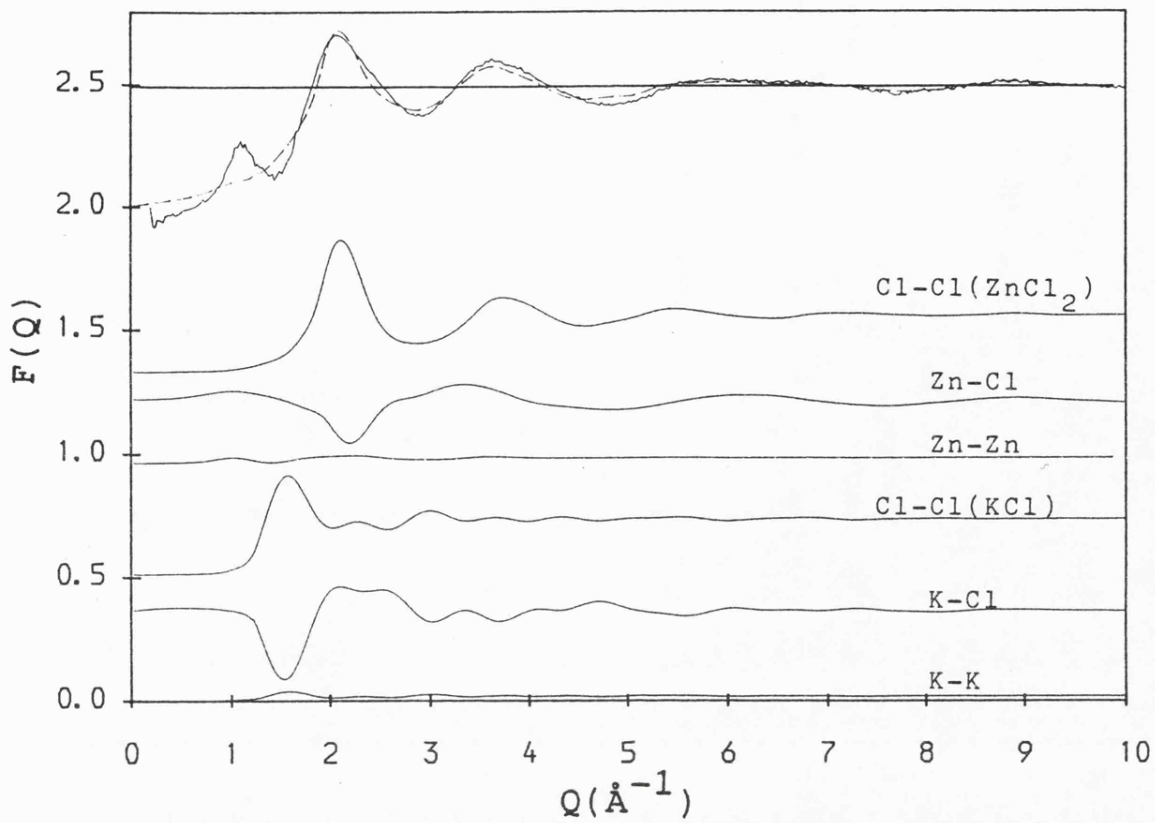


Figure 7.10. The total structure factor and distribution function of the 66.7%KCl solution compared with the recombined partials (see caption for figure 7.8).

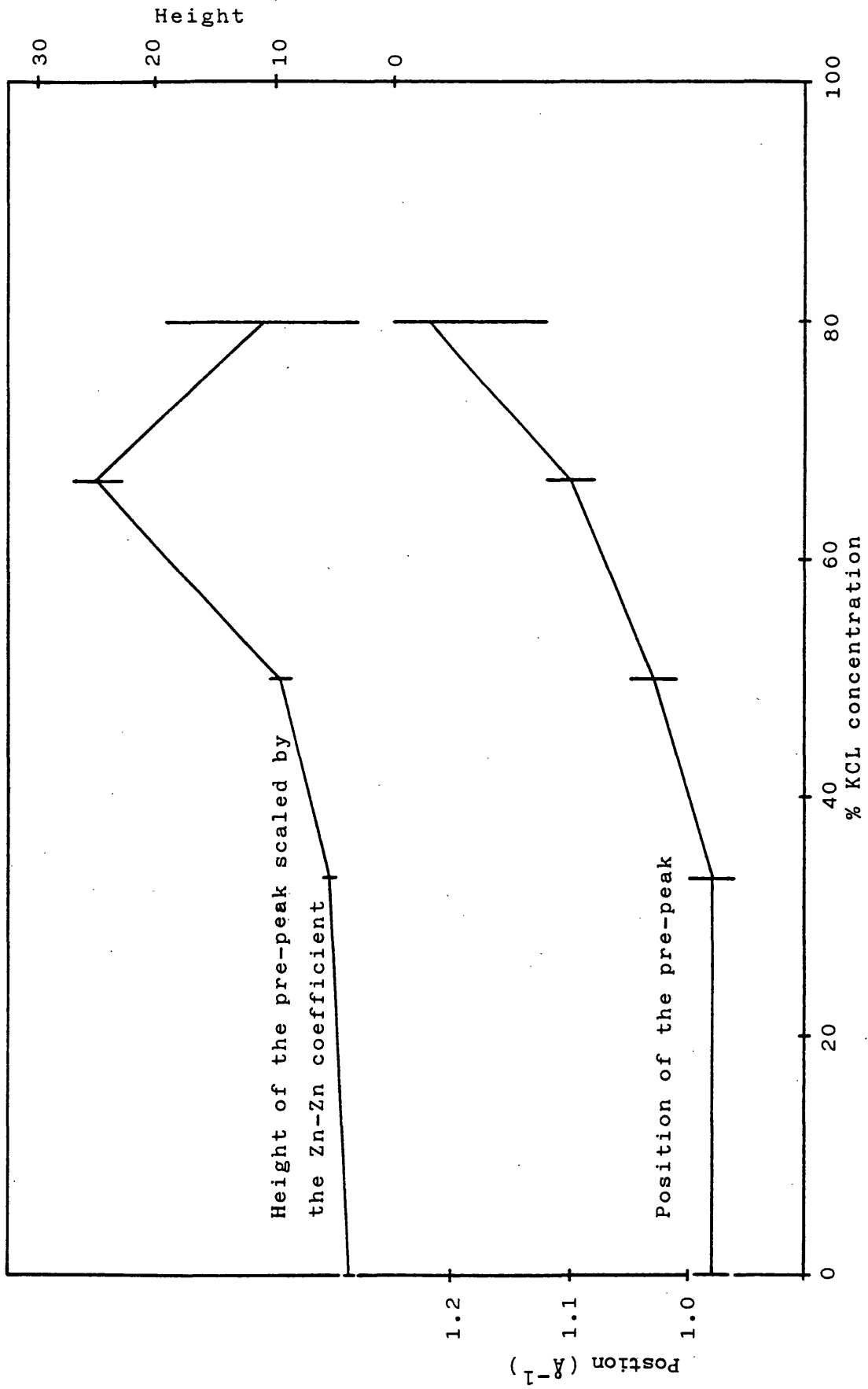


Figure 7.11. Behaviour of the pre-peak with KCl concentration. The values for pure  $\text{ZnCl}_2$  and the 81%KCl solution are those expected at  $450^\circ\text{C}$ .

## CHAPTER 8

### MOLTEN MIXTURES OF NICKEL IN NICKEL HALIDES

#### 8.1 Metal-Molten Salt Solutions

The nature of mixtures of metals in their molten salts has long been of interest to chemists, but it wasn't until the late 1950's that it was established from phase diagrams and electrical conductivity measurements on alkali metal-alkali halide systems (Bredig and Johnson, 1960), that true solutions are formed rather than colloidal dispersions as had earlier been proposed - see for example Ellis (1960).

One can divide metal-molten salt solutions into two categories:

i) Those in which the added metal imparts metallic behaviour to the solution. This class of solutions exhibit mixed ionic and electronic conductance even at low metal concentration (<5mol%), and include most of the alkali metal-alkali halide solutions.

ii) Those for which the electrical conductance and its temperature coefficient are typical of ionic solutions. The conductivity of such solutions does not increase much upon addition of metal, indeed for the case of cadmium in cadmium chloride at low temperatures, it actually decreases. This class of solutions includes many polyvalent metal halides such as the bismuth halides, mercury halides and alkaline earth halides.

The metallic behaviour of the solutions of the former category has been attributed to the existence in the melt of mobile electrons. The metal dissolves according to the equation  $M \longrightarrow M^{n+} + ne^{-}$ . Various models have been proposed to account for the observed behaviour, including a free electron model by Wilson (1963), in which it is assumed that all of the valence electrons are free. Rice (1961) considered the electrons to be localised on cations, giving a conductivity which is determined by thermally activated hopping of electrons between atoms and cations according to the equation  $M \rightleftharpoons M^{+} + e^{-}$ . Durham and Greenwood (1976) and Littlewood (1981) proposed models whereby a certain fraction of the electrons are localised, while the electronic

conduction is due to the remainder. Another form of electron localisation appropriate to alkali metals in their salts, is the F-centre analogue proposed by Pitzer (1962), in which electrons occupy anion vacancies and electronic conduction is by hopping between F-centre sites. For a recent model based on this picture see Warren (1986).

For the second class of metal-molten salt mixtures, the lack of electronic contribution to the conductivity at the salt rich end of the composition range, is usually attributed to the removal of conduction electrons by the formation of cationic species of lower oxidation state than that found in the pure salt. Mixtures belonging to this class are often designated 'subhalide' solutions. A number of polymeric subhalide species have been proposed such as  $\text{Na}_2$  in Na-NaBr,  $(\text{M}_2)^{2+}$  for divalent cationic melts such as  $\text{Cd}_2^{2+}$  in Cd-CdCl<sub>2</sub> and even larger complexes such as  $\text{Bi}_3^{3+}$ ,  $\text{Bi}_4^{4+}$  or even  $\text{Bi}_9^{5+}$  in Bi-Bi halide melts. In addition, some metals in their molten salts form monomeric ions of lower than normal oxidation state.

As pointed out by Nachtrieb (1974), the distinction between these two classes of solution ('metallic' and 'subhalide') lies in the relative depth of the trap for valence electrons. It is shallow for the metallic type of solutions, where the electrons are localised by F-centre analogues or by conduction band tailing due to potential fluctuations in the liquid (Katz and Rice, 1972), and deep for subhalide solutions where electron localisation is on lower valence cations or polymeric species.

## 8.2 Nickel in Nickel Halides

Very little structural data exists for polyvalent metals in their molten salts. Ichikawa and Matsumoto (1981) studied molten Bi in BiI<sub>3</sub> across the composition range by pulsed neutron diffraction and concluded that  $\text{BiI}_n^{3-n}$  complexes were formed. The results however were derived from single total diffraction patterns, and their interpretation was not unambiguous.

In this chapter neutron diffraction results are presented for Ni in molten NiI<sub>2</sub> and NiBr<sub>2</sub> at 9 molar percent

concentration. Previous neutron diffraction studies on the pure salts  $\text{NiCl}_2$ ,  $\text{NiBr}_2$  and  $\text{NiI}_2$  have been undertaken here at Leicester by Newport et. al. (1985), Wood and Howe (1988) and Wood et. al. (1988). The favourable conditioning of the three simultaneous equations obtained by isotopic substitution of nickel for the nickel halide series (section 4.4), has enabled direct determination of the three partial structure factors and distribution functions for each of the three pure salts. All of these molten halides possess a close-packed anion structure which is remarkably stable throughout this series, with the nickel cations residing in tetrahedrally coordinated sites within this structure. It is the aim of the experiments reported in this chapter to determine the nature of the dissolved metal in nickel-nickel halide solutions. In particular, whether polymeric subhalide species proposed for polyvalent metal-molten salt solutions are formed.

### 8.3 Nickel in Nickel Iodide

As an initial investigation, time-of-flight neutron diffraction measurements were made on two isotopically distinct samples of  $\text{NiI}_2$  + 9 molar percent Ni using GPPD at Argonne National Laboratory. In a previous experiment on this instrument the three partial structures of pure  $\text{NiI}_2$  had been determined. An investigation of the phase diagram of Ni and molten  $\text{NiCl}_2$  has been carried out by Johnson et. al. (1958), and a eutectic was found at 9 molar percent of Ni and at a temperature of  $32^\circ\text{C}$  below the melting point of the pure salt. It would be reasonable to expect nickel to have higher solubilities in the other nickel halides, and the choice of 9 percent mixtures for the investigations discussed in this chapter was thought to be a safe one.

#### 8.3.1 Experimental

The two nickel isotopic mixes that were used for the solution experiment were natural nickel and 'zero' nickel, for which the coherent scattering length of nickel is zero. The isotopic compositions, exact nickel concentrations and the scattering cross-sections used for the data analysis are

listed in table 8.1. In the absence of any available data for the density of  $\text{NiI}_2$  or  $\text{NiI}_2+\text{Ni}$ , the density used for the analysis was chosen to be consistent with that used for the pure salt data and with the known behaviour of the density of  $\text{NiCl}_2+\text{Ni}$  determined by Galka et. al. (1972).

The coefficients for the two structure factors determined are:

$$\text{'zero' } F(Q) = 0.117 S'_{\text{II}}$$

$$\text{'Nat' } F(Q) = 0.116 S'_{\text{II}} + 0.133 S'_{\text{NiNi}} + 0.249 S'_{\text{NiI}} \quad (8.1)$$

where  $S'_{\alpha\beta} = S_{\alpha\beta}(Q) - 1$ .

Although there was a slight difference in the concentration of the nickel between the two samples, this was not considered significant, but was taken into account when analysing the data.

The samples were prepared by vacuum drying and pre-melted as described in section 3.4. For the final sample tubes, fused silica containers with a nominal wall thickness of 1mm and internal diameter of 8.5mm were used. These were held in the Leicester vanadium foil furnace at 825°C, some 30°C above the melting point of the pure salt, and from the temperature profile measurements made by Wood (1987), there was not expected to be a temperature variation of more than about 5°C over the length of the sample even at this high temperature. The beam height was set at 1¼" and the molten sample lengths extended beyond this illuminated region.

Neutron scattering spectra were measured by the fixed detector banks at the nominal angles of  $\pm 20^\circ$ ,  $\pm 30^\circ$ ,  $\pm 60^\circ$ ,  $\pm 90^\circ$  and  $\pm 150^\circ$  for a total of approximately two days, with the data being stored after the first day. Also, scattering from an empty silica container, a ¼" diameter vanadium bar and the hot empty furnace were also measured. It was also intended to make another measurement on a sample of pure molten natural  $\text{NiI}_2$  in order to compare with the data for the natural  $\text{NiI}_2$  from the previous experiment, but this sample (fortunately the last one) was lost after a short time in the molten state, and the data was not of sufficient statistical

accuracy to be of any use. There was agreement with the previous results as far as one could tell.

### 8.3.2 Results

The vanadium spectra were fitted with fourth order polynomials after the Bragg peaks had been removed and after normalisation of the sample spectra to the monitor and vanadium spectra, no differences were observed between the data collected on the two days, or the data collected by the counter banks at the same angles on opposite sides. The total structure factors obtained after data reduction and the application of corrections are shown for the two samples in figures 8.1 and 8.2. Separate angle spectra are shown for the ranges over which they were used, together with the reverse transform of the final smoothed distribution functions obtained. Slight renormalisation of the spectra was required, but this was the same for all of the angles. The main source of the error here is likely to be the uncertainty in the density.

### 8.3.3 Summary of Observations

The 'zero'  $\text{NiI}_2+\text{Ni}$   $F(Q)$  yields directly the iodine-iodine partial structure factor shown in figure 8.3(a). Also shown is the partial structure factor for the pure salt together with the reverse transform of the smoothed  $g(r)$  obtained for the solution. The data has been binned into constant  $\Delta Q$  bins of  $0.05\text{\AA}^{-1}$ . Comparison of the two results in  $Q$ -space shows that the anion structure is largely unperturbed by the addition of this much excess nickel, with peak positions and amplitudes being the same for both samples, although there are slight differences over the second peak in  $S(Q)$ . The same structural invariance is seen in real space in figure 8.3(b).

Rescaling the 'zero'  $F(Q)$  for  $\text{NiI}_2+\text{Ni}$  by  $0.116/0.117$  and subtracting it from the natural  $F(Q)$  yields a function

$$F'(Q) = 0.133 S'_{\text{NiNi}} + 0.249 S'_{\text{NiI}} \quad (8.2)$$

which is shown in figure 8.4(a) together with the equivalent combination of partial structure factors for the pure salt. The similarity of the two functions for the pure salt and the mixture suggests that very little change occurs in the Ni-Ni and Ni-I partial structures when nickel is dissolved in nickel iodide, contrary to what one might expect if subhalide complexes were being formed. The transforms of these functions, to which the Ni-Ni partial makes a 35% contribution, are shown in figure 8.4(b). It should be noted that the Ni-Ni partial is largely structureless for the pure salt, so that changes to this partial may not be visible. Any well defined Ni-Ni distances associated with the formation of subhalide complexes should however be observable.

#### 8.4 Nickel in Nickel Bromide

The structural investigation of  $\text{NiI}_2 + \text{Ni}$  using two isotopic compositions of nickel did not yield unambiguous information about the Ni-Ni and Ni-I partial structures, and small changes in these partials may not have been observable. A full partial structural investigation of a molten nickel halide and nickel mixture was therefore desirable.

##### 8.4.1 Experimental

Steady-state neutron diffraction patterns were measured for three isotopically distinct samples of  $\text{NiBr}_2 + 9\text{mol}\% \text{Ni}$  on the D4B diffractometer at the ILL which is described in section 3.2.2. This was the same instrument that was used to determine the structure of pure  $\text{NiBr}_2$ . The three nickel isotopic mixtures used were natural Ni,  $^{62}\text{Ni}$  and 'zero' Ni. The isotopic compositions, scattering lengths and parameters used for the data analysis are listed in table 8.2 for these samples.

The coefficients for the three total structure factors are as follows:

$$\text{'zero' } F(Q) = 0.192 S'_{\text{BrBr}}$$

$${}^{62}\text{F}(Q) = 0.192 S'_{\text{BrBr}} + 0.082 S'_{\text{NiNi}} - 0.251 S'_{\text{NiBr}} \quad (8.3)$$

$$\text{'Nat' } F(Q) = 0.192 S'_{\text{BrBr}} + 0.133 S'_{\text{NiNi}} + 0.320 S'_{\text{NiBr}}$$

where  $S'_{\alpha\beta} = S_{\alpha\beta}(Q) - 1$ .

The samples were prepared by the method described in section 3.4 and held in fused quartz containers of 7.7mm internal diameter and 1mm wall thickness. The diameter was chosen so as to reduce the fraction of the scattering that is from the container and to keep the sample length short, while keeping the total scattering at less than 10% for the purposes of accurate determination of the absorption and multiple scattering corrections. The sample lengths in these diameter tubes were 28 - 32mm. The samples were melted in a vanadium foil furnace at  $995 \pm 2^\circ\text{C}$ , some  $30^\circ$  above the melting point of pure  $\text{NiBr}_2$ , and there was not expected to be a temperature gradient of greater than  $5^\circ\text{C}$ .

The measurements were made with  $0.7049\text{\AA}$  neutrons: the wavelength and machine zero angle being determined by a nickel powder scan. The low angle detector (detector 1) stepped round in  $1.5^\circ$  steps and covered an angular range of  $1.6^\circ \leq 2\theta \leq 64.7^\circ$ , while detector 2 covered the range  $46.8^\circ \leq 2\theta \leq 131^\circ$  in  $2^\circ$  steps. Due to electronic noise, some of the detector elements were not included in the final averaging of the measured intensities.

Each scan lasted approximately two hours and the samples were scanned seven times. The empty container scattering was also counted for five scans. Scattering from a 5mm vanadium bar, the empty furnace (sample background) and empty instrument (i.e. without the furnace) was also measured. The resulting intensities for the 'zero' Ni and natural Ni samples, the empty container and the furnace, after normalisation to the monitor are shown in figure 8.5. For the purposes of comparing the two detector banks on the

same plot, the data has also been normalised to the scattering from the vanadium bar.

#### 8.4.2 Results

Comparison of the scans for both the natural and  $^{62}\text{Ni}$  samples revealed a diffraction pattern that was changing with time. This is now believed to be due to the nickel metal dissolving into the salt. Although the samples had been pre-melted for fifteen and ten hours respectively, some or all of the metal must have crystallised out of solution upon freezing.

As a test of how much nickel metal was actually dissolving into the salt and whether it was uniformly dispersed, another sample of natural  $\text{NiBr}_2 + 9.0 \text{ mol}\% \text{ Ni}$  was prepared from reagent grade  $\text{NiBr}_2$  in exactly the same manner as the sample used for the diffraction experiment. This was quantitatively analysed by titration by Philip Gullidge at the University of Bristol. The solid  $\text{NiBr}_2 + \text{Ni}$  pellet, formed after melting and cooling, was divided into four sections along its length. Each section, when dissolved in water, was found to contain nickel in its metallic state and  $\text{NiBr}_2$ . The percentage of  $\text{NiBr}_2$  found in each section was, within the experimental error, that expected for a 9mol% nickel solution. The percentage concentration of nickel metal, however, was found to be  $9.2 \pm 0.2$  in the section from the bottom of the melting tube,  $8.9 \pm 0.1$  in the section above that,  $7.4 \pm 0.1$  in the next section and  $7.7 \pm 0.1$  in the top section. A third component was also present in this lower purity sample which was not present in the high purity sample used for the experiment. This was in the form of a green solid which was identified as  $\text{NiO}$ . However, this impurity was only present at a concentration of 0.37 weight percent, and was concentrated mainly at the bottom of the sample. The distribution of nickel metal found for this sample shows that nickel did in fact dissolve to at least 7.7 mol%, since the nickel was originally in the form of a 2mm diameter wire at the bottom of the tube and could only have reached the top section by dissolution. The higher concentration of nickel found in the lower sections of the tube is possibly due to

nickel coming out of solution at temperatures below the liquidus and falling towards the bottom.

In order to obtain diffraction data for a 9 mol% solution from the observed changing diffractions patterns for the  $^{62}\text{Ni}$  sample, a method of extrapolation to infinite time was employed. The differences between the raw data for the first scan and that for each successive scan were obtained. The magnitude of a particular feature in these difference spectra was plotted as a function of time and an estimate of the asymptotic magnitude was made. The particular feature used was that resulting from the difference between two slightly different peaks, since the first peak in the diffraction pattern for the  $^{62}\text{Ni}$  sample was shifting to lower  $Q$  as the nickel dissolved. Other features in these difference spectra were small by comparison and were not much greater than the noise. The fifth, sixth and seventh scans were 'extrapolated' to what one would expect them to be after an infinite time, by adding to them the appropriate difference spectra that were necessary to bring the magnitude of this feature to its asymptotic limit. For example, the difference between the third and fourth scans was almost the same as that between the sixth scan and the estimated asymptotic limit. Therefore, this difference was added to the sixth scan. The final spectrum that was used for the data analysis was that obtained from a weighted mean of these three extrapolated scans. The statistical quality of this spectrum was equivalent to that of one original scan, but was still sufficient for obtaining partial structure factors.

For the data for the natural nickel sample, only very small changes were observed during the time of the final three scans, so these were combined using the flux weighting method. The diffraction pattern for the zero nickel sample showed very little change between the first and final scans. For the purposes of data analysis, the final four scans were combined.

The method of extrapolation to infinite time, used for the data for the  $^{62}\text{Ni}$  sample, assumes that the particular feature in the difference spectra that was used to estimate the asymptotic behaviour is representative of the whole of the spectra. Since all other changes with time observed for

this sample were small in comparison, and since all of the changes observed were small compared with that between the total structure factors for the pure salt and the solution, then the uncertainty in  $F(Q)$  introduced by using this method is not considered to be significant.

The possible effect of uncertainty in the nickel concentration was investigated by analysing the data twice: first assuming a 9mol% nickel solution and then assuming a pure salt. The main differences observed between the results for these extreme cases were to be found in  $S_{\text{NiNi}}(Q)$ , where the amplitude of the first main peak was 27% greater for the  $S_{\text{NiNi}}(Q)$  obtained by assuming that no extra nickel was present. These differences were small compared with those between the partial structure factors obtained for the pure salt in the previous experiment and those obtained for the mixture in this one. It was concluded, therefore, that even with a small uncertainty in the concentration of the dissolved nickel and the uncertainty introduced by the time dependence of the diffraction data, any changes observed in the structure factors of  $\text{NiBr}_2$  upon addition of nickel metal are real and that the structure factors presented here are representative of those of a 9 mol% nickel solution.

The total structure factors obtained for the three samples after container and background subtraction and vanadium normalisation as described in section 4.2, are shown in figure 8.6, together with the results of recombining the partial structure factors obtained by inverse Fourier transformation of the final distribution functions. These total structure factors have been corrected for absorption in the sample and container, multiple scattering and incoherent scattering by the methods described in section 4.2. Also, the Placzek correction for inelastic scattering was applied to the measured intensity for the vanadium bar, which was then fitted with a cubic function.

As before, in the absence of any available data for the density of pure  $\text{NiBr}_2$  and  $\text{NiBr}_2+\text{Ni}$ , the density used for the analysis was chosen to be consistent with that used for the analysis of the pure salt data (Wood and Howe, 1988) and with the known behaviour of the density of  $\text{NiCl}_2+\text{Ni}$ . Renormalisation was required as mentioned in section 4.2.6.

The three partial structure factors were separated as described in section 4.4. The  $F(Q)$  for the 'zero'  $\text{NiBr}_2+\text{Ni}$  sample yielded  $S_{\text{BrBr}}(Q)$  directly, while the other two partial structure factors were obtained from the natural Ni and  $^{62}\text{Ni}$   $F(Q)$ 's after the subtraction of the  $F(Q)$  for the 'zero' Ni sample. No smoothing was used for this analysis and the results, together with the back-transforms of the final  $g(r)$ 's are shown in figure 8.7.

In order to Fourier transform these structure factors, it was necessary to fit a low order polynomial to extrapolate the data to the low  $Q$  limit. No compressibility data is available for either the pure metal halides or their mixtures with nickel, so a guess was made as to the  $S_{\alpha\beta}(0)$  values by looking at the data. The long wavelength limit for the three partials was chosen consistently in accordance with the set of equations 4.12. Fortunately the dependence of the  $g_{\alpha\beta}(r)$ 's on this part of the structure factors is only very slight, so that the uncertainty in the  $S_{\alpha\beta}(0)$  values was of little consequence.

Prior to transformation, the structure factors were binned into constant  $\Delta Q$  bins and the two counter banks combined as described in section 4.3.4. Interpolation onto a constant  $\Delta Q$  grid of  $0.025\text{\AA}^{-1}$  was then necessary for the evaluation of the integrals. The Fourier transformations were carried out by the direct method to yield the distribution functions shown in figures 8.8 to 8.10 and also by the maximum entropy method - the results of which are shown at the bottom of these figures. A flat default level of  $g(r)=1$  was used for all of these maximum entropy solutions and also for the solutions to fit the pure  $\text{NiBr}_2$  data, which are shown on the same figures for comparison. The low amplitude of the ripples in the  $g_{\text{NiBr}}(r)$  and  $g_{\text{BrBr}}(r)$  obtained by direct transformation of the  $S(Q)$ 's, reflects both the good statistical accuracy of the data and the good conditioning of the three equations for  $F(Q)$  for the nickel isotopic substitution (equation 4.11).

A smoothed  $g_{\text{NiNi}}(r)$  was obtained by a cubic spline method and the leading edge of the first peak in the three  $g_{\alpha\beta}(r)$ 's brought smoothly to zero by fitting polynomials. The  $g_{\alpha\beta}(r)$ 's obtained were then back-transformed and compared

with the  $S_{\alpha\beta}(Q)$ 's to see if they were acceptable solutions. This process was repeated until acceptable  $g_{\alpha\beta}(r)$ 's were obtained. These are shown in figure 8.11 and their corresponding back-transforms are compared with the partial structure factors in figure 8.7. These were then combined with the appropriate coefficients to give recombined total structure factors, which are compared with the original  $F(Q)$ 's in figure 8.6.

Coordination numbers were calculated by using the integration to the first minimum in  $r^2g(r)$  and the  $r^2g(r)$  symmetric methods described in section 4.6.2. A summary of these and other derived structural parameters for pure  $\text{NiBr}_2$  and  $\text{NiBr}_2 + 9\text{mol}\% \text{Ni}$  is given in table 8.3.

#### 8.4.3 Summary of Observations

From the partial structure factors and distribution functions shown in figures 8.7 to 8.11, a number of observations can be made.

i) As for the  $\text{NiI}_2 + \text{Ni}$  experiment, the anion-anion partial is seen to be insensitive to the addition of this concentration of excess nickel. It has a similar amplitude in  $Q$  space and real space to that of the pure salt and the nearest neighbour coordination number, evaluated by integration of  $r^2g(r)$  to the first minimum in  $r^2g(r)$ , remains at around the same value of  $11.7 \pm 0.2$ , compared with  $11.0 \pm 0.3$  for the pure salt. The close contact coordination number, evaluated by the  $r^2g(r)$  symmetric method, gives a value of  $8.6 \pm 0.4$  compared with  $8.6 \pm 0.7$  for the pure salt. This indicates that the close packed nature of the anion structure is maintained, and is not greatly perturbed by the addition of excess nickel.

ii) The Ni-Br partial structure factor is also seen to be unchanged for  $Q > 3\text{\AA}^{-1}$  upon addition of nickel. The oscillations have the same amplitude, phase and extent, as far as one can tell with this range of observation. However, changes are observed in the structure factor for the region of lower  $Q$ . The dip at  $Q = 1.95\text{\AA}^{-1}$  in the pure salt  $S_{\text{NiBr}}(Q)$  is

shifted to lower  $Q$  upon addition of excess nickel, and is at a position of  $1.90\text{\AA}^{-1}$  for the solution. Its depth is also reduced from  $-0.78$  for the pure salt to  $-0.68$  for the mixture.

This dip in  $S_{+-}(Q)$  is a well established feature of liquids which exhibit charge alternation (see for example Rovere and Tosi, 1986 or March and Tosi, 1984) and occurs for such systems at the same position as the first main peaks in  $S_{++}(Q)$  and  $S_{--}(Q)$ . Copestake and Evans (1982) argued that this feature, although indicative of charge ordering within the liquid, does not necessarily mean Coulombic interactions.

In real space, the principal peak in  $g_{\text{NiBr}}(r)$  is unaltered by the presence of excess nickel: it has the same position, height, width and shape as it had for the pure salt, and the mean nearest neighbour coordination number remains the same within the error at  $4.55 \pm 0.15$  bromide ions around each nickel ion. From the observed values of  $\bar{r}_{\text{BrBr}}$  and  $\bar{r}_{\text{NiBr}}$  (the peak positions in  $r^2g(r)$ ), the ratio  $\bar{r}_{\text{BrBr}}/\bar{r}_{\text{NiBr}}$  for the pure salt is  $1.60 \pm 0.02$  compared with  $\sqrt{8/3} = 1.633$  for a perfect tetrahedral arrangement. This value is not changed for the 9% solution and this, together with the coordination number, indicates that the local configuration of bromide ions around each nickel ion averaged over the volume of the sample, is not changed.

Some filling in of the first minimum after the principal peak in  $g_{\text{NiBr}}(r)$  is observed and the second neighbour peak is increased slightly to higher  $r$ . There are no new well defined Ni-Br distances that would indicate the presence of large complexes of the type  $\text{Ni}_n\text{Br}_m$  containing many bromine atoms. It appears therefore that the excess nickel atoms are occupying vacant tetrahedrally coordinated sites within the largely unperturbed anion structure.

iii) The only major structural change observed upon addition of excess metal is to be seen in the Ni-Ni partial structure. In  $S_{\text{NiNi}}(Q)$  we observe a significant loss of amplitude, with the principal peak height being reduced from  $2.34 \pm 0.13$  for the pure salt to  $1.72 \pm 0.05$  for the mixture and little structure is observed beyond this peak. There is also a shift to lower  $Q$  from  $1.99 \pm 0.01\text{\AA}^{-1}$  to  $1.95 \pm 0.02\text{\AA}^{-1}$ , but the peak

remains coincident with the dip in  $S_{\text{NiBr}}(Q)$ .

The pre-peak observed for pure nickel bromide at  $Q = 0.98 \pm 0.02 \text{ \AA}^{-1}$  is still present for the mixture at the slightly lower  $Q$  position of  $0.95 \pm 0.02 \text{ \AA}^{-1}$ . Its height appears to be slightly reduced and its width broadened, but this is difficult to quantify since the trough following this peak has been filled in by the shift and broadening of the principle peak.

The loss of structure in  $S_{\text{NiNi}}(Q)$  is reflected in real space as an overall reduction in the structural ordering of the nickel species. This is seen by the reduction in peak heights and filling in of the troughs: the first peak height is reduced from  $1.7 \pm 0.1$  for the pure salt to  $1.3 \pm 0.1$  for the mixture.

## 8.5 Discussion

### 8.5.1 Subhalide Complex ion Formation

If molecular ions such as  $(\text{Ni}_2)^{2+}$  were being formed, which had lifetimes long enough to be considered as distinct structural entities, then these would give rise to a peak in  $g_{\text{NiNi}}(r)$  with a well defined interatomic separation at a closer distance than that found between the  $\text{Ni}^{2+}$  ions. No new structural features are observed in  $g_{\text{NiNi}}(r)$ , indeed the reduction in ordering of the nickel species is at odds with what one would expect with the formation of complexes containing more than one nickel atom. If the dissolved nickel metal is not forming complex or molecular ions, then the question remains of what state the unassociated nickel ion is in. A number of possibilities will now be discussed.

### 8.5.2 Non Complex-Forming Subhalide Ions

A study of molten  $\text{NiCl}_2 + \text{Ni}$  has been carried out by Johnson et. al. (1958), who observe a freezing point depression for the salt upon addition of nickel metal. From their measurements and the calculated enthalpy of fusion, they infer that the univalent nickel ion is formed according to the equation  $\text{Ni} + \text{Ni}^{2+} \longrightarrow 2\text{Ni}^+$ . Although nickel does not normally exist in this oxidation state, it has been observed

in some complexes in aqueous solutions. Their data is not unambiguous, since only small negative deviations from Raoult's law were observed, and they do not rule out the possibility of nickel existing in solution as atoms.

Considering the possibility of univalent nickel ions. If  $\text{Ni}^+$  ions exist and are occupying existing tetrahedral sites within the anion structure of  $\text{NiBr}_2$ , then a broadening of the main Ni-Br peak in  $g(r)$  should be observed, due to the larger size of this ion. The observed interionic distance between nickel and bromide ions is 7% less in pure  $\text{NiBr}_2$  than the sum of the ionic radii given by Pauling (1960) for  $\text{Ni}^{2+}$  and  $\text{Br}^-$  - a typical value for molten salts. Although ion size data is not available for  $\text{Ni}^+$ , one would expect the radius to be markedly greater than the value of  $0.72\text{\AA}$  for the  $\text{Ni}^{2+}$  ion, whose 4s shell has been emptied. No such broadening is observed, but the trough following this peak is filled in.

If nickel atoms were present in the melt, then one would expect to see a Ni-Br distance of  $3.1\text{-}3.2\text{\AA}$  from the atomic and ionic radii. No peak is observed in this region, but the trough following the main peak is filled in over the region  $3.0\text{-}4.3\text{\AA}$ . The Br-Br separation associated with such an expansion of the tetrahedral structure would be in the region of  $4.9\text{-}5.2\text{\AA}$ , but no increase in  $g_{\text{BrBr}}(r)$  is observed in this region, although a distorted tetrahedron will give rise to a lower value of  $\bar{r}_{--}$ .

In summary, there is no clear evidence that either nickel atoms or  $\text{Ni}^+$  ions are present within the solution.

### 8.5.3 Double Ionisation

Another possible dissolution process for the excess nickel is the formation of doubly charged nickel cations according to the equation  $\text{Ni} \longrightarrow \text{Ni}^{2+} + 2e^-$ . The lack of substantial change observed for the Ni-Br and Br-Br partials suggests that the excess nickel is occupying similar sites within the anion structure to the nickel already present and is, therefore, of the same size.

Such a dissolution results in dissociated electrons, which will exist in extended states or be localised in shallow traps and therefore be relatively mobile. Thus

metallic behaviour is imparted to the solution by the dissolved metal and the solution belongs to the first 'metallic solution' category. As pointed out by Durham and Greenwood (1976), the effect upon the interionic potentials of the presence of conduction electrons is one of screening.

Copestake and Evans (1982), using a restricted primitive model, obtained structure factors using HNC and MSA calculations based on Coulombic and screened Coulombic (Yukawa) potentials. The short range screened potential gave similar results to the stronger and longer range Coulomb potential, indicating that the gross structural features of liquids with strong attractive forces between unlike species are insensitive to the exact form of the potentials present. They observed little difference in  $S_{+-}(Q)$  beyond the first peak, but the dip in  $S_{+-}(Q)$  was reduced in depth for the screened potential, indicating a reduction in the level of charge ordering. Also, the first peak in their  $S_{++}(Q)$  was reduced in height, with a corresponding loss of structural ordering in real space, although this was not pronounced. The changes obtained by Copestake and Evans resulting from the application of screened Coulombic interactions, are qualitatively the same as those observed here for the  $S_{NiBr}(Q)$  and  $S_{NiNi}(Q)$ . This supports the possibility that mobile electrons are present in the  $NiBr_2 + Ni$  mixture.

The model used by Copestake and Evans assumed equally sized cations and anions having the same charge. This is clearly not the case here, where the cation is doubly charged and has a diameter of  $1.38\text{\AA}$  with a nearest neighbour separation of  $\bar{r}_{++} = 3.9\text{-}4.3\text{\AA}$ , and the singly charged anion has an ionic diameter of  $3.9\text{\AA}$  and a nearest neighbour separation of  $\bar{r}_{--} \approx 3.9\text{\AA}$ . Thus one would expect the Ni-Ni interactions to be modified by screening of the Coulombic repulsions, whereas the close packed bromide structure, being determined by short range overlap forces between the bromide ions, would be largely unperturbed.

Because of the already structureless form of  $g_{NiNi}(r)$  for pure  $NiI_2$  and the small contribution that this term makes to the reduced structure factor  $F'(Q)$  of figure 8.4, changes in this structure of the kind seen for  $NiBr_2+Ni$  (i.e. loss of structural ordering for the nickel species) would not be

expected to be visible.

#### 8.5.4 Intermediate Range Order

The origin of the pre-peak observed for molten salts with relatively small divalent cations was discussed in chapter 6, where the evidence for the importance of bond directionality in producing the ordering between tetrahedra was discussed. The mutual Coulomb repulsions between the doubly charged cations appears to be less important in producing inter-tetrahedral structural ordering.

The pre-peak observed in  $S_{\text{NiNi}}(Q)$  for the  $\text{NiBr}_2+\text{Ni}$  data presented here, when compared with that observed for the pure salt, is seen to be less sensitive to the addition of excess nickel than the rest of the Ni-Ni structural ordering. This is consistent with the view that its origin is in angle dependent bonding between cations and polarised anions, rather than Coulomb repulsions between the cations themselves.

The pre-peak observed for the  $\text{NiI}_2+\text{Ni}$  experiment is unchanged upon addition of excess nickel to this salt.

#### 8.6 Summary

From the results presented for the  $\text{NiI}_2+\text{Ni}$  and  $\text{NiBr}_2+\text{Ni}$  solutions, the close packed anion structure is seen to be unperturbed by the addition of excess nickel metal. The partial structure factors and distribution functions derived for the  $\text{NiBr}_2+\text{Ni}$  mixture indicate that the additional nickel is occupying similar sites within the anion structure to that already present, and that subhalide complexes involving many nickel atoms are not formed.

The results are consistent with ionisation according to the equation  $\text{Ni} \longrightarrow \text{Ni}^{2+} + 2\text{e}^-$ , where the screening of Coulombic interactions due to mobile electrons is substantially reducing the Ni-Ni interionic ordering, while leaving the close packed Br-Br structure and intermediate range inter-tetrahedral ordering largely unperturbed.

The presence of  $\text{Ni}^+$  ions or neutral Ni atoms, occupying similar sites within the liquid, cannot be ruled out on the

basis of structural information alone. Electrical conductivity measurements for Ni-Ni halide solutions should decide which category ('metallic' or 'subhalide') the solutions belong to and whether mobile electrons are present in the melt.

#### 8.6.1 Structural Models

As an aid to visualizing the structure of these tetrahedrally coordinated molten salts, it is useful to consider a solid state counterpart structure which may exist in the melt over short ranges. The high halide ion coordination number obtained by integration of  $r^2 g_{XX}(r)$  to the first minimum ( 11 for  $\text{NiBr}_2$ , 13.8 for  $\text{NiCl}_2$  and 13 for  $\text{NiI}_2$ ) means that there are only two appropriate solid state structures: the hexagonal close packed and the face centred cubic. Both of these structures have coordination numbers of 12, but it must be remembered that with the relaxing of symmetry constraints for the liquid higher mean coordination numbers may be possible.

Figure 8.12 shows a hcp array of anions. Into this array are placed cations in sites which are tetrahedrally coordinated by anions and which share their corners with other tetrahedra. It is this corner sharing arrangement which gives equivalence of M-M and X-X nearest neighbour distances. It is also possible, in both hcp and fcc structures, to have edge and face sharing tetrahedra.

Table 8.1. The isotopic compositions and nickel concentrations of the nickel iodide samples, and the parameters used for the data analysis.

	Natural NiI <sub>2</sub> + Ni	'Zero' NiI <sub>2</sub> + Ni
mol% of added Ni	8.9±0.3	8.27±0.10
% of natural Ni	35.26	1.81
% of <sup>60</sup> Ni	0	23.54
% of <sup>62</sup> Ni	0	9.76
% of iodine	64.74	64.88
Coh. scattering lengths (10 <sup>-12</sup> cm)*		
$\bar{b}_{Ni}$	1.03	0
$\bar{b}_I$	0.528	0.528
Scattering cross-sections (barns)*		
$\sigma_{inc}$	2.56	2.31
$\sigma_{abs}$	5.59	6.22
Sample radius (mm)	4.23	4.23
Density (gcm <sup>-3</sup> )	4.37	

\* From Sears (1984).

Table 8.2. The isotopic compositions and nickel concentrations of the nickel bromide samples, and the parameters used for the data analysis.

	Nat.NiBr <sub>2</sub> +Ni	'Zero'NiBr <sub>2</sub> +Ni	<sup>62</sup> NiBr <sub>2</sub> +Ni
mol% of added Ni	9.01±0.10	9.01±0.10	8.97±0.10
% of natural Ni	35.46	1.84	1.17
% of <sup>60</sup> Ni	0	23.72	0
% of <sup>62</sup> Ni	0	9.89	34.28
% of bromine	64.54	64.54	64.55
Coh. scattering lengths(10 <sup>-12</sup> cm)*			
$\bar{b}_{Ni}$	1.03	0	-0.807
$\bar{b}_{Br}$	0.679	0.679	0.679
Scattering cross-sections (barns)*			
$\sigma_{inc}$	2.25	2.9	6.98
$\sigma_{abs}$	2.38	2.62	3.74
Sample radius(mm)	3.85	3.84	3.84
Density (gcm <sup>-3</sup> )	3.88		

\* From Sears (1984).

Table 8.3. Structural parameters in real and reciprocal space for molten NiBr<sub>2</sub> + 9%Ni and pure NiBr<sub>2</sub>.

	NiBr <sub>2</sub> + Ni	NiBr <sub>2</sub>
<u>Ni-Br Partial</u>		
Main peak position in $r^2g(r)$	2.45±0.03	2.45±0.03
Main peak position in $g(r)$	2.42±0.02	2.42±0.03
Peak height	≥5.57	≥5.76
Peak width	≤0.41	≤0.41
Depth of first trough	0.55±0.03	0.44±0.04
Coordination number:		
Int. to 1 <sup>st</sup> min. in $r^2g(r)$	4.55±0.15	4.62±0.15
Int. to 1 <sup>st</sup> min. in $g(r)$	4.74±0.15	4.88±0.15
$r^2g(r)$ symmetric method	3.43±0.15	3.63±0.1
Reciprocal space:		
Position of 'Coulomb dip' (Å <sup>-1</sup> )	1.90±0.02	1.95±0.02
Depth of dip	-0.68±0.02	-0.78±0.06
<u>Br-Br Partial</u>		
Main peak position in $r^2g(r)$	3.91±0.03	3.92±0.05
Main peak position in $g(r)$	3.72±0.02	3.69±0.04
Peak height	1.91±0.02	1.85±0.02
Coordination number:		
Int. to 1 <sup>st</sup> min. in $r^2g(r)$	11.7±0.2	11.0±0.3
Int. to 1 <sup>st</sup> min. in $g(r)$	14.5±0.3	11.8±1.2
$r^2g(r)$ symmetric method	8.6±0.4	8.6±0.7
$\bar{r}_{--}/\bar{r}_{+-}$	1.60±0.02	1.60±0.03
<u>Ni-Ni Partial</u>		
Main peak position in $r^2g(r)$	4.3±0.1	3.9±0.2
Main peak position in $g(r)$	3.9±0.1	3.7±0.2
Peak height	1.3±0.1	1.7±0.1
Depth of first trough	0.78±0.06	0.69±0.06
Coordination number:		
Int. to 1 <sup>st</sup> min. in $r^2g(r)$	4.6±0.5	5.3±1.0
Int. to 1 <sup>st</sup> min. in $g(r)$	6.5±0.4	6.3±0.5
$r^2g(r)$ symmetric method	6.9±0.5	4.2±1.2
Reciprocal space:		
Main peak posit'n in $S(Q)$ (Å <sup>-1</sup> )	1.95±0.02	1.99±0.02
Main peak height	1.7±0.1	2.3±0.2
Pre-peak position (Å <sup>-1</sup> )	0.95±0.02	0.98±0.02
Pre-peak height	0.89±0.07	0.95±0.1

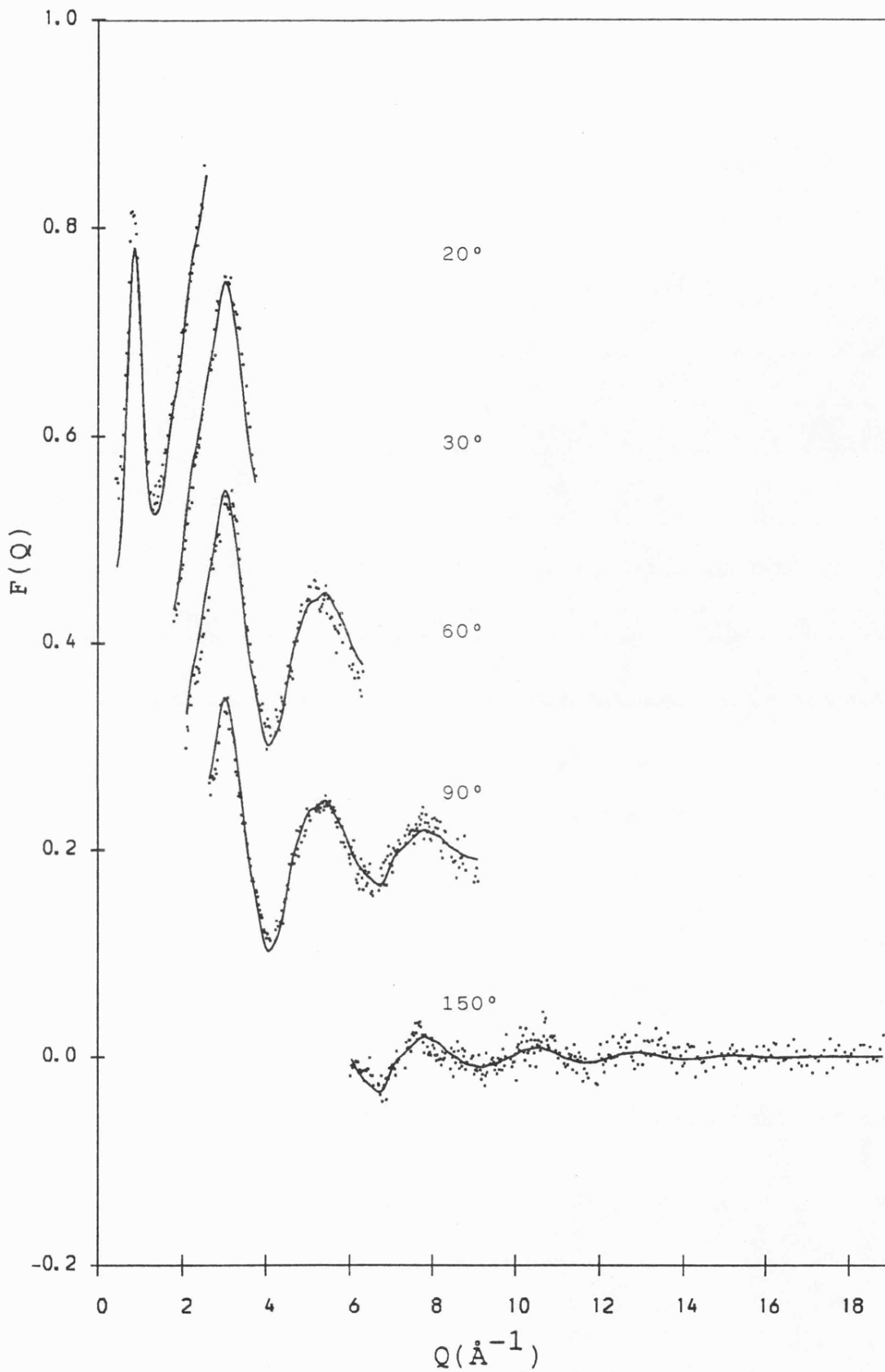


Figure 8.1. The total structure factor of natural  $\text{NiI}_2$  + 9 mol% Ni.  $F(Q)$  is shown for each detector over the range which contributes to the final  $F(Q)$  and each successive curve is displaced by 0.2. The full line is the back-transform of the smoothed  $G(r)$ .

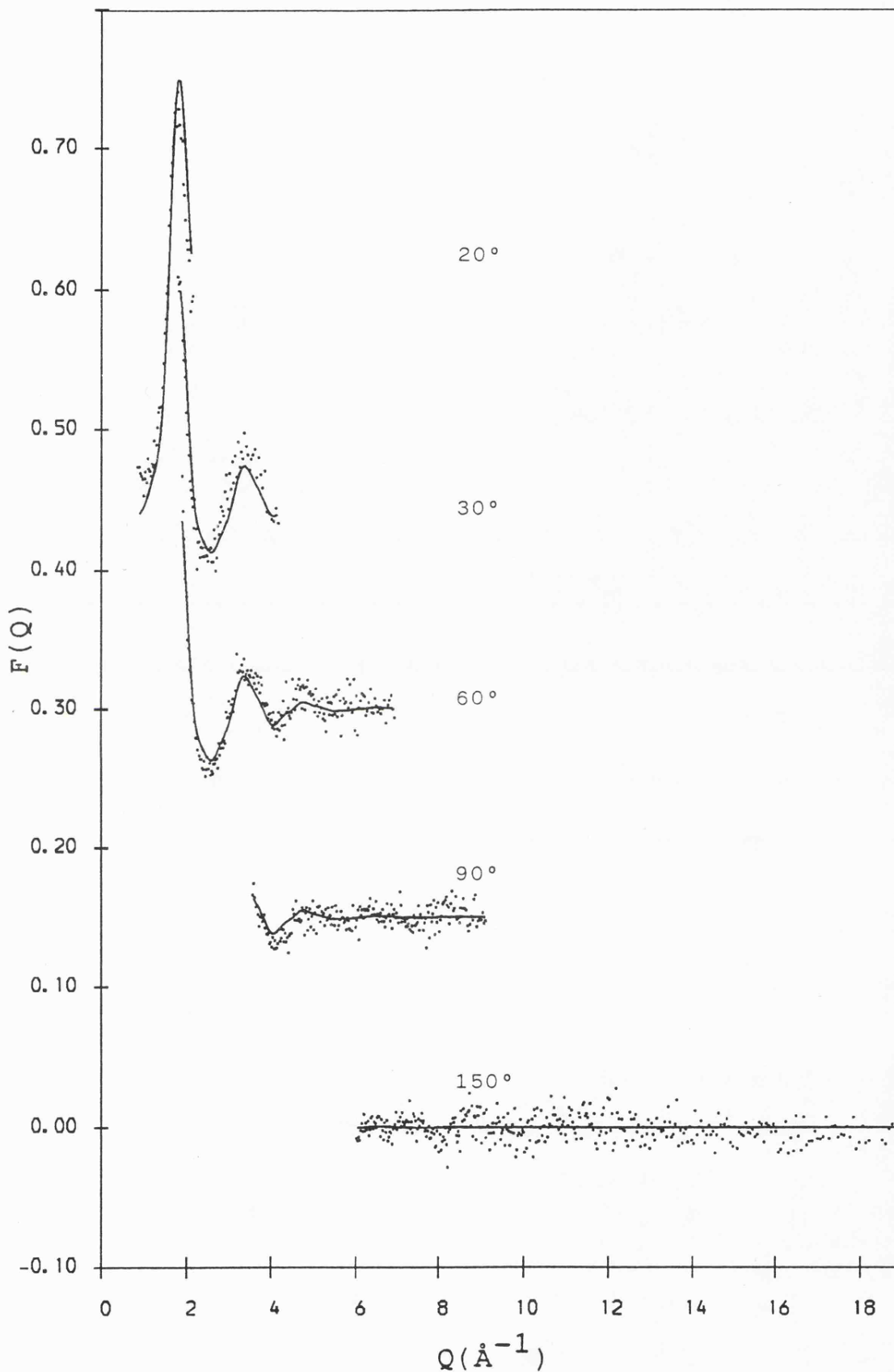


Figure 8.2. The total structure factor of 'zero'  $\text{NiI}_2 + 9 \text{ mol\% Ni}$ , shown separately for each scattering angle. The full curve is from the smoothed  $g_{\text{II}}(r)$  and successive curves are displaced by 0.15.

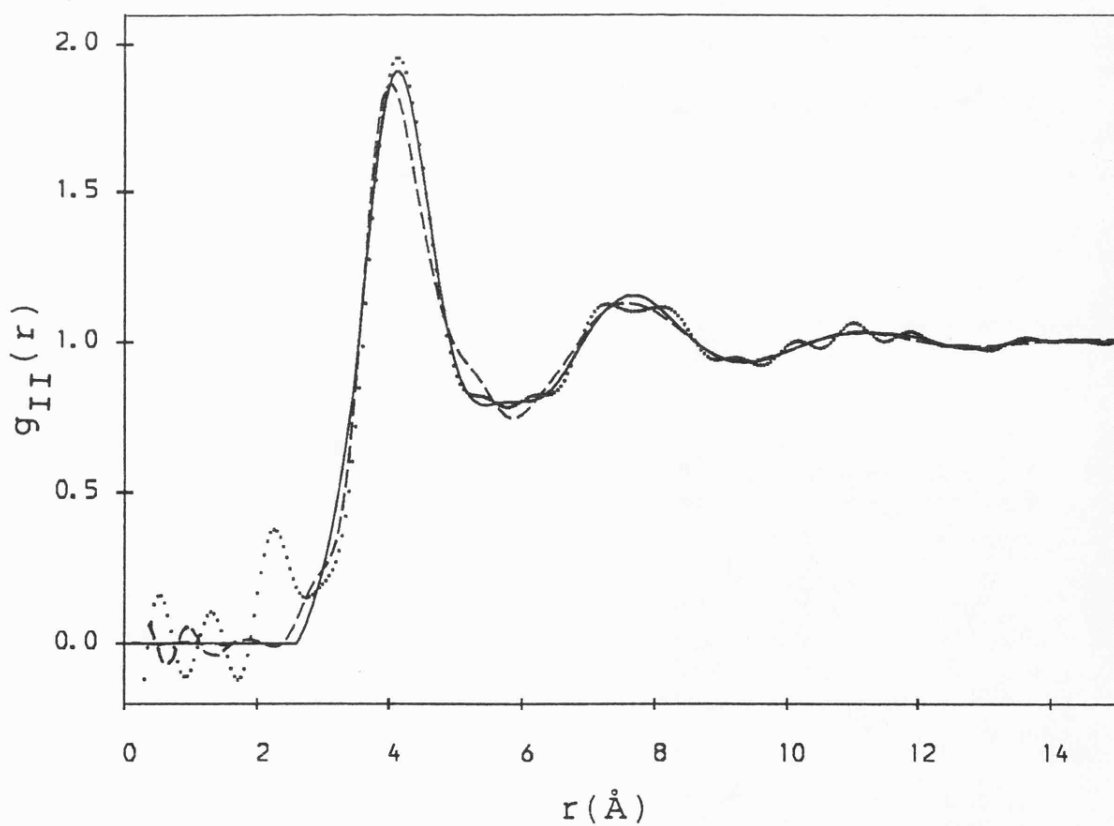
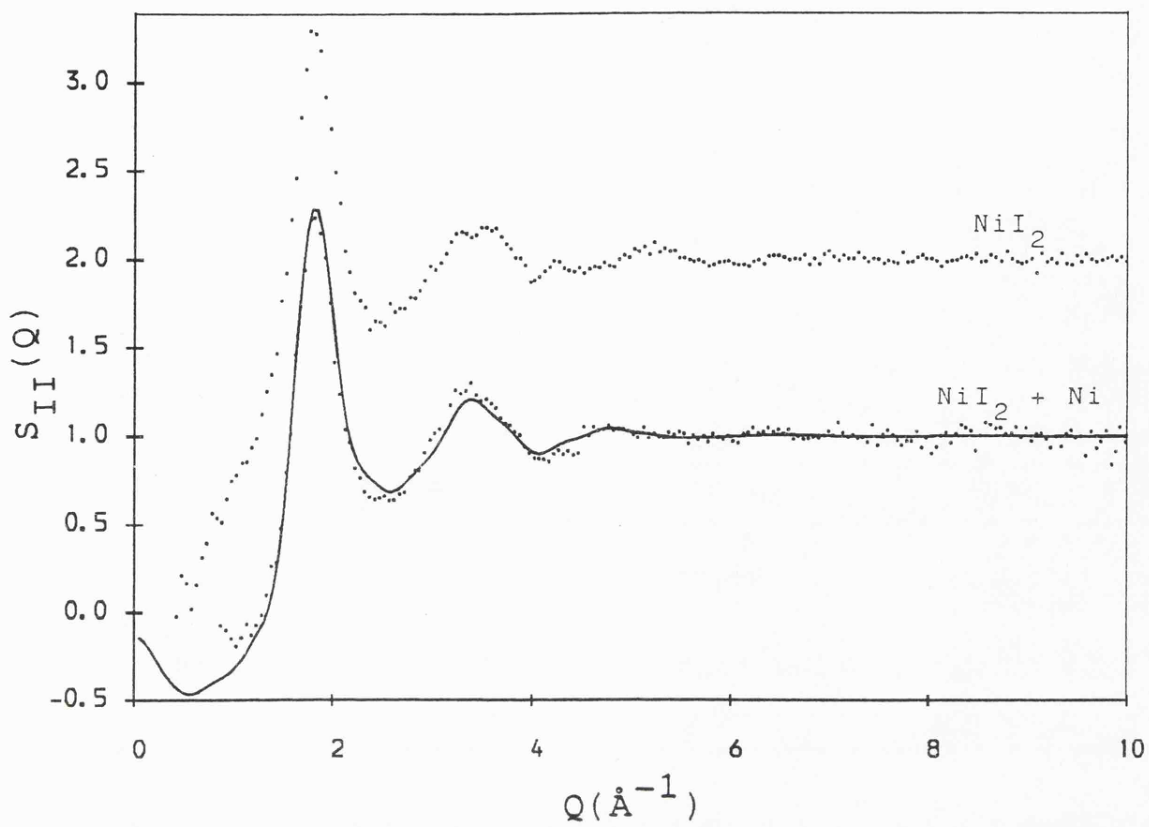


Figure 8.3. Top- The anion-anion partial structure factor for pure  $\text{NiI}_2$  and  $\text{NiI}_2 + 9\text{mol}\% \text{Ni}$ . Bottom-  $g_{\text{II}}(r)$  for pure  $\text{NiI}_2$  (dots) and  $\text{NiI}_2 + 9\text{mol}\% \text{Ni}$  (broken line). The full line is a smooth fit to  $g_{\text{II}}(r)$  for the solution.

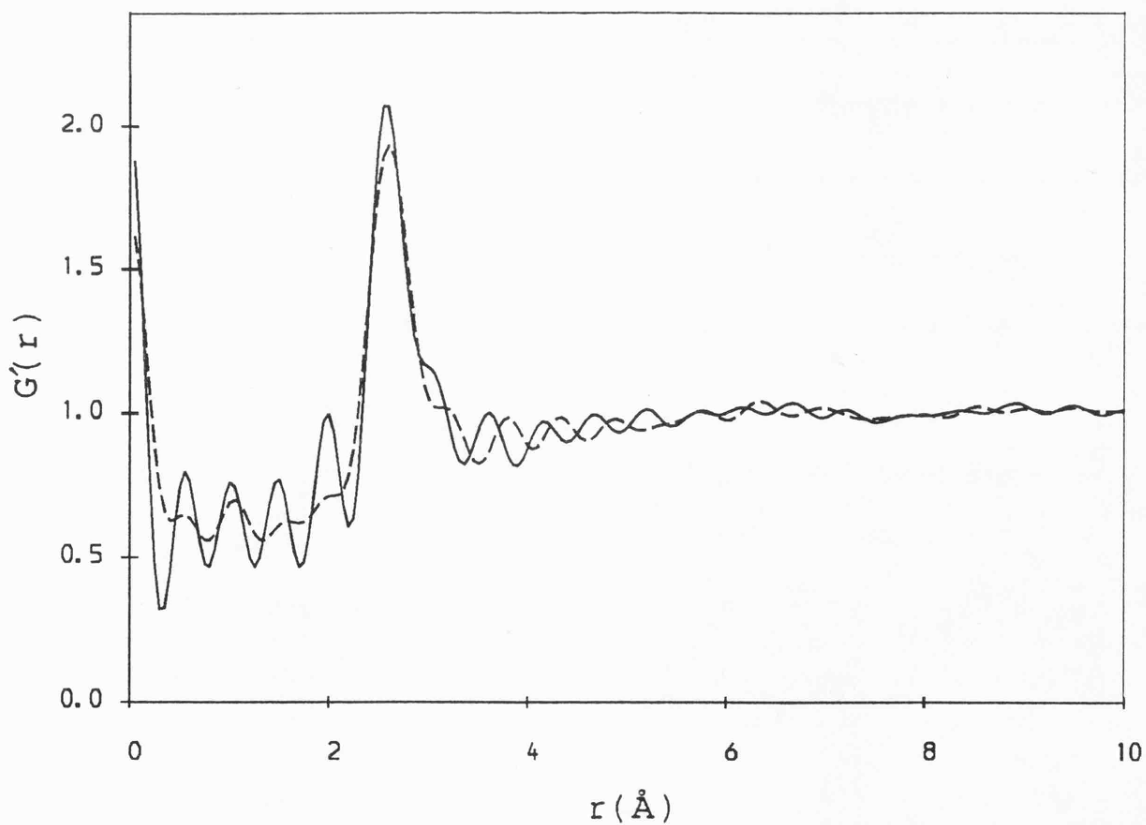
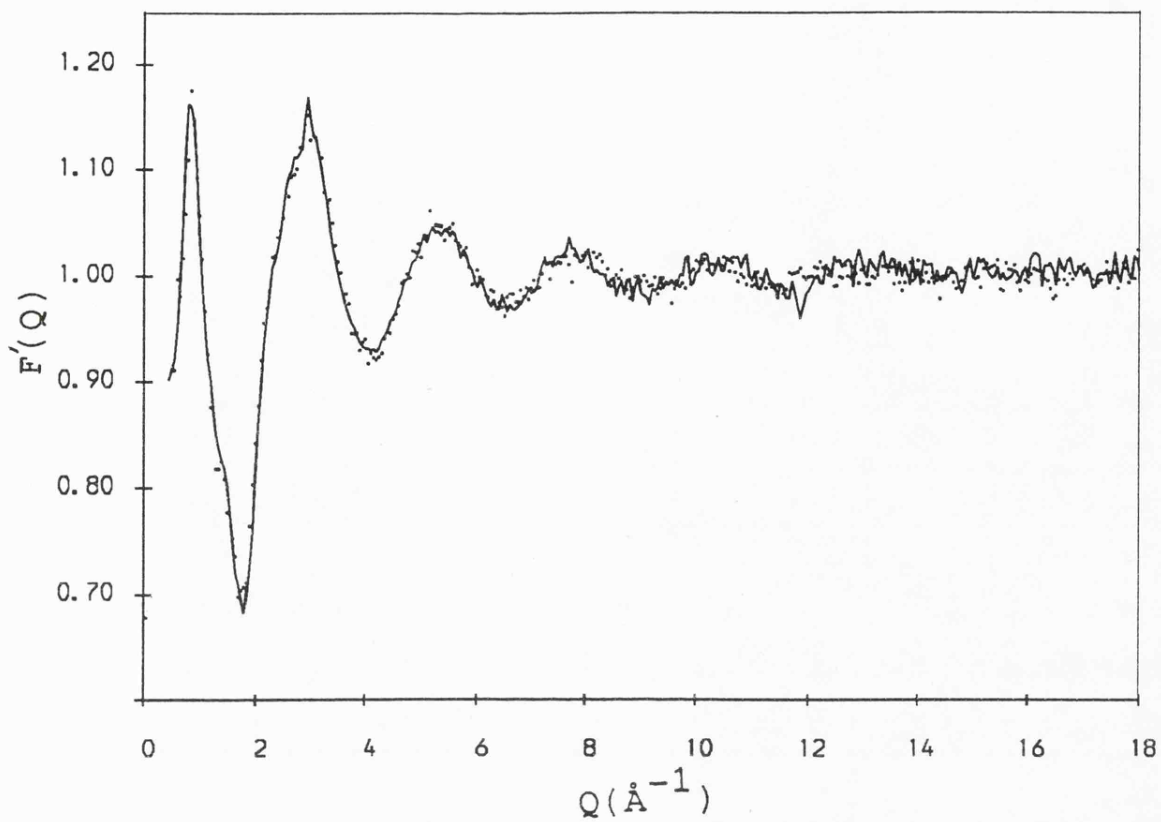


Figure 8.4. Top-  $F'(Q) (=1+0.133(S_{\text{NiNi}}-1)+0.249(S_{\text{NiI}}-1))$  for pure  $\text{NiI}_2$  (dots) and  $\text{NiI}_2 + 9\text{mol\% Ni}$  (full). Bottom-  $G'(r)$  for pure  $\text{NiI}_2$  (broken line) and  $\text{NiI}_2 + 9\text{mol\% Ni}$  (full).

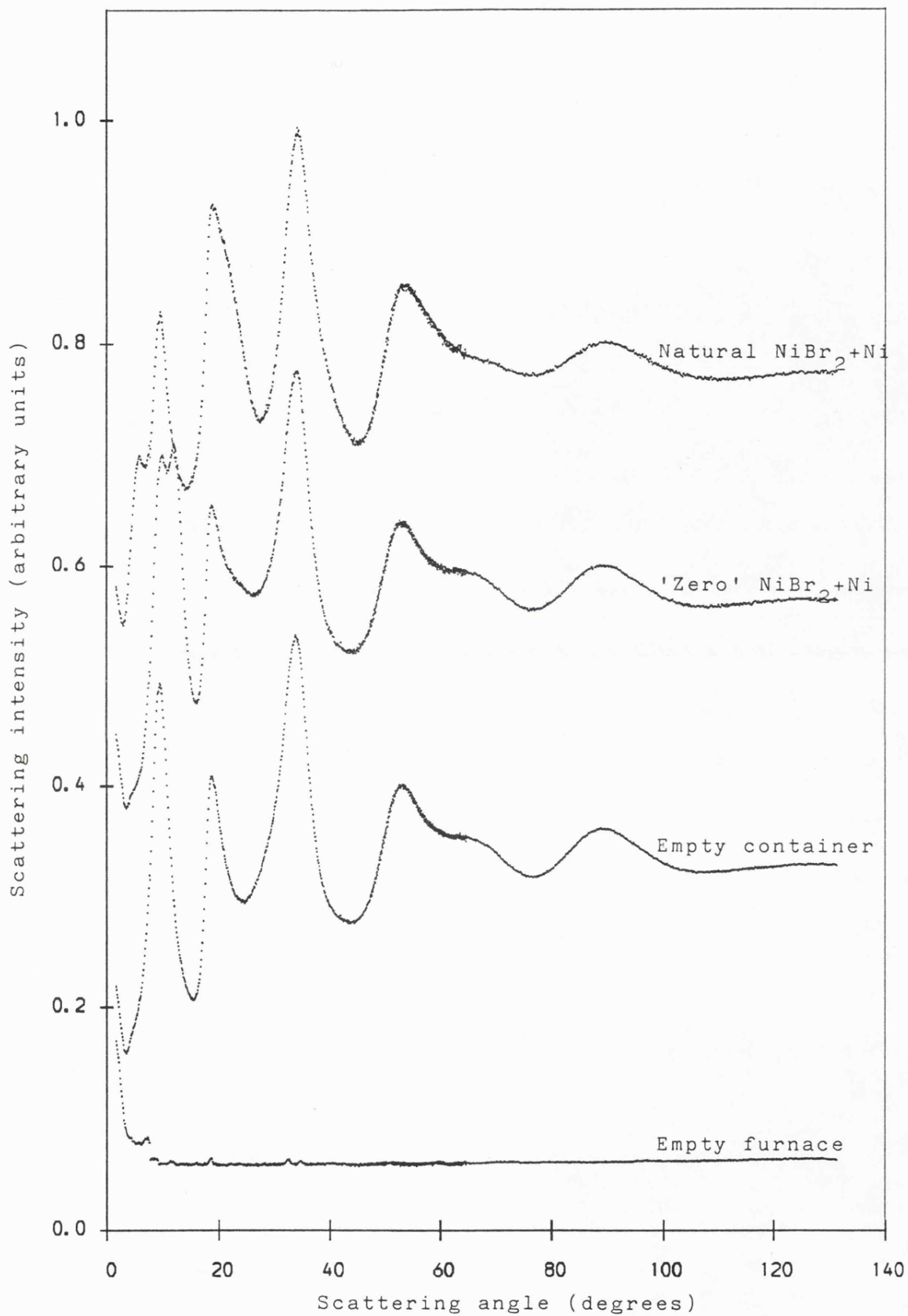


Figure 8.5. Raw data for two isotopes of molten  $\text{NiBr}_2 + 9$  molar % Ni, an empty container and the furnace, measured on D4B. The data has been normalised to the scattering from a vanadium bar in order to include both counter banks.

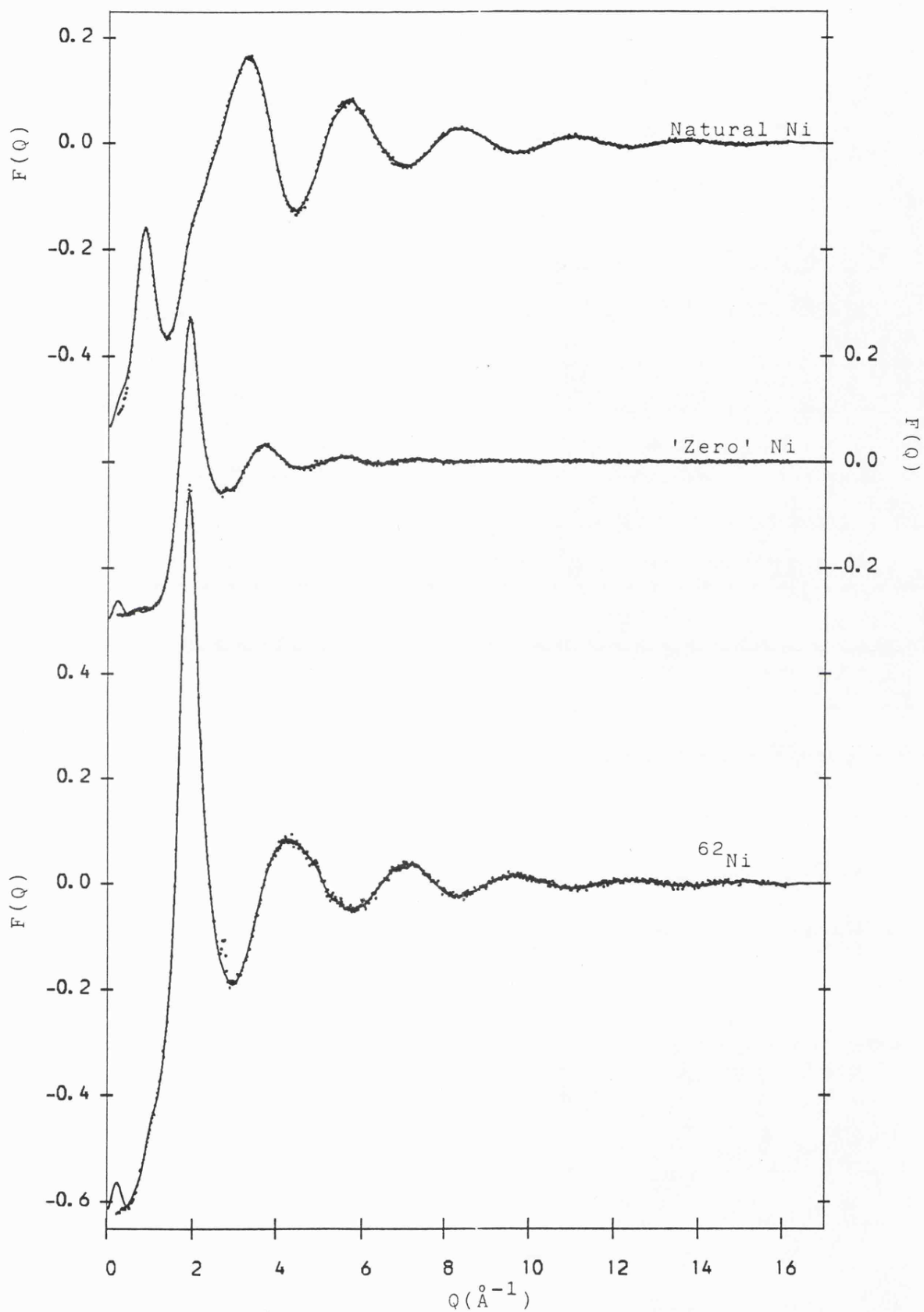


Figure 8.6. The total structure factors of the three isotopic samples of  $\text{NiBr}_2 + 9\% \text{Ni}$ . The full lines are obtained from the back-transforms of the final partial distribution functions.

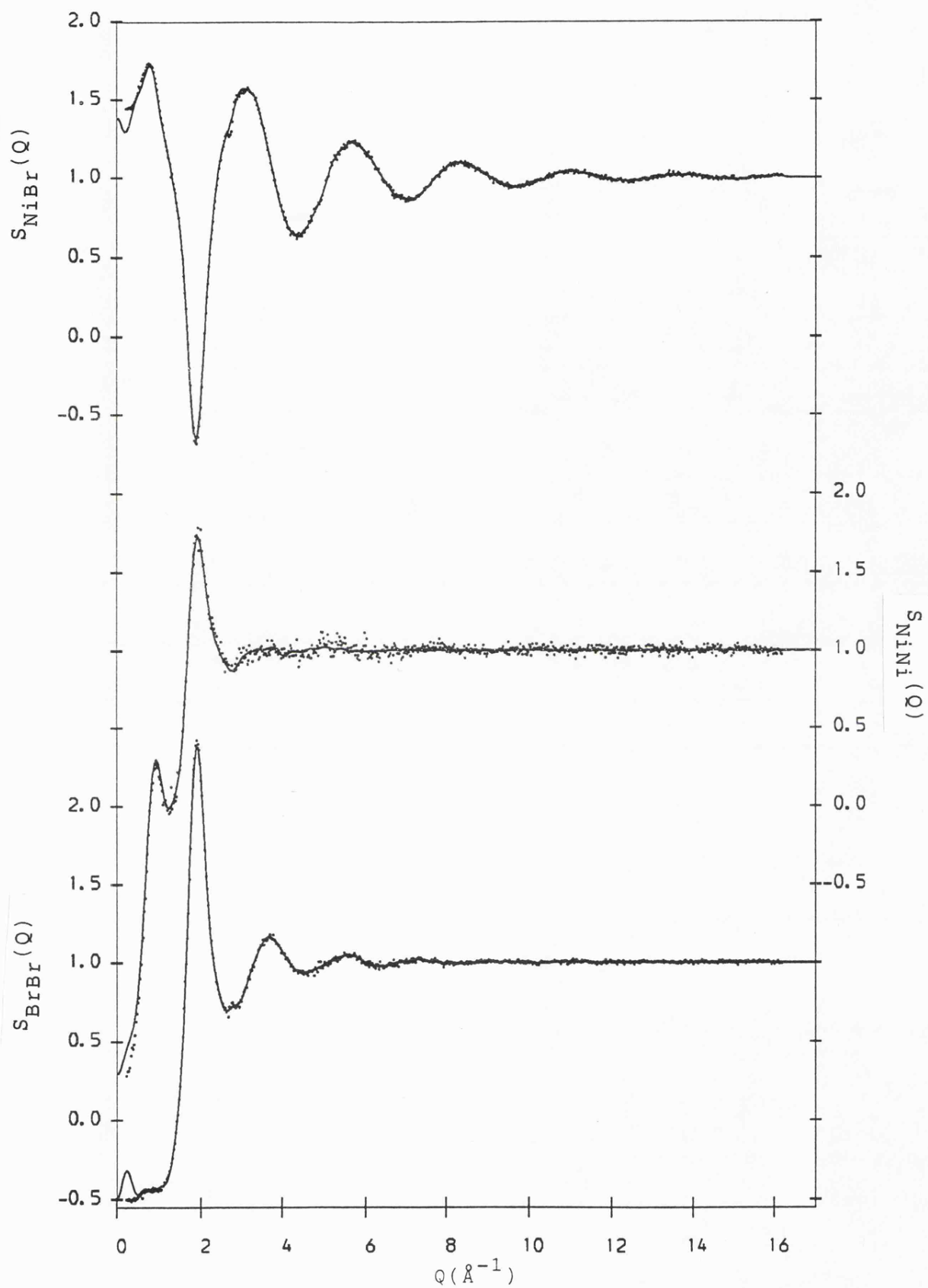


Figure 8.7. The three partial structure factors for  $\text{NiBr}_2 + 9\% \text{ Ni}$ . The full lines are the back-transforms of the final  $g(r)$ 's.

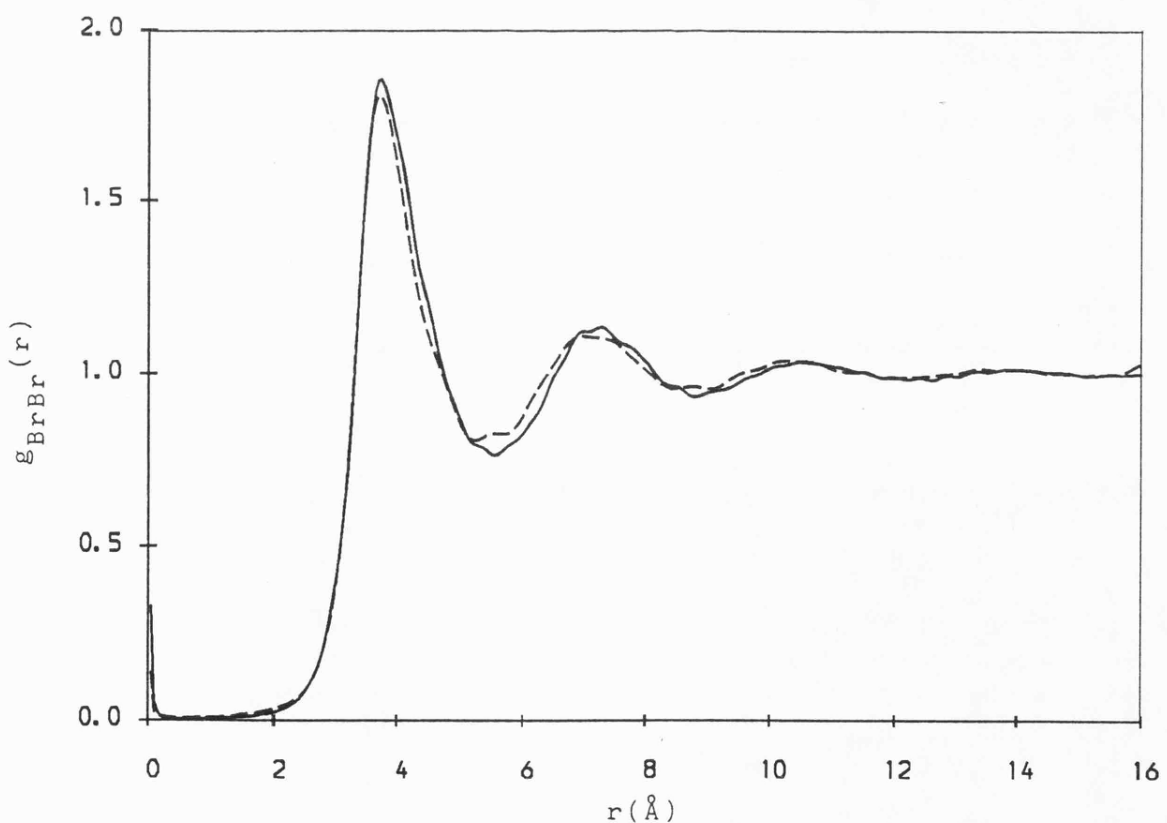
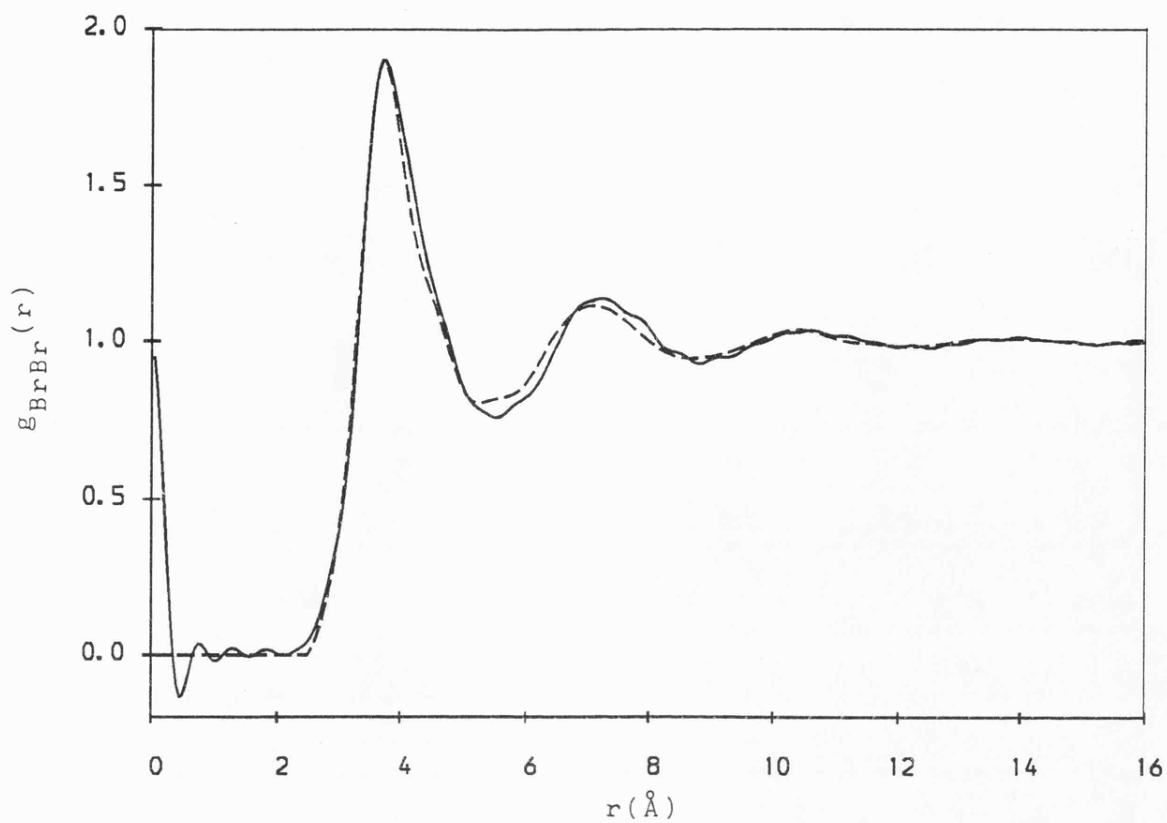


Figure 8.8. The Br-Br partial  $g(r)$ . Top- smoothed function for the pure salt (broken line) compared with a raw transform for  $\text{NiBr}_2 + 9\% \text{ Ni}$  (full line). Bottom- maximum entropy solutions to fit  $S_{\text{BrBr}}(Q)$  for the pure salt (broken line) and the mixture (full line). A default level of 1.0 was used.

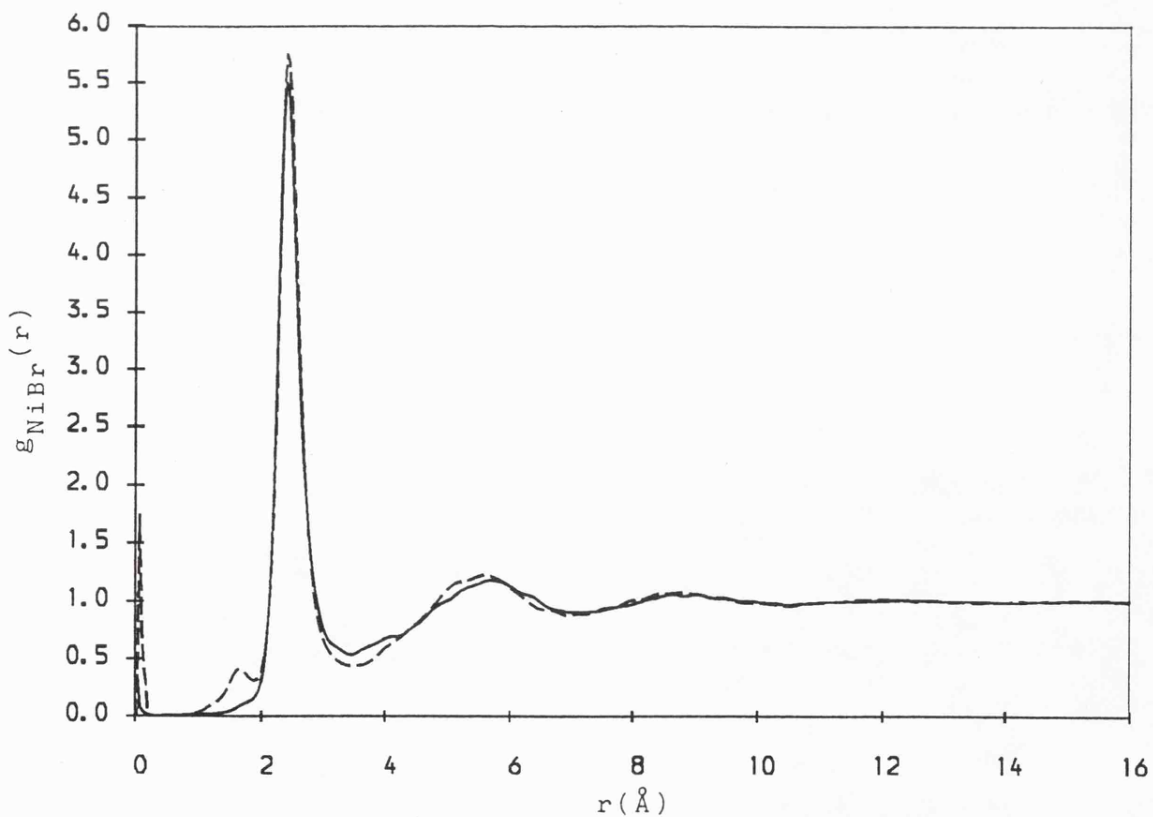
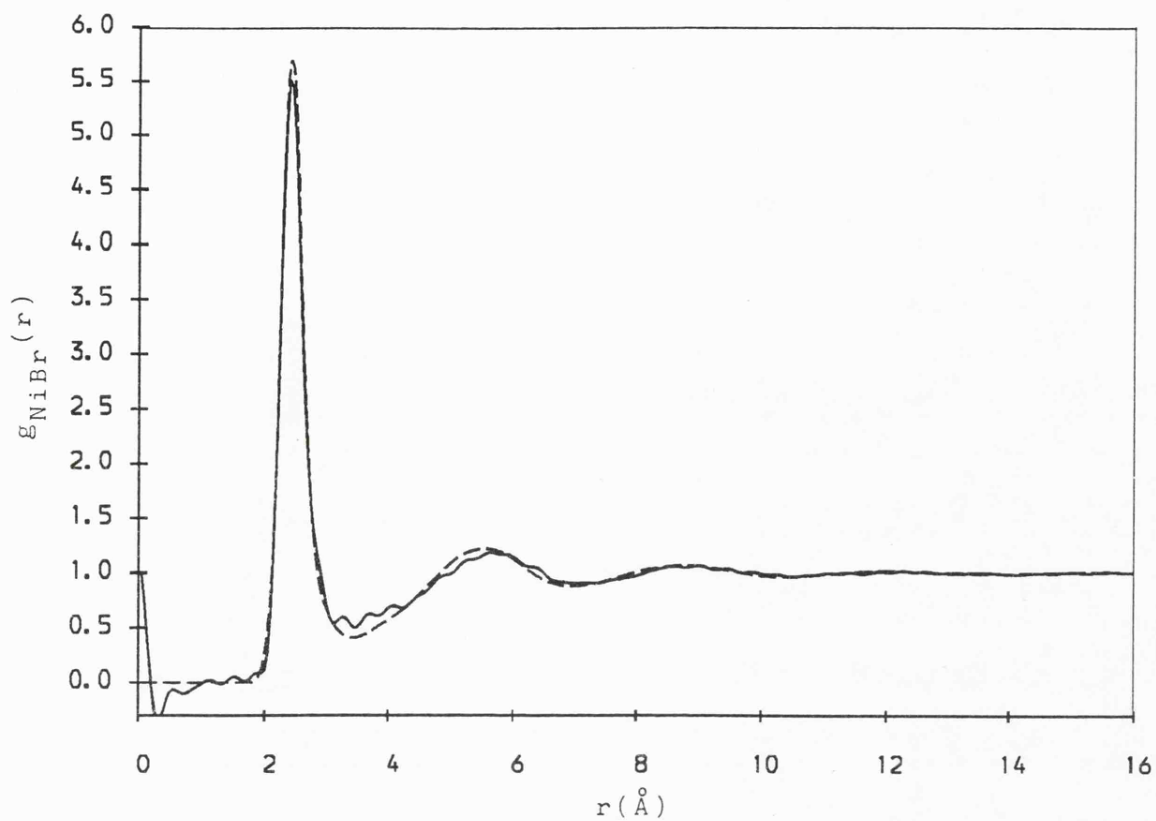


Figure 8.9. The Ni-Br partial  $g(r)$ . Top- comparison of smoothed function for the pure salt (broken line) with a raw transform for  $\text{NiBr}_2 + 9\% \text{ Ni}$ . Bottom- maximum entropy solutions for the pure salt (broken line) and mixture (full line). A default level of 1.0 was used.

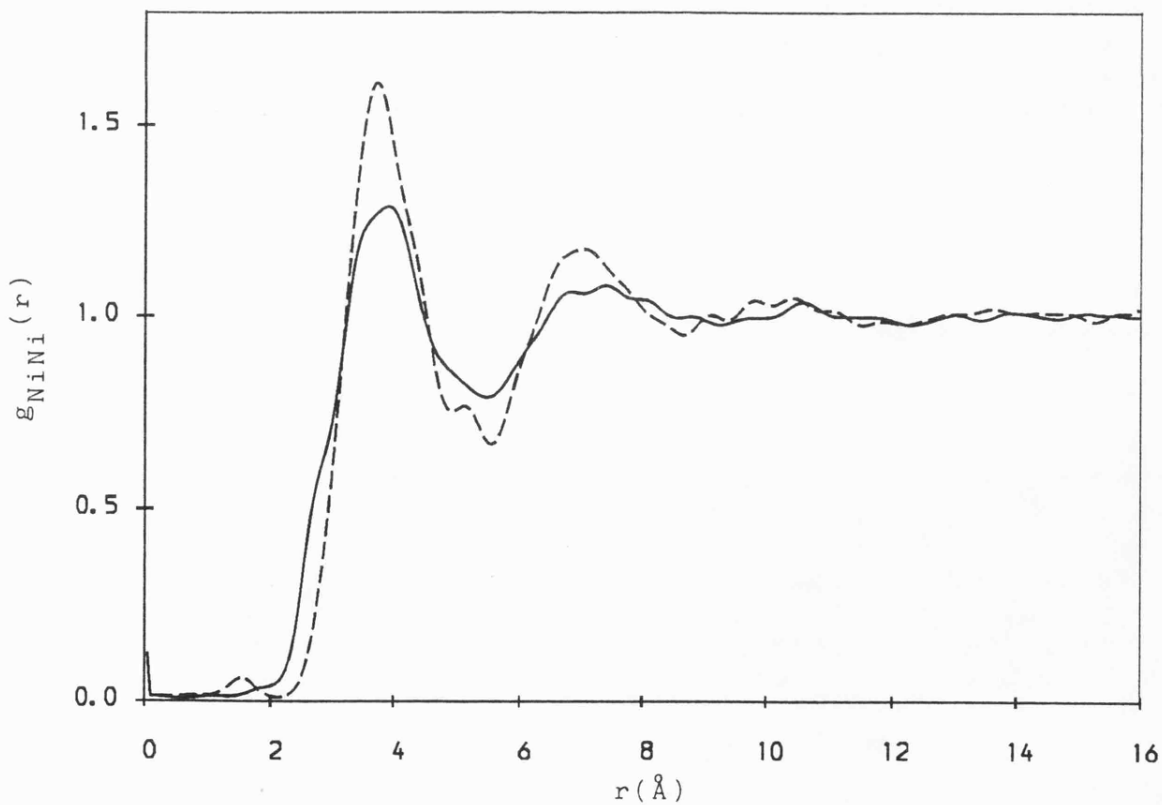
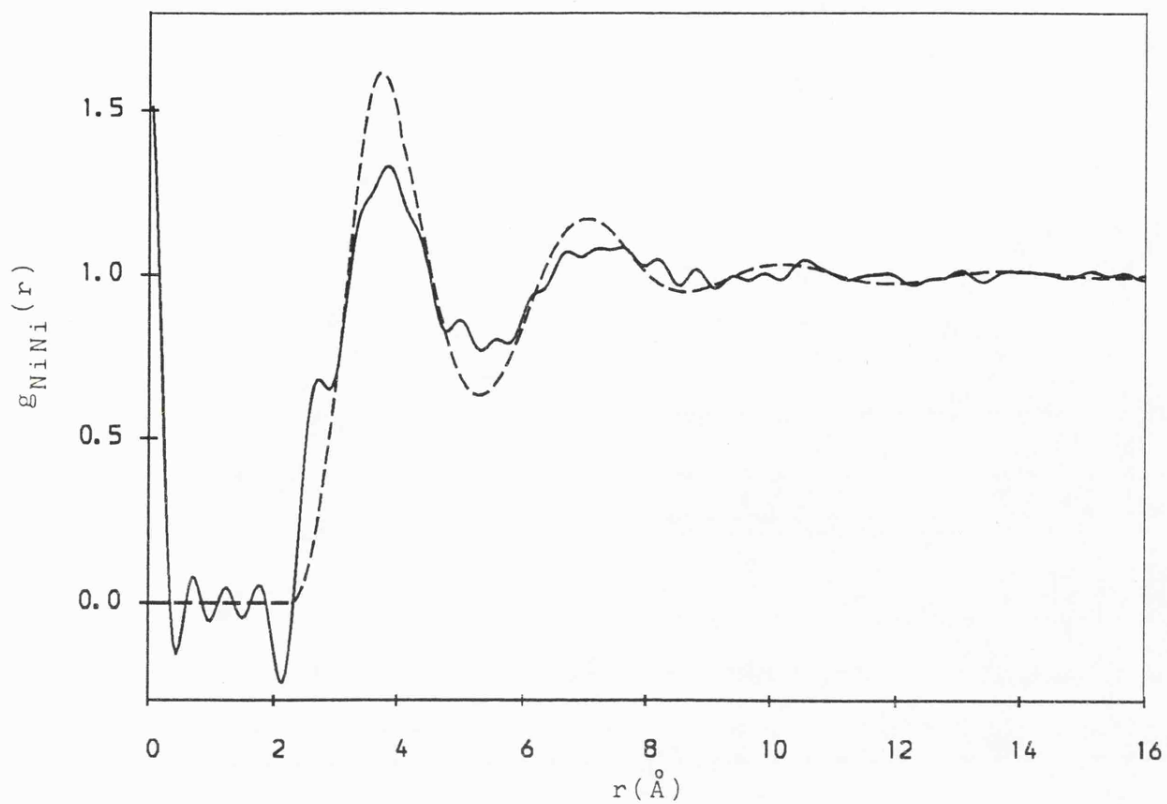


Figure 8.10. The Ni-Ni partial  $g(r)$ . Top- comparison of smoothed function for the pure salt (broken line) with a raw transform for  $\text{NiBr}_2 + 9\% \text{ Ni}$ . Bottom- maximum entropy solutions for the pure salt (broken line) and the mixture (full line). A default level of 1.0 was used.

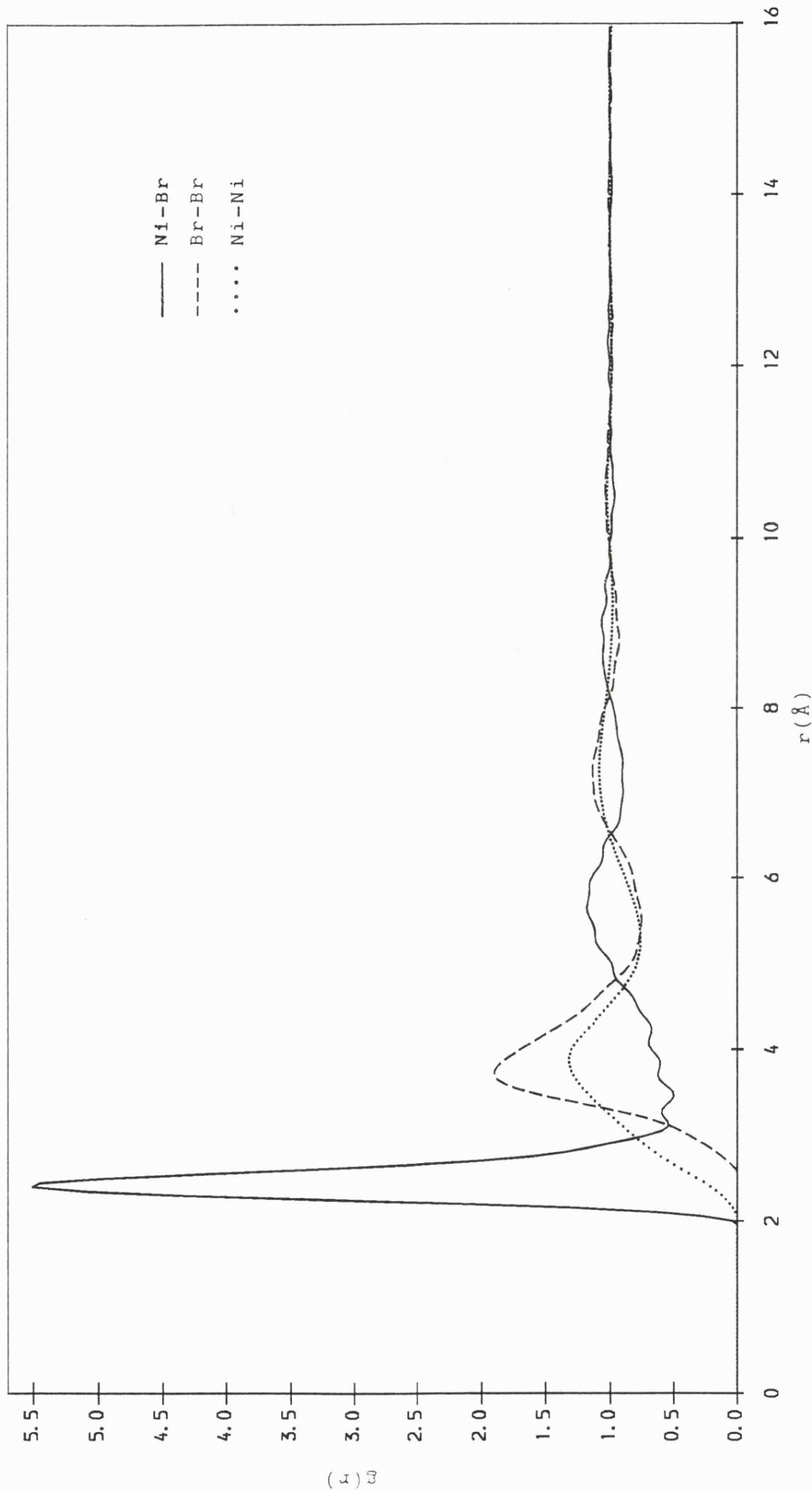


Figure 8.11. The final  $g(r)$ 's for molten  $\text{NiBr}_2 + 9\% \text{ Ni}$ , from which the back-transforms were obtained.

## CHAPTER 9

### CONCLUSIONS

#### 9.1 Introduction

The work presented in this thesis has continued the programme of study into the structure of molten salts, by using pulsed neutron diffraction to investigate the structure of molten zinc halides. The results have been discussed with reference to previous diffraction measurements on other molten 2:1 salts, in particular the nickel halide series. In addition, the work on pure molten salts has been supplemented by a pulsed neutron diffraction investigation into the structural modification of zinc chloride by the addition of 'structure breaking' potassium chloride. An investigation into structural modification by the addition of excess metal has also been carried out, using neutron diffraction on solutions of nickel in two of its molten halides. Both pulsed and steady-state diffraction techniques have been used and information on the partial structure factors has been obtained by using isotopic substitution of nickel. The results have been compared with those of previous investigations into the structure of the pure molten salts. The maximum entropy method of obtaining probability distributions has been applied to the problem of the analysis of structure factor data. This method has proved useful in the interpretation of some of the data presented in this thesis. In this chapter, the results of these studies are summarized, and some suggestions for further work are made.

#### 9.2 Summary of Results and Suggestions for Further Work

##### 9.2.1 The Structure of Molten Zinc Halides

The structure of molten zinc halides has been investigated and a local tetrahedral arrangement of anions around each cation has been found for all three halides studied. The use of a pulsed neutron source to obtain the structure factors has revealed extremely well defined first shell structures for molten  $\text{ZnCl}_2$  and  $\text{ZnBr}_2$  near their melting points.  $\text{ZnI}_2$  however, possesses a more relaxed

nearest neighbour cation-anion structure, due perhaps to greater mobility of the  $\text{Zn}^{2+}$  ion within its nearest neighbour 'cage'. An inelastic neutron scattering study of molten  $\text{ZnI}_2$  would provide information on ionic diffusion within this liquid. In a similar study of molten and glassy  $\text{ZnCl}_2$  on IN6 by Fairbanks (1987), the increase in ionic diffusion between 368°C and 568°C was clearly discernible from the quasielastic scattering. Also observed were modes associated with the bending and stretching motions expected from a set of  $\text{ZnCl}_4^{2-}$  tetrahedra. In the present study, the nearest neighbour anion-anion separation, as well as the cation-anion separation within each tetrahedral unit, was found to be proportional to the sum of the rigid ion sizes throughout this series of salts.

In addition to the short range structure, information on medium range structure was also obtained for this series. The pre-peak at  $Q \approx 1.0\text{\AA}^{-1}$ , commonly found for molten 2:1 salts with large ion size ratios, was also observed for all three halides studied. Indeed, the trend in magnitude of the pre-peak was that of increasing from  $\text{ZnCl}_2$  through the series to  $\text{ZnI}_2$ . This trend is consistent with previous observations of pre-peaks in molten 2:1 salts, and supports the argument that intermediate range ordering between cations has its origin in directional dependence of interionic forces associated with covalency. The structure of  $\text{ZnCl}_2$  has never been successfully simulated by theoretical modelling, although qualitative success has been achieved to some extent by the somewhat artificial method employed by Ballone et. al. (1986). There is a need for more theoretical studies of molten 2:1 salts in order to investigate the effects of ion polarizability in producing directional dependent forces and to see how this determines the structure. Such a study would have to take into account the distortion of the electronic shells of ions by the presence of a nearby polarizing ion, and the effect this has upon interionic forces. A computer simulation, in which the instantaneous positions of all of the ions are known, is therefore necessary for such a study. The deformation dipole polarizable ion model used by Gartrell-Mills and McGreevy (1988) has made a considerable improvement over the rigid ion simulation for molten  $\text{CsCl}$

(Locke et. al., 1985). This shows that some of the experimental structural observations for molten salts can indeed be explained by ion polarization. However, there has yet to be a polarizable ion simulation study for a molten 2:1 salt.

The real space periods corresponding to the positions of the pre-peaks for all of the three salts also scales with the sum of the two ion sizes. It has therefore been concluded that both the local tetrahedral structure around each cation and the medium range ordering between the zinc ions at the centre of occupied tetrahedra, remains basically the same throughout this series of halides. The observed changes are in the scale of the structure, the degree of intermediate range ordering and how well defined the nearest neighbour cation-anion separation is. It would be interesting to complete the series by studying the structure of molten zinc fluoride, which has an ion size ratio of 2.20 and a large electronegativity difference between the species of 2.4. If the origin of the pre-peak is in reduced ionicity, then one would not expect to observe a pre-peak for such a highly ionic compound. However, a pre-peak has been observed for all molten 2:1 salts studied to date which have an ion size ratio of greater than about 2.0. A study of molten  $\text{ZnF}_2$  should help to clarify which is the dominant factor in producing medium range ordering.

In addition to studying three zinc halides at temperatures near to their melting points, the total structure factor of  $\text{ZnCl}_2$  at  $600^\circ\text{C}$  was also determined. The pre-peak was seen to persist at this higher temperature and is, therefore, a proper feature of the liquid state. The same observation was made from a similar study of  $\text{NiI}_2$  at  $900^\circ\text{C}$ . In the main, there was little structural change at this elevated temperature, with peaks being thermally broadened and reduced in height as expected. However, a lowering of the mean coordination number of chloride ions around each zinc ion at this temperature was interpreted as the introduction of voids into the network structure, and was related to the density change over this temperature range. To investigate this change in coordination, information on coordination number distributions at various temperatures for  $\text{ZnCl}_2$  from

computer simulations is desirable. Previous simulations have been molecular dynamics simulations at high temperatures, because of the low ionic diffusion rates in  $\text{ZnCl}_2$  at lower temperatures, and have not given the required coordination number information. A Monte Carlo simulation at lower temperatures would be sufficient.

### 9.2.2 The Effect of a 'Structure Breaking' Alkali Halide on the Structure of a Network Liquid

The local tetrahedral coordination of anions around each cation in liquid zinc chloride was found to be stable upon addition of potassium chloride, and  $\text{ZnCl}_4^{2-}$  structural units were observed at high KCl concentration. From the calculated mean coordination numbers of chloride ions around each zinc ion, it was concluded that the species  $\text{ZnCl}_3^-$  and  $\text{ZnCl}_2$  do not exist in significant concentrations in these mixtures. However, there is evidence from the coordination number that species of a lower coordination are formed at higher temperatures in the lower KCl concentration mixtures. This is consistent with the observed drop in  $n_{\text{ZnCl}}$  for pure molten  $\text{ZnCl}_2$ . The maximum entropy method of structure factor analysis proved particularly useful in extracting information in the low  $r$  region of  $G(r)$  from the data sets for the high KCl concentration samples where, due to the low zinc concentration, the principal peak in  $g_{\text{ZnCl}}(r)$  becomes hidden by ripples in  $G(r)$  when straightforward Fourier transformation is applied to the data.

In contrast to the stability of the local structure in  $\text{ZnCl}_2$ , the structure of KCl is readily perturbed by the addition of small concentrations of  $\text{ZnCl}_2$ , due to the formation of  $\text{ZnCl}_4^{2-}$  units. Indeed, from model fits to the data using the recombined partials for the pure salts, the anion structure at 66.7% KCl concentration was seen to be much more like that of pure  $\text{ZnCl}_2$  than that of pure KCl.

Contrary to what was expected, the addition of a 'structure breaking' alkali halide did not reduce the magnitude of the pre-peak observed for pure  $\text{ZnCl}_2$ . Indeed, if this peak is due only to zinc-zinc correlations, then it does in fact increase considerably. The origin of this observed

behaviour cannot be deduced from this diffraction study alone. One possible explanation offered was that the alkali ion was now making a contribution to the intermediate range ordering through zinc-alkali or alkali-alkali correlations. In the absence of suitable potassium and zinc isotopes, a possible means of investigating this suggestion would be a diffraction study of the  $\text{ZnCl}_2\text{-LiCl}$  system using the  $^7\text{Li}$  isotope. From Raman scattering studies, this system is believed to behave in a similar way, but it would be wrong to assume that  $\text{Li}^+$  ions occupy the same sites within the liquid as  $\text{K}^+$  ions. However, a contribution to the pre-peak from partial structure factors involving  $\text{Li}^+$  ions, if observed, would show that alkali cations can play a role in producing intermediate range order. Information on the local structure around each potassium ion can be gained from an EXAFS study of these mixtures, and would be useful in considering the possible role of the alkali ion in the structure of these solutions.

Another possible explanation which was considered was that intermediate range ordering not involving alkali cations was persisting in the melt even when the network was broken, due to preferential alignment between  $\text{ZnCl}_4^{2-}$  units, some of which were now isolated and therefore free from any constraints of the network. Preferential alignment could arise from either packing of  $\text{ZnCl}_4^{2-}$  units or from directional interionic forces. A molecular dynamics study of these mixtures, similar to the ones carried out by Saboungi et. al. (1984) and Blander et. al. (1986) on  $\text{AX}_3\text{-MX}$  solutions, would answer the question of whether purely Coulombic potentials are sufficient to produce stable  $\text{ZnCl}_4^{2-}$  units, as well as ordering between these units. This ordering should be revealed by preferred Zn-Zn distances and Zn-Cl-Zn angles between corner sharing  $\text{ZnCl}_4^{2-}$  units, as well as preferred Zn-Zn-Zn angles between isolated units.

Perhaps the region of the phase diagram of greatest interest is that between the 66.7% and 81% KCl concentrations. It is at 66.7% KCl concentration that there are sufficient chloride ions for every zinc ion to be fourfold coordinated by non-sharing anions, and it is between these concentrations that most of the structural change is

observed to occur. Unfortunately, it proved difficult to produce samples within this region, due to chemical attack of the quartz and container fracture upon cooling. In order to more fully understand the change in the anion structure over this concentration region, a diffraction experiment using a 66.7% KCl concentration sample and isotopic substitution of chlorine has been proposed on LAD. This will use the isotopes  $^{35}\text{Cl}$ ,  $^{37}\text{Cl}$  and  $^{\text{mix}}\text{Cl}$  (made from a mixture of natural chlorine and  $^{37}\text{Cl}$ ) and should yield  $S_{\text{ClCl}}(Q)$  to reveal what is happening to the anion structure in this transition region from a pure  $\text{ZnCl}_2$ -like structure to that of pure KCl. In addition, this proposed study will yield a linear combination of the  $S_{\text{ZnCl}}(Q)$  and  $S_{\text{KCl}}(Q)$ . Due to the clear distinction between these partials in the pure salts (in particular the separation of the two principal peaks in  $G(r)$ ), this should provide information on the K-Cl partial as well as a more accurate determination of the principal peak in  $g_{\text{ZnCl}}(r)$  which, if the constraints of the network are relaxed, should be sharper and narrower than in pure  $\text{ZnCl}_2$ .

### 9.2.3 The Addition of Excess Metal to a Molten 2:1 Salt

From the two diffraction studies of nickel dissolved in molten nickel bromide and nickel iodide, the closely packed anion structure was seen to be virtually unperturbed by the addition of 9 molar percent of nickel metal. Similarly, the cation-anion structure showed only slight changes and the mean coordination number of anions around each cation remained at about 4.6 for  $\text{NiBr}_2$ , which indicated that the excess nickel was occupying similar tetrahedrally coordinated sites within the closely packed anion structure. Changes to the structure of  $\text{NiBr}_2$  were observed in the cation-cation partial structure. The cation species was seen to be less structurally ordered overall, with significant loss of amplitude for the peaks and troughs in  $g_{\text{NiNi}}(r)$ . There was no evidence for the formation of subhalide complexes containing several cations, as has been suggested in the past.

A model has been proposed in which the nickel dissolves according to the equation  $\text{Ni} \rightarrow \text{Ni}^{2+} + 2e^-$ , imparting mobile electrons to the melt. The loss of structural ordering

between the cations and the reduction in the depth of the 'Coulomb dip' in  $S_{+-}(Q)$  has been attributed to the effect of screening by these electrons. To substantiate this model, it would be useful to measure the electrical conductivity of both a pure molten nickel halide and nickel in nickel halide solutions. No such measurements have yet been published even for the pure salts, probably because of the considerable problems of making electrical contact with high temperature, volatile corrosive liquids. Attempts have been made to measure the a.c. electrical conductivity of molten  $\text{NiBr}_2$  and  $\text{NiI}_2$ , using a sample tube consisting of a capillary U-tube with one end closed and the other end open so that the tube could be filled with molten sample by pressurising the liquid to five atmospheres with an inert gas. Electrical contact was made by graphite plugs inserted and clamped into ultrasonically drilled holes in the capillary tube - the outside of the tube was also pressurised. However, the problems of containment and sample vaporization require that very tightly fitting plugs and even higher pressures than were achievable with the existing apparatus are required. Glass to metal seals using noble metals, such as rhodium or iridium, may be a more successful way of making electrical contact if these metals can be sealed into fused quartz.

Loss of structural ordering of the cation species in molten 2:1 salts has previously been attributed to enhanced mobility of the cation. Wood et. al. (1988) interpreted a rather structureless  $g_{\text{II}}(r)$  for molten  $\text{NiI}_2$  as indicating highly mobile  $\text{Ni}^{2+}$  ions in the melt and the possibility of superionic behaviour below the melting point. This was later substantiated by an inelastic neutron scattering study. A similar study of molten  $\text{NiBr}_2$  and  $\text{NiBr}_2+\text{Ni}$ , using isotopic substitution of nickel, would give information about the diffusion of nickel ions through the anion structure for the pure salt and the solution. This would confirm whether the loss of structural ordering of the nickel species upon addition of excess metal does indeed reflect an increase in cation mobility, rather than just a loss of ordering between the cation sites themselves. Such an experiment could make use of two 'zero' nickel isotopic mixtures with different incoherent scattering cross-sections in order to obtain the

nickel self dynamical structure factor,  $S_{Ni}^S(Q, \omega)$ , from the double differential cross-section

$$\frac{d^2\sigma}{d\Omega d\omega} = \frac{N}{4\pi} \frac{k}{k_0} \left\{ C_{Ni} \sigma_{Ni}^{inc} S_{Ni}^S(Q, \omega) + C_I \sigma_I^{inc} S_I^S(Q, \omega) \right. \\ \left. + C_{Ni} \sigma_{Ni}^{coh} S_{NiNi}(Q, \omega) + C_I \sigma_I^{coh} S_{II}(Q, \omega) \right. \\ \left. + 2(C_{Ni} C_I \sigma_{Ni}^{coh} \sigma_I^{coh})^{1/2} S_{NiI}(Q, \omega) \right\}$$

### 9.3 The State of Neutron Diffraction Instrumentation for Molten Salts

The use of the D4B diffractometer has enabled the separation of the partial structure factors for the nickel halides, including the least well determined partial  $S_{NiNi}(Q)$ . Furthermore, changes in this partial as nickel metal is added to  $NiBr_2$  have been resolved by this instrument. This experiment would not have been feasible on LAD, which currently has the highest count rate of any pulsed liquids diffractometer available. However, the high momentum transfers available from ISIS and LAD has enabled the determination of the structure of molten zinc halides with a real space resolution which is not attainable using reactor sources. Thus both steady-state and pulsed neutron sources have made a unique contribution to the work presented in this thesis.

The arrival of SANDALS (the Small Angle Diffractometer for Liquids and Amorphous Samples) at ISIS will extend the  $Q$  range over which good statistical accuracy is attainable from  $Q \sim 0.1 \text{ \AA}^{-1}$  to  $Q \sim 40 \text{ \AA}^{-1}$ . The detectors on this instrument will be concentrated at low angles so that effects due to inelastic scattering are minimised - a feature which will be particularly useful for diffraction from light elements. The use of zinc sulphide scintillator detectors should provide the high count rate necessary for isotopic substitution experiments with a resolution which is sufficient for liquid diffraction experiments.

#### 9.4 Concluding Remarks

From the studies of molten 2:1 salts to date, the tetrahedral arrangement of anions around each cation has been found to be a common one for salts with large anion to cation size ratios. It is only  $\text{MgCl}_2$  which has been observed not to possess such a structure. This local structure appears to be very stable, and shows no immediate change upon addition of excess metal or excess anions (in the form of an alkali halide). Whether this latter result is generally the case for molten 2:1 salts, or is just true for  $\text{ZnCl}_2$ , is not yet known. An experiment to study the system  $\text{MgCl}_2$ -KCl across the composition range using LAD is envisaged, in order to investigate what happens to the short and medium range structure in a non-tetrahedral 2:1 salt upon addition of an alkali halide.

Intermediate range ordering between the cations in molten 2:1 salts appears, from the trend observed so far, to arise from a directional dependence of interionic forces due to covalent character of the bonding. However, the electronic structure of the cation also appears to play a role. There is a need for both more theoretical studies, as well as structural studies of other transition metal halides such as  $\text{CuCl}_2$ , which possesses a similar electronegativity difference to  $\text{ZnI}_2$  and  $\text{NiBr}_2$  but a much smaller ion size ratio of 1.89, in order to investigate further the roles of electronic structure and ion size in determining the structure of molten 2:1 salts.

## REFERENCES

- Aliotta, F., Maisano, G., Migliardo, P., Vasi, C.,  
Wanderlingh, F., Pedro Smith, G. and Triolo, R., 1981, J.  
Chem. Phys., 75, 613
- Angell, C.A. and Wong, J., 1970, J. Chem. Phys., 53, 2053
- Bacon, G.E., 1962, "Neutron Diffraction", 1st edition, Oxford  
University Press, London
- Ballone, P., Pastore, G., Thakur, J.S. and Tosi, M.P., 1986,  
Physica B, 142, 294
- Baranyai, A., Ruff, I. and McGreevy, R.L., 1986, J. Phys. C,  
19, 453
- Bertagnolli, H., Chieux, P. and Zeidler, M.D., 1976, Mol.  
Phys., 32, 759
- Bhatia, A.B. and Thornton, D.E., 1970, Phys. Rev. B, 2, 3004
- Biggin, S. and Enderby, J.E., 1981a, J. Phys. C, 14, 3129
- Biggin, S. and Enderby, J.E., 1981b, J. Phys. C, 14, 3577
- Biggin, S., Gay, M. and Enderby, J.E., 1984, J. Phys. C, 17,  
977
- Blander, M., Saboungi, M-L. and Rahman, A., 1986, J. Chem.  
Phys., 85, 3995
- Blech, I.A. and Averbach, B.L., 1965, Phys. Rev. A, 137, 1113
- Bockris, J.O'M., Crook, E.H., Bloom, H. and Richards, N.E.,  
1960, Proc. Roy. Soc. A, 255, 558
- Born, M. and Green, H.S., 1947, Proc. Roy. Soc. A, 190, 455

- Bredig, M.A., 1964, in "Molten Salt Chemistry", ed. Blander, M., Interscience
- Bredig, M.A. and Johnson, J.W., 1960, J. Phys. Chem., 64, 1899
- Brooker, M.H. and Huang, C.H., 1980, Can. J. Chem., 58, 168
- Clarke, J.H.R., Hartley, P.J. and Kuroda, Y., 1972, J. Phys. Chem., 76, 1831
- Copestake, A.P. and Evans, R., 1982, J. Phys. C, 15, 4961
- Coulson, C.A. and Rushbrooke, G.S., 1939, Phys. Rev., 56, 1216
- Desa, J.A.E., Wright, A.C., Wong, J. and Sinclair, R.N., 1982, J. Non-Cryst. Sol., 51, 57
- Derrien, J.Y. and Dupuy, J., 1975, J. Physique C, 36, 191
- Duke, F.R. and Fleming, R.A., 1957, J. Electrochem. Soc., 104, 251
- Durham, P.J. and Greenwood, D.A., 1976, Phil. Mag., 33, 427
- Edwards, F.G., 1977, Ph.D. Thesis, University of Leicester, "The Structure of Molten Salts"
- Edwards, F.G., Enderby, J.E., Howe, R.A. and Page, D.I., 1975, J. Phys. C, 8, 3483
- Edwards, F.G., Howe, R.A., Enderby, J.E. and Page, D.I., 1978, J. Phys. C, 11, 1053
- Ellis, R.B., 1960, Chem. Eng. News, 38, 96
- Ellis, R.B., 1966, J. Electrochem. Soc., 113, 485
- Enderby, J.E., North, D.M. and Egelstaff, P.A., 1966, Phil. Mag., 14, 961
- Faber, T.E. and Ziman, J.M., 1965, Phil. Mag., 11, 153

- Fairbanks, M.C., 1987, Ph.D. Thesis, University of Oxford,  
"Neutron and Light Scattering Studies of Molten Salts"
- Galka, J., Moscinski, J. and Suski, L., 1972, J. Chem.  
Thermodynamics, 4, 849
- Gardner, P.J. and Heyes, D.M., 1985, Physica B, 131, 227
- Gartrell-Mills, P.R. and McGreevy, R.L., 1988, Clarendon Lab.  
Rep., 16/88
- Grantham, L.F. and Yosim, S.J., 1966, J. Chem. Phys., 45,  
1192
- Gull, S.F. and Skilling, J., 1984, in "Indirect Imaging", ed.  
Roberts, J.A., Cambridge University Press, London
- Gunn, J.M.F., 1988, in "Neutron Scattering at a Pulsed  
Source", ed. Newport, R.J., Rainford, B.D. and Cywinski,  
R., Adam-Hilger, Bristol
- Hansen, J.P. and McDonald, I.R., 1986, "Theory of Simple  
Liquids", 2nd edition, Academic Press, London
- van Hove, L., 1954, Phys. Rev., 95, 249
- Howe, M.A. and McGreevy, R.L., 1988, Phil. Mag. B, 58, 497
- Howells, W.S., 1986, RAL Report RAL-86-042, "The Analysis of  
Structure Factor Data on a Pulsed Source"
- Huggins, M.L. and Mayer, J.E., 1933, J. Chem. Phys., 1, 643
- Ichikawa, K. and Matsumoto, T., 1981, Phys. Lett., 83A, 35
- Itoh, M., Sakai, K. and Nakamura, T., 1982, Inorg. Chem., 21,  
3552
- Janz, G.J., 1967, "Molten Salts Handbook", Academic Press,  
New York

- Jiang, Z., Hu, X., and Hou, L., 1986, J. Non-Cryst. Sol., 80, 543
- Johnson, J.W., Cubicciotti, D. and Kelley, C.M., 1958, J. Chem. Phys., 62, 1107
- Katz, I. and Rice, S.A., 1972, J. Am. Chem. Soc., 94, 4824
- Kirkwood, J.G., 1935, J. Chem. Phys., 3, 300
- Kirkwood, J.G. and Buff, F.P., 1951, J. Chem. Phys., 19, 774
- de Leeuw, S.W., 1978a, Mol. Phys., 36, 103
- de Leeuw, S.W., 1978b, Mol. Phys., 36, 765
- de Leeuw, S.W., 1979, Mol. Phys., 37, 489
- Littlewood, P., 1981, Phys. Rev. B, 24, 1710
- Locke, J., Messolaras, S., Stewart, R.J., McGreevy, R.L. and Mitchell, E.W.J., 1985, Phil. Mag. B, 51, 301
- Lorch, E., 1969, J. Phys. C, 2, 229
- Lovering, D.G. (editor), 1982, "Molten Salt Technology", 1st edition, Plenum Press, New York
- Ma, F., Lau, J. and Mackenzie, J.D., 1986, J. Non-Cryst. Sol., 80, 538
- McGreevy, R.L., 1981, Ph.D. Thesis, University of Oxford, "The Study of the Structure and Dynamics of Molten Salts by Neutron Scattering"
- McGreevy, R.L., 1987, Sol. St. Phys.: Adv. Res. Appl., 40, 247
- McGreevy, R.L. and Mitchell, E.W.J., 1982, J. Phys. C, 15, 5537

- McGreevy, R.L., Baranyai, A. and Ruff, I., 1986, Phys. Chem. Liq., 16, 47
- Mackenzie, J.D. and Murphy, W.K., 1960, J. Chem. Phys., 33, 366
- March, N.H. and Tosi, M.P., 1984, "Coulomb Liquids", 1st edition, Academic Press, London
- Mitchell, E.W.J., Poncet, P.F.J. and Stewart, R.J., 1976, Phil. Mag., 34, 721
- Nachtrieb, N.H., 1974, Adv. Chem. Phys., 31, 465
- Newport, R.J., Howe, R.A. and Wood, N.D., 1985, J. Phys. C, 18, 5249
- North, D.M., Enderby, J.E. and Egelstaff, P.A., 1968, J. Phys. C, 1, 784
- Paalman, H.H. and Pings, C.J., 1962, J. Appl. Phys., 33, 2635
- Page, D.I. and Mika, K., 1971, J. Phys. C, 4, 3034
- Pastore, G., Ballone, P. and Tosi, M.P., 1986, J. Phys. C, 19, 487
- Pauling, L., 1960, "The Nature of the Chemical Bond", 3rd edition, Cornell University Press, New York
- Perry, G., 1989, private communication
- Pitzer, K.S., 1962, J. Am. Chem. Soc., 84, 2025
- Placzek, G., 1952, Phys. Rev., 86, 377
- Powles, J.G., 1973, Adv. Phys., 22, 1
- Rice, S.A., 1961, Discuss. Faraday Soc., 32, 181

- Rovere, M. and Tosi, M.P., 1986, Rep. Prog. Phys., 49, 1001
- Saboungi, M-L., Rahman, A. and Blander, M., 1984, J. Chem. Phys., 80, 2141
- Sakai, K., Nakamura, T., Umesaki, N. and Iwamoto, N., 1984, Phys. Chem. Liq., 14, 67
- Salstrom, E.J., 1933, J. Am. Chem. Soc., 55, 1029
- Sears, V.F., 1984, "Thermal Neutron Scattering Lengths and Cross-Sections for Condensed-Matter Research", Atomic Energy of Canada Ltd., Chalk River Nuclear Labs., AECL-8490
- Shannon, C.E., 1948, Bell Sys. Tech. J., 27, 379 and 623
- Shore, J.E. and Johnson, R.W., 1980, IEEE Trans., IT-26, 26
- Sinclair, R.N. and Wright, A.C., 1974, Nucl. Inst. Meths., 114, 451
- Skilling, J. and Bryan, R.K., 1984, Mon. Not. Roy. Astr. Soc., 211, 111
- Strange, P. and Barnes, A.C., 1985, J. Phys. F., 15, L263
- Susic, M.V. and Mentus, S.V., 1975, J. Chem. Phys., 62, 744
- Vineyard, G.H., 1954, Phys. Rev., 96, 93
- Warren Jr., W.W., 1986, 5th Int. Symp. on Molten Salts, ed. Saboungi, M-L., Johnson, K.E., Newman, D.S. and Inman, D., Proc. Electrochem. Soc., 86-1
- Wilson, E.G., 1963, Phys. Rev. Lett., 10, 432
- Windsor, C.G., 1981, "Pulsed Neutron Scattering", 1st edition, Taylor and Francis, London

- Wong, J. and Lytle, F.W., 1980, J. Non-Cryst. Sol., 37, 273
- Wood, N.D., 1987, Ph.D. Thesis, University of Leicester, "The Study of the Structure of Molten Nickel Halides by Neutron Scattering"
- Wood, N.D., 1989, private communication
- Wood, N.D. and Howe, R.A., 1988, J. Phys. C, 21, 3177
- Wood, N.D., Howe, R.A., Newport, R.J. and Faber Jr., J., 1988, J. Phys. C, 21, 669
- Woodcock, L.V., Angell, C.A. and Cheeseman, P., 1976, J. Chem. Phys., 65, 1565
- Wright, A.C. and Leadbetter, A.J., 1976, Phys. Chem. Glasses, 17, 122
- Yarnell, J.L., Katz, M.J., Wenzel, R.G. and Koenig, S.H., 1973, Phys. Rev. A, 7, 2130
- Yvon, J., 1935, "La Théorie Statistique des Fluides et l'Equation d'Etat", Actualités Scientifiques et Industrielles, 203, Hermann, Paris